Swansea
University

Prifysgol
Abertawe

College of Engineering

Engineering Doctorate Research Project

2016 - 2021

**Investigation of Corrosion Mechanisms of Coated and
Uncoated Magnesium Alloys**

Name: **Christos Kousis**

Supervisor: **Professor Geraint Williams**

Discipline: **Materials Engineering**

Investigation of Corrosion Mechanisms of Coated and Uncoated Magnesium Alloys

Christos Kousis

A thesis submitted to Swansea University in fulfilment of the requirements for the Degree of Doctor of Engineering
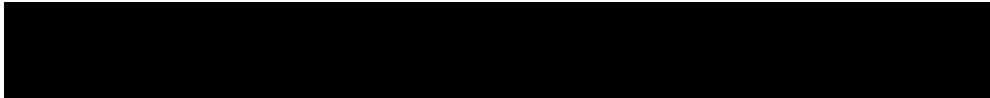
College of Engineering, Swansea University, 2021
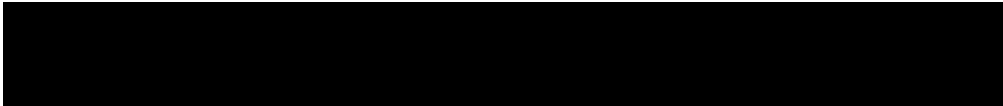
Christos Kousis

Declarations

Statement 1

This work has not previously been accepted in substance for any degree and is not being concurrently submitted in candidature for any degree.

Signed…… █████████████████████████████

Date..05/09/2021..

Statement 2

This thesis is the result of my own investigations, except where otherwise stated. Other sources are acknowledged by footnotes giving explicit references.

Signed:… ████████████████████████████

Date:…………………………….05/09/2021...
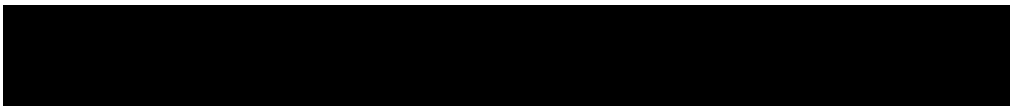
Statement 3

I hereby give consent for my thesis, if accepted, to be available for photocopying and for inter-library loan, and for the title and summary to be made available to outside organisations.

Signed:......... █████████████████████████████

Date:...................…………….05/09/2021..

Statement 4

The University's ethical procedures have been followed and, where appropriate, that ethical approval has been granted.

Signed:...... █████████████████████████████

Date:...................…………….05/09/2021..

Abstract

The corrosion-driven organic coating failure of Mg alloys and in particular the E717 alloy was investigated using a combination of in-situ Scanning Kelvin Probe (SKP) analysis and time-lapse photography where two principal failure mechanisms were identified: cathodic delamination and filiform corrosion. Initiation of underfilm corrosion by application of group I chloride salt to a coating defect produced a cathodic-driven coating delamination. The delamination distance increased linearly with time and the delamination occurred both in the presence and absence of oxygen. Post-corrosion elemental analysis of the delaminated regions using secondary-ion mass spectrometry revealed an abundance of group I cation, but no chloride. Experiments using the SKP and Stratmann-type Mg samples showed that the delamination rates remained linear even at protracted holding times and were insensitive to the type of group I cation present in the initiating electrolyte. Additional experiments on AZ31 and AZ91 Mg alloys revealed that both alloys are susceptible to organic coating delamination with the latter alloy being the most resistant to coating deadhesion. The mechanism was discussed in terms of anodic dissolution at the defect coupled predominantly with underfilm hydrogen evolution, producing organic coating disbondment under conditions where cations are able to transport ionic current within a region of increased pH.

The second focus of this thesis was to study the filiform corrosion (FFC) of organic coated E717, AZ31 and AZ91 Mg alloys. The FFC was inoculated by applying $MgCl_2$, HCl and $FeCl_2$ in a coating defect and the FFC propagation rates were quantified by determining the underfilm corroded area with time, which were shown to increase as a function of $log[Cl^-]$, remain unaffected by the absence of oxygen, but strongly dependent on the relative humidity of the holding environment. SEM-EDX surface analysis of FFC affected regions was used in combination with in-situ SKP mapping to elucidate the mechanism of FFC propagation, where chloride-induced anodic dissolution at the disbondment front is coupled with the reduction of water on a cathodically activated corroded surface behind with progressive Cl^- entrapment in the FFC tail.

Finally, the localised corrosion behaviour of the E717 Mg alloy immersed in chloride-containing electrolytes was investigated using an in-situ Scanning Vibrating Electrode Technique (SVET) coupled with Time-lapse Imaging (TLI). The localised corrosion was characterised by discrete local anodes corresponding with the leading edges of dark filiform-like features that combine with time to produce a mobile anodic front leaving a cathodically activated corroded surface behind similar to what was observed with the FFC mechanism. Breakdown potential, measured using time-dependent free corrosion potential transients and potentiodynamic polarisation at neutral and high alkalinity respectively, were shown to vary with the $log[Cl^-]$ and the time for corrosion initiation was progressively decreased with increasing chloride concentration.

Acknowledgements

Table of Contents

List of Figures

List of Symbols and Abbreviations

A	Ampere
E	Electrode potential
E$_b$	Breakdown potential
E$_{corr}$	Free corrosion potential
E$_{intact}$	Corrosion potential at intact regions
F	Faraday's constant (96487 C mol^{-1})
g	Gram
h	Hour
Hz	Hertz
I	Current
I$_{corr}$	Corrosion current
J$_z$	Normal current density
J$_a$	Area-averaged anodic current density
K	Degrees Kelvin
m	Metre
min	Minute
mm	Millimetre
mV	Millivolt
Sec	Seconds
V	Volt
wt.(%)	Weight percentage
x, y, z	Directional co-ordinates
μm	Micrometre

EDM	Electric Discharge Machining
EDS	Energy Dispersive X-Ray Spectroscopy
FFC	Filiform Corrosion
HE	Hydrogen Evolution
NDE	Negative Difference Effect
OCP	Open-Circuit Potential
ppm	Parts Per Million
PVB	Polyvinyl Butyral
RH	Relative Humidity
SCE	Saturated Calomel Electrode
SEM	Scanning Electron Microscopy
SHE	Standard Hydrogen Electrode
SiC	Silicon Carbide
ToF-SIMS	Time of Flight - Secondary Ion Mass Spectrometry
SKP	Scanning Kelvin Probe
SVET-TLI	Scanning Vibrating Electrode Technique - Time-Lapse Imaging
TeMg	Total Mg Loss

Overview

The use of low-density materials like Magnesium (Mg) alloys is finding increased application in the automotive industry because of the need to increase fuel efficiency and to reduce CO_2 emissions by lowering the weight of the automotive bodies. Applications of Mg alloys in the transportation market segment is limited due to the difficulties in achieving the desired corrosion resistance, especially in the presence of chloride ions in aqueous media. The relatively poor corrosion resistance of Mg alloys originates from magnesium's high chemical activity. Consequently, Mg alloy surfaces need to be coated to improve the corrosion resistance for most of their applications and understanding the corrosion behaviour of coated Mg alloys is key for levelling their practical applications and unhindering their usage. The research conducted in this thesis was directed to achieve this by investigating corrosion-driven coating failures of organic coated Mg alloys, but also to study the corrosion behaviour of uncoated Mg alloys (E717 alloy) in dilute chloride containing aqueous solutions.

Chapter 3: The failure mechanism of model organic coatings from Mg alloy surfaces is characterised by a combination of in-situ Scanning Kelvin Probe and time-lapse photography. Upon identifying a distinct type of coating failure in the presence of group I chloride salts, a further aim was established, to investigate and characterise the controlling factors in organic coating delamination in order to elucidate the prevailing disbondment mechanism.

Chapter 4: A further study on the organic coating delamination of the E717 Mg alloy along with other technologically important AZ-series Mg alloys. Results are presented from the usage of the Scanning Kelvin Probe and a different experimental sample set-up to answer some questions risen from Chapter 3 regarding the cathodic coating disbondment from Mg alloy surfaces.

Chapter 5: A second corrosion-driven coating failure mechanism (anodic disbodnment) of organic coated Mg alloys is systematically investigated using in-situ time-lapse photography and the Scanning Kelvin Probe. Factors such as chloride ion concentration, oxygen and relative humidity are studied to ascertain their influence on the underfilm corrosion rates.

Chapter 6: The localised corrosion behaviour of E717 magnesium alloy immersed in chloride-containing electrolyte is studied using the Scanning Vibrating Electrode Technique (SVET)

coupled with time-lapse imaging. These results are backed up by conventional electrochemical methods, open circuit potential (OCP), potentiodynamic measurements as well as volumetric hydrogen gas capture, with these methods also being used to determine the influence of chloride ion concentration on the localised corrosion of the E717 alloy under immersion conditions.

Background

1.1 Introduction

Magnesium (Mg) is the 8th most abundant element on earth, making 0.1% by mass of the oceans and 2% by mass of the earth's crust and it is one of the lightest structural metals with a density of 1.7 g/cm^3 [1]. It can be extracted from lithospheric compounds like dolomite [$CaCO_3 \cdot MgCO_3$], magnesite [$MgCO_3$] and brucite [$Mg(OH)_2$], but also from salt brines that contain $MgCl_2$ [2,3]. Mg is a very intriguing material with many appealing properties and it has been a common option in lightweight applications, medical implant components and electronics, with one of its early uses serving as a sacrificial anode to provide cathodic protection to cast iron pipes, bridges, ship hulls and various steel structures [4].

Mg and its alloys have been utilised in the automotive and aerospace industry due to their low weight and good mechanical properties [5], in the electronics industry due to their conductivity [6] and for biomedical applications due to their biocompatibility and bioabsorbability [7]. In the automotive industry, Mg alloys have been used for casting products such as car seats and door frames, gearboxes, clutch pedals and instrument panels [8,9]. When it is compared with other engineering metals like Aluminium (Al) and steel, Mg is 35% lighter than Al and 75% lighter than steel [8]. The low weight of Mg alloys is not their only advantage, Mg alloys have an excellent strength-to-weight ratio, they are easily machined, they are nontoxic and quite importantly they can be easily recycled.

The automotive industry is currently seeking to reduce the weight of vehicles by using low-density materials like Al and Mg alloys. By replacing heavy steel components with light-weight materials like Mg alloys, the weight of the vehicle can be significantly reduced. This will lead to the reduction of Carbon Dioxide (CO_2) emissions and the improvement of fuel efficiency [8]. CO_2 is widely known as one of the main gases responsible for increasing the global temperature and transportation (ground, air and marine) accounts for approximately 20% of the total greenhouse gas emissions [10]. Reducing these emissions is an essential step to stop climate change and deal with the problem of global warming.

Researchers at the Multi-Material Lightweight Vehicle project have designed a lightweight vehicle named Mach-II (based on a Ford Fusion model) where they used Mg alloys and other lightweight

materials to reduce the weight of the vehicle by 50%. The Mach-II design contains by weight 62% Mg alloys in the closures, 100% Mg alloys in the sub-frames, 54% Mg alloys in the chassis and 6% Mg alloys in the body-in-white [11]. The schematic diagram in Figure 1.1 [11] demonstrates the percentage of materials used for the body in white and closures for the Mach-II vehicle designed by Vehma, Ford and the U.S Department of Energy. By replacing the heavy materials used in the original Ford Fusion model according to the design in Figure 1.1, a mass reduction of 50% (761 kg) can be attained [11]. This achievement showcases the potential of Mg alloys in the automotive industry.
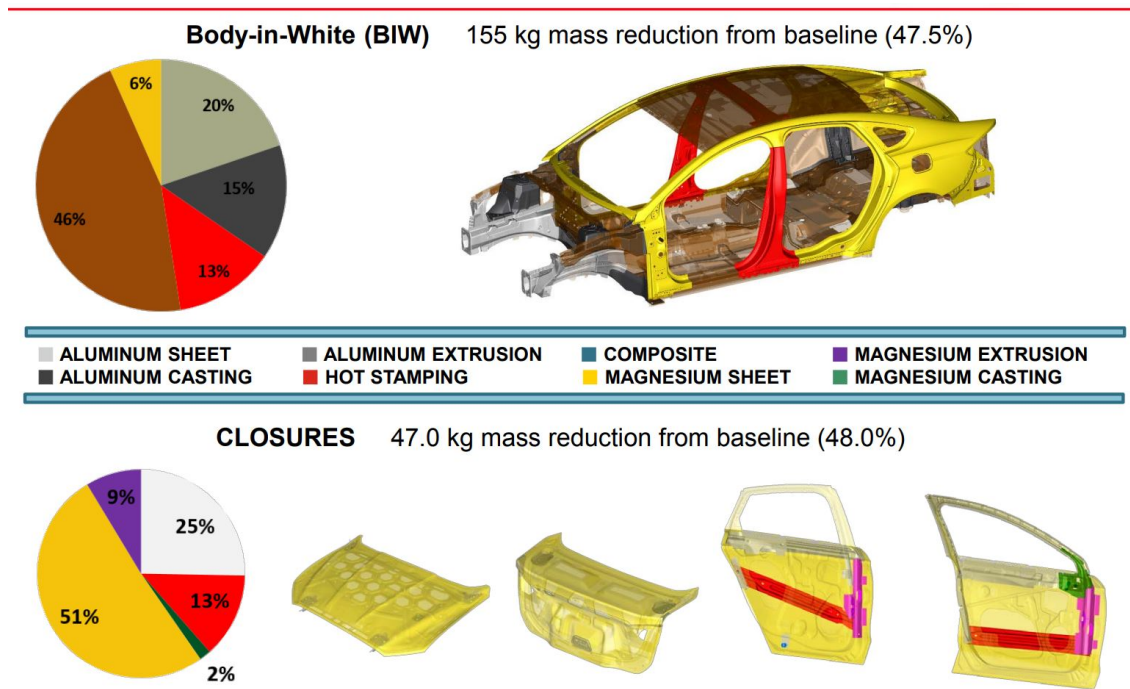
Figure 1.1: Percentages in weight of Mg materials that are used for passenger doors, hood and deck lid for the Mach II design from Vehma/Ford/U.S. DOE Multi-Material Lightweight Vehicle project [11].

On the other hand, the Achilles' heel of Mg is its notably poor corrosion resistance that significantly has hindered its potential in these applications [6]. Mg and its alloys are prone to galvanic corrosion due to their high chemical reactivity and low open-circuit potential. In most applications, the Mg alloys are the active anode when they are in contact with common metals like stainless steel and

Al alloys [12–14] due to their negative potential. Generally, the annual direct cost of corrosion is extremely high, and it is estimated that the cost worldwide is around £2 trillion, which is ca. 3.4% of the global Gross Domestic Product. It is estimated that by using corrosion prevention methods, this amount can be reduced by 15–35% [15].

A lot of effort has been done to increase the corrosion performance of the Mg and its alloys over the last years. One strategy is to use surface treatments capable of protecting Mg and its alloys from corrosion. These protection treatments can be thermal spray, physical vapour deposition, electro-deposition, conversion or organic/polymer coatings [16,17]. It is very common to alloy Mg with elements such Al, Zinc (Zn), Manganese (Mn) and Rare Earth elements (RE) including Cerium (Ce), Neodymium (Nd) and Lanthanum (La) to dramatically increase the corrosion resistance and mechanical properties of Mg [18–20]. Mg alloys like the E717 (ZE10A type) that contain Zr and Nd have been used to warm forming of a door panel [21], which previously was not feasible due to the limited formability of Mg sheet [22]. Despite the many efforts and the attention given to Mg alloys, there are still many aspects about its corrosion behaviour that need to be elucidated in order to unlock its potential in the automotive industry.

1.2 Definition of Corrosion

Corrosion has been given many definitions over the past years. For this work, only metallic corrosion is considered, which can be defined as the electrochemical reaction between a material and the environment it is surrounded by [23]. A detailed and specific definition of corrosion is given in ISO 8044 and this definition is used by the Corrosion Education Manual of the European Federation of Corrosion [24]:

"Corrosion: Physicochemical interaction between a metal and its environment which results in changes in the properties of the metal and which may often lead to impairment of the function of the metal, the environment, or the technical system of which these form a part."

Most metals tend to revert to their natural and lowest energy state. When a metal is exposed in a corrosive environment, it can be observed that the metal has the tendency of returning to ore (original state). Fontana [25] in 1986, stated that corrosion could be considered as extractive metallurgy in reverse.

1.3 Aqueous Corrosion of Mg

Generally, the reactions that govern the corrosion of Mg in an aqueous environment are written as shown in the Reaction (1.1) – (1.4). More specifically, the Reaction (1.1) shows the Mg dissolution, which is the anodic reaction, while the cathodic reaction is the water reduction that predominates at such negative potentials [26]. From Reaction (1.1), there is a production of magnesium hydroxide (Mg[OH]$_2$), while Reaction (1.2) shows the production of OH$^-$ ions as well as evolution of hydrogen (H$_2$) gas [27–29].

$$Mg \rightarrow Mg^{2+} + 2e^- \text{ (Anodic Reaction)} \tag{1.1}\#$$

$$2H^+ + 2e^- \rightarrow H_2 \text{ or } 2H_2O + 2e^- \rightarrow H_2 + 2OH^- \text{ (Cathodic Reaction)} \tag{1.2}\#$$

$$Mg^{2+} + 2OH^- \rightarrow Mg(OH)_2 \text{ (Product Formation)} \tag{1.3}\#$$

$$Mg + 2H_2O \rightarrow Mg(OH)_2 + H_2 \text{ (Overall Corrosion Reaction)} \tag{1.4}\#$$
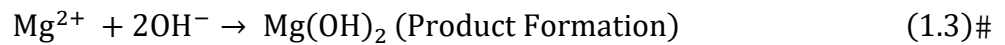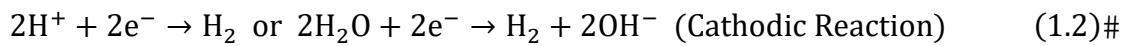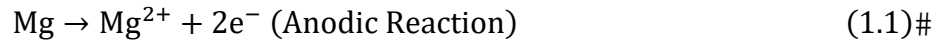
Reaction (1.4) shows the overall corrosion reaction of Mg dissolution in an aqueous environment [27]. It is expected that the corrosion reactions of Mg alloys are similar to those (Reaction 1.1-1.4) for pure Mg [6].

When Mg is exposed to an aqueous environment the entire surface of Mg will be covered by a dual-layer mixture of MgO and a porous Mg(OH)$_2$ layer (dissolution-precipitation) with the thickness of the film depending on the immersion time in the aqueous media (see Figure 1.2) [30–34]. The Mg(OH)$_2$ outer layer that results from hydration of the MgO layer thickens with time whereas the thickness of the MgO inner layer appears to remain relatively constant [31]. Taheri et al. [32] recorded the open circuit potential (OCP) of Mg immersed in pure water and they have suggested that the rise of the OCP at an initial stage is attributed to the hydration of the MgO layer, however, the film produced on the surface of Mg is considered to lack the ability to provide adequate corrosion protection. This is ascribed to the porosity of the film in the outer region, which is suggested to be created due to the stress rupture of the film occurring from the higher molar volume of the Mg(OH)$_2$ in comparison to the volume of MgO [35].
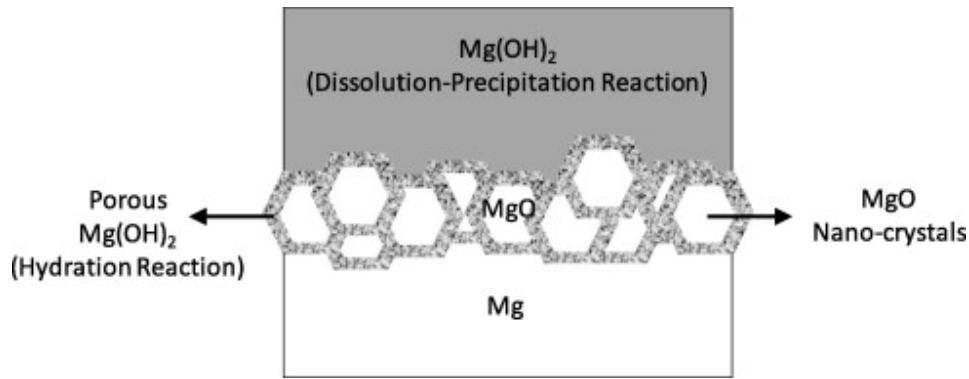
Figure 1.2: Schematic diagram of the bi-layer surface film formed on Mg after a 48 h immersion in pure H_2O [32].

1.3.1 Thermodynamics

Thermodynamics can provide valuable information about the materials that are being studied. The tendency of the metal to corrode is directly related to its standard electrode potential. The standard electrode potential of Mg is −2.6 V versus saturated calomel electrode (SCE) and −2.37 V versus a standard hydrogen electrode (SHE) making it one of the most reactive metals [36]. The considerable difference of reduction potential between the two half-reactions Reaction (1.1) (E^0_{ox} = −2.37 V (vs. SHE) and (1.2) (E^0_{red} = −0.83 V (vs. SHE)) is the thermodynamic means for initiation of Mg corrosion. The potential (E_{corr}) of a freely corroding pure Mg and its alloys in aqueous chloride (Cl) containing solution is ~ −1.4 to −1.8 V_{SCE} and the E_{corr} has been shown to decrease when the chloride concertation is increased [37]. Table 1.1 provides the standard electrode potentials of some basic metals in 1 mol dm^{-3} H$^+$ at 25 ºC.

Table 1.1: Standard Electrode Potentials (SHE) at 25 ^{0}C [36].

	Reduction Half-Reaction			Potential - E$^\theta$ / Volts
Strongest Oxidizing Agent	Fe^{3+} (aq) + e$^-$	$\rightarrow$ Fe^{2+} (aq)	**Weakest Reducing Agent**	+0.77
	Cu^{2+} (aq) + 2e$^-$	$\rightarrow$ Cu^{2+} (s)		+0.34
	2H$^+$ (aq) + 2e$^-$	**$\rightarrow$ H$_2$ (g)**		**+0.00**
	Pb^{2+} (aq) + 2e$^-$	$\rightarrow$ Pb (s)		-0.13
	Fe^{2+} (aq) + 2e$^-$	$\rightarrow$ Fe (s)		-0.44
	Zn^{2+} (aq) + 2e$^-$	$\rightarrow$ Zn (s)		-0.76
	Al^{3+} (aq) + 3e$^-$	$\rightarrow$ Al (s)		-1.66
	Mg^{2+} (aq) + 2e$^-$	$\rightarrow$ Mg (s)		-2.37
	Na^+ (aq) + e$^-$	$\rightarrow$ Na (s)		-2.71
Weakest Oxidizing Agent	K^+ (aq) + e$^-$	$\rightarrow$ K (s)	**Strongest Reducing Agent**	-2.92

1.3.2   Pourbaix Diagrams

The stability of the metal under study depends on different factors that may change depending on the environment that the metal is exposed to. Two of these factors are the pH and the oxidising/reducing power of the environment the metal is exposed to [38]. Pourbaix diagrams or (E-ph) diagrams is a useful tool that can provide invaluable information about the composition of the corrosion products and predict changes in the aqueous environment in terms of potential and pH [38]. These diagrams show the potential and pH values of the material of interest in which it will be immune to corrosion, form a passive oxide film (passivate) or corrode. Although Pourbaix diagrams can be very insightful, it is important to note that they do not provide any information with regards to the kinetics of the different reactions or the actual corrosion rates. In this thesis, most of the work is conducted on the E717 (Mg-1.25Zn), AZ31 (Mg-3Al-1Zn) and AZ91 (Mg-9Al-1Zn) Mg alloys and the Pourbaix diagrams of each primary constituent of the these alloys are shown in Figure 1.3, Figure 1.4 and Figure 1.5 [39] respectively. It is important to note, that these E-pH diagrams carry the assumption that the oxide layer is capable of passivation only if it covers the surface completely, which sometimes is not the case in practical corrosion situations [40].
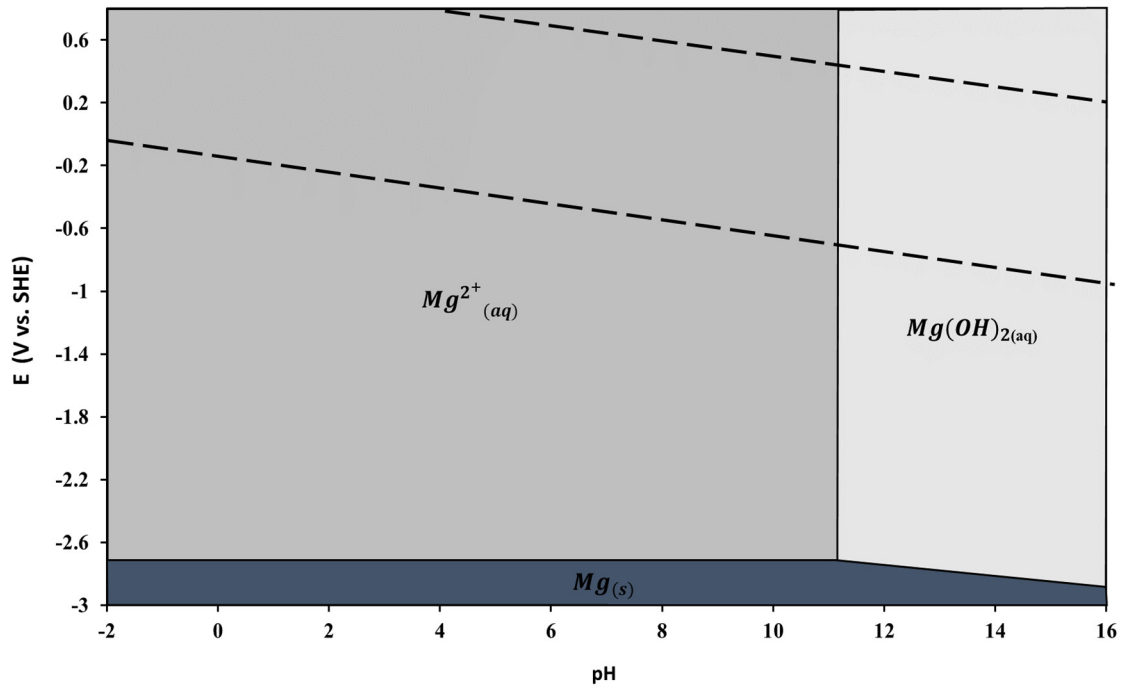
Figure 1.3: Pourbaix diagram for Mg. Passivation for pH higher than 11 and corrosion for lower than 11 [39].
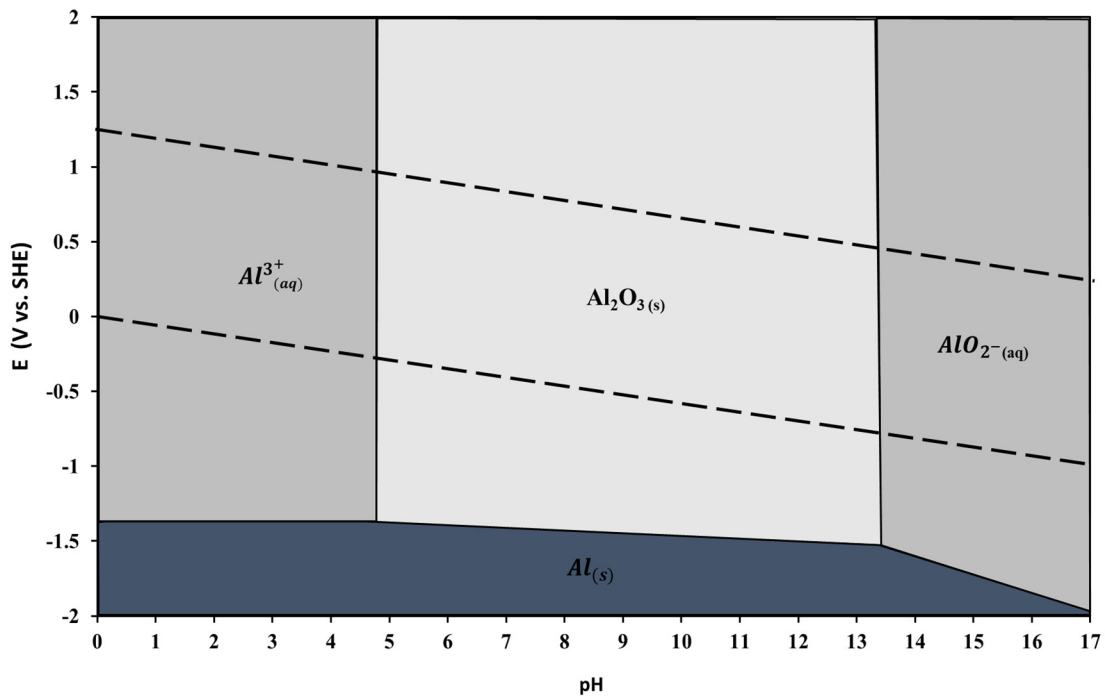
Figure 1.4: Pourbaix diagram for Al illustrating the passivation region and Al_2O_3 (pH 5 and 13). The corrosion region is in the region of below pH 5 and more than pH 13 [39].
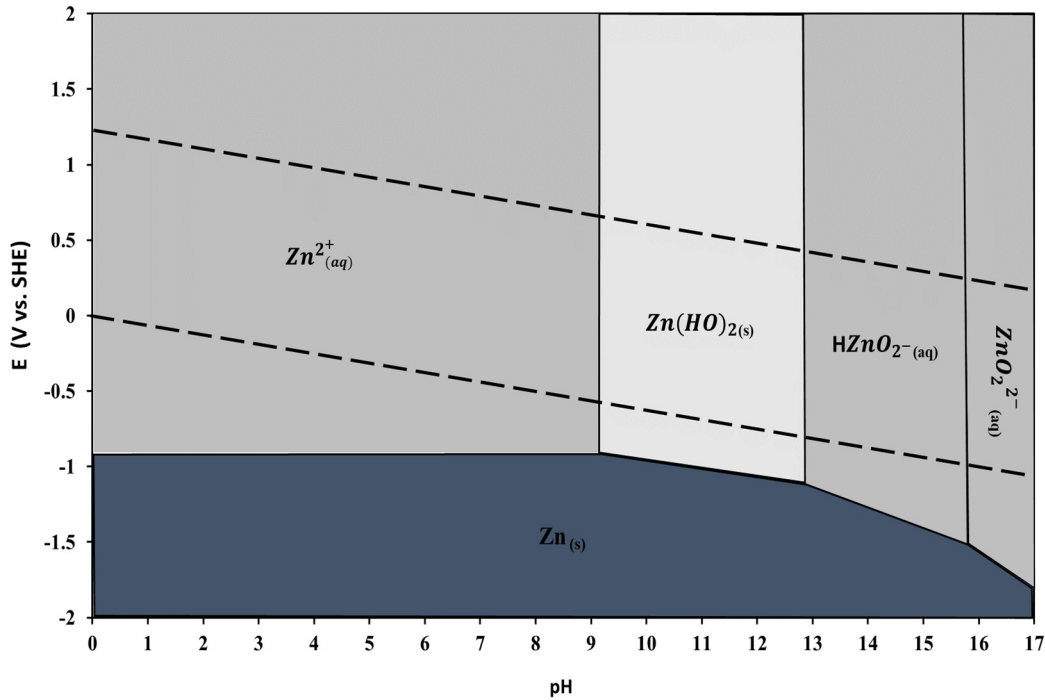
Figure 1.5: Pourbaix diagram for Zn illustrating the passivation region and the corrosion region in pH greater than 13 and less than pH 9 [39].

Finally, although these diagrams can provide invaluable information about the metal under study and can be used as a guide, one must take into consideration that this methodology will hold true for a simple system e.g a pure Mg in water. The Pourbaix diagrams will change and become more complicated when the metal under study is heavily alloyed with other metals and immersed in more complicated aqueous solutions. Although Mg is passive in alkaline solutions, if it is alloyed with other metals e.g. Zn, its corrosion behaviour will change accordingly, and the alloy system will behave differently at high pH where Zn does not exhibit passivity.

1.3.3 Anomalous Hydrogen Evolution

The anomalous hydrogen evolution (HE) or commonly known as the negative difference effect (NDE), is a phenomenon that occurs on Mg and its alloys. When Mg and its alloys are immersed in aqueous solution and anodically polarised, there is an increased hydrogen evolution rate that is not very common with other metals like iron and zinc [41]. The NDE is often explained as the difference between the hydrogen evolution rate (HER) during anodic polarisation and the HER

under open circuit conditions. For an applied anodic potential (E), the HER will correspond to a higher current density value ($I_{H,appl}$) than the current density value of the HE at the free corrosion potential ($I_{H,OCP}$), and thus the difference between these current density values under these conditions will result to a negative difference effect.

One of the first researchers who reported this phenomenon was Beetz [42] in 1866, where they noted that there was an unusual evolution of hydrogen gas emanating from the Mg surface during anodic polarisation. This phenomenon has been of great interest and numerous studies have tried to explain it, however, there has not been a universally accepted mechanism. One of the first mechanisms [43] was based on the existence of univalent Mg ion (Mg^+) being responsible for the NDE [44–47] however the presence of Mg^+ species in electrolytes has not been proven experimentally [48] and there have been several studies supporting that the dissolution of Mg does not occur via the Mg^+ mechanism [26,49–57]. A relatively new interesting study [58] showed that magnesium hydride (MgH_2) species are present in the leading edges of the corrosion filaments of the Mg alloy E717 and suggested that the chemical decomposition of the MgH_2 formed during Mg dissolution may be responsible for the anomalous hydrogen evolution.

Another plausible explanation of this phenomenon is that the anomalous hydrogen evolution is driven by the surface film and the enrichment of the Mg surface with noble impurities (e.g. Fe). A detailed study by Williams and McMurray [54] demonstrated that the corrosion film formed during the anodic dissolution of Mg can efficiently support the hydrogen evolution. This phenomenon is often referred to as cathodic activation where the cathodic reaction (i.e. H_2 evolution) is enhanced by the anodic dissolution of Mg. In more detail, it has been shown by using the SVET [54] that as the film forms on the surface, the surface becomes more effective towards supporting hydrogen evolution where the previously anodic areas convert into cathodic areas and the size of these cathodic areas seem to increase with longer holding times [49,53,54,59]. It has also been noted that following Mg dissolution, the Mg surface was characterised by an increased hydrogen evolution rate over time possibly resulting from noble impurity enrichment of the Mg surface, with many researchers observing high accumulation of noble impurities in the surface film [60–63]. Other studies have claimed that previously dissolved metal impurities from the Mg matrix can re-deposit on the Mg surface and act as remote cathodic sites for hydrogen evolution [60,64–66]. However, Lysne et al. [62] proposed that the noble impurities might not contribute significantly to

the overall anodic hydrogen evolution, while Fajardo et al. [67–69] suggested that both the surface film and the impurities contribute a small fraction compared to the overall hydrogen evolution of Mg during anodic polarisation. Other researchers have shown that the rate of HE on an Mg surface covered with $Mg(OH)_2$ is faster than on pristine Mg surface suggesting that the $Mg(OH)_2$ corrosion product formed on the surface may be a possible source of cathodic activation [49,70,71]. However, it should be borne in mind that the conductivity of $Mg(OH)_2$ is relatively low (MgO is a large band-gap semiconductor), and thus the transportation of current through this film would be quite arduous.

1.3.4   Localised Corrosion and the Effects of Alloying Elements

Localised corrosion is a form of corrosion that is usually observed on bare Mg and its alloys when they are immersed in an aqueous solution. The localised corrosion in aqueous NaCl solutions is characterised by the appearance of dark corrosion products that propagate on the surface in a disk-form or a filiform-like attack. The disk-form localised corrosion attack is characterised by a black disk that expands radially with time and is more commonly observed on pure Mg (especially in more concentrated solutions) [72]. The filiform-like corrosion takes the appearance of thread-like filaments that propagate laterally in rather random directions on the surface and is observed on pure Mg and its alloys. The morphology of the localised corrosion attack is generally dependant on the type of the aqueous solution, the solution concentration (ohmic dependant) and the concentration of impurities in pure Mg samples [72].

1.3.5   Pure Mg

The localised corrosion of pure Mg has been investigated by several researchers and it has been reported that the localised corrosion can take the form of disk-like or filiform-like corrosion. One factor that affects the morphology of the localised corrosion features is the concentration of the chloride-containing aqueous media. The filiform-like localised corrosion tends to occur when pure Mg samples are immersed in more dilute chloride-containing aqueous solutions [73,74], while disk-like corrosion seems to dominate in more concentrated chloride-containing aqueous solutions [49,54,72]. The changes in the morphology of the localised corrosion of pure Mg in different levels of salinity is attributed to the conductivity of the solution denoting that these features are ohmically controlled. Williams et al. [72] have investigated the controlling factors in the localised corrosion

morphologies of pure Mg samples containing different iron impurity levels immersed in concentrated NaCl solution and they found that the samples containing Fe ≥ 280 ppm led to higher rates of localised corrosion, which take the form of disk-like features. However, when they tested higher purity Mg samples (≤ 80 ppm) in the same solution, they found that the localised corrosion took the form of filiform-like features rather than disk-like localised corrosion [53,72]. The change from disk-like to filiform-like corrosion has been suggested to take place when inadequate cathodic current is being produced on the corroded surface to sustain radial growth [72]. A visual comparison of these two localised corrosion morphologies can be seen in Figure 1.6.

Due to the localised corrosion behaviour of Mg, the SVET is a suitable tool for the investigation of this kind of phenomena and it has provided pivotal information about the mechanism of localised corrosion on pure Mg. Williams and McMurray [54] have used the SVET to elucidate certain aspects of the mechanism of localised corrosion of Mg in 0.86 M of NaCl solution and they identified that the centre of the disk-like attack is the cathode while the circumference of the expanding disk is the local anode (see Figure 1.6(i) [54]). Initially, when the sample was immersed in a concentrated aqueous solution of NaCl, the SVET detected a few cathodic spots on the surface, which was suggested to be the location of cathodic impurity particles or surface film defects [54]. Furthermore, they immersed a pure Mg sample in 0.86 M NaCl solution and measured the free corrosion potential against time and they found that there was an initial increase of potential that could attributed to the thickening of an aqueous film formed on the surface [32,54]. After 1 minute of immersion, a sharp drop of the free corrosion potential was observed that correlated to the appearance of a dark spot on the surface, which with time has expanded radially forming a disk-like corrosion feature on the surface [54]. It was proposed by the same researchers that the cathodic activation of corroding pure Mg occurs due to the presence of more noble impurity elements (Fe) that can act as cathodic reaction sites [54].

In a different study [74], a pure Mg sample was immersed in a 0.01 M NaCl solution and within minutes dark, filiform-like corrosion tracks started propagating on the surface. By using the SVET to analyse these propagating tracks, it was revealed that the leading edge of these localised corrosion filaments is strongly anodic and galvanically coupled with the hydrogen evolution on a cathodically activated corroded surface [74].
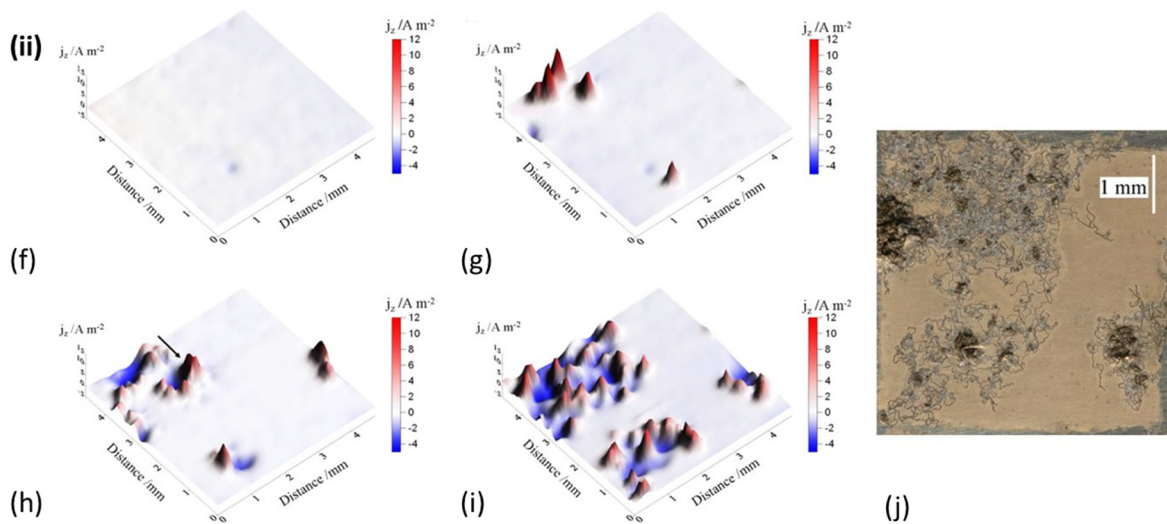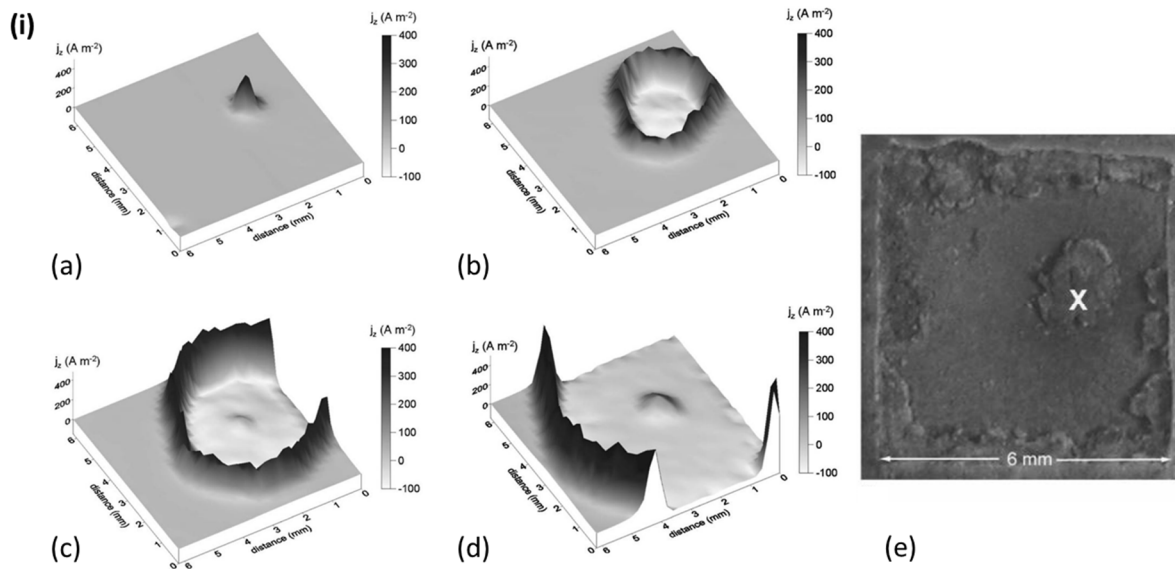
Figure 1.6: SVET surface plots of Commercial Pure (CP) Mg corroding in different salinity levels. (i) SVET derived current density distribution plots for CP Mg freely corroding in 0.86 M NaCl aqueous solution after (a) 6 min, (b) 24 min, (c) 36 min, (d) 54 min and (e) is the appearance of the sample after 80 min of immersion [54]. (ii) SVET derived current density distribution plots for CP Mg freely corroding in 0.01 M NaCl aqueous solution after (f) 25 min, (g) 41 min, (h) 66 min, (i) 100 min and (j) is the appearance of the sample after 100 min of immersion [74]. Reproduced from Williams et al. [54,74].

This can be seen in Figure 1.6(ii) [74] where the SVET derived current density plots indicate the location of the anodes and the cathodes on the surface of a freely corroding Mg. It is important to note that the current density values vary significantly between the two different salinity levels for the same CP Mg sample as it can be observed from Figure 1.6. This demonstrates the significance of the throwing power of the electrolyte and its control over the morphology of the localised corrosion of nominally pure Mg.

1.3.6   Rare Earth (RE) Containing Mg Alloys

Rare earth elements like Neodymium (Nd) and Lanthanum (La) are usually being added to Mg as grain refiners [75] and to improve the mechanical properties of Mg alloys at high temperatures. From the corrosion perspective, the RE additions in Al-series Mg alloys can have the benefit of reducing the size of noble β-phase particles that have been proposed to reduce the Mg corrosion rate. It has also been suggested in the past that RE improve the corrosion resistance of Mg by not allowing the formation of intermetallic impurities, which are well known to affect the corrosion performance of Mg [76,77]. Binary Mg alloys containing cerium, lanthanum and neodymium are considered to have a decreased corrosion resistance according to some studies [78,79], however, Arrabal et al. [80] revealed that additions of Nd to Mg alloys like the AM50 and AZ91D improved their corrosion resistance. The addition of rare earth elements can refine the microstructure and helps the formation of Al–RE phases that have lower cathodic activity than the β-$Mg_{17}Al_{12}$ phase, which subsequently can reduce micro-galvanic coupling in Mg alloys [81–83].

A significant portion of this work is based on the rare earth-containing Mg alloy E717 due to the increasing interest in utilising this alloy in automotive applications. The E717 is an Mg alloy that contains small quantities of the rare earth element Neodymium (Nd), along with Zirconium (Zr) and Zinc (Zn) and was primarily used in biomedical applications [84,85]. Recent studies on the corrosion behaviour of the E717 in aqueous NaCl solution have demonstrated that the Mg alloy undergoes localised corrosion in the form of filiform-like discrete tracks [58,86] at low Cl^- concentration, but covering larger areas of the exposed surface at higher Cl^- concentration [86]. This type of localised corrosion is known to occur on several technologically important Mg alloys like the AZ31 [59,87–89], AZ61 [87] and AZ91 [45,89,90]. The AZ series alloys will be separately discussed in the following section. Mechanistically, the filiform-like localised corrosion on Mg alloys can be described as the leading edges of the filiform-like tracks being the intense local

anodes while the dark surface left behind is cathodically activated with respect to the uncorroded surface and the majority of the H_2 evolution occurring at the local anode. Asmussen et al. [86] have used scanning electron microscopy to investigate the microstructure of the E717 and they identified several intermetallic phases including tertiary Mg–Zn–Nd (T-phase), Zn–Zr and Fe-containing Zr along with discrete Zr particles. Other researchers [91] have studied the surface film that is being formed on the surface of the E717 under immersion conditions and the influence of the chloride ion concentration. They found that the presence of Cl^- in the bulk solution results to a thicker nano porous outer layer whereas in water a dense bilayer film consisting of an inner MgO and an outer $Mg(OH)_2$ was observed.

1.3.7 AZ Series Mg Alloys

The AZ series are technologically important Mg alloys that contain Aluminium (Al) and Zinc (Zn) as their main constituents hence their codename AZ. The most widely used and technologically important AZ series Mg alloys are the AZ31 and AZ91 with some additional variations in their names like the AZ31B and the AZ91D. According to the ASTM B951 - 11 standard, the letter "B" that is used in the codification name of the AZ31B explains the tolerance limits of impurities including iron (0.005 wt.%) while the letter "D" at the end of AZ91D designation means high pressure die casting and it has a specified impurity limit [92]. The AZ31 and the AZ91 contain 3% and 9% Al respectively and 1% Zn. It is very common for the AZ series Mg alloys to contain a small percentage (~0.35%) of Manganese (Mn) which according to some studies [77,93–95] can help with the removal of impurities like Iron (Fe) and Copper (Cu) that are well known for their negative impact on the corrosion of Mg due to the formation of active intermetallic compounds. Additionally, when Mn is added in conjunction with Al, Al–Mn–(Fe) particles are being formed that can reduce the presence of Fe particles in the microstructure by removing them during the melting stage [94].

The addition of Al in Mg alloys has primarily the purpose of improving their mechanical properties, by increasing their strength and hardness and decreasing their ductility. However, it has been suggested that the corrosion resistance of the Mg alloy will decrease if the Al content is too high or if the concentration of Al surpasses the solubility limit (ca. 12 wt.% in Mg) [96]. Although reports by Baril et al. [97] and Pardo et al. [98] mention that the corrosion resistance will increase with increasing Al content, others [89,99] have stated that the rate of corrosion will increase with

higher Al additions. Some researchers have noted that the increase/decrease of the corrosion rates are due to the formation of secondary phases like the $Mg_{17}Al_{12}$ acting as a barrier [100,101] of the anodic reaction or promoting the corrosion of the Mg alloy by micro-galvanically coupling with the Mg matrix [45,87,102,103]. This β-phase is very common in the microstructure of the AZ series alloys with Al percentage higher than ca. 3 wt.% [96,104]. Others researchers [105–108] have found that Al additions in Mg alloys can increase the potency of its film against aqueous corrosion by forming Al rich films on the surface of the alloy. Although there is a contradiction in the literature with regards to the role of Al additions in Mg alloy corrosion, studies on the atmospheric corrosion of Al-containing alloys tend to suggest that higher Al additions increase the corrosion resistance of Mg [109–113]. It is important to note however that the concentration of Al in the Mg matrix is not the only factor influencing its corrosion behaviour, but also the distribution, shape and size of the secondary phases.

Zn is the second element in the AZ series Mg alloys, and it added to the Mg alloys to improve their mechanical properties [114] by increasing the in-room temperature strength, but it has the disadvantage of making Mg alloys softer. Zinc additions of around 1% will have the advantage of increasing the tolerance limits and reduce the toxic effects of impurities such as Fe, Copper (Cu) and Nickel (Ni) [115,116]. Higher additions of Zn can significantly reduce the corrosion resistance of the Mg alloys due to the formation of noble particles (MgZn) leading to micro-galvanic corrosion [96,117].

The corrosion behaviour of the AZ series alloys has been intensively investigated over the years. The AZ31 is considered to be a single phase alloy with Al–Mn intermetallic particles in the matrix with these second phase particles primarily being identified as Al_8Mn_5 although other Al–Mn intermetallic phases have also being reported (i.e. $Al_{11}Mn_4$) [95,98,118–122]. These intermetallic particles have also been detected in other AZ series Mg alloys like the AZ91D and the AZ80 [118]. The β-$Mg_{17}Al_{12}$ phase that is present in other AZ series with higher Al content is considered to be mainly absent from the microstructure of the AZ31 Mg alloy [87,121,123,124].

Williams and co-workers [59] have investigated the localised corrosion of the AZ31B in 0.86 M NaCl and they revealed that this alloy undergoes localised corrosion in the form of filiform-like corrosion in a similar manner to the corrosion behaviour observed on pure Mg. These thin filiform-like features on the exposed surface of the AZ31 have also been reported by other researchers

during immersion in chloride-containing solutions [87,89,124,125]. It was revealed that the initiation of localised corrosion was characterised by the appearance of local anodes at the heads of the filaments [59]. These local anodes were traversing the surface of the AZ31B and they were coupled to the cathodically activated corroded areas left in the wake of these propagating anodes. The researchers suggested that the cathodic activation of the filiform-like features on the AZ31B can be attributed to the presence of Al–Mn particles in the dissolving Mg matrix [59]. Finally, they proposed a mechanism for the localised corrosion of AZ31 in an aqueous solution that is presented in Figure 1.7 also including a typical SVET derived j_z profile [59].
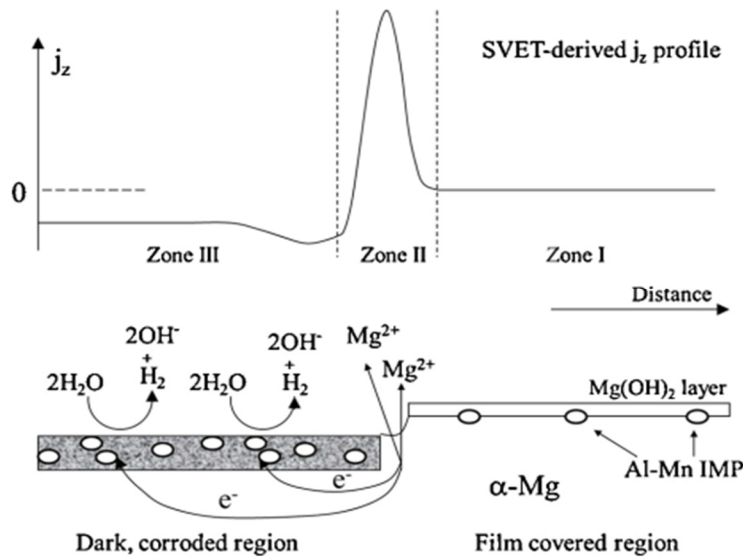
Figure 1.7: Schematic diagram of the localised corrosion mechanism of AZ31 in aqueous solution with a characteristic SVET derived j_z profile. [59]

1.4   Corrosion-driven Coating Failures

As it was mentioned before, Mg and its alloys have relatively poor corrosion resistance and this has hindered its widespread usage. One way of overcoming this problem is to protect Mg and its alloy by using organic coatings. The usage of organic coatings has the primary purpose of preventing corrosion occurring on Mg surfaces by separating the substrate from the environment and acting as a barrier to aggressive ions. In addition, organic coatings further protect against

abrasion and improve the aesthetic appearance [126]. The performance of the organic coating can vary depending on the coating type, surface adhesion, surface pre-treatment of the substrate and it can further be improved by suspending adequate inhibitors in the coating system. An organic coating can protect the substrate against corrosion better if it remains intact and undamaged throughout its service. If a coating becomes damaged during its service, it may result in a catastrophic failure of the coating-metal system.

In this section, two common coating failure phenomena are discussed, the cathodic driven coating delamination and the anodic driven filiform corrosion (FFC). These phenomena can occur on organic coated metals when the applied coating is damaged. If this damage takes the form of a penetrative coating defect, an electrolyte can ingress in the coating/substrate interface and cause significant impairment to the system.

1.4.1 Coating Delamination

Cathodic delamination is a very common organic coating failure where the coating disbonds from the surface due to the ingress of an electrolyte through a penetrative coating defect or a cut edge. This phenomenon can occur on coated iron (mild steel) and zinc (galvanized) [127–134] and has been extensively studied over the years, however there is a significant gap in the scientific literature concerning this phenomenon and its occurrence on organic coated Mg and its alloys. In order for cathodic delamination to occur on coated iron or zinc, a coupling between the anodic and cathodic reaction must take place underneath the coating. In more detail, the anodic reaction (metal dissolution) occurs on the exposed surface (the coating defect), which couples with the cathodic reaction (oxygen reduction) at the site of coating disbondment by a thin layer of electrolyte. Due to the oxygen reduction reaction, there is a formation of a high alkaline environment caused by the production of hydroxyl ions. To this day, the primary reason for the disbondment is still debatable and some suggested mechanisms include base catalysed polymer degradation, base catalysed hydrolysis of interfacial bonds, dissolution of an amphoteric metal oxide film at the metal-coating interface and attack on the polymer by short-lived intermediates produced during oxygen reduction [135]. Coating delamination has been extensively investigated on organic coated surfaces like iron and zinc and the Scanning Kelvin Probe (SKP) has revealed quite useful information about the mechanism on both metals.

A typical schematic diagram along with the relevant SKP-obtained potential profile is presented in Figure 1.8. The schematic diagram indicates that the coating delamination process can be divided into different phases.
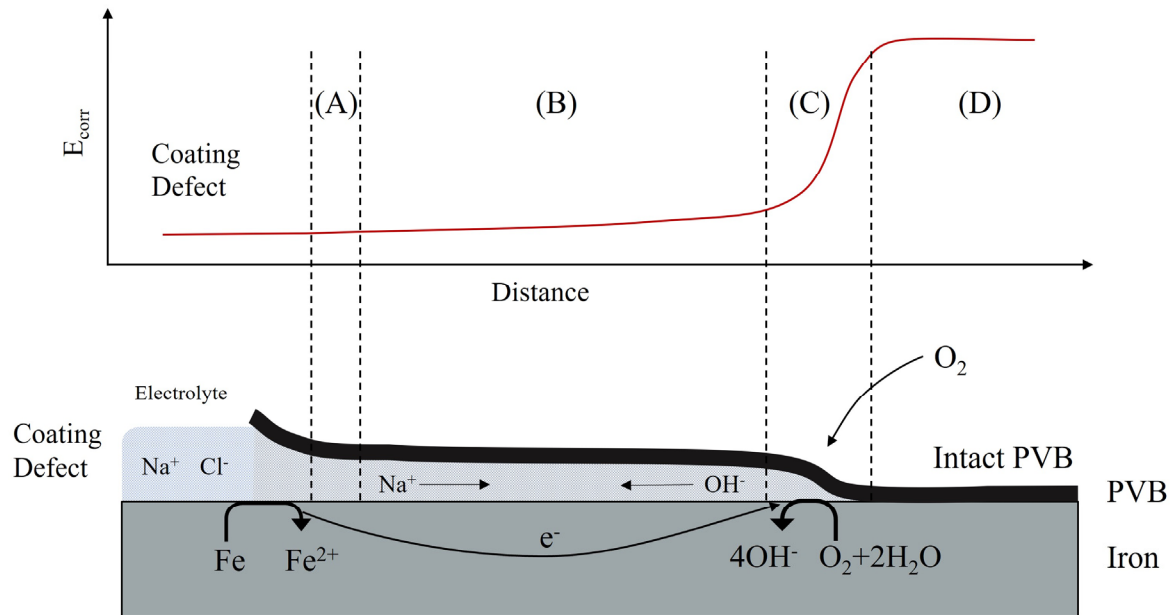
Figure 1.8: Schematic representation of the delamination of a polyvinyl-butyral (PVB) coating from an iron surface along with various regions of the time dependent $E_{corr}(x)$ profile.

A. A region where anodic metal dissolution takes place and the E_{corr} values will adopt similar values to that of a freely corroding uncoated iron.

B. This region links the coating defect region (A) with the delamination front region (C). This is a region of a gradual increase of the E_{corr} that results from the ohmic resistance to the ionic current flowing in the underfilm electrolyte responsible for linking the two regions.

C. In this region, a sharp change of E_{corr} to higher values can be observed corresponding to the delamination front where the coating disbonds from the surface.

D. This region is where the organic coating is still intact and undelaminated.

1.4.1.1 Delamination Mechanisms

There are various mechanisms that have been suggested over the years to be responsible for the delamination of organic coatings from iron and zinc surfaces. It has been proposed that more than one disbondment mechanism can exist in a system [135] however it is important to note that the mechanism that proceeds at the fastest rate will be the dominant mechanism. There are two principal possible mechanisms for coating disbondment: the alkaline dissolution of an oxide layer at the metal/coating interface and the destruction of the chemical bonds between the coating and the substrate.

Although many similarities exist between Zn and Fe, it has been suggested [136,137] that in the case of Zn, the loss of adhesion is attributed to the dissolution of an amphoteric zinc oxide film at the coating/metal interface. In the case of Fe, the delamination of the organic coating from the surface has been attributed to the breakage of the bonds between the coating and the substrate by reactive intermediate species and hydrogen peroxide produced by the cathodic reaction (oxygen reduction) [128,138].

In more detail, it is known that the Zn oxides are strongly amphoteric indicating that they will dissolve in the presence of high pH while the Fe (III) oxides (weakly amphoteric) will only dissolve at very high pH. Therefore, it can be said that the difference in the coating delamination mechanism between these two metallic oxides is ascribed to their stability at an alkaline pH. Ritter and Kruger [139] investigated cellulose nitrate coatings on Fe and they found that the pH in the delaminated region was close to 14. Although under the same study, it is more likely that the delamination occurred when the value of pH was ca. 11 according to their measurements using ellipsometry [135,139]. An investigation on hot dip galvanised (HDG) Zn, have estimated that the pH in the underfilm electrolyte in the delaminated region is between 10 – 11 [133].

It has been suggested that the oxidation of Zn will lead to the production of $Zn(OH)_2$ (Reaction (1.5)) when the oxidation takes places in a zone of high pH [136].

$$Zn_{(s)} + 2H_2O \leftrightarrow Zn(OH)_{2(s)} + 2H^+_{(aq)} + 2e^- \qquad (1.5)$$
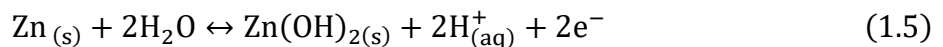
The increased pH will cause the dissolution of the amphoteric $Zn(OH)_2$, leading to the production of bizincate ($HZnO_2^-{}_{(aq)}$) and zincate ($ZnO_2^{2-}{}_{(aq)}$) via Reactions (1.6) and (1.7) respectively.

$$Zn(OH)_{2\,(S)} \leftrightarrow HZnO_{2\,(aq)}^- + H_{(aq)}^+ \tag{1.6}$$

$$Zn(OH)_{2\,(S)} \leftrightarrow ZnO_{2\,(aq)}^{2-} + 2H_{(aq)}^+ \tag{1.7}$$

$$Zn_{(s)} + 2H_2O \leftrightarrow HZnO_{2\,(aq)}^- + 3H_{(aq)}^+ + 2e^- \tag{1.8}$$
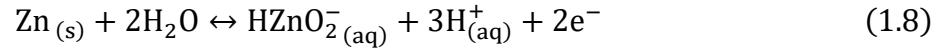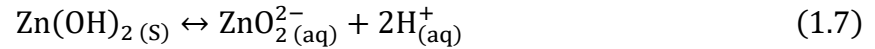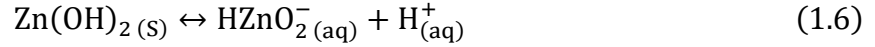
It has been suggested in the past that in the presence of very alkaline conditions, Zn can be directly oxidised to bizincate ($HZnO_2^-$) (Reaction (1.8)) [136]. Thus, this is possible to occur in the delaminated region under the coating where the pH is considered to be much higher than 10.37 [133].

The stability of Fe (III) oxides at highly alkaline conditions signify that surface of the Fe will remain passive in the delaminated zone, thus it is expected that the anodic reaction will not take place [128]. It is possible for Fe (III) to be reduced to a more soluble form (Fe (II)), however it has been demonstrated by using X-ray photoelectron spectroscopy (XPS) that the reduction of Fe only occurs in localised areas within the delaminated region, but also it was indicated that it is possible to occur after the coating has delaminated [140].

Polymer coatings that have ester functionalities, urea linkages and epoxy esters can delaminate from the surface due to hydrolysis by a highly alkaline electrolyte [135,141,142]. Leng et al. [130] have stated that the chemical bonds (Fe-oxygen-polymer bonds) responsible for the adhesion of the coating on the iron surface can be damaged by short-lived intermediates including hydrogen peroxide, which are formed during the oxygen reduction. Intermediate radicals that form during the oxygen reduction can lead to base-catalysed polymer degradation and base catalysed hydrolysis of the interfacial bonds.

In the past, the SKP has been successfully used to measure the delamination kinetics in systems where a PVB coating has been applied on Fe and Zn substrates where the delamination has been initiated using 0.86 M NaCl and the samples were subjected to high relative humidity (93%). As it has been discussed previously, the delamination front can be detected by the SKP and it is identified as a location where a sharp change of the E_{corr} is observed (see E_{corr} profile in Figure 1.8). The transportation of the electrolyte cations is considered to be the rate that determines the delamination kinetics of the systems mentioned above. Thus, in the systems where delamination

is initiated with NaCl (aq) containing electrolyte, it is expected that the rate determining step for the delamination to be the transportation of Na^+ travelling from the artificial coating defect to the delamination front. The following Equation (1.9) [136,143] defines the relationship between the distance from the edge of the defect from which the delamination has initiated (x_{del}) and time of delamination (t_{del}).

$$x_{del} = k_{del}(t_{del} - t_i)^{\frac{1}{2}} \tag{1.9}$$

Where k_{del} is the delamination rate constant and t_i is the time taken for delamination to initiate [136,143]. The literature [129,136,144,145] suggests that the delamination kinetics of organic coated Fe or HDG substrate exhibit a linear behaviour when the kinetics are plotted as x_{del} vs. $(t_{del}-t_i)^{1/2}$. The linear behaviour of the delamination distance versus square root of time denotes that the interfacial diffusion of cations in the substrate/coating interface is the rate determining step of the cathodic delamination [129,146]. Under circumstances where the delamination kinetics do not vary linearly with the square root of time, it would be expected that the migration of cations to the delamination front is not the rate limiting step of the process and the kinetics are plotted against time $(t_{del}-t_i)$. This probably suggests that the underfilm cathodic reaction replaced the cation migration process as the rate limiting step of the cathodic delamination of the coating from the substrate [147–149]. A typical example of SKP-derived delamination kinetics plot for unpigmented and with Ce^{3+} pigment 30 μm PVB coating on HDG Zn substrate is presented in Figure 1.9 [144]. Figure 1.9 demonstrates that the delamination kinetics for HDG Zn substrate coated with unpigmented PVB are linear signifying that the rate of delamination is controlled by the migration of cations from the anodic region to the cathodic region through the underfilm electrolyte.
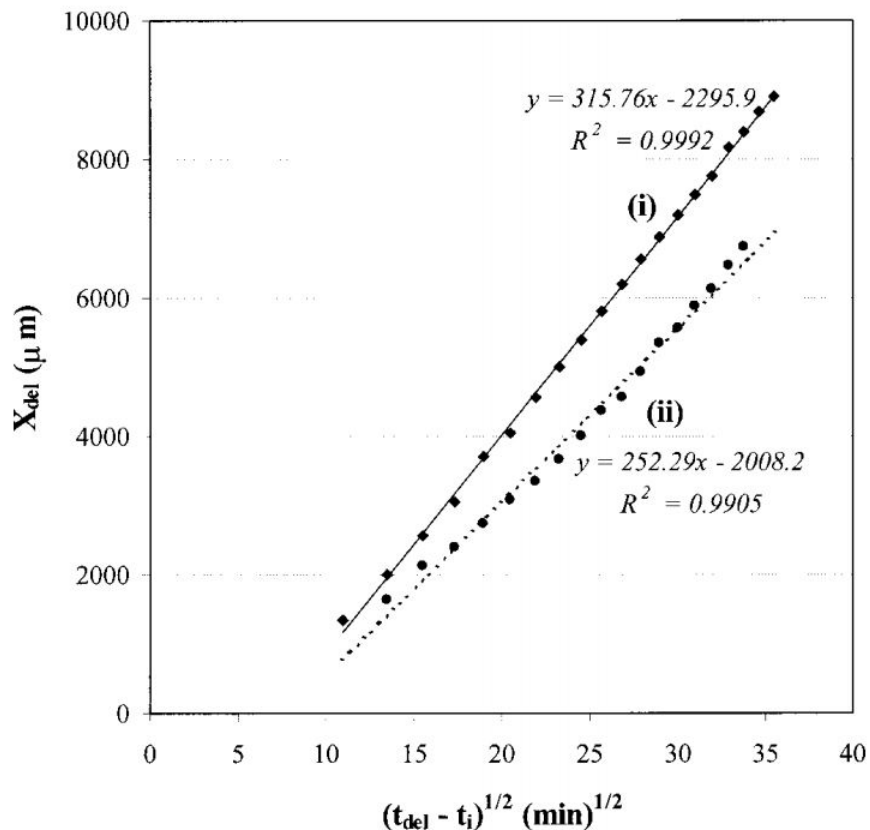
Figure 1.9: Plots of x_{del} vs. $(t_{del}-t_i)^{1/2}$ for unpigmented PVB (30 µm) coating on HDG Zn surface. The electrolyte used is 0.86 M NaCl (i) uninhibited and (ii) inhibited with 2.5×10^{-3} M $CeCl_3$ [144].

1.4.1.2   Influencing Factors

It has been proven that the cation type can significantly influence the cathodic delamination in both Fe and Zn. Koehler [150] showed that cathodic delamination will only occur if there is a presence of group I cations in the electrolyte available to act as counter ions to OH^- generated by the cathodic oxygen reduction. It has been mentioned before that the delaminated regions are dominated by a very alkaline pH and only the group I cations do not hydrolyse and have the necessary solubility to support this alkaline electrolyte [135]. It is not expected for Group II salts to induce cathodic delamination because the hydroxides produced by this group only have a limited solubility [150,151].

A different study [152] has demonstrated that when delamination is initiated with electrolytes containing Group I cations, the delamination rate will be influenced by the diffusion coefficients of the Group I cations and their mobility in aqueous electrolytes. The diffusion coefficients

determined for these cations moving in the electrolyte layer beneath the delaminated coating were considerably smaller than those in water. It was then thought that this electrolyte is a polymer gel-like layer resulting from chemically degraded polymer [129]. The delamination rate ranked in order of the highest to the lowest rate is $Cs^+ > K^+ > Na^+ > Li^+$ [129,152,153]. In more detail, the lowest delamination rate is exhibited by the small Li^+ ions, which when dissolved in water produce the largest solvation shell compared to the rest of the Group I cations, making Li^+ the least mobile cation [129,153].

Leng et al. [129] have further studied the influence of the anion type on the delamination kinetics by using NaCl, NaBr, $NaClO_4$ and NaF solutions. They found that the identity of the counter anion (Cl^-, Br^-, ClO_4^- and F^-) did not seem to have any notable influence on the delamination rate and there was no evidence of anions present beneath the coating, rather, they remained in the defect region as it was confirmed with Auger analysis. In this very thorough study by Leng et al. [129], they employed the SKP and various concentrations of NaCl (aq) to investigate the effect of the electrolyte concentration on the cathodic delamination rate. They proved that the delamination rate of the coating increased with increasing NaCl concentration, but they also noted that delamination did not occur when the concentration of the electrolyte was below 0.05 M. It was then suggested that there were not enough ions available to establish a galvanic couple between the artificial coating defect and the intact polymer/metal interface [129].

1.4.2   Filiform Corrosion (FFC)

Filiform corrosion (FFC) is considered to be a type of atmospheric corrosion occurs under a film. This corrosion phenomenon is characterised by 'worm-like' or 'thread-like' corrosion tracks that can occur on coated metals like steel (iron) Fe, Al and Mg. Sharman [154] in 1944, used the term FFC to describe propagating hair-like corrosion tracks on lacquer-coated steel that were observed under the microscope. The FFC occurrence on coated metals is unwanted and aesthetically unpleasant and it is predominantly considered that FFC does not significantly affect the structure of the metals however in some cases FFC can be a sign of serious problems in the metal structure. A typical example of the appearance of FFC on coated Mg alloys is presented in Figure 1.10.
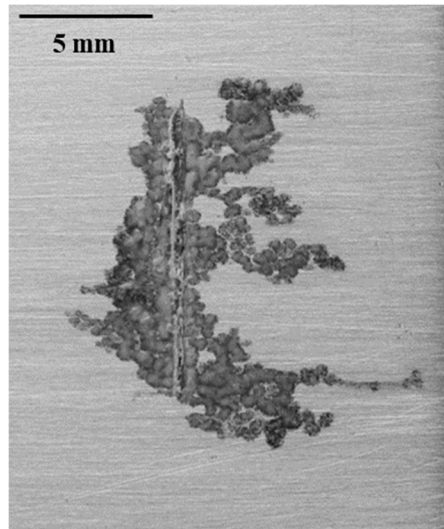
Figure 1.10: Photographic image of a PVB coated Mg alloy undergoing FFC.

1.4.2.1 Influencing Factors

As it was stated previously, FFC occurs under organic coated metals like steel, aluminium and magnesium where FFC can be initiated when aggressive species (e.g. Cl$^-$) access the substrate metal through a defect, cut edge or weakness in the coating. It is known that for FFC to occur, there is a need for high relative humidity (RH) and oxygen to be present with the caveat that the influence of RH on FFC differentiates from metal to metal. For example, FFC will occur on coated steel only when the RH is above 60% [155] but below 95%. It has been reported [156] that underfilm corrosion will take the form of blistering rather than FFC when coated steel is exposed to RH levels above 95%. In the case of organic coated Al alloys, it has been reported that FFC can occur under a wider range of RH (30–95%) [157], while on organic coated Mg, FFC can take place only when RH levels ≥ 31%, with higher levels of RH giving also a higher rate of FFC [74].

The second important factor that needs to be present in order for FFC to occur is oxygen. This is the case for coated metals like Al and Fe since the propagating mechanism (which is discussed later) is under the control of differential aeration meaning that if oxygen is absent from the environment, the FFC will cease or the underfilm corrosion will take the form of blistering [135,155]. However, this is not the case with organic coated Mg. It has been shown in the past [74], that the FFC of organic coated Mg substrates is not influenced by the absence/presence of oxygen indicating that the mechanism of FFC initiation and propagation in these substrates is not the same as with coated Fe and Al.

1.4.2.2 Mechanisms of FFC

1.4.2.2.1 Aluminium and Iron

Although there are notable mechanistic differences in the FFC of Al and Fe, there are many general principals that hold true for both metals. The corrosion filaments of FFC initiate at a normal direction from a defect on the coating and in most cases, the filaments are propagating in straight lines in random directions. Although this is valid for most cases, there have been reports where the FFC filaments propagating on Al surfaces follow the rolling direction lines on the surface [156]. The rolling lines, as well as the griding lines, that can be formed during the surface preparation procedure offer a path where the filaments can follow if that is the path of the least resistance [135,156]. The FFC filaments normally are separated in two parts: the head and the tail of the filament. The head of the filament is filled with electrolyte containing metal cations and Cl⁻, while the tail consists of dry corrosion product.

In the case of Al, the presence of chloride-containing salts can breakdown the passive layer and localised sites of anodic metal dissolution will be caused on the surface of the Al [135]. The scientific literature suggests that one possible mechanism of FFC on coated Al substrates is differential aeration where the transportation of oxygen to the substrate is carried out by the thin electrolyte layer [155,156]. As the theory of differential aeration suggests, the anodic metal dissolution will take place where the oxygen concentration is lower (lower availability), which in this case is the metal/electrolyte/coating interface, whereas the cathodic oxygen reduction will take place at a site where oxygen is more concentrated. The migration of Cl⁻ underneath the coating (preservation of electroneutrality) and the water being drawn into the system via osmosis, will cause the formation of a small amount of electrolyte acting as the head of the FFC filament [135,158] while the propagation of FFC is expected to be controlled by the difference in oxygen concentration [155,156,159,160]. The anodic dissolution taking place at the head of the filament (leading edge) will generate Al^{3+} cations that will then migrate towards the trailing edge of the active head and react with the OH⁻ (produced by the cathodic reaction) and the reaction product of the combination of Al^{3+} cations and OH⁻ will lead to the eventual precipitation of insoluble $Al(OH)_3$ [155,156,160]. It is important to note here that the leading edge of the filiform head is normally characterised by low pH values of ca. 2–3 [161]. The Cl⁻ migration towards the anodic head of the filament will result in the retention of soluble ions and water will then be drawn to the

filament head via osmosis [155,156]. This was confirmed by Williams and McMurray [159] where they demonstrated using secondary ion mass spectrometry (SIMS) that Cl⁻ are conserved in the head of the filaments even at protracted holding times. The same researchers showed that the propagation rate of FFC on organic coated Al alloy is significantly dependent upon the Cl⁻ concentration in the head of the filaments [159].

The schematic diagram presented in Figure 1.11 [135] describes the initiation and propagation of FFC in organic coated Al alloys. McMurray and Williams [135] have also described the process in terms free corrosion profiles (E_{corr}) obtained by scanning a propagating filament using the Scanning Kelvin Probe (SKP) and the result of their study is presented in Figure 1.11b. Figure 1.11b indicates that the E_{corr} values at the leading edge of the active filament head are lower, whereas the E_{corr} values at the trailing edge are higher denoting that the anodic dissolution is taking place in the areas with more negative potentials.
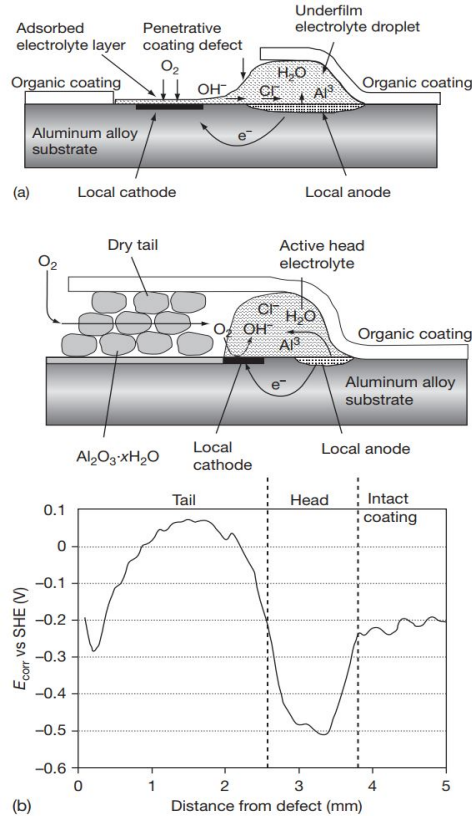
Figure 1.11: Schematic diagram showing the FFC mechanism in an organic coated Al alloy a) initiation and b) propagation. The E_{corr} values were obtained by using the SKP to scan a propagating filament on organic-coated AA2024 [135].

As it was stated above for the FFC of Al, the filament in the FFC of organic coated Fe consists of a head and a tail, where the cathodic oxygen reduction is taking place at the trailing edge of the filament, whereas the anodic dissolution occurs in the leading-edge of the head that is filled with electrolyte (metal cations and Cl$^-$ anions) [135,162]. The mechanism of FFC on Fe suggests that the FFC advancement is controlled by differential aeration where the transportation of oxygen occurs through the tail of the filament [155,156]. Williams and McMurray [163] investigated the FFC of organic coated Fe where they initiated FFC using FeCl$_2$ electrolyte. In this study it was found that a dark brown substance had precipitated in the coating defect and they suggested that this was caused by the oxidation of Fe^{2+} to Fe^{3+}. In the literature [164], it is also proposed that there is a production of mono and polynuclear hydroxy-complexes due to the propensity of Fe^{3+} to undergo hydrolysis that will lead to the precipitation of insoluble solid Fe(OH)$_3$.

Generally, it is considered that the initiation of FFC is caused by osmosis due to the FCC occurring only at higher levels of relative humidity. As a small amount of electrolyte ingresses into a penetrative coating defect, the anodic dissolution of Fe is expected to take place leading to the release of Fe^{2+} into the electrolyte. The difference in oxygen concentration between some sites where the electrolyte is present will cause the acidification of the electrolyte and thus the oxygen deficient sites are expected to become the basis of the anode while the surrounding sites will form the cathode. The filament head is characterised by a rather acidic pH between 1–4, which is attributed to the cation hydrolysis while the back of the head is considered to be more alkaline with a pH of ca. 12 [156,157]. The filament head transverses the surface of Fe leaving behind a tail filled with porous corrosion product and the porous morphology of the tail allows for a better supply of oxygen. The diffusion of oxygen and water via the filament tail towards the head of the filament causes a differential aeration cell and subsequently the anode and the cathode will be separated. Thus, the insufficient oxygen supply to the head of the filament (front) is further establishing the anode while the back of the filament head becomes the cathode due to the high availability of oxygen occurring via the porous tail. The FFC will then propagate due to the different oxygen concentration between the front and the back of the head, with the front of the head anodically undermining the coating.

In a study conducted by Williams and McMurray [163], it was demonstrated that there is a potential gradient between the front and back of the head of the filament indicating that cations

migrate to the back and the anions migrate to the front of the head. The Fe^{2+} that has been formed during the oxidization of Fe (front of the head) will move at the back of the head. As it was stated before, the presence of higher oxygen concentration at the back of the head that migrated through the porous tail will cause the further oxidation of the Fe^{2+} to Fe^{3+}. As the filament advances on the Fe surface, the corrosion products dehydrate and convert into inert corrosion products (FeOOH) in the tail of the filament with the borders between the electrolyte in the head of the filament and the tail being marked by a V-shaped feature [165]. Finally, it is important to note that alternative mechanisms on the FFC of Fe have been reported, primarily concerning the location of the cathodic activity. It has been suggested that the cathodic oxygen reduction is located in a region in front of the leading edge of the filament [166,167], while other researchers have proposed that the front part of the filament head is the location where the cathodic activity is taking place [156,168].

1.4.2.2.2 Magnesium

It is important to start by noting here that there have been a few reports [73,90] where the term FFC is being used to describe the localised corrosion mechanism occurring on bare (uncoated) Mg surfaces immersed in bulk electrolytes. This term was used in these studies due to the similar appearance of the localised corrosion products (dark, worm-like tracks) with the FFC on coated metals however in this subsection only the FFC of organic coated Mg substrates is discussed.

Early reports [169–171] have suggested that the mechanism of FFC on organic coated Mg is very similar to the mechanisms that were described above for Fe and Al. However, it is well established in the scientific literature that hydrogen evolution (Reaction (1.2)) is the primary cathodic reduction of a corroding Mg suggesting that the mechanism of FFC is not caused by differential aeration as it is considered for Al and Fe. As it was described above, the pH in the head of the filaments in the FFC of Al and Fe is acidic due to the hydrolysis of Al^{3+} and Fe^{3+}. The hydrolysis equilibrium constants (pK_{a1}) of Al and Fe are 5 and 2.2 [172,173] respectively, denoting that their nature is acidic [74]. The low pH in the filament head is an essential component in the propagation of FFC in Al and Fe, however, it would be expected that the non-acidic nature of the Mg^{2+} ($pk_{a1} \approx$ 11.4) [173] to not allow a low pH to be maintained in the filament head for a long period. It is expected that the pH of the electrolyte in the head of the filament will adopt a more basic pH due the production of hydroxides by the cathodic hydrogen evolution (Reaction 1.2) [74]. However, a very low pH (2–3) has also been reported in the filament head regions [171].

The mechanism of FFC of organic coated Mg was described in great detail by Williams and Grace [74] where they inoculated FFC by applying a small amount of aqueous HCl in a penetrative coating defect. They proposed that the FFC initiates at the artificially induced coating defect when the anodic dissolution of Mg via Reaction (1.1) takes place leading to the undercutting of the coating along with the migration of Cl$^-$ underneath the coating to preserve electroneutrality. As MgCl$_2$ is being produced at the front of the FFC, water is drawn to the filament head (via osmosis) and a small amount of electrolyte will be formed at the head of the filament [74]. It was then shown that in the case of coated Mg, the FFC is primarily dependent upon the availability of water, but also can proceed under conditions where oxygen is absent in a similar manner as in air. The former assertion was demonstrated by varying the level of relative humidity between 31% to 93%, which revealed that the FFC propagation rate increased with increasing levels of relative humidity showing high dependence on water availability. By taking into consideration the aforementioned results, as well as in-situ Scanning Kelvin Probe (SKP) potentiometric results, they proposed that a differential aeration mechanism does not occur in the propagation of FFC, but a differential electrocatalytic activation phnomenon [74]. The FFC propagation occurs due to the coupling of the anodic filament head with the cathodic hydrogen evolution in the tail. This mechanism is similar to the filiform-like corrosion mechanism that occurs on bare Mg surfaces immersed in bulk chloride-containing solutions where the corroded surface left behind the anodic front is electrocatalytically activated towards hydrogen evolution, but it has been suggested in the literature [112] that the primary site of hydrogen evolution is the anodic regions rather than the already corroded regions. The suggested mechanism of FFC occurring on organic coated Mg alloys is presented schematically in Figure 1.12 along with an SKP-derived E$_{corr}$ profile corresponding to the behaviour of the main features on the localised FFC filament [74].
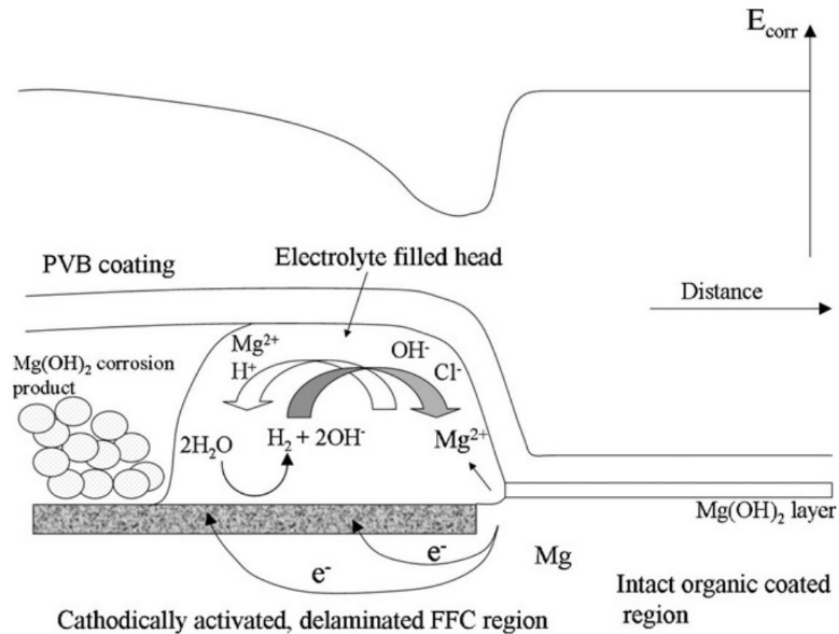
Figure 1.12: Schematic diagram showing the FFC mechanism in an organic coated Mg surface with a typical SKP derived E_{corr} profile showing the potential difference between the important FFC features [74].

The schematic diagram in Figure 1.12, shows that the E_{corr} values are more negative at the head of the filament due to the Mg dissolution while the corroded surface behind the head adopts more positive values indicating that the cathodic hydrogen evolution takes place behind the head of the filament. The same researchers [74] also noted that the main cause for the propagation of the FFC filaments in organic coated Mg surfaces is the activation of the previously corroded surface towards the cathodic reaction (hydrogen evolution) resulting in the anodic deactivation of the already corroded surface. This is caused by the precipitation of corrosion products (primarily $Mg(OH)_2$), high pH but also noble impurities (e.g. Fe) [74]. There have been some other interesting reports [174,175] of FFC occurring on coated Mg alloys however no explanation was given on the mechanism of the FFC in these systems.

1.5   Scanning Kelvin Probe (SKP)

The SKP also referred to as Kelvin's Vibrating Capacitor Technique is a very sensitive technique ideal for determining metallic work functions and it has been extensively used in corrosion science to investigate underfilm corrosion phenomena including delamination and filiform corrosion. The SKP enables the electrochemical mapping of these phenomena occurring beneath thin and polymeric films without touching the surface of the sample under investigation.

One of the first to use this technique to study atmospheric corrosion phenomena was Martin Stratmann. The SKP does not need a reference electrode to conduct a measurement and it has been used to study atmospheric corrosion phenomena since it has the advantage of not needing electrolytic conduction to connect the scanning electrode with a reference electrode. However, the SKP has the disadvantage of not being able to detect electrical current, meaning that it cannot provide insightful information about the rate of electrochemical reactions.

1.5.1   Operation of the SKP

In this section, the principles of the SKP operation are discussed. The tip of the reference probe electrode of the SKP is positioned above the sample under investigation and these two constitute the two plates of a parallel plate capacitor. The capacitor dialectic is the air or gas between the two plates. By using the following relationship (1.10), the capacitance (C) can be calculated.

$$C = \frac{\varepsilon \times \varepsilon_0 \times A}{d} \qquad (1.10)$$

Where ε is the dielectric constant of the capacitor dielectric, ε_0 is the permittivity of free space, A is plate area and d is the distance between the capacitor plates. The reference probe is sinusoidally vibrated relative to the sample's surface at a frequency, ω, such that d varies with time, t as the following Equation (1.11).

$$d = \overline{d} + \Delta d \sin(\omega t) \qquad (1.11)$$

where $\overline{d}$ is the mean separation of the plates while Δd is the maximum difference in the amplitude of vibration.

As the reference probe vibrates it produces a periodic fluctuation C and an alternating current i_{ac} will be induced in the circuit (Probe - Sample) if there is a Volta potential difference ($\Delta\Psi$ or ΔV) between the probe and the surface of the sample. This current is obtained by Equation (1.12).

$$i_{ac} = \Delta\Psi \frac{dC}{dt} \qquad (1.12)$$

By adjusting the value of the externally applied DC bias voltage (V_{bias}) to null the alternating current, the value of $\Delta\Psi$ can be obtained indirectly. Under these circumstances the Equation (1.13) holds true and the value of $-V_{bias=0}$ is the one that is being used as $\Delta\Psi$ or Kelvin probe potential (E_{KP}).

$$-V_{bias=0} = \Delta\Psi = E_{KP} \qquad (1.13)$$

The diagram presented in Figure 1.13 describes schematically the principles of the SKP operation.
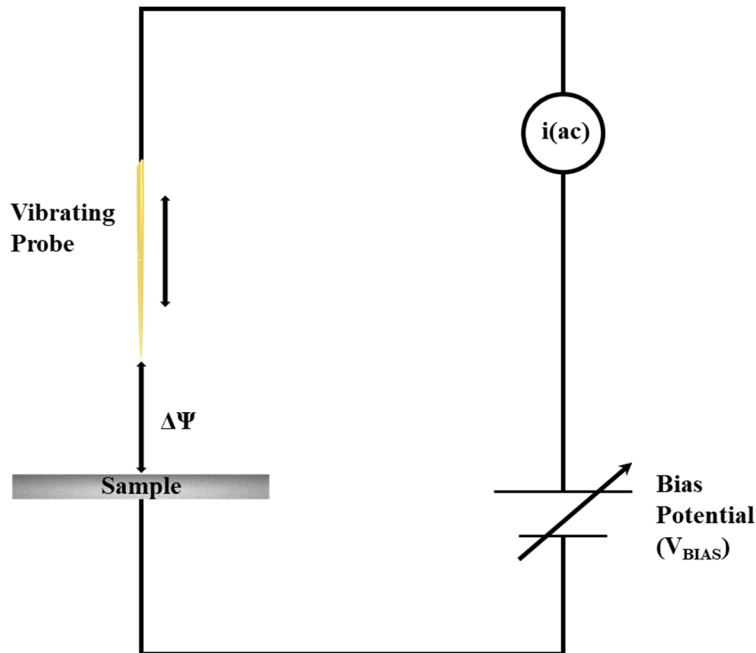
Figure 1.13: Schematic diagram of the SKP operation.

1.5.2 Scanning Kelvin Probe Calibration

The SKP measurements in most cases are performed in the presence of humid air with the relative humidity being between 50% to 99%. In the body of work presented here, the SKP measurements were carried out on organic coated Mg samples exposed to a relative humidity of ca. 93%. In conditions such as these, the E_{KP} values are expected to deviate due to the large number of potential differences that are contributed by the humid atmosphere and the polymer, thus the E_{KP} values will not only be governed by the metallic work functions. It has been shown that this E_{KP} value is proportional to the corrosion potential (E_{corr}) of the metal under study such as:

$$E_{corr} = E_{KP} + \text{constant} \qquad (1.14)$$

For an uncoated metallic surface covered with a layer of an electrolyte solution, the half-cell potential ($E_{1/2}$) is given by:

$$E_{1/2} = \frac{\alpha_e^{ref}}{F} - \chi_{gas}^{el} + \Delta\Psi_{el}^{ref} \qquad (1.15)$$

where α_e^{ref} is the work function of the material of the reference probe, F is the Faraday constant, χ_{gas}^{el} is the dipole potential of the solution/gas interface and $\Delta\Psi_{el}^{ref}$ is the Volta potential difference measured between the probe and the solution. To determine the half-cell potential ($E_{1/2}$) for a polymer-coated metal, the Equation (1.15) can be changed to:

$$E_{1/2} = \frac{\alpha_e^{ref}}{F} - \chi_{gas}^{pol} + \Delta\Psi_{pol}^{ref} \qquad (1.16)$$

where α_e^{ref} is the work function of the material of the reference probe, F is the Faraday constant, χ_{gas}^{pol} is the dipole potential of the polymer/gas interface and $\Delta\Psi_{pol}^{ref}$ is the Volta potential difference measured between the surface of the polymer and the probe. As it was mentioned before, the SKP has been used extensively to investigate delamination of organic coatings from Fe and Zn and as it was discussed earlier in this chapter (Section 1.5.1), an electrolyte layer exists between the metal and the polymer when delamination takes place. The Equation (1.16) can then be modified accordingly to account for the layer of electrolyte present between the metal substrate and the polymer. So, the new $E_{1/2}$ is given by:

$$E_{1/2} = \Delta\varphi_D + \frac{\alpha_e^{ref}}{F} - \chi_{gas}^{pol} + \Delta\Psi_{pol}^{ref} \tag{1.17}$$

where $\Delta\varphi_D$ ($\varphi_{el} - \varphi_{pol}$) represents the Donnan potential, which is equivalent to the Galvani potential difference established between the electrolyte and the polymer. The quantities $\frac{\alpha_e^{ref}}{F}$, χ_{gas}^{el} and χ_{gas}^{pol} are expected to remain constant with the assumption that the gas phase composition within the SKP environmental chamber does not vary with time.

The free corrosion potential can be expressed in terms of a reference electrode with the help of the following expression:

$$E_{corr} = E_{1/2} + E_{1/2}^{ref} \tag{1.18}$$

the $E_{1/2}$ can be obtained by Equations (1.15) – (1.17) while $E_{1/2}^{ref}$ is the half-cell potential of the reference electrode. By using Equation (1.14), the E_{corr} can be obtained for a metal simply covered with an electrolyte layer (Equation (1.19)) and for a polymer-coated metal (Equation (1.20)).

$$E_{corr} = A + \Delta\Psi_{el}^{ref} \tag{1.19}$$

$$E_{corr} = B + \Delta\Psi_{pol}^{ref} \tag{1.20}$$

where the A and B are constants and can be obtained experimentally by using the "SKP calibration curves". The plots of E_{corr} (vs. SHE) against $\Delta\Psi_{el}^{ref}$ and $\Delta\Psi_{pol}^{ref}$ for Ag/Ag$^+$, Cu/Cu^{2+}, Fe/Fe^{2+} and Zn/Zn^{2+} redox couples with and without a PVB film are presented in Figure 1.14 [136]. The values of constants A and B for uncoated and polymer film respectively can be obtained from the intercepts of each line, which is 0.555 V for the former and 0.330 V for the latter (Figure 1.14). The difference in the values between A and B (indicated with a black double arrow in Figure 1.14) is 0.225 V and this difference is ascribed to the dipole potential difference between the χ_{gas}^{el} and χ_{gas}^{pol}.
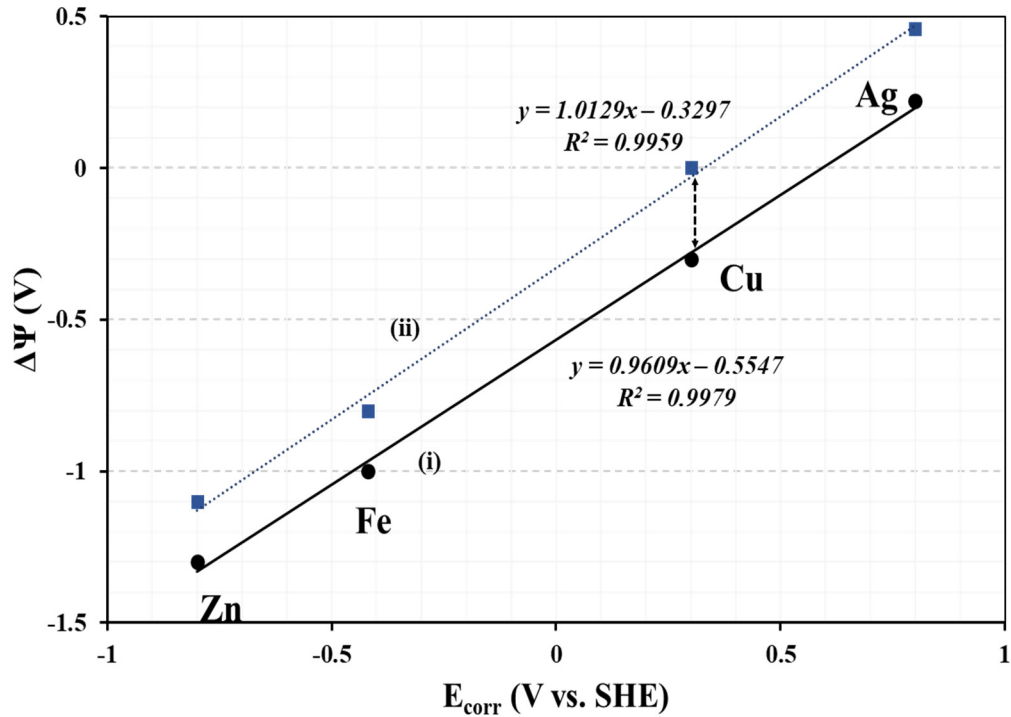
Figure 1.14: SKP calibration plots. Plots of Volta potential difference as a function of E_{corr} vs SHE. (i) (uncoated) $\Delta\Psi_{el}^{ref}$ vs. E_{corr} (ii) (PVB coated) $\Delta\Psi_{pol}^{ref}$ vs. E_{corr} [136].

Although the SKP has been used significantly in the past to study atmospheric corrosion phenomena beneath thin and polymeric films on Fe and Zn, the same does not hold true for Mg where only a small number of studies have employed this powerful technique [74,176]. A good example is the study conducted by Williams and Grace [74] that revealed very important findings about the atmospheric corrosion of Mg under high RH. They used the SKP to map local free corrosion potentials (E_{corr}) under a polymeric coating, which provided useful insights for the elucidation of the underfilm corrosion mechanism of organic coated Mg as it was discussed in Section 1.5.2. This showcased the potential of this technique to study atmospheric corrosion phenomena on organic coated Mg and this technique has been used extensively throughout this thesis.

1.6   Scanning Vibrating Electrode Technique (SVET)

The Scanning Vibrating Electrode Technique (SVET) and its predecessor the Scanning Reference Electrode Technique (SRET) have been extensively used in the past to investigate the localised corrosion phenomena in corrosion science. Isaacs [177,178] was one of the first researchers who used the SVET in corrosion science in 1984. By scanning periodically the surface of the sample under investigation with a microtip a series of spatially resolved maps (current distribution maps) can be produced providing valuable information about the kinetics and mechanisms of corrosion in aqueous environments. The SVET detects small changes in the localised electrochemical activity on the surface by vibrating a platinum microtip electrode relative to the scanned surface without touching the surface making this technique less perturbating than others.

It is known that when a metal corrodes in a bulk solution, the process involves the flow of ionic current from an anodic site to a distributed cathode. The electrons produced during this process can flow through the highly conductive bulk metal, which presents almost no ohmic potential gradients. However, the aqueous electrolyte that the specimen is immersed in, is significantly less conductive than the metal meaning when the ionic currents pass through the electrolyte significant higher ohmic potential gradients are produced. These ohmic potential gradients have been described as a series of isopotential lines that lie perpendicular to the ionic current flux.

By using the Laplace equation and Ohm's law the distribution of potential and the ionic current in the aqueous electrolyte can be calculated. The Equation (1.21) gives the potential at any point in the x,y or z plane that is inversely proportional to the distance from the source (point current source (i) at z = 0).

$$E = \frac{i}{2\pi\kappa\sqrt{(x^2+y^2+z^2)}} \tag{1.21}$$

where κ is the conductivity of the electrolyte and x,y,z refer to the coordination system (Cartesian). The SVET microtip electrode can register an alternating potential at the vibrational frequency that is proportional to the potential gradient in the direction of the vibration caused by the ionic current flux moving through the bulk electrolyte while the material corrodes. The alternating potential is caused by the oscillation of the SVET microtip electrode in the potential field. The signal from the SVET is directly proportional to the component of ionic current density that is parallel to the probe

vibration. The vibrating SVET tip measures the normal electrical field strength (F) and these values can be obtained by differentiating Equation (1.21), $\frac{d(E)}{dz}$.

$$F = \frac{dE}{dz} = -\frac{iz}{2\pi\kappa(x^2+y^2+z^2)^{1.5}} \tag{1.22}$$

The magnitude of the field strength is influenced by the height of the probe from the point current source with the maximum field strength at height z occurring when the SVET tip is directly above the point source so the x and y will be 0. The F_{max} then is given by:

$$F_{max} = -\frac{i}{2\pi\kappa z^2} \tag{1.23}$$

Although, SVET can be a powerful tool to characterise local electrochemical phenomena it does have some limitations. If the sample under investigation undergoes general corrosion, the fixed scanning height of the SVET (h) will be its limitation since the distance between the anode and the cathode will be less than h and the current flux lines will not cross the plane of scan and thus they will not be detected.

It is important to note that the distance from the probe to the surface of the metal (probe height) can significantly affect the magnitude of the normal current density. If the probe is too close to the surface it might affect the measurement because it may stir the electrolyte while if the probe height is high there may be a loss of spatial resolution. The theoretical spatial resolution of the SVET can be calculated using Equation (1.24), which is derived by Equation (1.23) and the signal peak width at half maximum peak height (whm) is a measure of the theoretical spatial resolution of this technique.

$$whm = 1.533z \tag{1.24}$$

Isaacs [179] has performed a series of model studies verifying the theoretical distribution of F over appoint current source. The SVET method has contributed significantly to the understanding of the corrosion mechanisms of Mg and its alloys. One of the first researchers who successfully used the SVET to investigate the localised corrosion behaviour of an Mg in an aqueous solution was Williams and McMurray [54]. They used the SVET to identify the location of the local anodic and cathodic activity on the surface of corroding Mg. In this study, the SVET identified an intense

anodic activity at the front of an expanding corrosion ring and the local cathode was detected at the centre of the ring. These SVET-derived findings have significantly contributed to the understanding of the corrosion behaviour of the Mg and its alloys. The SVET has also been used to investigate the localised corrosion on many technologically important Mg alloys like the AZ31B [59,88,119], Mg–Nd alloys [180], Mg–Al–Mn alloy joints [181] and Mg–Sn [182] alloys. Furthermore, this technique has been employed to study numerous topics in the corrosion of Mg, including studies on the localised corrosion morphologies of Mg [72], the role of transition metals in the cathodic activation of corroding Mg [64], protection films on AZ31 [183,184] as well as investigations on the hydrogen evolution on anodically polarised Mg [53,68,69]. Although the SVET can be used to measure the hydrogen evolution rate by numerically integrating the SVET data, it is important to take into consideration that the SVET can underestimate the actual HE rate since this technique has the disadvantage of not being able to detect local cathode sites that are close or immediately behind the anodic Mg dissolution [64].

1.7 Summary

Mg and its alloys have been utilised in the automotive industry due to their low weight and good mechanical properties with the purpose of lowering the vehicle weight and thus reducing the overall environmental impact. However, Mg and its alloys have poor corrosion resistance and this has hindered their usage in the automotive industry. The low corrosion corrosion resistance of uncoated Mg and its alloys has been a topic that has gained a lot of attention over the last decades. Most of the research has focused on examining the underlaying mechanisms of the localised corrosion of Mg alloys (e.g., AZ-series alloys) immersed in chloride containing solutions but only a few studies have been carried out on the localised corrosion behaviour of the E717 Mg alloy, which is an important candidate for automotive applications. Recent investigations on this alloy have indicated that it is susceptible to localised corrosion, which takes the form of filiform-like corrosion, however, it is clear from the current scientific literature that relatively little electrochemical characterisation of the corrosion behaviour of this alloy has been carried out so far. The work presented herein is aimed to fill the gap in the scientific literature with regards to the corrosion behaviour of the uncoated E717 Mg alloy, by examining in detail its localised

corrosion behaviour immersed in chloride-containing electrolytes by using a combination of conventional potentiostat-based studies along with in-situ SVET.

There is significant current interest in developing protective coatings for Mg alloys to overcome the problem of poor corrosion resistance and one way of protecting them is by employing organic coatings. However, the majority of the scientific work has focused on scrutinising inorganic barrier coatings and relatively only a few publications have focused on the corrosion protection of Mg alloys using organic coatings. Over the years, there has been a significant number of scientific papers reporting on the underfilm corrosion phenomena (i.e., anodic and cathodic disbondment) of organic coated Al and Fe but only a few researchers have focused on these important phenomena on Mg and its alloys. Previous studies demonstrated that commercially pure organic coated Mg is susceptible to underfilm corrosion when a chloride containing electrolyte ingresses in a penetrative coating defect and this underfilm corrosion takes the form of FFC. Despite this previous research, the precise mechanism of organic coating failure of Mg alloys has not been fully addressed to date. In this work, the primary goal is to address the lack of work in this area and elucidate the mechanisms of corrosion-driven organic coating failures of Mg alloys by investigating the underfilm corrosion phenomena of technologically important Mg alloys, with special attention to the E717 alloy. The underfilm corrosion is studied by applying group I and group II chloride salts in a penetrative coating defect, where two different modes of corrosion-driven coating failure are identified and investigated using electrochemical and surface characterisation techniques.

1.8 References

[1] E.J.T. Frederick K. Lutgens, Essentials of geology, 2000.

[2] R. Neelameggham, 1 - Primary production of magnesium, in: M.O. Pekguleryuz, K.U. Kainer, A.B.T.-F. of M.A.M. Arslan Kaya (Eds.), Woodhead Publ. Ser. Met. Surf. Eng., Woodhead Publishing, 2013: pp. 1–32.

[3] G. Simandl, H. Schultes, J. Simandl, S. Paradis, Magnesium - Raw materials, metal extraction and economics - Global picture, in: Proc. Ninth Bienn. SGA Meet., Dublin, 2007.

[4] S.S. Pathak, S.K. Mendon, M.D. Blanton, J.W. Rawlins, Magnesium-based sacrificial anode cathodic protection coatings (Mg-rich primers) for Aluminum alloys, Metals (Basel). 2 (2012).

[5] A.A. Luo, 8 - Applications: aerospace, automotive and other structural applications of magnesium, in: M.O. Pekguleryuz, K.U. Kainer, A.B.T.-F. of M.A.M. Arslan Kaya (Eds.), Woodhead Publ. Ser. Met. Surf. Eng., Woodhead Publishing, 2013: pp. 266–316.

[6] G.-L. Song, A. Atrens, Corrosion mechanisms of magnesium alloys, Adv. Eng. Mater. 1 (1999) 11–33.

[7] P.K. Mallick, Materials, design and manufacturing for lightweight vehicles, 2010.

[8] M.K. Kulekci, Magnesium and its alloys applications in automotive industry, Int. J. Adv. Manuf. Technol. 39 (2008) 851–865.

[9] H. Friedrich, S. Schumann, Research for a "New Age of Magnesium" in the automotive industry, J. Mater. Process. Technol. 117 (2001) 276–281.

[10] R.. Pachauri, L.. Meyer, IPCC, 2014: Climate Change 2014: synthesis report. Contribution of working groups I, II and III to the fifth assessment report of the intergovernmental panel on Climate Change, Geneva,Switzerland, 2014.

[11] T. Skszek, J. Conklin, D. Wagner, M. Zaluzec, Multi-Material Lightweight Vehicles, U.S. DOE, 2015 Annu. Merit Rev. Present. (2015) June 11.

[12] ASTM G82-98(2021)e1, Standard guide for development and use of a galvanic series for

predicting galvanic corrosion performance, ASTM International, West Conshohocken, PA, 2009.

[13] E. Ghali, W. Dietzel, K.U. Kainer, General and localized corrosion of magnesium alloys: A critical review, J. Mater. Eng. Perform. 22 (2013) 2875–2891.

[14] G. Song, B. Johannesson, S. Hapugoda, D. StJohn, Galvanic corrosion of magnesium alloy AZ91D in contact with an aluminium alloy, steel and zinc, Corros. Sci. 46 (2004) 955–977.

[15] E. Bowman, G. Koch, J. Varney, N. Thompson, O. Moghissi, M. Gould, J. Payer, International measures of prevention, application, and economics of corrosion technologies study, Houston, TX, 2016.

[16] R.-G. Hu, S. Zhang, J.-F. Bu, C.-J. Lin, G.-L. Song, Progress in Organic Coatings: Recent progress in corrosion protection of magnesium alloys by organic coatings, Prog. Org. Coatings. 73 (2011) 129–141.

[17] J. Zhang, C. Wu, Corrosion and protection of Magnesium alloys - A review of the patent literature, Recent Patents Corros. Sci. 2 (2010) 55–68.

[18] M.P. Staiger, A.M. Pietak, J. Huadmai, G. Dias, Magnesium and its alloys as orthopedic biomaterials: A review, Biomaterials. 27 (2006) 1728–1734.

[19] M.M. Avedesian, H. Baker, ASM specialty handbook: magnesium and magnesium alloys, ASM Int. Mater. Park. OH. (1999) 15.

[20] A. Krause, N. Von Der Höh, D. Bormann, C. Krause, F.W. Bach, H. Windhagen, A. Meyer-Lindenberg, Degradation behaviour and mechanical properties of magnesium implants in rabbit tibiae, J. Mater. Sci. 45 (2010) 624–632.

[21] X.P. Niu, T. Skszek, M. Fabischek, A. Zak, Low temperature warm forming of magnesium ZEK 100 sheets for automotive applications, Mater. Sci. Forum. 783–786 (2014) 431–436.

[22] F. Berge, L. Krüger, M. Ullmann, C. Krbetschek, R. Kawalla, Anisotropy of the mechanical properties of twin-roll cast, rolled and heat-treated AZ31 as a function of temperature and strain rate, Mater. Today Proc. 2 (2015) S233–S241.

[23] J. Davis, Corrosion: Understanding the basics, 2000.

[24]   International Organization for Standardization, Corrosion of metals and alloys — Basic terms and definitions (ISO 8044:1999), Online Brows. Platf. (1999) 819.

[25]   M. Fontana, Corrosion Engineering. 1987, McGraw-Hill. (1987) 173.

[26]   G.S. Frankel, A. Samaniego, N. Birbilis, Evolution of hydrogen at dissolving magnesium surfaces, Corros. Sci. 70 (2013) 104–111.

[27]   G.L. Makar, J. Kruger, Corrosion of magnesium, Int. Mater. Rev. 38 (1993) 138–153.

[28]   G.L. Makar, Corrosion studies of rapidly solidified magnesium alloys, J. Electrochem. Soc. 137 (1990) 414–421.

[29]   R.C. Zeng, J. Zhang, W.J. Huang, W. Dietzel, K.U. Kainer, C. Blawert, W. Ke, Review of studies on corrosion of magnesium alloys, Trans. Nonferrous Met. Soc. China (English Ed. 16 (2006).

[30]   J.H. Nordlien, S. Ono, N. Masuko, K. Nisancioglu, A TEM investigation of naturally formed oxide films on pure magnesium, Corros. Sci. 39 (1997) 1397–1414.

[31]   M. Santamaria, F. Di Quarto, S. Zanna, P. Marcus, Initial surface film on magnesium metal: A characterization by X-ray photoelectron spectroscopy (XPS) and photocurrent spectroscopy (PCS), Electrochim. Acta. 53 (2007) 1314–1324.

[32]   M. Taheri, R.C. Phillips, J.R. Kish, G.A. Botton, Analysis of the surface film formed on Mg by exposure to water using a FIB cross-section and STEM–EDS, Corros. Sci. 59 (2012) 222–228.

[33]   M.P. Brady, G. Rother, L.M. Anovitz, K.C. Littrell, K.A. Unocic, H.H. Elsentriecy, G.-L. Song, J.K. Thomson, N.C. Gallego, B. Davis, Film breakdown and nano-porous $Mg(OH)_2$ formation from corrosion of magnesium alloys in salt solutions, J. Electrochem. Soc. 162 (2015) C140–C149.

[34]   L.G. Bland, K. Gusieva, J.R. Scully, Effect of crystallographic orientation on the corrosion of magnesium: Comparison of film forming and bare crystal facets using Electrochemical Impedance and Raman Spectroscopy, Electrochim. Acta. 227 (2017) 136–151.

[35]   M. Taheri, M. Danaie, J.R. Kish, TEM Examination of the Film Formed on Corroding Mg

Prior to Breakdown, J. Electrochem. Soc. 161 (2013) C89–C94.

[36] W.M. Latimer, The oxidation states of the elements and their potentials in auqeous solutions, Second, Prentice-Hall, Inc., Englewood Cliffs, New Jersey, New Jersey, 1952.

[37] T. Cain, L.G. Bland, N. Birbilis, J.R. Scully, A compilation of corrosion potentials for magnesium alloys, Corrosion. 70 (2014) 1043–1051.

[38] P.R. Roberge, Corrosion Engineering: Principles and Practice, McGraw-Hill Education, 2008.

[39] M. Pourbaix, Atlas of electrochemical equilibria in aqueous solutions, Pergamon Press, Oxford, 1966.

[40] E. McCafferty, Introduction to corrosion science, 2010.

[41] M.G. Fontana, Corrosion Engineering, Third, McGraw-Hill Series in Materials Science and Engineering, 1986.

[42] W. Beetz, On the development of hydrogen from the anode, London, Edinburgh, Dublin Philos. Mag. J. Sci. 32 (1866) 269–278.

[43] R.L. Petty, A.W. Davidson, J. Kleinberg, The anodic oxidation of magnesium metal: Evidence for the existence of unipositive magnesium, J. Am. Chem. Soc. 76 (1954) 363–366.

[44] G. Song, A. Atrens, D. Stjohn, J. Nairn, Y. Li, The electrochemical corrosion of pure magnesium in 1 N NaCl, Corros. Sci. 39 (1997).

[45] G. Song, A. Atrens, X. Wu, B. Zhang, Corrosion behaviour of AZ21, AZ501 and AZ91 in sodium chloride, Corros. Sci. 40 (1998) 1769–1791.

[46] A. Atrens, W. Dietzel, The Negative Difference Effect and unipositive Mg+, Adv. Eng. Mater. 9 (2007) 292–297.

[47] G. Song, A. Atrens, D. St. John, X. Wu, J. Nairn, The anodic dissolution of magnesium in chloride and sulphate solutions, Corros. Sci. 39 (1997).

[48] A. Samaniego, B.L. Hurley, G.S. Frankel, On the evidence for univalent Mg, J. Electroanal.

Chem. 737 (2015) 123–128.

[49] M. Curioni, The behaviour of magnesium during free corrosion and potentiodynamic polarization investigated by real-time hydrogen measurement and optical imaging, Electrochim. Acta. 120 (2014) 284–292.

[50] N.T. Kirkland, G. Williams, N. Birbilis, Observations of the galvanostatic dissolution of pure magnesium, Corros. Sci. 65 (2012) 5–9.

[51] A.D. King, N. Birbilis, J.R. Scully, Accurate electrochemical measurement of magnesium corrosion rates; a combined impedance, mass-loss and hydrogen collection study, Electrochim. Acta. 121 (2014) 394–406.

[52] S. Lebouil, A. Duboin, F. Monti, P. Tabeling, P. Volovitch, K. Ogle, A novel approach to on-line measurement of gas evolution kinetics: Application to the negative difference effect of Mg in chloride solution, Electrochim. Acta. 124 (2014) 176–182.

[53] G. Williams, N. Birbilis, H.N. Mcmurray, The source of hydrogen evolved from a magnesium anode, Electrochem. Commun. 36 (2013) 1–5.

[54] G. Williams, H. Neil McMurray, Localized corrosion of magnesium in chloride-containing electrolyte studied by a Scanning Vibrating Electrode Technique, J. Electrochem. Soc. 155 (2008) C340.

[55] M.K.J.J. Rossrucker L. Frankel G. S. and Birbilis N., Investigating the real time dissolution of Mg using online analysis by ICP-MS, J. Electrochem. Soc. 161 (2014) C115.

[56] N. Birbilis, A.D. King, S. Thomas, G.S. Frankel, J.R. Scully, Evidence for enhanced catalytic activity of magnesium arising from anodic dissolution, Electrochim. Acta. 132 (2014) 277–283.

[57] R.M. Souto, A. Kiss, J. Izquierdo, L. Nagy, I. Bitter, G. Nagy, Spatially-resolved imaging of concentration distributions on corroding magnesium-based materials exposed to aqueous environments by SECM, Electrochem. Commun. 26 (2013) 25–28.

[58] W. Jeffrey Binns, F. Zargarzadah, V. Dehnavi, J. Chen, J.J. Noël, D.W. Shoesmith, Physical and electrochemical evidence for the role of a Mg hydride species in Mg alloy corrosion,

CORROSION. 75 (2019) 58–68.

[59]   G. Williams, H. ap Llwyd Dafydd, R. Grace, The localised corrosion of Mg alloy AZ31 in chloride containing electrolyte studied by a Scanning Vibrating Electrode Technique, Electrochim. Acta. 109 (2013) 489–501.

[60]   D. Höche, C. Blawert, S. V Lamaka, N. Scharnagl, C. Mendis, M.L. Zheludkevich, The effect of iron re-deposition on the corrosion of impurity-containing magnesium, Phys. Chem. Chem. Phys. 18 (2016) 1279–1291.

[61]   S. V Lamaka, D. Höche, R.P. Petrauskas, C. Blawert, M.L. Zheludkevich, A new concept for corrosion inhibition of magnesium: Suppression of iron re-deposition, Electrochem. Commun. 62 (2016) 5–8.

[62]   D. Lysne, S. Thomas, M.F. Hurley, N. Birbilis, On the Fe enrichment during anodic polarization of Mg and its impact on hydrogen evolution, J. Electrochem. Soc. 162 (2015) C396–C402.

[63]   M. Taheri, J.R. Kish, N. Birbilis, M. Danaie, E.A. McNally, J.R. McDermid, Towards a physical description for the origin of enhanced catalytic activity of corroding magnesium surfaces, Electrochim. Acta. 116 (2014) 396–403.

[64]   E. Michailidou, H.N. McMurray, G. Williams, Quantifying the role of transition metal electrodeposition in the cathodic activation of corroding magnesium, J. Electrochem. Soc. 165 (2018) C195–C205.

[65]   D. Mercier, J. Światowska, S. Zanna, A. Seyeux, P. Marcus, Role of segregated iron at grain boundaries on Mg corrosion, J. Electrochem. Soc. 165 (2018) C42–C49.

[66]   T. Cain, S.B. Madden, N. Birbilis, J.R. Scully, Evidence of the enrichment of transition metal elements on corroding magnesium surfaces using Rutherford Backscattering Spectrometry, J. Electrochem. Soc. 162 (2015) C228–C237.

[67]   S. Fajardo, G.S. Frankel, Effect of impurities on the enhanced catalytic activity for hydrogen evolution in high purity magnesium, Electrochim. Acta. 165 (2015) 255–267.

[68]   S. Fajardo, C.F. Glover, G. Williams, G.S. Frankel, The source of anodic hydrogen

evolution on ultra high purity magnesium, Electrochim. Acta. 212 (2016) 510–521.

[69] S. Fajardo, C.F. Glover, G. Williams, G.S. Frankel, The evolution of anodic hydrogen on high purity magnesium in acidic buffer solution, CORROSION. 73 (2017) 482–493.

[70] S.H. Salleh, S. Thomas, J.A. Yuwono, K. Venkatesan, N. Birbilis, Enhanced hydrogen evolution on Mg(OH)2 covered Mg surfaces, Electrochim. Acta. 161 (2015) 144–152.

[71] M. Curioni, F. Scenini, T. Monetta, F. Bellucci, Correlation between electrochemical impedance measurements and corrosion rate of magnesium investigated by real-time hydrogen measurement and optical imaging, Electrochim. Acta. 166 (2015) 372–384.

[72] G. Williams, N. Birbilis, H.N. McMurray, Controlling factors in localised corrosion morphologies observed for magnesium immersed in chloride containing electrolyte, Faraday Discuss. 180 (2015) 313–330.

[73] P. Schmutz, V. Guillaumin, R.S. Lillard, J.A. Lillard, G.S. Frankel, Influence of dichromate ions on corrosion processes on pure magnesium, J. Electrochem. Soc. 150 (2003) B99.

[74] G. Williams, R. Grace, Chloride-induced filiform corrosion of organic-coated magnesium, Electrochim. Acta. 56 (2011) 1894–1903.

[75] Y. Fan, G. Wu, H. Gao, G. Li, C. Zhai, Influence of lanthanum on the microstructure, mechanical property and corrosion resistance of magnesium alloy, J. Mater. Sci. 41 (2006) 5409–5416.

[76] W.E. Mercer, J.E. Hillis, The critical contaminant limits and salt water corrosion performance of magnesium AE42 alloy, (1992).

[77] J.D. Hanawalt, C.E. Nelson, J.A. Peloubet, Corrosion studies of magnesium and its alloys, (1941).

[78] N. Birbilis, M.A. Easton, A.D. Sudholz, S.M. Zhu, M.A. Gibson, On the corrosion of binary magnesium-rare earth alloys, Corros. Sci. 51 (2009) 683–689.

[79] A.D. Sudholz, K. Gusieva, X.B. Chen, B.C. Muddle, M.A. Gibson, N. Birbilis, Electrochemical behaviour and corrosion of Mg–Y alloys, Corros. Sci. 53 (2011) 2277–2282.

[80] R. Arrabal, A. Pardo, M.C. Merino, M. Mohedano, P. Casajús, K. Paucar, G. Garcés, Effect of Nd on the corrosion behaviour of AM50 and AZ91D magnesium alloys in 3.5wt.% NaCl solution, Corros. Sci. 55 (2012) 301–312.

[81] W. Liu, F. Cao, L. Chang, Z. Zhang, J. Zhang, Effect of rare earth element Ce and La on corrosion behavior of AM60 magnesium alloy, Corros. Sci. 51 (2009) 1334–1343.

[82] J. Zhang, J. Wang, X. Qiu, D. Zhang, Z. Tian, X. Niu, D. Tang, J. Meng, Effect of Nd on the microstructure, mechanical properties and corrosion behavior of die-cast Mg–4Al-based alloy, J. Alloys Compd. 464 (2008) 556–564.

[83] T. Zhang, G. Meng, Y. Shao, Z. Cui, F. Wang, Corrosion of hot extrusion AZ91 magnesium alloy. Part II: Effect of rare earth element neodymium (Nd) on the corrosion behavior of extruded alloy, Corros. Sci. 53 (2011) 2934–2942.

[84] H. Waizy, A. Weizbauer, C. Modrejewski, F. Witte, H. Windhagen, A. Lucas, M. Kieke, B. Denkena, P. Behrens, A. Meyer-Lindenberg, F.-W. Bach, F. Thorey, In vitro corrosion of ZEK100 plates in Hank's Balanced Salt Solution, Biomed. Eng. Online. 11 (2012) 12.

[85] D. Dziuba, A. Meyer-Lindenberg, J.M. Seitz, H. Waizy, N. Angrisani, J. Reifenrath, Long-term in vivo degradation behaviour and biocompatibility of the magnesium alloy ZEK100 for use as a biodegradable bone implant, Acta Biomater. 9 (2013) 8548–8560.

[86] R.M. Asmussen, W.J. Binns, P. Jakupi, D. Shoesmith, The influence of microstructure on the corrosion of magnesium alloy ZEK100, Corrosion. 71 (2014) 242–254.

[87] A. Samaniego, I. Llorente, S. Feliu, Combined effect of composition and surface condition on corrosion behaviour of magnesium alloys AZ31 and AZ61, Corros. Sci. 68 (2013) 66–71.

[88] G. Williams, R. Grace, R.M Woods, Inhibition of the localized corrosion of Mg alloy AZ31 in chloride containing electrolyte, Corrosion. 71 (2015) 184–198.

[89] L. Wang, T. Shinohara, Z. B.-P. Zhang, Corrosion behavior of Mg, AZ31, and AZ91 alloys in dilute NaCl solutions, J. Solid State Electrochem. 14 (2010) 1897–1907.

[90] O. Lunder, J.E. Lein, S.M. Hesjevik, T.K. Aune, K. Nişancioğlu, Corrosion morphologies

on magnesium alloy AZ91, Mater. Corros. 45 (1994) 331–340.

[91] M.P. Brady, G. Rother, L. Anovitz, K. Littrell, K. Unocic, H. Elsentriecy, G.-L. Song, J. Thomson, N. Gallego, B. Davis, Film breakdown and nano-porous Mg(OH)2 formation from corrosion of magnesium alloys in salt solutions, J. Electrochem. Soc. 1621416182 (2015) 140–14935.

[92] ASTM Int., B951-11, Standard practice for codification of unalloyed magnesium and magnesium-alloys, cast and wrought, in: Annu. B. ASTM Stand., West Conshohocken, PA, PA, 2011.

[93] Y. Cheng, T. Qin, H. Wang, Z. Zhang, Comparison of corrosion behaviors of AZ31, AZ91, AM60 and ZK60 magnesium alloys, Trans. Nonferrous Met. Soc. China. 19 (2009) 517–524.

[94] D.S. Gandel, M.A. Easton, M.A. Gibson, N. Birbilis, Influence of Mn and Zr on the corrosion of Al-free Mg alloys: Part 1-Electrochemical behavior of Mn and Zr, CORROSION. 69 (2012) 666–671.

[95] N.N. Aung, W. Zhou, Effect of grain size and twins on corrosion behaviour of AZ31B magnesium alloy, Corros. Sci. 52 (2010) 589–594.

[96] K. Gusieva, C.H.J. Davies, J.R. Scully, N. Birbilis, Corrosion of magnesium alloys: the role of alloying, Int. Mater. Rev. 60 (2014) 169–194.

[97] G. Baril, C. Blanc, N. Pébère, AC impedance spectroscopy in characterizing time-dependent corrosion of AZ91 and AM50 magnesium alloys characterization with respect to their microstructures, J. Electrochem. Soc. 148 (2001) B489.

[98] A. Pardo, M.C. Merino, A.E. Coy, R. Arrabal, F. Viejo, E. Matykina, Corrosion behaviour of magnesium/aluminium alloys in 3.5wt.% NaCl, Corros. Sci. 50 (2008) 823–834.

[99] M.-C. Zhao, P. Schmutz, S. Brunner, M. Liu, G. Song, A. Atrens, An exploratory study of the corrosion of Mg alloys during interrupted salt spray testing, Corros. Sci. 51 (2009) 1277–1292.

[100] O. Lunder, J.E. Lein, T.K. Aune, K. Nisancioglu, The Role of Mg17Al12 Phase in the

Corrosion of Mg Alloy AZ91, CORROSION. 45 (1989) 741–748.

[101] M.C. Zhao, P.J. Uggowitzer, M. Liu, P. Schmutz, G. Song, A. Atrens, Corrosion of AZ91 - Influence of the β-phase morphology, in: Mater. Sci. Forum, 2009.

[102] G.-L. Song, Recent progress in corrosion and protection of magnesium alloys, Adv. Eng. Mater. 7 (2005) 563–586.

[103] I.B. Singh, M. Singh, S. Das, A comparative corrosion behavior of Mg, AZ31 and AZ91 alloys in 3.5% NaCl solution, J. Magnes. Alloy. 3 (2015) 142–148.

[104] M. Pekguleryuz, K. Kainer, A.A. Kaya, Fundamentals of magnesium alloy metallurgy, 2013.

[105] J.H. Nordlien, K. Nişancioglu, S. Ono, N. Masuko, Morphology and structure of oxide films formed on MgAl alloys by exposure to air and water, J. Electrochem. Soc. 143 (1996) 2564–2572.

[106] J.H. Nordlien, K. Nişancioglu, Morphology and structure of water-formed oxides on ternary MgAl alloys, J. Electrochem. Soc. 144 (1997) 461.

[107] S. Mathieu, C. Rapin, J. Steinmetz, P. Steinmetz, A corrosion study of the main constituent phases of AZ91 magnesium alloys, Corros. Sci. 45 (2003) 2741–2755.

[108] M. Danaie, R.M. Asmussen, P. Jakupi, D.W. Shoesmith, G.A. Botton, The role of aluminum distribution on the local corrosion resistance of the microstructure in a sand-cast AM50 alloy, Corros. Sci. 77 (2013) 151–163.

[109] M. Jönsson, D. Persson, Accelerated corrosion tests for magnesium alloys: Do they really simulate field conditions, in: 65th Annu. World Magnes. Conf. Pol., 万方数据资源系统, 2008.

[110] M. Esmaily, D.B. Blücher, J.E. Svensson, M. Halvarsson, L.G. Johansson, New insights into the corrosion of magnesium alloys — The role of aluminum, Scr. Mater. 115 (2016) 91–95.

[111] R. Arrabal, E. Matykina, A. Pardo, M.C. Merino, K. Paucar, M. Mohedano, P. Casajús,

Corrosion behaviour of AZ91D and AM50 magnesium alloys with Nd and Gd additions in humid environments, Corros. Sci. 55 (2012) 351–362.

[112] M. Esmaily, J.E. Svensson, S. Fajardo, N. Birbilis, G.S. Frankel, S. Virtanen, R. Arrabal, S. Thomas, L.G. Johansson, Fundamentals and advances in magnesium alloy corrosion, Prog. Mater. Sci. 89 (2017) 92–193.

[113] R. Lindström, J.-E. Svensson, L.-G. Johansson, The influence of carbon dioxide on the atmospheric corrosion of some magnesium alloys in the presence of NaCl, J. Electrochem. Soc. 149 (2002) B103.

[114] A. Das, G. Liu, Z. Fan, Investigation on the microstructural refinement of an Mg–6wt.% Zn alloy, Mater. Sci. Eng. A. 419 (2006) 349–356.

[115] J.E. Hillis, The effects of heavy metal contamination on magnesium corrosion performance, (1983).

[116] W.S. Loose, Corrosion and protection of magnesium, ASM International, Russell Township, OH, Ohio, 1946.

[117] N.T. Kirkland, M.P. Staiger, D. Nisbet, C.H.J. Davies, N. Birbilis, Performance-driven design of biocompatible Mg alloys, JOM. 63 (2011) 28–34.

[118] M.C. Merino, A. Pardo, R. Arrabal, S. Merino, P. Casajús, M. Mohedano, Influence of chloride ion concentration and temperature on the corrosion of Mg-Al alloys in salt fog, Corros. Sci. 52 (2010) 1696–1704.

[119] Z.P. Cano, J.R. Kish, J.R. McDermid, Effect of surface condition on the localized corrosion behavior of magnesium alloy AZ31B, in: M. Alderman, M. V Manuel, N. Hort, N.R. Neelameggham (Eds.), Magnes. Technol. 2014, Springer International Publishing, Cham, 2016: pp. 335–340.

[120] S. Pawar, X. Zhou, G. Thompson, G.M. Scamans, Z. Fan, The role of intermetallics on the corrosion initiation of twin roll cast AZ31 Mg alloy, J. Electrochem. Soc. 162 (2015) 442–448.

[121] G. Hamu, D. Eliezer, L. Wagner, The relation between severe plastic deformation

microstructure and corrosion behavior of AZ31 magnesium alloy, J. Alloys Compd. 468 (2009) 222–229.

[122] P. Cao, D.H. StJohn, M. Qian, The effect of manganese on the grain size of commercial AZ31 alloy, Mater. Sci. Forum. 488–489 (2005) 139–142.

[123] L. Shang, I.H. Jung, S. Yue, R. Verma, E. Essadiqi, An investigation of formation of second phases in microalloyed, AZ31 Mg alloys with Ca, Sr and Ce, J. Alloys Compd. 492 (n.d.) 173–183.

[124] Z.P. Cano, M. Danaie, J.R. Kish, J.R. McDermid, G.A. Botton, G. Williams, Physical characterization of cathodically-activated corrosion filaments on magnesium alloy AZ31B, CORROSION. 71 (2015) 146–159.

[125] L. Wang, T. Shinohara, B.-P. Zhang, Influence of chloride, sulfate and bicarbonate anions on the corrosion behavior of AZ31 magnesium alloy, J. Alloys Compd. 496 (2010) 500–507.

[126] B.N. Popov, Chapter 13 - Organic Coatings, in: B.N.B.T.-C.E. Popov (Ed.), Elsevier, Amsterdam, 2015: pp. 557–579.

[127] H. Leidheiser, W. Wang, L. Igetoft, The mechanism for the cathodic delamination of organic coatings from a metal surface, Prog. Org. Coatings. 11 (1983) 19–40.

[128] A. Leng, H. Streckel, M. Stratmann, The delamination of polymeric coatings from steel. Part 1: Calibration of the Kelvin probe and basic delamination mechanism, Corros. Sci. 41 (1998) 547–578.

[129] A. Leng, H. Streckel, M. Stratmann, The delamination of polymeric coatings from steel. Part 2: First stage of delamination, effect of type and concentration of cations on delamination, chemical analysis of the interface, Corros. Sci. 41 (1998) 579–597.

[130] A. Leng, H. Streckel, K. Hofmann, M. Stratmann, The delamination of polymeric coatings from steel Part 3: Effect of the oxygen partial pressure on the delamination reaction and current distribution at the metal/polymer interface, Corros. Sci. 41 (1998) 599–620.

[131] N.W. Khun, G.S. Frankel, Effects of surface roughness, texture and polymer degradation

on cathodic delamination of epoxy coated steel samples, Corros. Sci. 67 (2013) 152–160.

[132] E.L. Koehler, Technical Note: The mechanism of cathodic disbondment of protective organic coatings—aqueous displacement at elevated pH, CORROSION. 40 (1984) 5–8.

[133] W. Fürbeth, M. Stratmann, Scanning Kelvin Probe investigations on the delamination of polymeric coatings from metallic surfaces, Prog. Org. Coatings. 39 (2000) 23–29.

[134] W. Fürbeth, M. Stratmann, Investigation of the delamination of polymer films from galvanized steel with the Scanning Kelvinprobe, Fresenius. J. Anal. Chem. 353 (1995) 337–341.

[135] H.N. Mcmurray, G. Williams, Under Film/Coating Corrosion, Shreir's Corros. 2 (2010) 988–1004.

[136] G. Williams, H.N. McMurray, Chromate inhibition of corrosion-driven organic coating delamination studied using a Scanning Kelvin Probe technique, J. Electrochem. Soc. 148 (2001) B377–B385.

[137] W. Fürbeth, M. Stratmann, The delamination of polymeric coatings from electrogalvanized steel – a mechanistic approach. Part 1: delamination from a defect with intact zinc layer, Corros. Sci. 43 (2001) 229–241.

[138] M. Stratmann, R. Feser, A. Leng, Corrosion protection by organic films, Electrochim. Acta. 39 (1994) 1207–1214.

[139] J.J. Ritter, J. Kruger, Corrosion control by organic coatings, Leidheiser, Jr. Ed., NACE, Houston, TX. 28 (1981).

[140] J.E. Castle, J.F. Watts, Corrosion control by organic coatings, NACE. (1981) 78.

[141] J.S. Hammond, J.W. Holubka, R.A. Dickie, Surface analysis of interfacial chemistry in corrosion-induced paint adhesion loss, J. Coatings Technol. 51 (1979) 45–49.

[142] H. Leidheiser, Corrosion control by organic coatings., Natl Assn Of Corrosion En, 1981.

[143] G. Williams, S. Geary, H.N. McMurray, Smart release corrosion inhibitor pigments based on organic ion-exchange resins, Corros. Sci. 57 (2012) 139–147.

[144] G. Williams, H.N. McMurray, D.A. Worsley, Cerium(III) inhibition of corrosion-driven organic coating delamination studied using a Scanning Kelvin Probe technique, J. Electrochem. Soc. 149 (2002) B154.

[145] W. Fürbeth, M. Stratmann, The delamination of polymeric coatings from electrogalvanized steel – a mechanistic approach.: Part 3: delamination kinetics and influence of CO_2, Corros. Sci. 43 (2001) 243–254.

[146] P.A. Sørensen, S. Kiil, K. Dam-Johansen, C.E. Weinell, Influence of substrate topography on cathodic delamination of anticorrosive coatings, Prog. Org. Coatings. 64 (2009) 142–149.

[147] G. Williams, R.J. Holness, D.A. Worsley, H.N. McMurray, Inhibition of corrosion-driven organic coating delamination on zinc by polyaniline, Electrochem. Commun. 6 (2004) 549–555.

[148] J.L. Davies, C.F. Glover, J. Van de Langkruis, E. Zoestbergen, G. Williams, The effect of Mg concentration on the resistance of PVD Zn-Mg coatings to corrosion driven organic coating delamination, Corros. Sci. 100 (2015) 607–618.

[149] G. Williams, A. Gabriel, A. Cook, H.N. McMurray, Dopant effects in polyaniline inhibition of corrosion-driven organic coating cathodic delamination on iron, J. Electrochem. Soc. 153 (2006) B425.

[150] E.L. Koehler, Influence of contaminants on the failure of protective organic coatings on steel, Corrosion. 33 (1977) 209–217.

[151] J.D.B. Sharman, J.M. Sykes, T. Handyside, Cathodic disbonding of chlorinated rubber coatings from steel, Corros. Sci. 35 (1993) 1375–1383.

[152] H. Leidheiser Jr., W. Wang, No Title, J.Coat.Technol. 53 (1981) 77.

[153] H. Leidheiser, Cathodic delamination of polybutadiene from steel-A review, J. Adhes. Sci. Technol. 1 (1987) 79–98.

[154] C.F. SHARMAN, Filiform underfilm corrosion of lacquered steel surfaces, Nature. 153 (1944) 621.

[155] R.T. Ruggeri, T.R. Beck, An analysis of mass transfer in filiform corrosion, CORROSION. 39 (1983) 452–465.

[156] A. Bautista, Filiform corrosion in polymer-coated metals, Prog. Org. Coatings. 28 (1996) 49–58.

[157] W.H.. Slabaugh, W.. Dejager, S.E.. Hoover, L.L. Hutchinson, Filiform corrosion of aluminum, J. Paint Technol. 44 (1972) 76–83.

[158] G. Williams, H. N. McMurray, D. Hayman, P. C. Morgan, Time-lapse potentiometric imaging of active filiform corrosion using a Scanning Kelvin Probe technique, PhysChemComm. 4 (2001) 26–31.

[159] G. Williams, H.N. McMurray, The kinetics of chloride-induced filiform corrosion on aluminum alloy AA2024-T3, J. Electrochem. Soc. 150 (2003) B380.

[160] N. Le Bozec, S. Joiret, D. Thierry, D. Persson, The role of chromate conversion coating in the filiform corrosion of coated aluminum alloys, J. Electrochem. Soc. 150 (2003) B561.

[161] G.M. Hoch, R.. Staehle, B.. Brown, J. Kruger, A. Agrawal, Localized Corrosion, in: NACE International, Houston, 1974: p. 134.

[162] N. LeBozec, D. Persson, D. Thierry, In-situ studies of the initiation and propagation of filiform corrosion on aluminum, J. Electrochem. Soc. 151 (2004) B440.

[163] G. Williams, H.N. McMurray, The mechanism of group (I) chloride initiated filiform corrosion on iron, Electrochem. Commun. 5 (2003) 871–877.

[164] F.A. Cotton, G. Wilkinson, C.A. Murillo, M. Bochmann, R. Grimes, Advanced inorganic chemistry, Wiley New York, 1972.

[165] T.M. Watson, A.J. Coleman, G. Williams, H.N. McMurray, The effect of oxygen partial pressure on the filiform corrosion of organic coated iron, Corros. Sci. 89 (2014) 46–58.

[166] W. Funke, Toward a unified view of the mechanism responsible for paint defects by metallic corrosion, Ind. Eng. Chem. Prod. Res. Dev. 24 (1985) 343–347.

[167] W. Funke, Blistering of paint films and filiform corrosion, Prog. Org. Coatings. 9 (1981)

29–46.

[168] P.P. Leblanc, G.S. Frankel, Investigation of filiform corrosion of epoxy-coated 1045 carbon steel by Scanning Kelvin Probe Force Microscopy, J. Electrochem. Soc. 151 (2004) B105.

[169] M. Van Loo, D.D. Laiderman, R.. Bruhn, Filiform corrosion, Corrosion. 9 (1953) 277–283.

[170] C. Hahin, Localised corrosion, in: Met. Handb. Corros. Ed. SC Dexter, Am. Soc. Met. Met. Park. OH, 9th ed., 1987: pp. 104–122.

[171] G.M. Hoch, A review of filiform corrosion(filiform corrosion of steel, magnesium and aluminum coated and uncoated surfaces in humid and corrosive atmospheres), in: Natl. Assoc. Corros. Eng. Int. Conf. Localized Corros. Williamsburg, Va, 1971: p. 1971.

[172] G. Wulfsberg, Principles of descriptive chemistry, Brooks/Cole Pub., Monterey CA. (1987) 23.

[173] J. Gregory, J. Duan, Hydrolyzing metal salts as coagulants, Pure Appl. Chem. 73 (n.d.) 2017–2026.

[174] J. Yang, C. Blawert, S. V Lamaka, D. Snihirova, X. Lu, S. Di, M.L. Zheludkevich, Corrosion protection properties of inhibitor containing hybrid PEO-epoxy coating on magnesium, Corros. Sci. 140 (2018) 99–110.

[175] H. Wang, R. Akid, M. Gobara, Scratch-resistant anticorrosion sol–gel coating for the protection of AZ31 magnesium alloy via a low temperature sol–gel route, Corros. Sci. 52 (2010) 2565–2570.

[176] M. Jönsson, D. Thierry, N. LeBozec, The influence of microstructure on the corrosion behaviour of AZ91D studied by Scanning Kelvin Probe Force Microscopy and Scanning Kelvin Probe, Corros. Sci. 48 (2006) 1193–1208.

[177] Y. Ishikawa, H.S. Isaacs, Electrochemical behavior of pits developed on aluminum in a dilute chloride solution, Boshoku Gijutsu. 33 (1984).

[178] H.S. Isaacs, Applications of current measurement over corroding metallic surfaces., Prog. Clin. Biol. Res. (1986) 37.

[179] H.S. Isaacs, The effect of height on the current distribution measured with a Vibrating Electrode Probe, J. Electrochem. Soc. 138 (1991) 722.

[180] G. Williams, K. Gusieva, N. Birbilis, Localized corrosion of binary Mg-Nd alloys in chloride-containing electrolyte using a Scanning Vibrating Electrode Technique, Corrosion. 68 (2012) 489–498.

[181] S.H. Salleh, G. Williams, S. Thomas, Z. Zeng, B. McNally, N. Birbilis, M. Musameh, K. Venkatesan, J. Kish, J. McDermid, C. Glover, Local electrochemical behaviour of friction stir welded Mg-Al-Mn alloy joints, CORROSION. (2020).

[182] T.W. Cain, C.F. Glover, J.R. Scully, The corrosion of solid solution Mg-Sn binary alloys in NaCl solutions, Electrochim. Acta. 297 (2019) 564–575.

[183] M.F. Montemor, M.G.S. Ferreira, Electrochemical study of modified bis-[triethoxysilylpropyl] tetrasulfide silane films applied on the AZ31 Mg alloy, Electrochim. Acta. 52 (2007) 7486–7495.

[184] D. Snihirova, S. V. Lamaka, M. Taryba, A.N. Salak, S. Kallip, M.L. Zheludkevich, M.G.S. Ferreira, M.F. Montemor, Hydroxyapatite microparticles as feedback-active reservoirs of corrosion inhibitors, ACS Appl. Mater. Interfaces. 2 (2010) 3011–3022.

Chapter 2

Experimental Procedures

Experimental Procedures

2.1   Materials

2.1.1   Metallic Specimens

The metals employed in this study are magnesium and Mg alloys and they were used as substrates with an organic coating deposited on top, but also as bare specimens in immersion testing in bulk solutions. The high purity (<80 ppm Fe) Mg specimens were supplied by Prof. A. Atrens (University of Queensland) and were cut into 30 mm square coupons of 5 mm thickness while the commercial purity (CP) Mg foil (99.9+) samples were cut in 25 mm square coupons with the main impurities being iron (280 ppm) and manganese (170 ppm) and it was obtained from Goodfellow Metals Ltd. The ZEK100 or E717 (Electron^{TM} 717) type alloy came in a sheet of 2 mm thickness provided by Chemetall GmbH with a nominal composition (all weight %): 1.25% Zn, 0.5% Zr, 0.22% Nd, 0.008% Cu, 0.004% Fe, 0.3% others, balance Mg, F temper, cut using electric discharge machining (EDM) into 50 x 50 mm specimens. Finally, two AZ series Mg alloys were used in this investigation, the AZ31 and the AZ91 alloy. The AZ31 specimens with composition (all weight %): 3.1% Al, 0.7% Zn, 0.24% Mn; balance Mg, and the AZ91 specimens with composition (all weight %): 8.9% Al, 0.8% Zn, and 0.26% Mn with balance Mg were supplied by Magnesium Electron Ltd and cut using EDM in the same sizes as the E717 Mg alloy.

2.1.2   Model Organic Coating

The model organic coating that was used in this study is the polyvinyl butyral-*co*-vinyl alcohol-*co*-vinyl acetate (PVB) with a molar weight of ~70,000 – 100,000 obtained from Sigma-Aldrich Ltd. (powder) and was mixed with ethanol (15.5% w/w). This organic coating was chosen because it does not pose any significant risks to health, but also it is simple to prepare and store.

2.1.3   Sample Preparation

Before any experiment, the already cut Mg samples were subjected to a sample preparation. The samples were gently wet abraded in successive grits with silicon carbide (SiC) paper from Buehler® and ethanol as lubricant. The wet ground was done up to 1000 [P2500] with successive grits of 320 [P400], 400 [P800] and 600 [P1200] towards the rolling direction of the samples, followed by rinsing with distilled water and ethanol. Finally, the samples were polished with an

aqueous slurry of 5 μm polishing alumina and then cleaned with detergent solution and rinsed with distilled water followed by ethanol.

2.2 The Scanning Kelvin Probe (SKP)

The SKP technique has been employed in this study to access the corrosion occurring under organic coatings in atmospheric conditions. The SKP was used to investigate the disbondment of organic coatings and filiform corrosion occurring on organic coated Mg surfaces. The same SKP instrument was used throughout this study except for the SKP experiments that were conducted under O_2 free conditions.

2.2.1 Sample Preparation

Two different cell configurations were employed depending on the phenomena studied with the SKP: the Stratmann-type cell and a cell where a coated Mg sample was scribed to create a penetrative coating defect (scribed defect). For both cell configurations, the samples were initially prepared as described in Section 2.1.3.

2.2.1.1 Standard Delamination Cell (Stratmann-type cell)

The standard delamination cell was prepared following a similar methodology to the one developed by Stratmann et al. [1,2] for the measurement of coating delamination. After following the experimental procedure described in Section 2.1.3, an area of 15 mm x 50 mm was covered using a clear adhesive tape at one side of the sample. Prior to application of the coating, two strips of adhesive insulating tape (RS) of thickness 90 μm were applied parallel to each other at the edges of the tape leaving a bare metal surface of 35 mm x 20 mm. These two strips of tape act as a guide to get an even coating distribution and a dry film thickness of ca. 20 ± 5 μm. A small amount of 15.5% w/w ethanolic solution of PVB was applied on the clear tape at one side of the sample and was then bar coated using a glass rod over the exposed metal surface. After the film was left to dry for 30 minutes, a Dektak 6 profilometer was used to confirm the film thickness. Then the clear tape was scribed using a clean scalpel and pulled back to expose a 20 x 15 mm area of bare metal. This area was then sealed off using a non-corrosive silicon rubber (RS components) to create a reservoir where an electrolyte can be applied. The raised clear tape acted as a coating defect where

the desired electrolyte can ingress in the coating model interface and initiate delamination. In most delamination experiments, 1 M of NaCl (aq) was applied unless otherwise stated. A schematic diagram of describing the entire preparation process is presented in Figure 2.1.
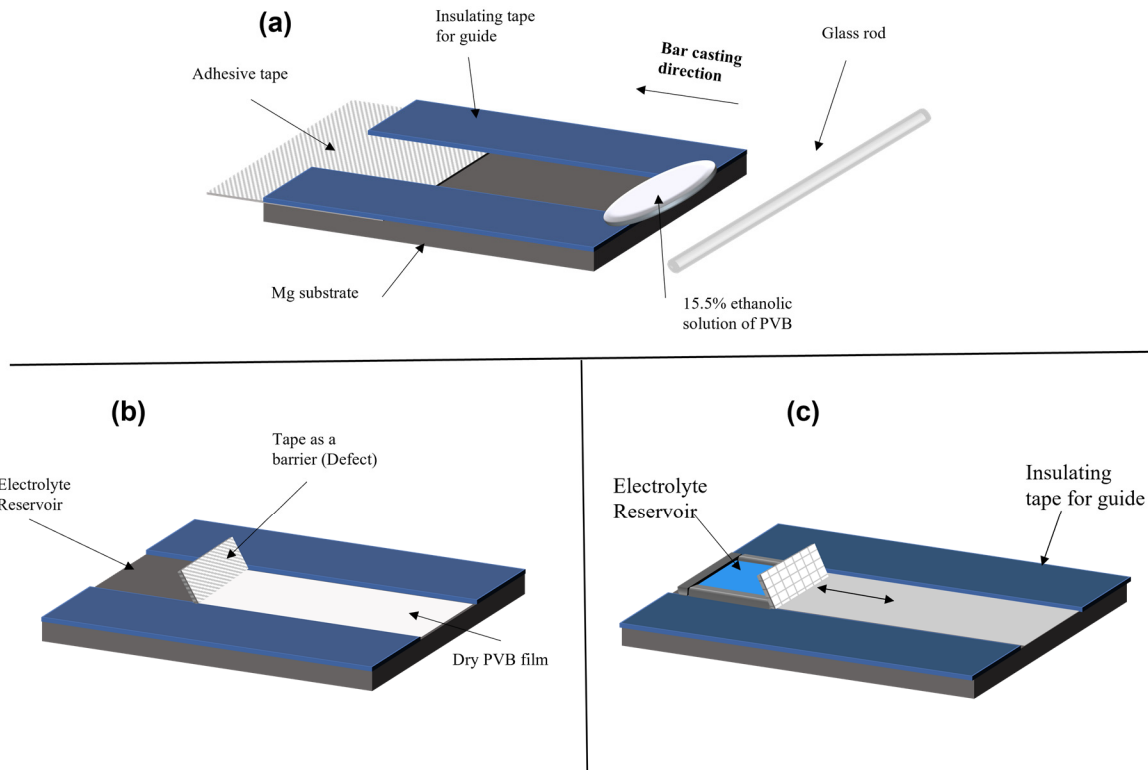
Figure 2.1: Schematic diagram of a sample being prepared to create a Stratmann-type cell (a) bar coating procedure of a PVB coating on an Mg substrate (b) lifting the tape to create a reservoir (c) coated sample ready with the reservoir (created using silicon rubber) and the defect.

2.2.1.2 **Scribed Defect Cell**

This cell configuration was used for delamination and filiform corrosion experiments. The preparation of this cell configuration is based on the methodology Williams and McMurray [3] followed to investigate underfilm corrosion on coated iron. After the sample was prepared following the experimental procedure described in Section 2.1.3, two stipes of insulating tape were applied on each side of the sample leaving a bare metal surface area of 30 mm x 50 mm. This tape was used as a height guide to get a dry film thickness of ca. 25 μm. Then a 15.5% ethanolic solution of PVB was bar casted on the exposed metal using a glass rod and the sample was left to dry in air

for 30 minutes. The ethanolic solution of PVB was applied parallel to the rolling direction of the Mg alloy. Depending on the phenomenon being studied, one or two 10 mm long penetrative coating defects were scribed into the PVB using a clean scalpel blade and perpendicular to the rolling direction of the Mg alloy. A schematic representation of the scribed defect cell method is shown in Figure 2.2.
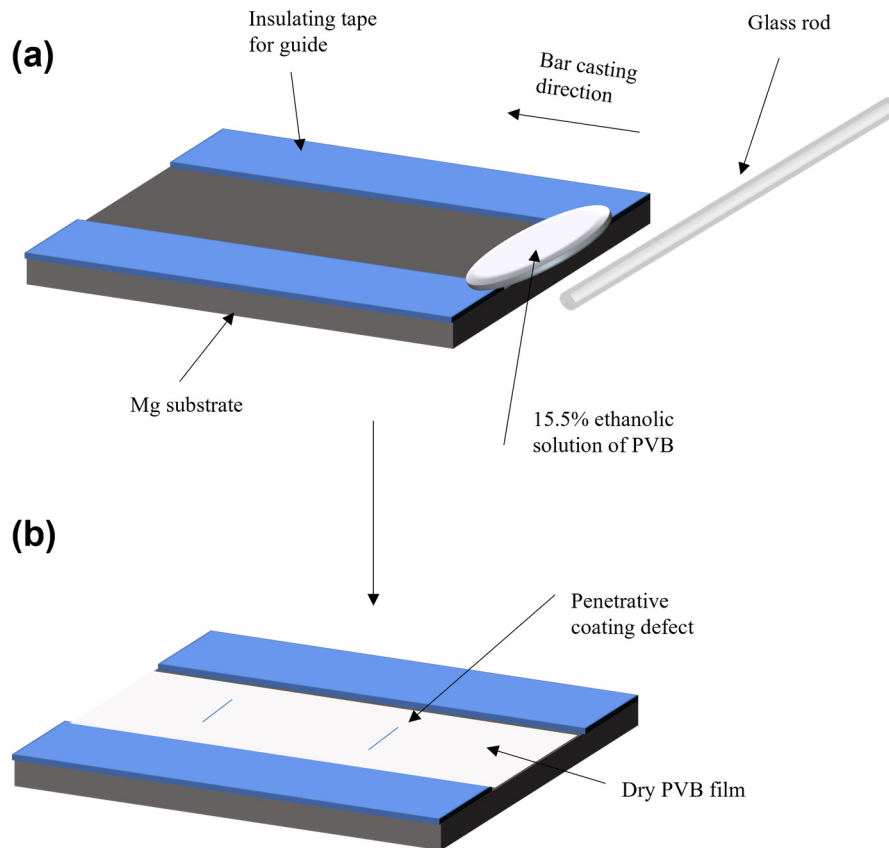
Figure 2.2: Schematic diagram of the sample preparation procedure for a scribed defect cell. (a) bar coating a PVB coating on Mg substrate (b) coating dried and sample scribed and ready for injection with the desired electrolyte.

2.2.2 Scanning Kelvin Probe Apparatus

The SKP used in this work was built in house by Swansea University. The SKP apparatus consists an environment chamber, sample holder, a tri-axial motor stage, reference probe, probe vibrator, lock-in amplifier, integrator and the system is controlled via a computer where the experimental data are also stored. A schematic diagram of the SKP apparatus set up that was used in this study is presented in Figure 2.3. The environment chamber was made out of stainless steel to exclude

electrostatic and electromagnetic noise (Faraday cage), while also maintaining a controlled environment of known relative humidity and gas composition. This chamber contained the sample holder that was directly connected to the external tri-axial motor controller (Time and Precision Ltd.) capable of moving the stage in the x, y and z direction. The reference probe (Kelvin probe) consisted of a 125 μm diameter 99.99% gold wire vibrating normal to the sample with the help of a loudspeaker. This loudspeaker was controlled to vibrate at the desired frequency (280 Hz in all cases) using a lock-in amplifier with an amplitude of 40 μm at a 100 μm distance from the sample surface. An alternating current is generated by the variation in the capacitance that occurs due to the oscillation of the Kelvin probe close to the sample's surface. The generated current is then amplified and converted to a voltage ($V_{a.c}$) by a current to voltage converter that is electrically connected to the sample. An analogous direct current (DC) output is being sent from the amplifier to an integrator (feedback circuit) adjusting the DC bias voltage. The output is then applied to the sample under investigation nulling the AC current and equalising the Galvani potentials of the probe and the specimen. After a stable Kelvin probe bias potential (V_{bias}) is achieved, the reverse bias is then converted to a digital signal by the lock-in amplifier and the Kelvin probe potential is logged on the computer.
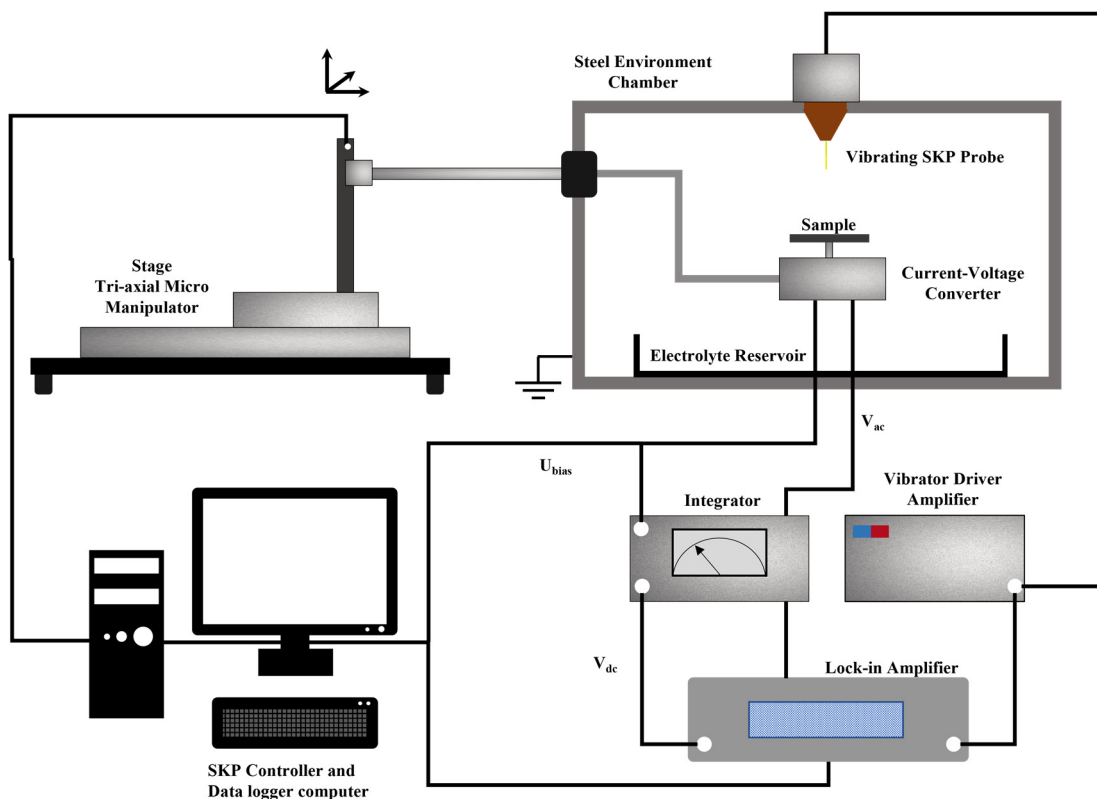
Figure 2.3: Schematic diagram of the SKP apparatus used in this study.

2.2.3   Calibration of the SKP

The theory behind the calibration procedure is discussed in detail in Section 1.6.2. Various standard redox couples such as Ag/Ag^+, $Cu/Cu^{2+,}$ Fe/Fe^{2+} and Zn/Zn^{2+} were used to calibrate the SKP in terms of electrode potential. To achieve this, calibration cells made from the relevant metals were used and these calibration cells consisted of wells of 15 mm diameter and 5 mm deep. In the machined wells a 0.5 M aqueous solution of the respective metal chloride salt (nitrate salt for Ag) was injected. The well was then carefully placed in the environment chamber and the probe was positioned 100 μm above the meniscus of the electrolyte and the E_{KP} values were recorded while the electrode potentials vs. SCE were measured using a Solartron 1280 potentiostat.

To account for the influence of the PVB film on the calibration of the SKP, a free-standing PVB film is placed over the calibration disk with the film being in contact with the electrolyte meniscus. The Volta potential value is then obtained after letting the PVB film to equilibrate with the

electrolyte for >6 h and this value has been found to be ca. −220 V [4]. This value can then be taken into consideration when calculating the E_{corr} values via Equation (2.1). A schematic diagram of this calibration procedure is shown in Figure 2.4 for metal X.

The plots of E_{corr} vs. SHE against ΔV for Ag/Ag^+, $Cu/Cu^{2+,}$ Fe/Fe^{2+} and Zn/Zn^{2+} with and without the PVB film are presented in Figure 1.14 (Section 1.6.2). In this thesis, the calibration of the SKP was achieved by using a copper well containing 0.5 M of $CuSO_4$. The E_{corr} value for the Cu/Cu^{2+} redox couple is known to be ca. 300 mV and the E_{KP} value can be experimentally obtained for the Cu/Cu^{2+} and it was found to be ca. 250 mV. Equation (2.1) was then used to calibrate the experimental data obtained using the SKP.

$$E_{corr} = E_{KP} + \text{constant} \tag{2.1}$$

The constant is obtained using Equation (2.1) and in order to account for the influence of the PVB film, the offset number of −220 mV is added to the constant value. This final number is the calibration value, which is added to the SKP derived data.
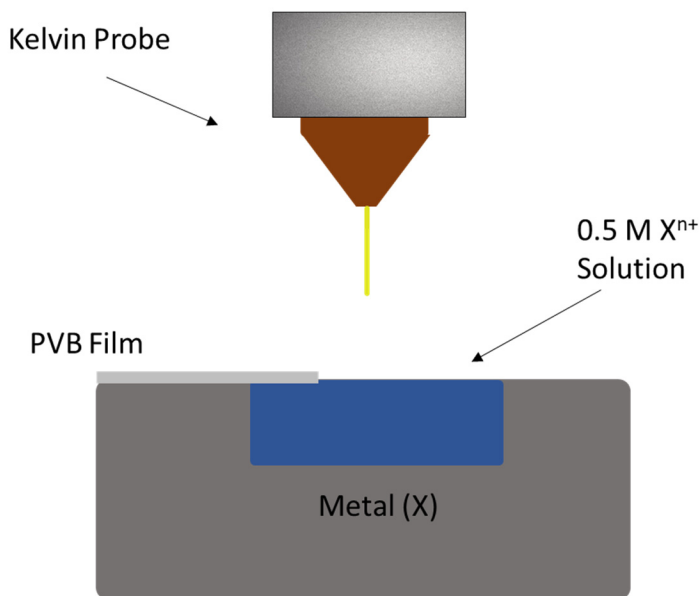
Figure 2.4: Schematic diagram of the Scanning Kelvin Probe calibration cell.

2.2.4 Rendering of the SKP Data

The data obtained from the SKP line scans were used to plot E_{corr} vs. Distance graphs for each scan (E_{corr} profiles plots). By further manipulation of these data, the delamination kinetics were plotted in the form of distance versus time. When the SKP was used to scan an area, the E_{corr} values obtained were inserted in a data mapping software (Surfer^{TM} by Golden Software).

2.2.5 SKP in the Absence of Oxygen

In order to investigate the influence of oxygen in the coating delamination phenomenon of Mg alloys, an SKP experiment was conducted under environmental conditions where only a very limited amount of oxygen (ca. < 1.4%) is present. This experiment was conducted in the laboratories of the industrial sponsor of this project (BASF Coatings GmbH) where they utilised an SKP apparatus with greater control of the environmental variables and the details of the SKP instrumentation employed in this experiment can be found elsewhere [5].

2.3 Time-Lapse Photography

The method of time-lapse photography was used extensively to investigate the delamination and filiform corrosion of coated Mg alloys. All experiments were carried out using an environment chamber unless otherwise stated. This environment chamber was comprised of a plastic box and a glass lid sealed on the top of the box to allow for better visibility allowing the coated Mg alloy specimens to be photographed in-situ when maintained in air at a constant RH. The maintenance of a constant relative humidity was achieved by adding the desired salt solution in the bottom of the environment chamber. To make sure that the lighting conditions remain the same throughout the experiment, two LED stripes were placed around the box. The camera used for this study was Canon EOS 77D fitted with AF micro lens and macrotubes to allow for close-up images of the surface. The image analysis to obtain the kinetics of the delamination and filiform corrosion was done by using Adobe Photoshop and ImageJ. The software was spatially calibrated by setting a set number of pixels to an already known distance (a ruler) within the photographic image.

2.4 Scanning Vibrating Electrode Technique (SVET) combined with Time-lapse Imaging (TLI)

A considerable amount of previous studies have successfully used SVET to understand the localised corrosion occurring on Mg surfaces under fully immersed conditions [6–10]. In this study, the SVET was combined with time-lapse imaging where a waterproof endoscope enabled the simultaneous capture of the current density maps with corresponding photographic images. The SVET is capable of resolving localised corrosion events taking place on the Mg surface, which can provide significant mechanistic information about the localised corrosion of Mg and its alloys.

In addition, the SVET can provide anodic and cathodic current density values that can be translated in terms of Mg dissolution and hydrogen evolution in a semi-quantitative way. The Mg dissolution and the hydrogen evolution may then be used for comparing the performance of different Mg alloys in the same solution as well as to evaluate the impact of the chloride ion concentration on the localised corrosion of the same Mg alloy. The specimens used in this investigation were E717 Mg alloys. These specimens were prepared as described in Section 2.1.3 with an area of 36 mm^2 exposed on the sample surface while the rest of surface was masked using a 90 μm thick extruded PTFE 5490 tape (3M Ltd.). To investigate the filiform-like localised corrosion phenomenon occurring on bare E717 Mg alloys, three different NaCl (aq) concentrations were used, 0.034 M, 0.17 M, and 0.86 M at pH 6. SVET scans were carried out at intervals of 10 minutes and thereafter for periods of up to 24 h, taking 144 scans in total. The SVET scans were carried out immediately after immersion of the Mg alloy in the electrolyte and then at intervals of every 10 minutes for up to 24 h. The scan area was 36 mm^2 for all experiments, and the data point density was 5 points per mm in the x (6 mm) and the y (6 mm) direction giving 900 data points for the entire scan for each scan.

2.4.1 SVET-TLI Apparatus

The SVET-TLI was used to investigate the localised corrosion behaviour of the Mg alloy E717, which takes the form of a filiform-like filaments. A schematic diagram of the SVET-TLI is given in Figure 2.5. The SVET-TLI measurements were conducted using a 125 μm diameter platinum micro-tip electrode, encased in borosilicate glass, which scanned across the surface of the E717 with a constant probe-to-sample height of 100 μm. The SVET platinum tip is kept in a Teflon^{TM}

sheath and attached to a glass push rod. The push rod is fixed to a loudspeaker and is responsible for the tip vibration. In order to shield and avoid any electromagnetic leakage, the pushrod and the loudspeaker are placed in a mu-metal case. The probe of the SVET is vibrated with the help of a lock-in amplifier (Perkin Elmer EG & G model 7625) at a frequency of 140 Hz and an amplitude of 25 μm with the same lock-in amplifier also measuring the signal detected by the probe. As the SVET probe vibrates and moves along the surface, it will detect and record an alternating potential by crossing the lines generated by the current flux (See Section 1.6). The measured SVET signal is proportional to the potential gradient in the same direction as the vibration that arises from the current source in the electrolyte [11].

The movement of the probe in the x,y and z direction over the surface of the Mg alloy was controlled by a micromanipulator platform (Time and Precision Ltd.) connected to a computer. To allow for visual data capture of the freely corroding Mg surface, a Supereyes Y002 waterproof endoscope camera was used. This camera was attached to the probe assembly by using a 3D-printed friction clamp and arm, which was responsible for keeping the camera parallel to the vibrating probe of the SVET [12]. After one SVET scan was completed, the SVET head was automatically moved to position of rest and the camera was moved over the surface of the Mg alloy and a picture was taken. This was repeated after every SVET scan and therefore 144 pictures were taken from the entire experiment, which then were correlated with the corresponding 144 SVET scans.
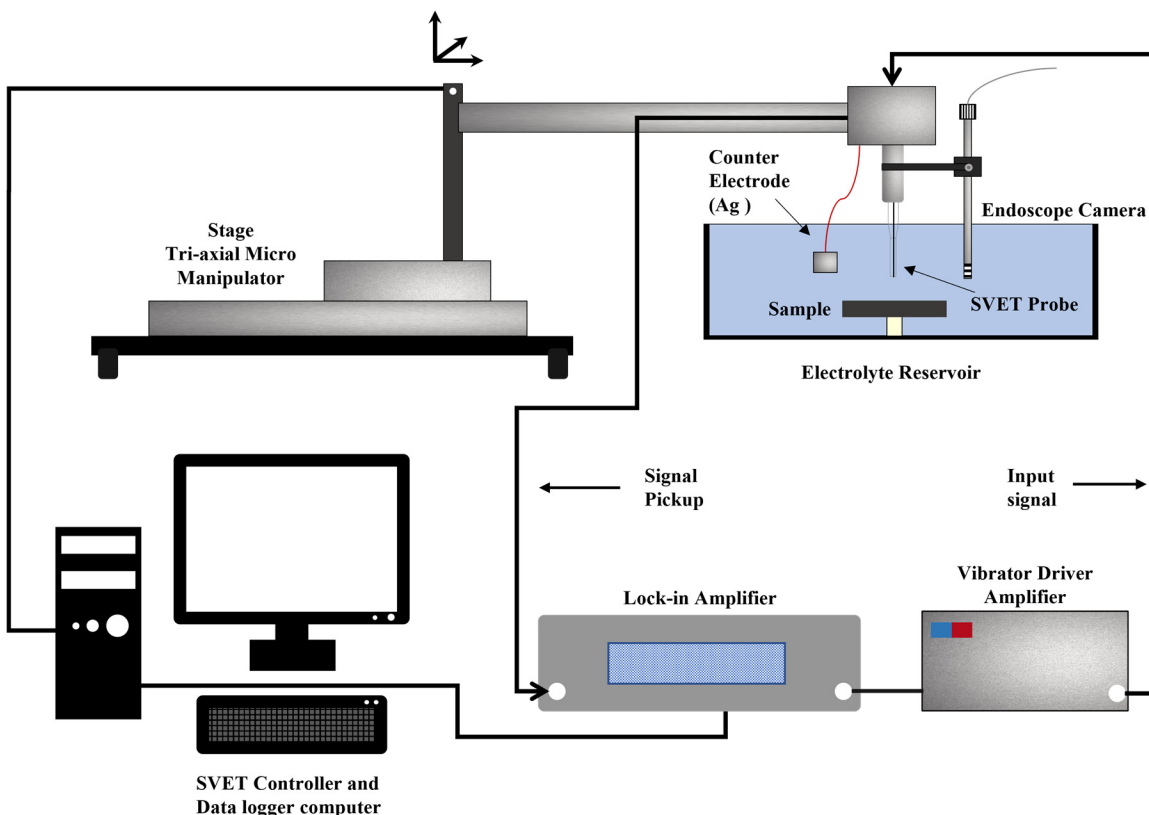
Figure 2.5: Schematic diagram of the SVET-TLI apparatus used in this study.

2.4.2 Calibration of the SVET-TLI

Without calibration, the SVET will record potential gradients in the solution. By calibrating the SVET, the recorded values of voltage can be converted into values of current density (A m^{-2}). The calibration of the SVET can be done by using a point current source where the SVET probe is vibrated at a constant height, frequency and vibration. By taking the Ohm's law into consideration, the current flux in the direction of vibration of the probe is related to the peak-to-peak voltage (V$_{pp}$) signal measured by the SVET. The current density along the axis of the probe vibration can be calculated by dividing the applied current by the hemispherical surface area (point current source profile) as given in Equation (2.2).

$$j_z = \frac{i}{2\pi z^2} \qquad\qquad 2.2$$

i = current source

z = height of probe above current source

The SVET a.c voltage signal can then be converted to a current density value in the axis of the probe vibration j_z by plotting the peak-to-peak voltage V_{pp} registered by the SVET versus the $i/(2\pi z^2)$.

In this study, the calibration of the SVET was achieved by the usage of a two-compartment cell where each compartment contains a 1 cm^2 Pt electrode with the electrolyte in question linking the compartments. This electrolyte was poured in a vertical glass tube and the SVET probe was lowered in the tube. A nano-galvanostat was then used to pass known currents through the tube and the current density was calculated since the area of the tube (5 mm diameter) was known. The current density is assumed to be uniform since the lines of current flux are parallel to the tube's length and the axis of vibration of the SVET probe. The relationship between the voltage measured by the SVET and the applied current density varies linearly, and the gradient obtained by plotting this relationship is the calibration factor of the SVET. This method of calibrating the instrument provides a way of converting voltage values into current density swiftly. These current density values can provide very useful insights for the localised corrosion of Mg alloys.

2.4.3 Manipulation of the SVET Data

By calibrating the data acquired by the SVET via the methodology outlined in Section 2.4.2, current density values in A m^{-2} were obtained. The calibrated data then were inserted into a data mapping software (Surfer^{TM} by Golden Software) and contour maps were created for every SVET scan. By using the contour mapping tool, the intensity and location of the anodic and cathodic areas can be easier detected on the exposed surface of the Mg alloy. The anodic activity is identified by the red colour, while the cathodic activity is marked by the blue colour and when there is no activity on the surface (electrochemically inert) a white colour predominates. The anodic/cathodic intensity is represented by colour intensity and the scale bar acts as a reference point to correlate the colour to current density values.

Reworking of the data obtained by the SVET can provide valuable information about the mechanisms under investigation. The time dependent evolution of local anodic (I_a) current for each scan can be obtained by numerical integration of the SVET-derived current density (j_z)

distributions (Equation (2.3)). The value obtained for each scan is the total anodic current sourcing from the exposed surface of the sample.

$$I_a = A \, j_a \geq \int_0^X \int_0^Y [j_{z(x,y)} > 0] \, dx \, dy \qquad 2.3$$

Where A is the exposed sample area, I_a is the anodic current, X and Y are the length and width of the SVET scan and j_z is the SVET-derived current density. The same process can also be used to obtain the equivalent current for the cathodic process by adjusting accordingly the formula above. In addition, the area averaged anodic current density values can also be obtained by diving I_a with the exposed surface area of the sample. By assuming that the corrosion activity remains constant between each scan (i.e. every 10 minutes), the Mg loss (anodic) or the hydrogen gas evolved (cathodic) can be calculated by using the Faraday's law. The total charge emitted from the surface of the Mg alloy over 10 minutes was calculated by using the Equation (2.4).

$$Q = I \times t \qquad 2.4$$

Where Q is the charge in C m^{-2}, I is the anodic current in A and t is the length of the scan in seconds. By utilising the Faraday's law and the charge Q the total Mg loss can be calculated for one scan.

$$TeMg = \frac{Q}{2F} \times M(Mg) \qquad 2.5$$

Where TeMg is the total equivalent Mg loss in g m^{-2}, M(Mg) is the molar mass of Mg (24.305 g mol^{-1}) and F is the Faraday's constant (96486 C mol^{-1}). It is also possible to calculate the total loss of Mg for the entire 24 h experiment by summing the individual mass loss values for each scan. By following a similar methodology, the total hydrogen evolution or the hydrogen evolution rate can be calculated. This can be achieved by using the cathodic current I_C and convert these values in time-dependent values of the moles of hydrogen evolved per unit area. For the estimation of total cathodic current I_c, the Equation (2.3) was applied to $j_{z(x,y)}$ for values < 0. The total quantity of hydrogen evolved can then be calculated from the area-averaged J_c current density and by applying Faraday's law.

2.5   Open Circuit Potential (OCP)

The samples for these experiments were prepared as described in Section 2.1.3. After the samples were prepared, a 90 µm thick extruded PTFE 5490 tape (3M Ltd.) was used to mask the sample leaving an area of 6 mm x 6 mm exposed as well as a small area on the top edge of the sample to allow for an electrical connection to be made. A conventional two-electrode setup was used for the studies of time-dependent free corrosion potential (E_{corr}) of the E717 Mg alloy in various salinity levels. The working electrode (WE) was the sample and a saturated calomel electrode (SCE) was used as the reference electrode (RE) that was placed next to the exposed surface of the sample. A Solartron 1280B Workstation was used to measure the time-dependent free corrosion potential in all cases. The WE and the RE were then immersed in aerated NaCl (aq) solutions at concentrations of 0.034 M, 0.17 M, 0.6 M, 0.86 M, 2 M, and 3.4 M at pH 6. Each open-circuit potential measurement was carried out for 180 minutes unless otherwise stated. After all data sets were collected, the free corrosion potential values were plotted against time for each experiment to allow for the direct comparison of the different levels of salinity.
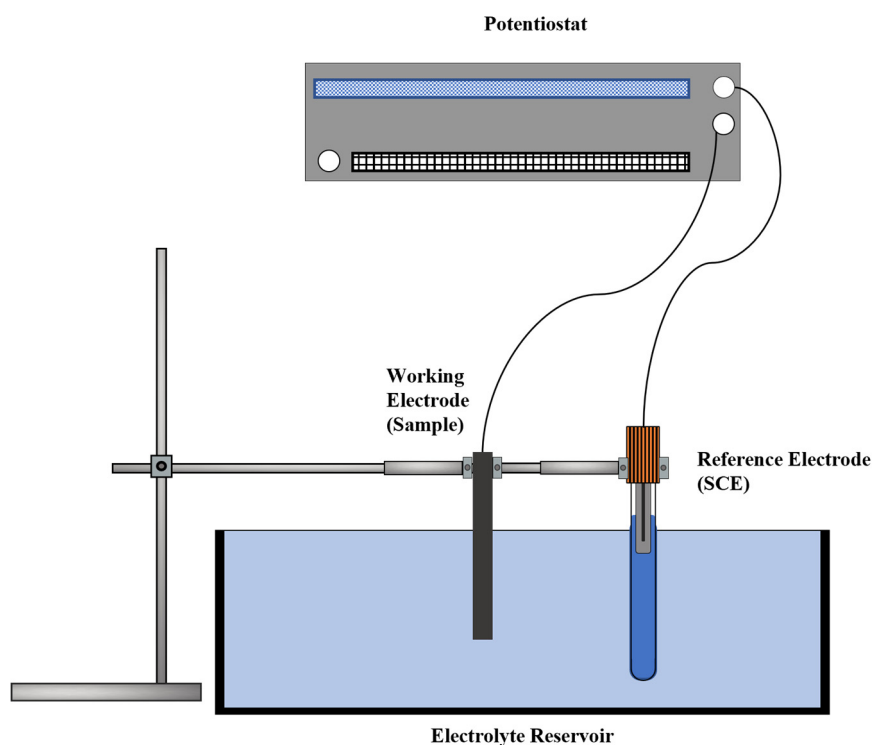
Figure 2.6: Schematic diagram of the experimental set-up used for open circuit potential (OCP) measurements.

2.6 Potentiodynamic Experiments

As with the open circuit potential measurements, the samples were prepared in the same way as described in Section 2.1.3. A 10 mm x 10 mm square was isolated in the centre of the sample and the rest of the sample was masked using a 90 μm thick extruded PTFE 5490 tape (3M Ltd.) leaving a small area exposed on the top edge of the sample to allow for electrical connection as with the OCP measurements. The potentiodynamic experiments were carried out using a three-electrode setup coupled with a Solartron 1280B Workstation. The three-electrode setup consisted of the Mg sample as the working electrode, a saturated calomel electrode as the reference electrode and a platinum gauze sheet (1 cm^2) serving as the counter electrode (CE). The sweep rate for all experiments was 1 mV s^{-1} and the measurements were taken between −1.9 V to –0.8 V unless otherwise stated. The potentiodynamic polarisation measurements were conducted using aerated aqueous solutions of 10^{-2} M, 0.034 M, 0.17 M and 0.86 M NaCl at pH 11. Prior to the start of potentiodynamic polarisation experiments, the solution was purged for 15 min using synthetic air to avoid any interference from carbonate species formed as a result of dissolved carbon dioxide.
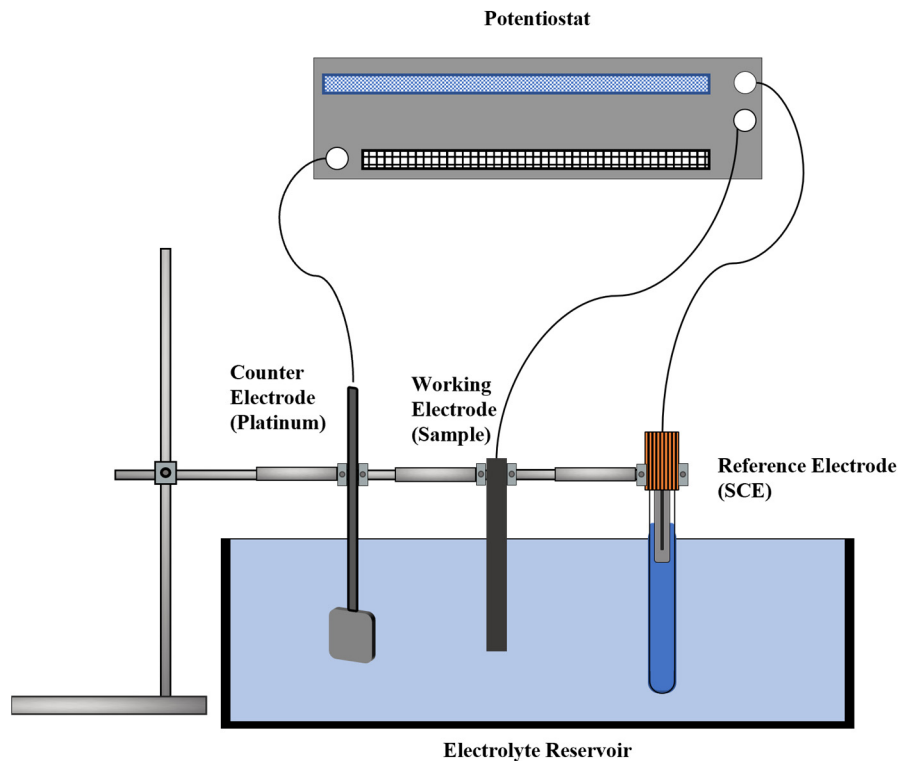
Figure 2.7: Schematic diagram of the experimental set-up used for potentiodynamic experiments.

2.7   Volumetric Hydrogen Gas Evolution Collection

The hydrogen gas evolution from the freely corroding Mg alloys in NaCl (aq) solution was collected volumetrically by using a 10 ± 0.02 cm^3 capacity conically ended burette. After the E717 and AZ31 samples were prepared as described in Section 2.1.3, they were masked using a 90 μm thick extruded PTFE 5490 tape leaving exposed a square area of 36 mm^2. The same tape was also used to secure the sample on the bottom of the beaker. The conical end of the burette was then placed on the top of the exposed surface leaving a small gap of few mm between the sample's surface and the burette's opening to allow for electrolyte to circulate whilst keeping a minimal distance from the surface to avoid any hydrogen gas escaping. After pouring the test electrolyte into the beaker, a syringe was attached to the other end of the burette and the electrolyte was drawn upwards to the 0 mark of the burette. Then the burette's tap was closed and when the electrolyte volume was displaced by the hydrogen gas evolution, the change of volume was recorded. A schematic diagram of the apparatus used for the volumetric hydrogen gas evolution collection is

presented in Figure 2.8. These series of experiments were performed in aerated NaCl (aq) solutions at concentrations of 10^{-3} M, 0.034 M, 0.17 M, 0.6 M and 0.86 M at pH 6.5. From the recorded displaced volume, the mols of hydrogen gas evolved per unit area were calculated and plotted against time to allow for comparison between different salinity levels and different Mg alloys.
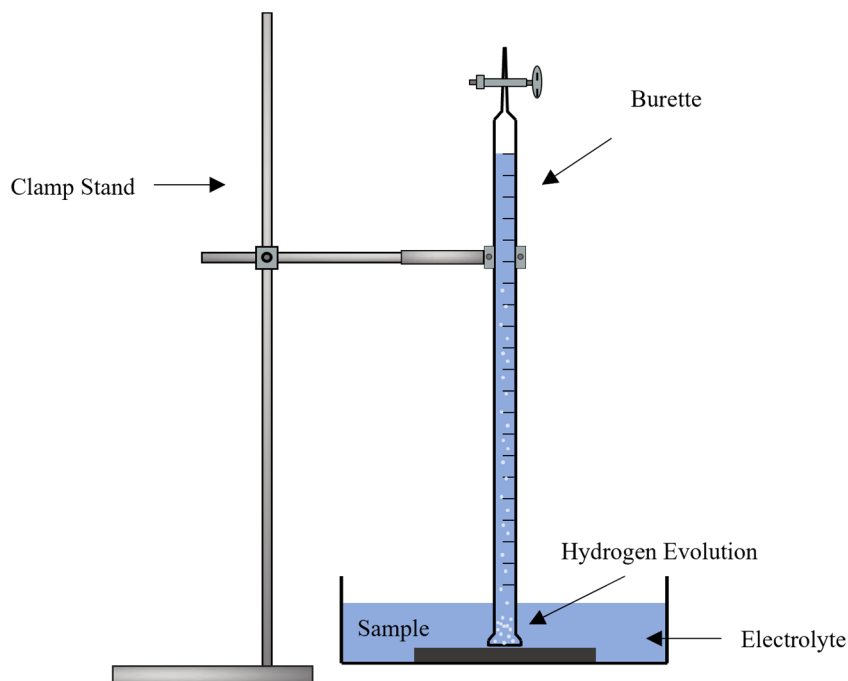
Figure 2.8: Schematic representation of the set-up used for hydrogen evolution collection (volumetrically) experiments.

2.8 Filiform Corrosion (FFC) Experiments

For this type of experiments the Mg samples were prepared as described in Section 2.1.3 and 2.2.1.2. The prepared and PVB coated samples were scribed with a scalpel and 10 mm long penetrative coating defects were made into the PVB coating. The FFC corrosion was then initiated by applying 1 µl (otherwise stated) of the selected electrolyte into each scribe with the use of a Hamilton® 2 µl syringe. A range of different aqueous electrolytes were used to investigate the influence of the initiating cation type on the chloride induced filiform corrosion of coated Mg alloys where 0.5 M of FeCl$_2$ (aq) and MgCl$_2$ (aq) was used while 1 M HCl (aq) was employed to ensure that the same amount of Cl$^-$ were present in the testing solutions. To understand the effect

of the chloride ion concentration, four different concentrations of $MgCl_2$ were used: 5×10^{-3} M, 0.02 M, 0.1 M, and 0.5 M. After the selected electrolyte was applied into the scribe, the sample was allowed to dry in air and then placed in a chamber with the selected level of relative humidity. The different levels of relative humidity (RH) used in this investigation were: 31%, 52%, 76%, 93% and 99%. These levels of relative humidity were achieved by using the respective saturated solutions of the following chemicals that were acquired by Sigma-Aldrich Chemical Co: $CaCl_2 \cdot 2H_2O$, $Ca(NO_3)_2$, NaCl, $Na_2SO_4 \cdot 10H_2O$ and DI water at 21 °C [13,14].

The relative humidity and temperature were constantly monitored via a data logger (EasyLog® from Lascar Electronics Limited) that was placed inside the environment chamber. After applying the respective electrolytes into the scribe, the samples were placed in bespoke environmental chambers where each relative humidity was attained. As it was described in Section 2.3, the environment chambers were made of a plastic box with a glass lid to allow for the FFC to be studied via time-lapse imaging. The samples were kept in the respective environment chambers for 21 days (unless otherwise stated) and a photographic image was taken every day until the termination of the experiment. The photographic images were then obtained and analysed using Adobe Photoshop and ImageJ software.

2.8.1   Filiform Corrosion (FFC) under Oxygen-free Conditions

This experiment was conducted in order to establish whether FFC occurs in organic coated Mg alloys in the absence of oxygen. The samples were prepared in a same way as it was described in Section 2.2.1.2 and then 1 μl of 0.5 M $MgCl_2$ (aq) was applied into the scribe. The sample then was placed into a container that had a similar configuration as the one described in Section 2.3 with the only difference being the inlet and the outlet positioned on each side of the container to allow for humidified air or nitrogen to be introduced. Nitrogen gas was humidified before it was introduced in the container by purging it through three Dreschel bottles (connected in series) containing a saturated solution of $Na_2SO_4 \cdot 10H_2O$. The sample was then kept in the container for 10 days with the N_2 gas flowing continuously into the chamber to make sure that no oxygen is infusing into the box. A Canon EOS 77D was set to time-lapse mode to take pictures every hour for more than 10 days and the set-up used is described in Section 2.3. The obtained photographic images were analysed using Adobe Photoshop and ImageJ software.

2.9 Delamination of Organic Coatings from Mg Surfaces (Scribed Defect Cell)

Initially, these experiments were conducted to investigate whether coating delamination can be initiated in organic coated Mg alloys. The methodology followed here is similar to the procedure used for filiform corrosion experiments described in Section 2.8. For this type of experiments the Mg samples were prepared as described in Section 2.1.3 and 2.2.1.2. The prepared and PVB coated samples were scribed with a clean scalpel and 10 mm long penetrative coating defects were made into the PVB coating. The underfilm corrosion was then initiated by applying 1 µl of 1 M (otherwise stated) aqueous solutions of either HCl, NaCl, LiCl, KCl, CsCl or 0.5 M $MgCl_2$ distributed evenly along the defect using a Hamilton® 2 µl syringe microlitre syringe. The samples were then placed in an environment chamber with conditions of 21 °C and 93% relative humidity in isopiestic equilibrium with a saturated solution of $Na_2SO_4.10H_2O$. The samples were kept in the environment chambers for 72 h (unless otherwise stated) until the termination of the experiment and a photographic image was taken every hour following the methodology described in Section 2.3. The photographic images were then analysed using Adobe Photoshop and ImageJ software.

2.9.1 Coating Delamination under Oxygen-free Conditions

This experiment was conducted to establish whether coating delamination will take place on organic coated Mg alloys in the absence of oxygen. The samples were prepared in a same way as it was described in Section 2.2.1.2 and then 1 µl of 1 M NaCl (aq) was injected into the scribe. The rest of the procedure is the same as the one described in Section 2.8.1. In this case, the sample was kept in the container, which also comprised an inlet and outlet allowing humidified nitrogen to be introduced with the N_2 gas flowing continuously into the chamber to ensure that no oxygen is infusing into the box. A Canon EOS 77D was set to time-lapse mode to take pictures every hour for the period of 72 h and the set-up used is described in Section 2.3. Photoshop and Image J software were then used to analyse the obtained photographic images.

2.10 Surface Characterisation

2.10.1 Scanning Electron Microscopy with Energy-dispersive X-ray Spectroscopy (SEM-EDS)

Scanning electron microscopy (SEM) with energy dispersive X-ray analysis (EDS) was used for post corrosion surface investigation of organic coated Mg samples that underwent FFC. Immediately after the FFC experiment was terminated, the PVB coating was carefully peeled off and the sample was analysed for Cl^- using a Hitachi TM3000 SEM with integrated Bruker Quantax 70 EDS Analyser. The SEM beam accelerating voltage was set at 15kV and 20kV and the EDS analyser was used for the detection of elements.

2.10.2 Time of Flight - Secondary Ion Mass Spectrometry (ToF - SIMS)

The secondary ion mass spectrometry was employed in this study to investigate the post corrosion Mg alloy surface where delamination of the organic coating has already occurred. The ToF-SIMS that was used in this study was MiniSIMS-ToF instrument supplied by SAI Ltd. The PVB coating was carefully peeled off immediately after the delamination experiment was terminated and the sample was inserted into the chamber of the SIMS. The surface that was affected by the halo detachment and its vicinity were then mapped for elements and the position of Cl^- and Cs^+ was located. The sample surface was pulsed by a particle beam (Ga) to remove chemical species from the area of the sample's surface under investigation with a kinetic energy of a few keV and the ionised secondary ions were detected by the Time of Flight (ToF) mass analyser [15].

2.11 References

[1]   M. Stratmann, A. Leng, W. Fürbeth, H. Streckel, H. Gehmecker, K.-H. Groβe-Brinkhaus, The Scanning Kelvin Probe; a new technique for the in situ analysis of the delamination of organic coatings, Prog. Org. Coatings. 27 (1996) 261–267.

[2]   W. Fürbeth, M. Stratmann, The delamination of polymeric coatings from electrogalvanised steel - a mechanistic approach. Part 1: delamination from a defect with intact zinc layer, Corros. Sci. 43 (2001) 207–227.

[3]   G. Williams, H.N. McMurray, The mechanism of group (I) chloride initiated filiform corrosion on iron, Electrochem. Commun. 5 (2003) 871–877.

[4]   G. Williams, H.N. McMurray, Chromate inhibition of corrosion-driven organic coating delamination studied using a Scanning Kelvin Probe technique, J. Electrochem. Soc. 148 (2001) B377–B385.

[5]   G.S. Frankel, M. Stratmann, M. Rohwerder, A. Michalik, B. Maier, J. Dora, M. Wicinski, Potential control under thin aqueous layers using a Kelvin Probe, Corros. Sci. 49 (2007) 2021–2036.

[6]   G. Williams, H.A.L. Dafydd, R. Grace, The localised corrosion of Mg alloy AZ31 in chloride containingelectrolyte studied by a Scanning Vibrating Electrode Technique, Electrochim. Acta. 109 (2013) 489–501.

[7]   G. Williams, R. Grace, Chloride-induced filiform corrosion of organic-coated magnesium, Electrochim. Acta. 56 (2011) 1894–1903.

[8]   G. Williams, K. Gusieva, N. Birbilis, Localized corrosion of binary Mg-Nd alloys in chloride-containing electrolyte using a Scanning Vibrating Electrode Technique, Corrosion. 68 (2012) 489–498.

[9]   G. Williams, N. Birbilis, H.N. McMurray, Controlling factors in localised corrosion morphologies observed for magnesium immersed in chloride containing electrolyte, Faraday Discuss. 180 (2015) 313–330.

[10]   E. Michailidou, H.N. McMurray, G. Williams, Quantifying the role of transition metal

electrodeposition in the cathodic activation of corroding magnesium, J. Electrochem. Soc. 165 (2018) C195–C205.

[11] D. A. Worsley, H. N. McMurray, A. Belghazi, Determination of localised corrosion mechanisms using a Scanning Vibrating Reference Electrode Technique, Chem. Commun. (1997) 2369–2370.

[12] R. Bolton, T. Dunlop, J. Sullivan, J. Searle, H. Heinrich, R. Westerwaal, C. Boelsma, G. Williams, Studying the influence of Mg content on the microstructure and associated localized corrosion behavior of Zn-Mg PVD coatings using SVET-TLI, J. Electrochem. Soc. 166 (2019) C3305–C3315.

[13] L. Greenspan, Humidity fixed points of binary saturated aqueous solutions, J. Res. Natl. Bur. Stand. (1934). 81 (1977) 89–96.

[14] R.. Weast, CRC Handbook of Chemistry and Physics, 69th ed., CRC Press, Boca Raton, FL, 1987.

[15] A. Schnieders, Time-of-Flight Secondary Ion Mass Spectrometry, Micros. Today. 19 (2011) 30–33.

Chapter 3

Corrosion-driven Organic Coating Failure on Mg alloys

Corrosion-driven Organic Coating Failure on Mg Alloys

3.1 Introduction

There is significant current interest in developing protective coatings for Mg alloys to overcome problems of poor corrosion resistance, which presently limit their widespread use. One of the most common methods of protecting Mg alloys from corrosion is by using inorganic barrier coatings and pre-treatments [1,2] and relatively few scientific studies of corrosion protection by organic coatings are available. A recent review identified types of protective organic coating technologies that could prove effective when applied to Mg based surfaces and highlighted methodologies that could potentially be used to quantify corrosion protection efficiency [3]. Electrophoretically deposited organic coatings (E-coat) [4,5] have also been evaluated as means of protecting Mg alloys and it was proposed that corrosive electrolyte penetration and the resultant formation of corrosion products at the coating/metal interface, such as magnesium hydroxide and hydrogen gas, caused delamination by physically forcing the coating from the metal surface [4]. A separate investigation showed that the presence of soluble inorganic salts at the metal/coating interface of polyester coated AZ91 Mg alloy caused osmotic blistering and subsequent corrosion-induced damage [6]. However, despite the previous efforts to investigate the organic coated Mg alloys, the precise mechanisms of organic coating failure remain unclear and there is an urgent need to better understand the processes that lead to corrosion-driven coating failure from Mg based surfaces.

It has been demonstrated by employing a model PVB coating applied to commercially pure Mg under atmospheric corrosion conditions, that the chloride-induced damage in the vicinity of a penetrative coating defect took the form of FFC [7]. The rate of filament propagation was shown to be insensitive to the presence of oxygen, and that chloride ions were conserved at the corrosion front, indicating an anodic undermining disbondment mechanism.

In the current chapter, the technologically important E717 Mg alloy is employed to investigate the underfilm corrosion of Mg alloys. The promising mechanical properties of this particular alloy for certain automotive applications [8,9] has led to a significant present interest in understanding its corrosion behaviour, both in the presence [5] and absence [10] of an organic protective coating. Using model PVB coatings applied to E717 substrates, underfilm corrosion is initiated by applying a range of different chloride based containing salts to a penetrative coating defect, including NaCl,

LiCl, KCl, CsCl, MgCl₂, and HCl. The coating failure rates are evaluated by a combination of time-lapse photography and in-situ Scanning Kelvin potentiometry while holding the specimens at a constant relative humidity. The SKP technique has been systematically utilised in the study of corrosion driven coating failures [7,11–14] due to its ability to map potential distributions beneath polymer coatings. The first aim of this chapter is to determine the role of the initiating chloride salt in the type of underfilm corrosion damage observed. Upon identifying a different type of coating failure in the presence of group I chloride salts, a further aim was established comprised of efforts of characterising the controlling factors in organic coating delamination in order to elucidate the prevailing disbondment mechanism.

―――――――――――――――――

The work shown in this chapter has been published elsewhere.

G. Williams, C. Kousis, H.N. McMurray, P. Keil, A mechanistic investigation of corrosion-driven organic coating failure on Mg and its alloys. npj Mater. Degrad. 3 (2019) 41.

3.2   Experimental Details

3.2.1   Materials and Sample Preparation

For this investigation, the technologically important E717 (Electron™ 717) Mg alloy was used, which came in sheets of 2 mm thickness and was cut into square coupons of 50 x 50 mm using electric discharge machining. More details about this Mg alloy can be found in Section 2.1.1. Prior to the application of the PVB model coating (polyvinyl butyral-*co*-vinyl alcohol-*co*-vinyl acetate), the coupons were prepared as stated in Section 2.1.3 and the polyvinyl butyral solution was prepared in ethanol (15.5 % w/w). All chemicals were obtained by Sigma-Aldrich Ltd. in analytical grade purity. In the current chapter, the underfilm corrosion experiments were performed by using a scribed defect cell as described in detail in Section 2.2.1.2.

3.2.2 Methods

In the current chapter, a series of electrolytes were used to identify the role of cation in the underfilm of a PVB coated E717 Mg alloy. Corrosion was initiated using 1 µl of 1 M aqueous solutions of either HCl, NaCl, LiCl, KCl, CsCl or 0.5 M $MgCl_2$ distributed evenly along the defect using a microlitre syringe (Hamilton Ltd) and the prepared samples were then placed in an environment chamber with conditions of 21 °C and 93% relative humidity in isopiestic equilibrium with a saturated solution of $Na_2SO_4 \cdot 10H_2O$. Similar methodology was also followed for the experiments under humidified N_2 and the detailed description of these methodologies are provided in Section 2.9. Time-lapse photography was used in order to quantify the kinetics of the halo detachment and the detailed methodology used is described in Section 2.3.

The post corrosion characterisation of the Mg alloy surface was carried out immediately after the specimen was removed from the humidified container using a ToF - SIMS and the details of this method are given in Section 2.10.2.

The in-situ potentiometric measurements under atmospheric corrosion conditions were carried out using the SKP instrumentation described in detail in Section 2.2. Briefly, the SKP reference probe was programmed to scan over the PVB coated E717 surface using a 125 µm diameter gold wire vibrated normal to the sample surface at 280 Hz, with a 30 µm peak-to-peak amplitude, and mid-amplitude probe-sample distance of 100 µm and was calibrated prior to its use using the methodology described in Section 2.2.3. Following initiation of underfilm corrosion as described above, PVB coated E717 samples were held initially in room air (ca. 20 °C and 50% RH) for 10 min and then transferred to the SKP environment chamber that was maintained at 20 °C and 93% RH in isopiestic equilibrium with a saturated aqueous $Na_2SO_4 \cdot 10H_2O$ reference solution. SKP scans were initiated immediately and repeated every 6 h for up to 72 h. Each scan comprised a rectangular grid of 120 × 140 data points over a 6 mm × 7 mm area situated to one side of the coating defect.

3.3 Results and Discussion

3.3.1 Delamination of Model Polymer Coated Alloy Surfaces

Preliminary experiments using PVB coated E717 specimens were designed to assess the difference between underfilm corrosion morphologies produced upon initiation by equivalent concentrations of either HCl (aq) or NaCl (aq). Previous investigations involving organic coated Al alloy surfaces have shown that the methodology employed here, involving the direct injection of a controlled quantity of aqueous chloride-containing solution directly into a fixed length of penetrative coating defect, reproducibly generates filiform corrosion in such a way as to facilitate kinetic investigations on underfilm corrosion propagation [15]. Figure 3.1 shows a series of images of a PVB coated E717 specimen, comprising two separate scribed coating defects, held in humid air for increasing time periods following initiation of corrosion. Underfilm corrosion was initiated using HCl (aq) on the left-hand side defect, while aqueous NaCl was applied to the defect on the right. A network of black tracks is observed in the vicinity of the left-hand side defect region, which appears to grow slowly with holding time, extending to a maximum distance of ca. 2 mm either side of the defect over a 3-day holding period.
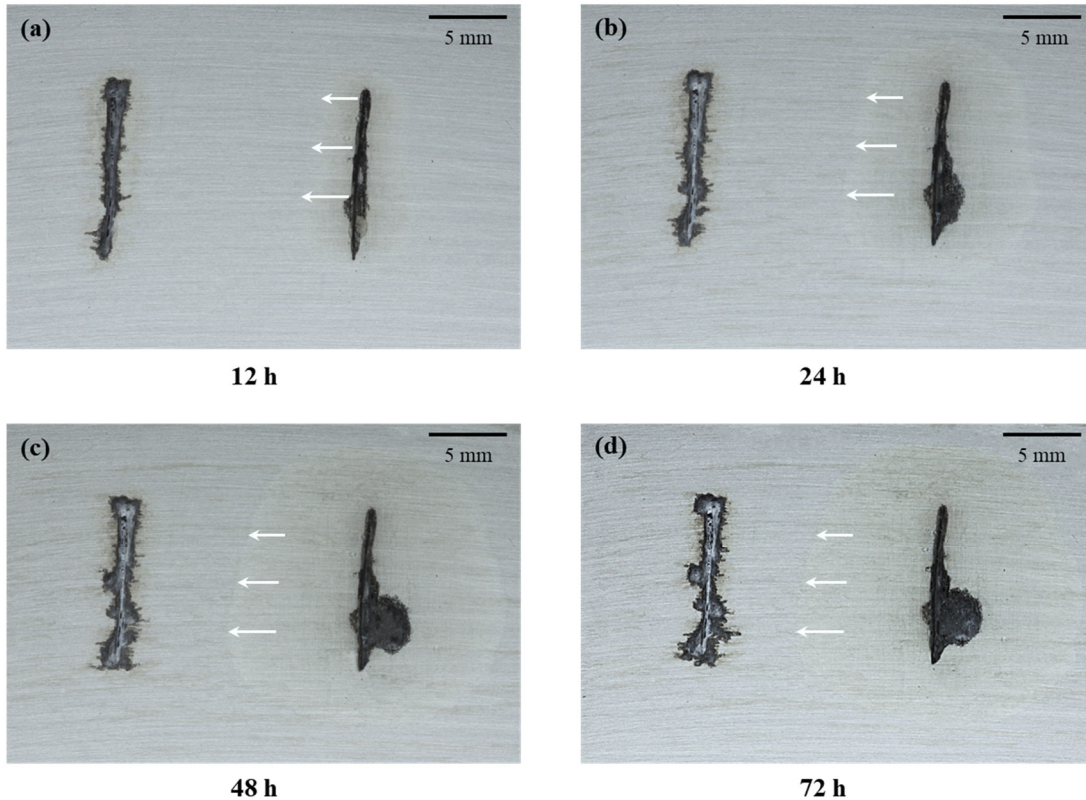
Figure 3.1: Photographic images of a PVB coated E717 alloy undergoing corrosion at a constant relative humidity of 93% after periods of (a) 12 h, (b) 24 h, (c) 48 h and (d) 72 h following corrosion initiation by applying HCl (aq) (left) and NaCl (aq) (right) to a penetrative coating scribe.

Initiation of underfilm corrosion using NaCl (aq) (right-hand side, Figure 3.1a–d) also produces a small amount of dark corrosion product in regions adjacent to the defect, which grow in area with respect to holding time. However, somewhat surprisingly underfilm corrosion is also characterised by the development of a halo surrounding the defect region, whose leading edge (see arrows on Figure 3.1a–d) extends further from the defect with time. Figure 3.1d shows that the visible halo edge has propagated over a distance of ca. 8 mm during the 3-day holding time. Although the leading edge of the halo remains highly visible at all times, the Mg alloy surface within the halo to the left side of the penetrative defect appears largely uncorroded and free of black corrosion product. No such halo could be observed in the vicinity of the defect region where corrosion was initiated via the application of HCl (aq). Upon removal of the specimen from the humidity chamber, it was confirmed that PVB coating was de-adhered from the Mg alloy surface in the

region occupied by the halo but remained adherent to the surface at a point marked by the leading edge. Repeat experiments carried out using different concentrations of NaCl (aq) in the 0.1 M–1 M range also gave similar results, where an apparently uncorroded region surrounding a penetrative defect was affected by organic coating delamination.

In order to determine the free corrosion potentials (E_{corr}) associated with the underfilm delamination cell apparently set-up in the presence of NaCl (aq) applied to a coating defect, a separate experiment was carried out by using the SKP to map an area of the coated E717 surface. Figure 3.2 shows a series of SKP-derived greyscale image maps obtained by in-situ scanning a region of the PVB coating surface to the right-hand side of the defect as indicated by the dashed rectangle on the photographic image of the post-corrosion surface (see Figure 3.2d). Average E_{corr} values in the −1 to −1.1 V (vs. SHE) range are measured for intact (un-corroded) surface to the far left of the maps, consistent with the alloy surface being in a passive state. The region adjacent to the defect, affected by the progress of underfilm corrosion, is shown as an expanding area of significantly lower E_{corr} in the range −1.2 to −1.3 V (vs. SHE). The percentage area occupied by the zone of more negative potential progressively increases with holding time and within 40 h of initiation, has propagated over the majority of the scanned area. De-adhesion of the model organic coating within the zone of depressed E_{corr} was confirmed at the end of the experiment by carefully peeling away the PVB coating from the substrate using tweezers. It was observed that the halo leading edge marked the boundary between a physically de-adhered region and one where the coating remained fully adherent to the Mg alloy surface. The time-dependent evolution of E_{corr} distributions associated with the development of underfilm corrosion are perhaps more clearly seen in Figure 3.3, which shows profiles of E_{corr} versus distance from the penetrative defect, obtained at various holding times following initiation. The profiles were recorded within the region indicated by the white dashed arrow in Figure 3.2b. It may be seen that the E_{corr} values measured for the intact (un-corroded) surface (E_{intact}) progressively increase with holding time, but appear to stabilise at values of −0.98 ± 0.02 V vs. SHE after 20 h.
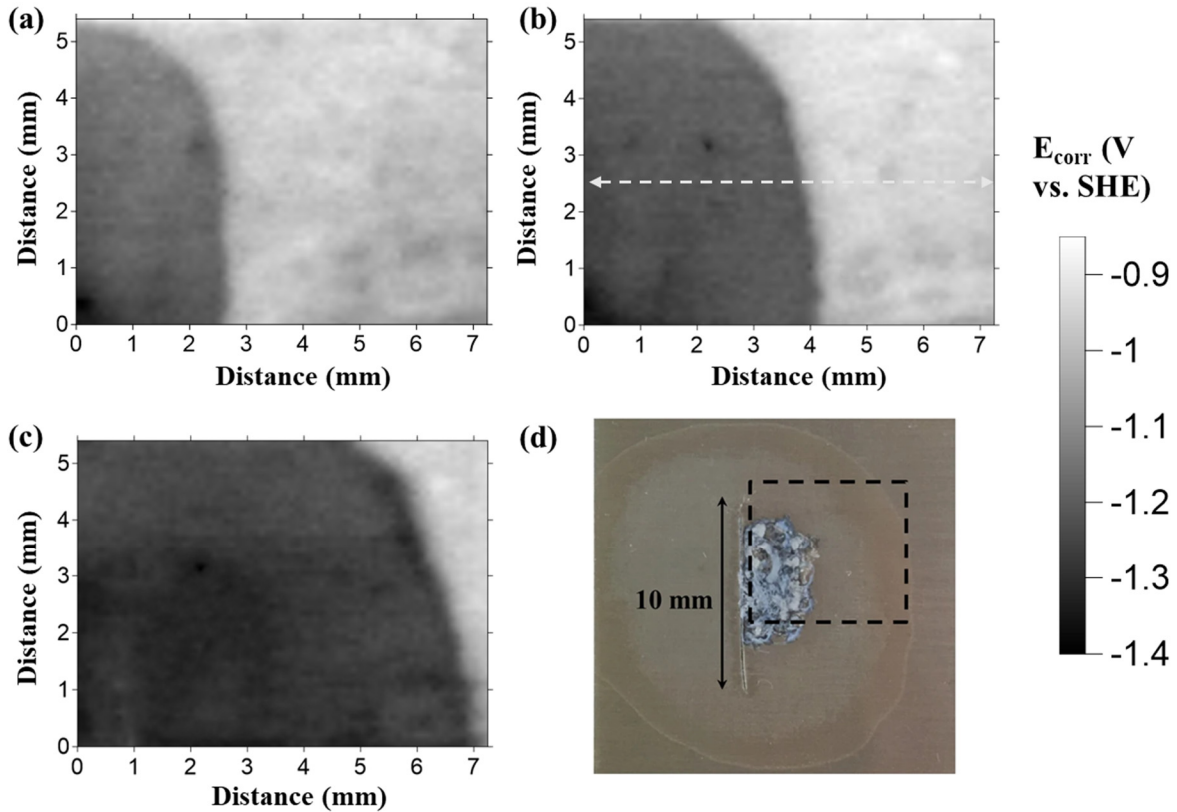
Figure 3.2: Greyscale image maps showing E$_{corr}$ distributions, measured by in-situ SKP, recorded over a PVB-coated E717 substrate following initiation of corrosion by applying 1 μl of 1 M NaCl (aq) electrolyte to the coating defect region. Time key: (a) 16 h, (b) 24 h and (c) 40 h, while (d) shows a photographic image of the sample after 40 h indicating the region of the coated surface that was scanned.

It is likely that this change in E$_{intact}$ values results from some initial atmospheric corrosion of highly reactive Mg alloy surface, even in the presence of an intact model organic coating, when introduced to the highly humid holding environment. The same behaviour was observed when a bare E717 surface was held over a protracted period in a humid environment, confirming that the rise in E$_{intact}$ derives from a change in the alloy surface rather than a change in the chemistry of the polymer coating. E$_{corr}$ values near the penetrative defect approach that expected for Mg actively corroding in the presence of aqueous chloride ions (ca. – 1.3 V vs. SHE) [7], whilst the leading edge of the zone of underfilm corrosion is marked by the sharp change in E$_{corr}$ with an estimated gradient of ca. 0.4 V mm^{-1} . The region that links the leading edge to the defect is characterised by a significantly lower positive gradient of ca. 8 mV mm^{-1}. There appears to be little change in

the magnitude the E_{corr}-distance slopes determined over the corroded surface and at the apparent disbondment front with progressively longer holding times. Therefore, assuming that the underfilm resistivity within these zones remain unchanged over the duration of the experiment, the observation of constant slopes indicates that the ionic current flux coupling the defect to the halo edge remains unaffected by the distance moved by the disbondment front.
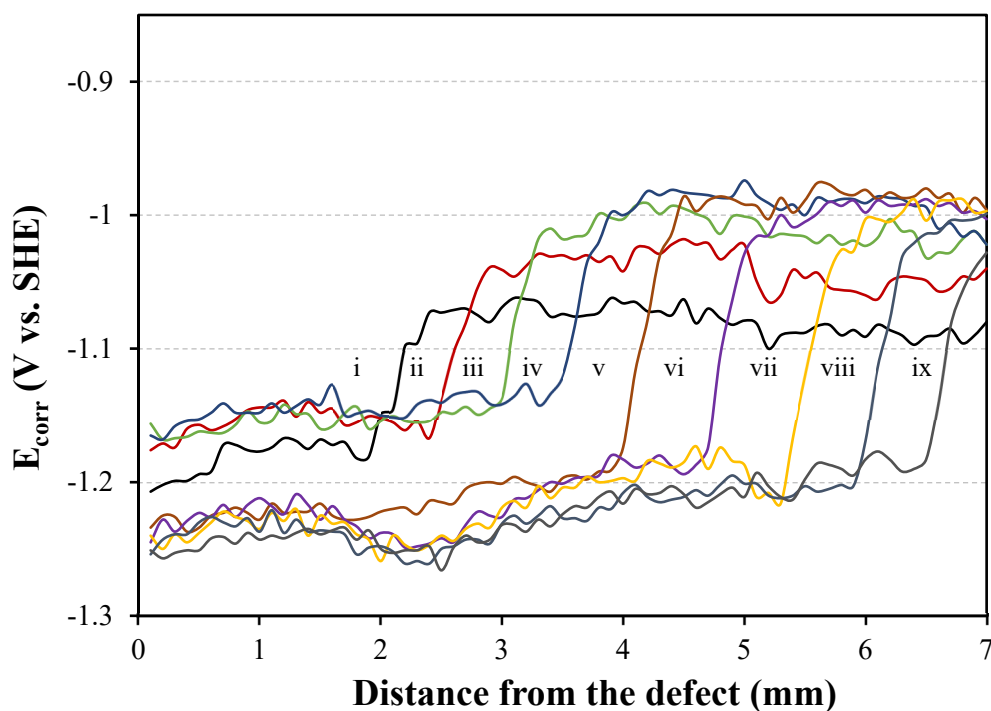
Figure 3.3: Profiles of E_{corr} versus distance from a penetrative coating defect obtained for a PVB-coated E717 sample at various times following initiation of corrosion using 1 µl volume of 1 M NaCl (aq). Time key (i) 6 h, (ii) 10 h, (iii) 14 h and 4 h intervals thereafter. The sample was maintained at room temperature and a constant R.H. of 93% throughout. The arrow on Figure 3.2b indicates the region of the scanned area where the profiles were recorded.

At first glance the characteristics of the E_{corr} versus distance profiles strongly resemble those reported previously for cathodic organic coating delamination on both Fe [14,16–18] and Zn [13,19,20] substrates, although the absolute values of E_{corr} are markedly more negative in the present case. Importantly, they do not appear to correlate well with previously published E_{corr} versus distance profiles obtained for commercially pure, PVB-coated Mg, actively undergoing anodic disbondment via HCl inoculated filiform attack [7]. In this case the profiles were

characterised by the appearance of an E_{corr} minimum immediately behind the advancing disbondment front that was coupled to the defect by a zone in which a negative E_{corr}-distance gradient was observed. It seems evident therefore that the presence of the Na^+ cations plays a significant role in directing the type of underfilm corrosion observed during chloride-induced atmospheric corrosion of the organic coated Mg alloy surface. The role of the cation was further investigated by using other group I chloride salts along with $MgCl_2$, applied at a concentration of 1 M (0.5 M for $MgCl_2$ (aq)) to a penetrative scribe in the model organic coating.
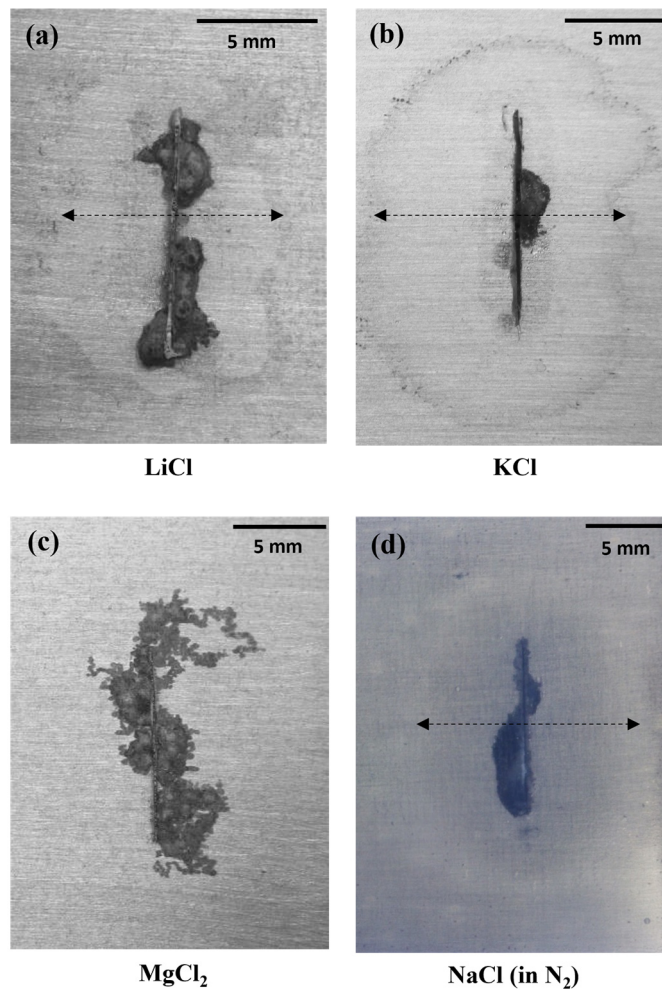
Figure 3.4: Photographic images of PVB coated E717 alloy specimens undergoing underfilm corrosion after a 72 h holding time at 93% RH, following initiation by applying aqueous 1 µl of 1 M (a) LiCl (aq), (b) KCl (aq) and (c) $MgCl_2$ (aq) (0.5 M) while (d) shows an E717 NaCl (aq) initiated specimen held in N_2 at 93% RH.

Figure 3.4a, b shows post-corrosion images of PVB-coated E717 samples taken after exposure to humid air for 3 days following initiation of corrosion using LiCl and KCl, respectively. In both cases, the appearance of a delaminated halo surrounding the defect is evident as indicated by the black dashed arrows. In the case of a $MgCl_2$ initiated specimen (Figure 3.4c), only dark filiform-like attack developed in the vicinity of the defect, where individual filaments were observed to lengthen progressively with time. Inspection of the post-corrosion surface showed that the coating was firmly adherent to the Mg alloy surface in regions close to the defect that were not affected by filiform-like activity.

3.3.2 Analysis of the Post-delamination Surface

In a separate experiment, where underfilm corrosion was initiated by applying 1 M CsCl (aq), the post-corrosion surface was subjected to elemental mapping using secondary ion mass spectrometry after carefully peeling away the model PVB coating. Figure 3.5a shows a photographic image of the post-corrosion surface, confirming that the appearance of the disbondment halo affects all group I chloride-initiated specimens. Cs and Cl distribution maps, corresponding with a region of the E717 surface indicated by the dashed rectangle, are shown in Figure 3.5b, c respectively as greyscale images. Figure 3.5b indicates that the entire delaminated halo region is abundant in Cs (shows as light regions), but that no Cs is detected beyond the leading edge of the disbondment front. Conversely Figure 3.5c confirms that Cl ions are not co-located with the Cs and are most likely conserved at or near the penetrative defect. The highly surface sensitive nature of the ToF-SIMS technique means that common contaminants such as chloride and sodium ions are typically detected on metallic uncorroded surfaces, and accounts for the weak chloride ion signal detected on the right-hand side of Figure 3.5c. The use of CsCl in preference to NaCl to initiate underfilm corrosion alleviates problems in elemental imaging caused by the ubiquitous nature of Na^+.
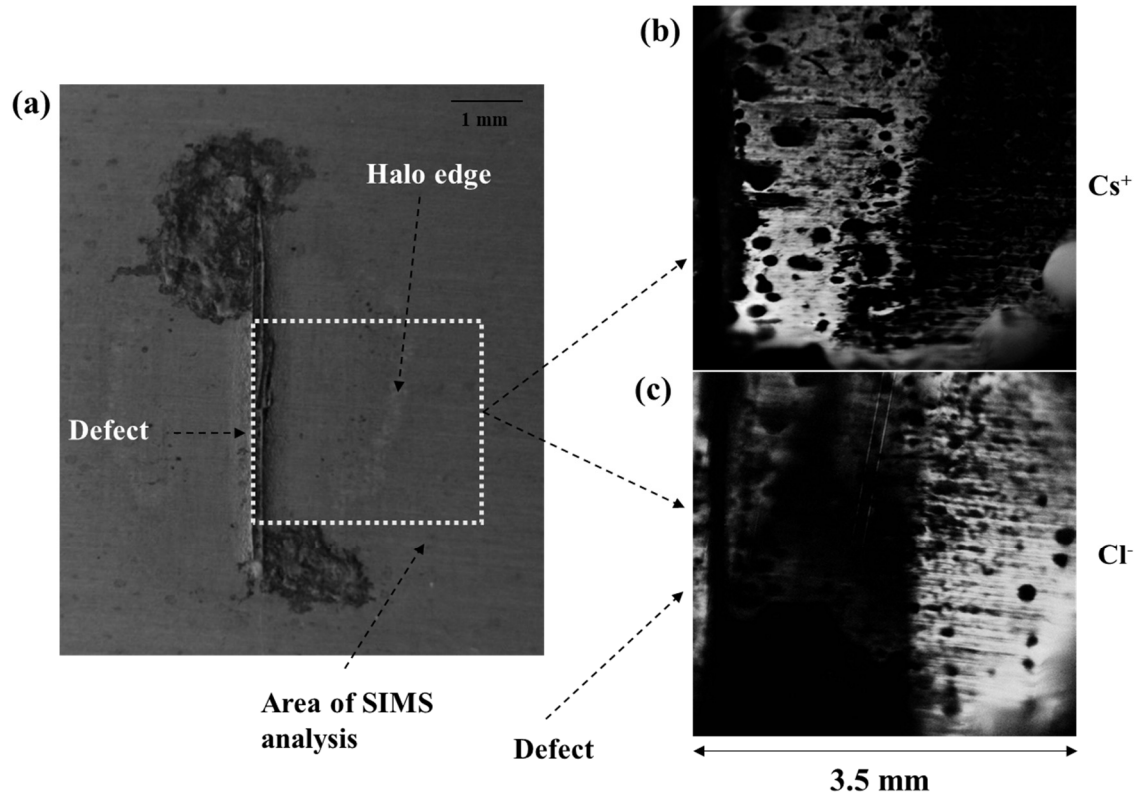
Figure 3.5: Post delamination E717 surface imaged using ToF-SIMS microscopy 48 h after initiation of underfilm corrosion using 1 μl of 1 M CsCl and following the removal of the PVB coating. (a) shows a photographic image indicating the sample area analysed, along with corresponding (b) cesium and (c) chlorine elemental distribution maps.

3.3.3 Quantification of the Delamination Kinetics

Figure 3.4d also shows a post-corrosion, NaCl-initiated E717 specimen, after holding at high humidity for 48 h, but in the absence of oxygen (i.e., held in a humidified N_2 flow). Again, the regions immediately adjacent to the defect are affected by dark corrosion product, while an elliptically shaped zone extending ca. 7 mm either side of the defect is also observed. In comparison with identically initiated specimens held in humid air, the halo observed in the absence of oxygen typically comprised a less well-defined leading edge, but a more tarnished interior, indicating a possible difference in atmospheric corrosion behaviour. Nevertheless, close examination of specimens held in humid nitrogen at the conclusion of the experiments confirmed that the halo of PVB coating surrounding the defect was not adherent to the Mg alloy surface.

Time-lapse photographic sequences recorded both in humidified air and nitrogen, used in combination with a 1 cm standard length enabled quantification of the time-dependence of disbondment front advance and the area propagation of the halo surrounding the defect.

Typical plots of delaminated distance, measured from the halo leading edge to the penetrative defect, versus holding time obtained for both humidified air and nitrogen environments are given in Figure 3.6. The magnitude of the error bars in plots i and ii for air and N_2 respectively reflects the greater difficulty in identifying the less clearly defined halo edge observed in the absence of oxygen. In both cases, the delamination distance increased linearly with time over the 40 h duration of the measurement, with slopes of 0.17 and 0.11 mm h^{-1} measured in air and nitrogen respectively. Duplicate experiments confirmed the repeatability of the slower delamination rate measured in the absence of oxygen.
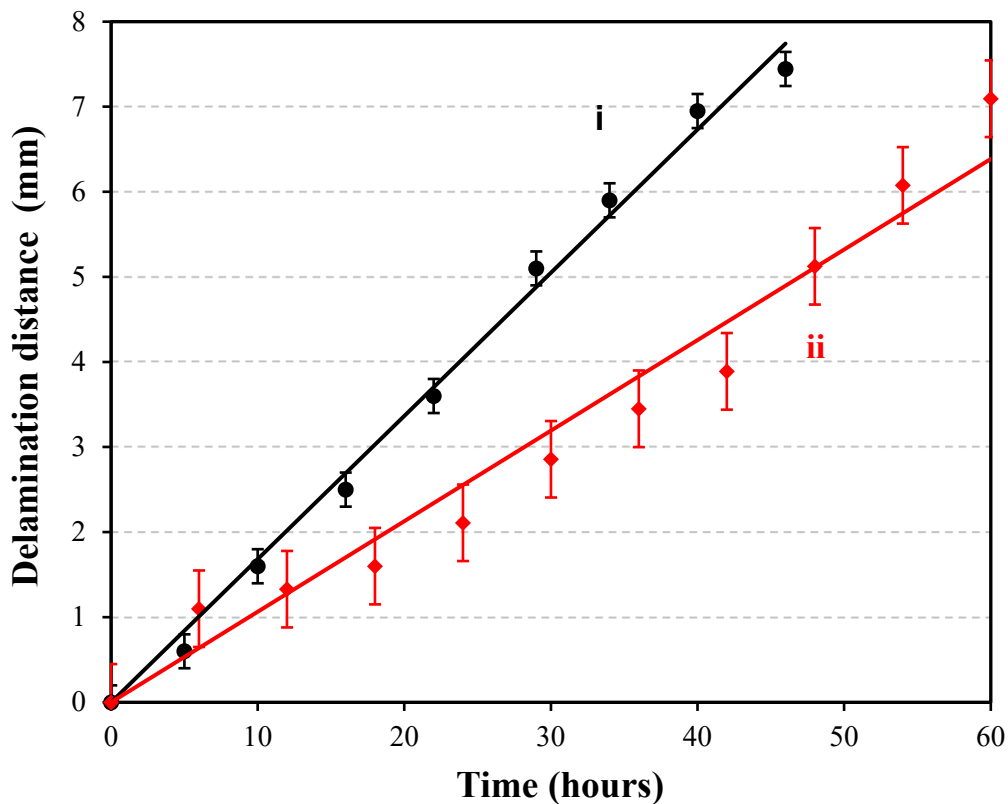
Figure 3.6: Plots of disbondment front distance from the coating defect versus time for PVB coated E717 alloy specimens held in (i) air and (ii) nitrogen at 93% RH. In both cases underfilm corrosion was initiated by applying 1 µl of 1 M NaCl (aq) to a 1 cm long penetrative coating defect. Average values from 3 repeat experiments are shown and the error bars represent the standard error of the mean.

Time-lapse sequences of halo development on group I chloride-initiated, PVB coated E717 surfaces were also analysed in terms of the time-dependence of coating area delamination. Figure 3.7 compares the increase in area occupied by the delaminated region surrounding the defect as a function of holding time at 93% RH in air for corroding specimens initiated with chloride salts of 4 different group I cations, namely Li^+, Na^+, K^+, and Cs^+. In turn the kinetics of halo area propagation are compared with those observed when an $MgCl_2$ salt was used (see Figure 3.7, plot v). Over an initial 30 h period, delaminated area increases linearly with time for all group I cations and there is little difference in the slopes of the respective slopes, which range from a minimum of 4.1 mm^2 h^{-1} (for Na^+) to a maximum 5.1 mm^2 h^{-1} (determined for K^+).
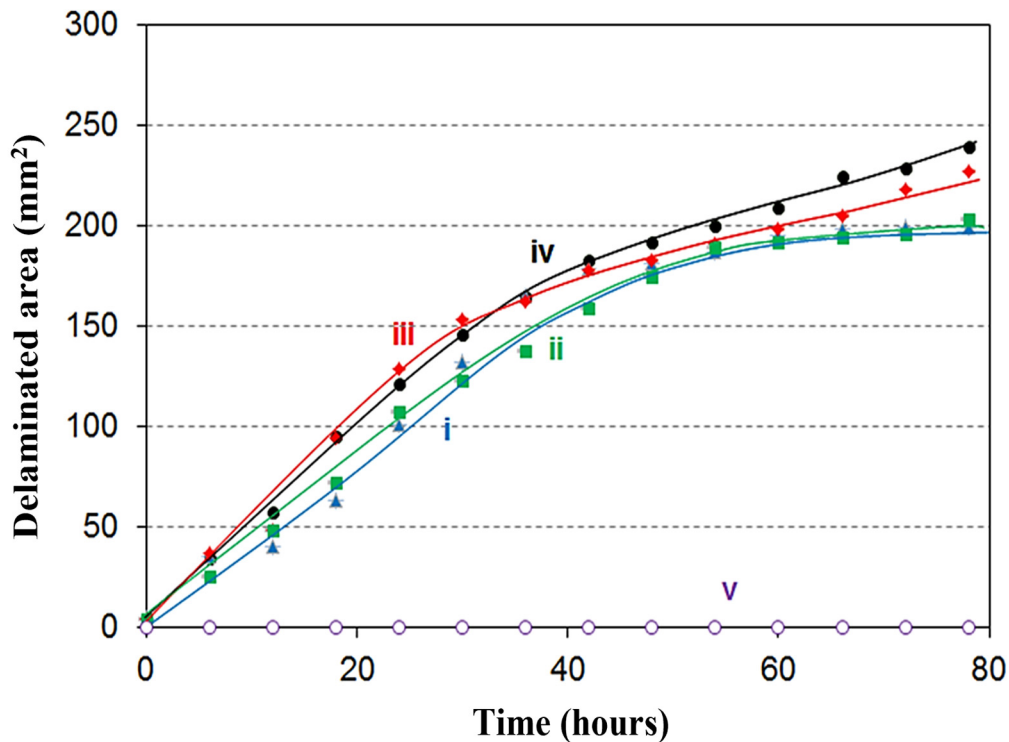
Figure 3.7: Plots of delaminated halo area versus time for PVB coated E717 alloy specimens held in air at 93% RH, where underfilm corrosion was initiated using 1 µl of 1 M aqueous solutions of the following: (i) NaCl, (ii) LiCl, (iii) KCl, (iv) CsCl and (v) $MgCl_2$ (0.5 M in this case).

In contrast, underfilm corrosion initiated using MgCl₂ did not show any delamination or caused a visible disbonded halo. It should be noted, that the observation that the rate of delamination appears to be independent of the group I cation type differs from the findings of others investigating organic cathodic disbondment on iron (Fe) [21]. In this case delamination kinetics are influenced by the diffusion coefficient of the cation and consequently LiCl-induced underfilm corrosion progresses at a significantly lower rate than for equivalent concentrations of KCl or CsCl. At holding times of > 50 h, Figure 3.7 also shows a deviation from linearity for each group I, where the area delamination rate slows significantly, presumably as the finite quantity of cations originally applied to the defect becomes progressively depleted as they become transported into the underfilm region.

3.3.4 The Mechanism of the Cathodic Disbondment

The difference in underfilm corrosion behaviour observed when using group I chloride salts compared with either HCl or MgCl₂ is highly evident in Figures 3.1, and 3.4. Delamination halos are produced whenever group I cations are present in the initiating electrolyte, but in their absence only filiform-like corrosion is produced. The divergence may be explained on the basis of the solubility of the group I hydroxides of the various cations. While all group I hydroxides are highly water soluble, magnesium hydroxide is only sparingly soluble. In order to establish a delamination cell comprising anodic Mg dissolution (according to Reaction (3.1)) located on exposed metal at a coating defect coupled with an adjacent underfilm cathode, then ionic current must flow between both sites as shown schematically in Figure 3.8. Under the atmospheric corrosion conditions employed in this study (air at 93% RH), both cathodic oxygen reduction and hydrogen evolution via Reactions (3.2) and (3.3) respectively are possible.

$$Mg \rightarrow Mg^{2+} + 2e^- \tag{3.1}$$

$$O_2 + 2H_2O + 4e^- \rightarrow 4OH^- \tag{3.2}$$

$$2H_2O + 2e^- \rightarrow H_2 + 2OH^- \tag{3.3}$$

However, regardless of the reduction reaction that predominates, the main product of the cathodic process will be hydroxide ions as indicated by both Reaction (3.2) and (3.3).

Therefore, to sustain the underfilm corrosion cell, cations must be transported to a local cathode within a zone where a counter current of hydroxide ions will be encountered. It should be noted that underfilm cathodic activity may not be limited to the location of the disbondment front but may also persist within the remainder of the halo region where coating disbondment has occurred. However, it is the local cathode at the halo edge that is of interest because it principally determines the rate of cathodic failure measured in the body of experimental work presented in this chapter.

Group I cations will therefore be able to carry ionic charge into a zone of elevated pH, but in the case of Mg^{2+} precipitation of solid $Mg(OH)_2$ will occur at a region where local concentrations of Mg^{2+} and OH^- are sufficiently high that the solubility product of $Mg(OH)_2$ is exceeded ($K_{sp} = 3 \times 10^{-11}$ mol^3 dm^{-9}) [22]. Consequently, there is no scope for cathodic disbondment according to the proposed mechanism represented schematically in Figure 3.8 and underfilm corrosion will be dominated by filiform-like attack, according to an anodic disbondment mechanism discussed in detail elsewhere [7]. The same will be true when HCl (aq) is employed to initiate underfilm corrosion as any H^+ ions will become neutralised during when migrating into a zone of elevated pH. In addition, hydroxide ions produced by cathodic HER accompanying Mg dissolution within the defect region will also tend progressively raise underfilm pH. The fact that no halo is observed when HCl (aq) is used, and that the resulting underfilm corrosion is exclusively filiform-like, suggests that the neutralisation of the initial low pH by the hydroxide product of cathodic HER is very rapid and there is insufficient proton concentration to cause any initiation of cathodic disbondment.
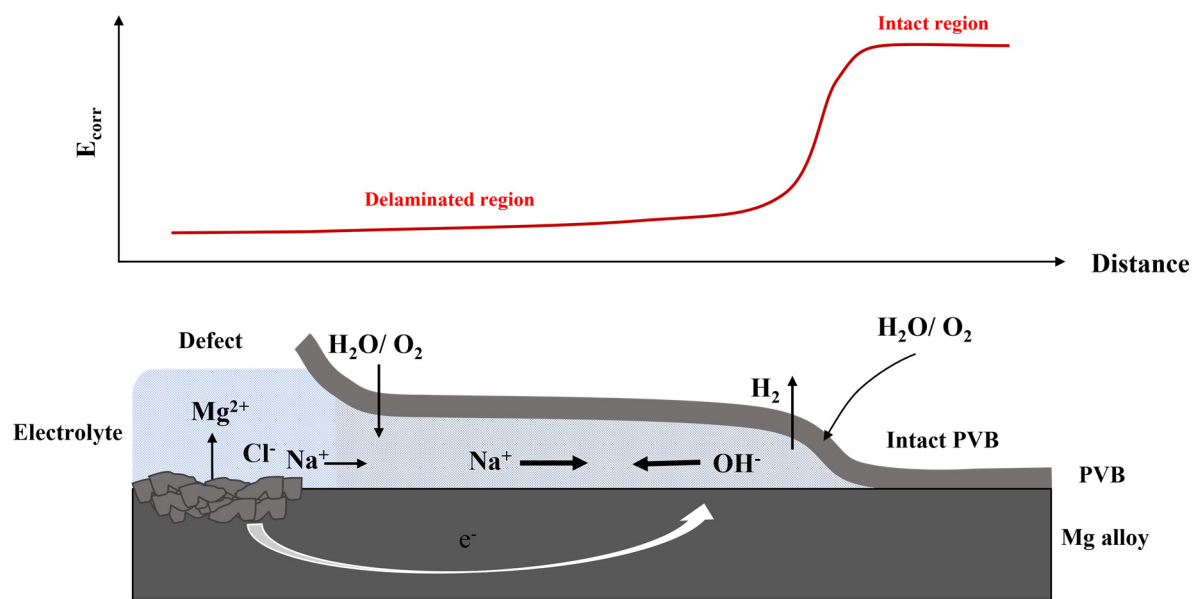
Figure 3.8: Schematic diagram showing localisation of the underfilm corrosion cell along with correlation to SKP-derived E_{corr} versus distance profile.

The close agreement of the characteristics of E_{corr} versus distance profiles with previously published results obtained for model PVB coatings applied to both Zn [13,20] and Fe [18,23] coupled with the findings of elemental mapping of the post corrosion surface (Figure 3.5), would tend to confirm the occurrence of a cathodic disbondment mechanism as illustrated schematically in Figure 3.8. However, there are also some notable differences in observed behaviour between PVB-coated E717 and these previous investigations involving other metallic surfaces. The first concerns the type of disbondment kinetics observed, where delamination distance characteristically varies as a function of the square root of time, indicating migration control due to a rate determining step involving transport of cations from the defect region to the cathodic front [21]. The linear relationship of distance with time typified in Figure 3.6 suggests that a different process controls the propagation of the delamination cell in the case of organic coated E717. Under circumstances where a similar deviation from parabolic kinetics has been observed for a PVB coated metal surface, the change has been ascribed to a situation where cathodic oxygen reduction rather than cation migration has become the rate limiting step [20,24].

This also seems consistent with observations of increased cathodic delamination resistance of zinc (Zn) surfaces in the presence of alloyed Mg, where the insulating nature of the surface magnesium (hydr)oxide film at the metal/coating interface serves as a barrier to electron transfer during underfilm cathodic oxygen reduction [24–26]. In addition, the insensitivity of delaminated area propagation to the type of group I cation present, observed in Figure 3.7, seems also to be in accordance with the change in the rate limiting step. As it was noted in Chapter 1, a migration-controlled mechanism would have revealed a significant dependence on cation type, where the mobility of cations differs markedly between Li^+ through to Cs^+. The small size and consequent high charge density of Li^+ ions dissolved in water produces a large solvation shell, rendering this cation the least mobile. However, Figure 3.7 shows that the delaminated area rate remains the same for both the least (Li^+, plot i) and most mobile (Cs^+, plot iv) cation types.

A question arises as to the role of oxygen reduction in the cathodic disbondment phenomenon observed for group I chloride initiated atmospheric corrosion of PVB-coated E717. Recent publications have proposed that oxygen reduction (Reaction (3.2)) may make a significant contribution to the total cathodic current during the corrosion of Mg alloy surfaces in the absence of external polarisation both under immersion [27] and atmospheric corrosion [28] conditions. In contrast, others have reported that the partial cathodic current due to oxygen reduction on a polarised pure Mg electrode under immersion remains insignificant compared to that due to the reduction of water [29]. The measurable difference in delamination distance versus time slopes measured in the presence and absence of oxygen shown in Figure 3.6 tends to suggest that Reaction (3.2) may contribute to the cathodic current at the site of coating disbondment. This notion is reinforced by the obvious visual difference between delaminated specimens held in humid air when compared with nitrogen. Nevertheless, the fact that an obvious delaminated halo develops in the absence of oxygen, at a significant rate implies that oxygen reduction provides a relatively minor contribution to the overall cathodic disbondment process.

A final question to be addressed refers to the exact nature of the physical and/or chemical processes that are directly responsible for the loss of organic coating adhesion from the Mg alloy surface. In the case of Fe, loss of adhesion by the destruction of polymer-metal bonds by hydrogen peroxide and other reactive intermediates in cathodic oxygen reduction is proposed [16,17], while the dissolution of an amphoteric zinc oxide film at the metal–coating interface can occur in the case

of organic coated Zn [13,30]. However, neither is possible in the case of Mg, where cathodic disbondment persists in the absence of oxygen and where the predominant surface oxide is nonamphoteric. It therefore seems plausible to suggest that the principal mode of de-adhesion consists of interfacial base catalysed polymer hydrolysis degradation, although it may also be possible that hydrogen gas bubbles, generated at the disbondment front may also play a role by mechanically forcing the coating from the Mg alloy surface.

3.4   Conclusion

The nature of chloride-induced underfilm corrosion occurring on PVB-coated E717 Mg alloy specimens was studied using a combination of in-situ time lapse photography and SKP analysis. Corrosion was initiated by applying various chloride-based salts to a penetrative scribed coating defect and samples were then held in air at 93% RH for periods of up to 3 days. All specimens showed evidence of filiform-like corrosion, characterised by the underfilm evolution of a network of dark tracks that lengthen with time. However, significant differences in corrosion behaviour were observed between specimens initiated using group I chlorides compared with those where either HCl or $MgCl_2$ was used. In the case of the former, propagation of dark filiform tracks was preceded by the rapid development of a halo of apparently disbonded coating surrounding the defect region, which expanded radially with time. When initiation was carried out using either HCl (aq) or $MgCl_2$ (aq), no evidence of a preceding halo was observed. By using in-situ SKP, it was demonstrated that the areas affected by the halo were characterised by E_{corr} values similar to the values for Mg actively corroding in the presence of aqueous media (ca. −1.3 V vs SHE), whereas the E_{corr} values measured for the intact surface (E_{intact}) were considerably more positive (ca. −1 V vs SHE). Post corrosion surface analysis using ToF-SIMS showed that the region affected by the halo was abundant in the initiating cation, but that chloride ions were not present. Further experiments carried out in a humidified nitrogen atmosphere showed that a halo was observed even in the absence of oxygen.

Taken together, the findings suggest that a cathodic disbondment mechanism is operational on certain model organic coated Mg alloys, where anodic activity at a penetrative defect is coupled with a underfilm reduction reaction predominantly involving cathodic hydrogen evolution. This

phenomenon is only observed when group I cations are available that can sustain ionic current within a region of high alkalinity. However, although the observations made above confirm that a cathodic disbondment mechanism is in operation, there are differences with behaviour reported on other metals such as iron and zinc. The linear relationship of disbondment front distance with respect to time suggests that the rate determining step may not involve transport of cations from the anode to the underfilm cathode, typically characterised by parabolic kinetics. Rather the observation suggests that electron transfer at the principal underfilm cathode may govern the overall rate. This appears to be consistent with the observed independence of delamination rate on the type of group I chloride salt used to initiate corrosion.

3.5   References

[1]   J.E. Gray, B. Luan, Protective coatings on magnesium and its alloys — a critical review, J. Alloys Compd. 336 (2002) 88–113.

[2]   X.B. Chen, N. Birbilis, T.B. Abbott, Review of corrosion-resistant conversion coatings for magnesium and its alloys, CORROSION. 67 (2011) 35005–35016.

[3]   R.-G. Hu, S. Zhang, J.-F. Bu, C.-J. Lin, G.-L. Song, Progress in Organic Coatings: Recent progress in corrosion protection of magnesium alloys by organic coatings, Prog. Org. Coatings. 73 (2011) 129–141.

[4]   S. Song, G.-L. Song, W. Shen, M. Liu, Corrosion and electrochemical evaluation of coated magnesium alloys, Corrosion. 68 (2012) 15005–15012.

[5]   M.P. Brady, D.N. Leonard, H.M. Meyer, J.K. Thomson, K.A. Unocic, H.H. Elsentriecy, G.-L. Song, K. Kitchen, B. Davis, Advanced characterization study of commercial conversion and electrocoating structures on magnesium alloys AZ31B and ZE10A, Surf. Coatings Technol. 294 (2016) 164–176.

[6]   B. Liu, Y. Wei, W. Chen, L. Hou, C. Guo, Blistering failure analysis of organic coatings on AZ91D Mg-alloy components, Eng. Fail. Anal. 42 (2014) 231–239.

[7]   G. Williams, R. Grace, Chloride-induced filiform corrosion of organic-coated magnesium, Electrochim. Acta. 56 (2011) 1894–1903.

[8]   X.P. Niu, T. Skszek, M. Fabischek, A. Zak, Low temperature warm forming of magnesium ZEK 100 sheets for automotive applications, Mater. Sci. Forum. 783–786 (2014) 431–436.

[9]   M.P. Brady, W.J. Joost, C.D. Warren, Insights from a recent meeting: current status and future directions in magnesium corrosion research, CORROSION. 73 (2017) 452–462.

[10]   M.P. Brady, G. Rother, L.M. Anovitz, K.C. Littrell, K.A. Unocic, H.H. Elsentriecy, G.-L. Song, J.K. Thomson, N.C. Gallego, B. Davis, Film breakdown and nano-porous $Mg(OH)_2$ formation from corrosion of magnesium alloys in salt solutions, J. Electrochem. Soc. 162 (2015) C140–C149.

[11]   M. Stratmann, A. Leng, W. Fürbeth, H. Streckel, H. Gehmecker, K.-H. Groβe-Brinkhaus, The Scanning Kelvin Probe; a new technique for the in situ analysis of the delamination of organic coatings, Prog. Org. Coatings. 27 (1996) 261–267.

[12]   W. Fürbeth, M. Stratmann, Scanning Kelvin Probe investigations on the delamination of polymeric coatings from metallic surfaces, Prog. Org. Coatings. 39 (2000) 23–29.

[13]   G. Williams, H.N. McMurray, Chromate inhibition of corrosion-driven organic coating delamination studied using a Scanning Kelvin Probe technique, J. Electrochem. Soc. 148 (2001) B377–B385.

[14]   M. Stratmann, H. Streckel, R. Feser, A new technique able to measure directly the delamination of organic polymer films, Corros. Sci. 32 (1991) 467–470.

[15]   G. Williams, H.N. McMurray, The kinetics of chloride-induced filiform corrosion on aluminum alloy AA2024-T3, J. Electrochem. Soc. 150 (2003) B380–B388.

[16]   M. Stratmann, R. Feser, A. Leng, Corrosion protection by organic films, Electrochim. Acta. 39 (1994) 1207–1214.

[17]   A. Leng, H. Streckel, M. Stratmann, The delamination of polymeric coatings from steel. Part 1: Calibration of the Kelvin probe and basic delamination mechanism, Corros. Sci. 41 (1998) 547–578.

[18]   G. Williams, H.N. McMurray, The mechanism of group (I) chloride initiated filiform corrosion on iron, Electrochem. Commun. 5 (2003) 871–877.

[19]   W. Fürbeth, M. Stratmann, The delamination of polymeric coatings from electrogalvanised steel - a mechanistic approach. Part 1: delamination from a defect with intact zinc layer, Corros. Sci. 43 (2001) 207–227.

[20]   G. Williams, R.J. Holness, D.A. Worsley, H.N. McMurray, Inhibition of corrosion-driven organic coating delamination on zinc by polyaniline, Electrochem. Commun. 6 (2004) 549–555.

[21]   A. Leng, H. Streckel, M. Stratmann, The delamination of polymeric coatings from steel. Part 2: First stage of delamination, effect of type and concentration of cations on

delamination, chemical analysis of the interface, Corros. Sci. 41 (1998) 579–597.

[22]   D.R. Lide, CRC Handbook of Chemistry and Physics, 78th edn., CRC Press Inc., Boca Raton, USA, 1997.

[23]   G. Williams, H.N. McMurray, Inhibition of corrosion driven delamination on iron by smart-release bentonite cation-exchange pigments studied using a Scanning Kelvin Probe technique, Prog. Org. Coatings. 102 (2017) 18–28.

[24]   J.L. Davies, C.F. Glover, J. Van de Langkruis, E. Zoestbergen, G. Williams, The effect of Mg concentration on the resistance of PVD Zn-Mg coatings to corrosion driven organic coating delamination, Corros. Sci. 100 (2015) 607–618.

[25]   R. Hausbrand, M. Stratmann, M. Rohwerder, Delamination resistant zinc alloys: simple concept and results on the system zinc-magnesium, Steel Res. Int. 74 (2003) 453–458.

[26]   R. Hausbrand, M. Stratmann, M. Rohwerder, Corrosion of zinc – magnesium coatings : Mechanism of paint delamination, Corros. Sci. 51 (2009) 2107–2114.

[27]   E.L. Silva, S. V Lamaka, D. Mei, M.L. Zheludkevich, The reduction of dissolved oxygen during magnesium corrosion, ChemistryOpen. 7 (2018) 664–668.

[28]   M. Strebl, S. Virtanen, Real-time monitoring of atmospheric magnesium alloy corrosion, J. Electrochem. Soc. 166 (2019) C3001–C3009.

[29]   J. Han, K. Ogle, Dealloying of MgZn2 intermetallic in slightly alkaline chloride electrolyte and its significance in corrosion resistance, J. Electrochem. Soc. 164 (2017) C952–C961.

[30]   W. Fürbeth, M. Stratmann, The delamination of polymeric coatings from electrogalvanized steel - a mechanistic approach. Part 2: delamination from a defect down to steel, Corros. Sci. 43 (2001) 229–241.

Chapter 4

Investigation of the Delamination of Organic Coated Mg Alloys using the Scanning Kelvin Probe

Investigation of the Delamination of Organic Coated Mg Alloys using the Scanning Kelvin Probe

4.1 Introduction

In Chapter 3, the nature of chloride-induced underfilm corrosion occurring on organic coated E717 Mg alloy was investigated using a combination of in-situ time-lapse photography and SKP analysis. It was shown that initiation of corrosion with HCl (aq) or $MgCl_2$ (aq), produced underfilm corrosion in the form of filiform corrosion. However, when underfilm corrosion was initiated by injecting group I chloride salts to a penetrative coating defect an apparent halo detachment is produced expanding radially with time. A preliminary in-situ SKP experiment demonstrated that the areas affected by a halo detachment were characterised by corrosion potential (E_{corr}) values similar to the values for Mg actively corroding in aqueous media, whereas the E_{corr} distributions measured for the intact surface (E_{intact}) were considerably more positive. Post-corrosion elemental analysis of the delaminated region using secondary ion mass spectrometry (ToF-SIMS) has shown an abundance of group I cation, but no chloride.

It is well known in the coating delamination mechanisms of other metals, that the cation mobility across the coating/substrate interface dictates the rate of delamination and thus linear disbondment kinetics with the square root of exposure time are observed [1]. The linear relationship of disbondment distance with time obtained using the time-lapse photographic sequences and the preliminary SKP data suggested that electron transfer at the underfilm cathode might be the rate limiting step in the delamination process rather than cation migration. In addition, experiments performed in a humidified N_2 environment to ascertain the role of oxygen, have suggested that the halo occurs in the absence of oxygen indicating that water reduction (Reaction (4.2)) is the predominant underfilm cathodic reaction. Taking together the findings from Chapter 3, it was concluded that a cathodic disbondment mechanism is taking place on a model organic coated E717 Mg alloy where the anodic Mg dissolution (Reaction (4.1)) is occurring at the penetrative coating defect and is coupled with the predominant cathodic reaction beneath the film.

$$Mg \rightarrow Mg^{2+} + 2e^- \tag{4.1}$$

$$2H_2O + 2e^- \rightarrow H_2 + 2OH^- \tag{4.2}$$

The deductions made from the results in Chapter 3, gave rise to a few questions with regards to the role of oxygen in the delamination process, whether this phenomenon is universal with Mg alloys, and last but not least, why there seems to be a decrease in delamination rate after protracted holding times. Previously, delamination kinetics under humidified N_2 were obtained by analysing photographic images of a sample placed in a vessel comprising a flat glass window allowing humidified N_2 gas to be introduced into the vessel. However, the halo observed in a nitrogen environment was not as clearly defined as that observed in air and so there is more uncertainty regarding the individual distance values and consequently the linearity of the distance-time relation. In this chapter, the delamination kinetics in the absence of oxygen are obtained by employing an SKP apparatus, which allows for greater control of the environment by significantly lowering the oxygen concentration in the testing chamber to < 2%.

Furthermore, the delamination cell employed in Chapter 3 (scribed defect cell) [2], has the disadvantage of only allowing for a small quantity (µl) of electrolyte to be introduced into the scribe. The rate of cathodic failure seemed to decrease after > ca. 50 h of holding time in a humid environment and it was postulated that the finite quantity of cations originally applied to the scribe progressively became depleted as they migrated to the underfilm region, thus reducing the delamination rate significantly. To assess whether or not this hypothesis is correct, a Stratmann-type [3] cell arrangement is employed in this chapter. This type of cell has the advantage of providing a significantly higher volume (1 ± 0.25 ml) of electrolyte to be applied to a coating defect allowing for a more detailed investigation of the delamination kinetics over longer holding times while also providing a well-defined artificial defect. Many studies [1,3,4] have utilised this type of cell to investigate the delamination of organic coatings from metallic substrates, and thus a comparative study on organic coated Mg alloys is essential.

Finally, in Chapter 3, all experiments were conducted solely on organic coated E717 Mg alloys due to their importance in the automotive industry. In this chapter, an effort has been made to investigate additional alloys, namely the AZ31 and AZ91 Mg alloys, which are technologically important for multiple lightweight applications. The AZ-series alloys are one of the most extensively researched [5,6] Mg alloys, however there is a gap in the literature regarding their behaviour under conditions where organic coating delamination can take place. So, the final aim of this chapter is to investigate organic coated AZ-series Mg alloys in order to establish whether

this coating delamination phenomenon is occurring only on E717 Mg substrates or whether the apparent cathodic delamination affects a range of coated Mg alloy surfaces.

4.2 Experimental Details

4.2.1 Materials and Sample Preparation

Three different Mg alloys were utilised in this chapter, namely E717 (Electron^{TM} 717), AZ31 and AZ91 Mg alloy. More details about these Mg alloys are provided in Section 2.1.1. These specimens were cut using electric discharge machining into 50 x 50 mm coupons and before the application of the model polymeric coating, the samples were prepared as it is described in Section 2.1.3. The model coating used in this chapter is the same as in Chapter 3, a PVB coating, which was prepared in ethanol (15.5% w/w). All the experimental electrolytes were prepared using analytical grade reagents and were obtained from Sigma-Aldrich Ltd.

In the current chapter, all experiments were performed using the Stratmann-type cell arrangement allowing for a more detailed kinetic investigation over longer holding times and the detailed description of the preparation of the Stratmann-type cell is given in Section 2.2.1.1.

4.2.2 Methods

The potentiometric measurements under atmospheric corrosion conditions were performed using the same Scanning Kelvin Probe (SKP) apparatus as in Chapter 3 and the full description of the SKP instrumentation is given in Section 2.2. The SKP reference probe was programmed to scan over the PVB coated Mg alloy surface using a 125 μm diameter gold wire vibrated normal to the sample surface at 280 Hz recording 20 E_{corr} data points per mm and was calibrated before its use following the methodology described in Section 2.2.3. The PVB coated Mg alloy samples were held initially in room air (20 °C and 50% RH) for 10 min and then transferred to the SKP environment chamber, which was maintained at 20 °C and 93% RH in isopiestic equilibrium with a saturated aqueous $Na_2SO_4 \cdot 10H_2O$ reference solution.

For the SKP experiments where a coated E717 Mg alloy was used, the SKP reference probe was programmed to scan in four lines of 10 mm over the surface unless otherwise stated, normal and adjacent with the boundary of the artificial coating defect/reservoir. The electrolytes used for the

initiation of the delamination were 1 M aqueous solutions of NaCl and LiCl and these were applied in the sample well. After the addition of the appropriate electrolyte, the SKP scans were initiated and repeated every 2 h over a period of 140 h unless otherwise stated. On separate SKP experiments where PVB coated AZ31 and AZ91 Mg alloys were used, the scans were carried out at < 2 h intervals for at least 120 h on a 10 mm × 3 mm area normal and adjacent with the boundary of the artificial coating reservoir. The scanning was initiated immediately upon the addition of the electrolyte in the sample reservoir, which in this case was 1 M NaCl (aq) solution. The potentiometric measurements in the absence of oxygen were carried out using the SKP apparatus located in the laboratories of the industrial sponsor of this project (BASF Coatings GmbH) and a detailed description of the apparatus is given elsewhere [7]. This experiment was conducted on a PVB coated E717 Mg alloy, which was exposed to 95% RH (20 °C) while the O_2 concentration was kept at < 1.4% throughout the experiment (100 h). The electrolyte used for this delamination experiment was a 1 M aqueous solution of NaCl.

4.3   Results and Discussion

4.3.1   Investigation of the Delamination Kinetics using a Stratmann Cell

In Chapter 3, it was clearly shown that the cathodic disbondment phenomenon affecting PVB coated E717 proceeds in humidified air when underfilm corrosion is inoculated with a group I chloride containing electrolyte. This was achieved by placing a scribed coated sample in a container that allowed humidified air or nitrogen to be introduced. In the current chapter, the cathodic disbondment phenomenon under atmospheric conditions is further investigated using a Stratmann-type cell analysed by in-situ Scanning Kelvin Probe (SKP) potentiometry to allow for a more detailed measurement of the delamination cell potentials and associated kinetics over longer holding times.

In order to determine the distribution of free corrosion potentials (E_{corr}) in the delaminated regions, the SKP was utilised to scan a 10 mm line up to the coating defect. Upon addition of an electrolyte of 1 M aqueous NaCl to the reservoir, the establishment of the distinctive time-dependent E_{corr}-distance delamination profile was observed and Figure 4.1 displays a series of these E_{corr} versus distance profiles measured at various times. The E_{corr} values measured in the vicinity of the coating

defect regions (ca. −1.25 V vs. SHE) are similar to the potential values expected for freely corroding Mg in the presence of a chloride-containing electrolyte. As reported from the potentiometric measurements described in Chapter 3, the sharp rise in the E_{corr} signifies the location of the delamination edge where the cathodic delamination is occurring while the region in front of the defect is where the coating remains intact, characterised by more positive E_{corr} values of ca. −1.05 V vs. SHE.

From Figure 4.1 it is observed that there is no significant variation in the magnitude of the E_{corr} vs. distance slopes determined over the corroded surface with longer exposure time. Even after 100 h of exposure at high relative humidity (RH) where the disbondment front has covered a distance over 7 mm, the slopes (disbonded region and disbonded front) remain constant. Similar observations were made in the previous chapter for shorter holding periods, and this was attributed to the constant ionic current flux connecting the disbondment front with the artificial coating defect, which is not influenced by the distance covered by the front over time. The delamination distance and therefore the rate of cathodic disbondment can be quantified by locating the position of the cathodic delamination edge situated at the steepest point of the potential gradient in the SKP derived E_{corr} profiles presented in Figure 4.1. Figure 4.2 demonstrates a plot of the delamination distance versus time (t_{del} - t_i) with the t_{del} being the delamination time following introduction of the electrolyte and t_i is the initiation period. It is important to note here that the time for the coating disbondment to initiate seems to vary between experiments especially between the AZ series alloys and the E717 samples presumably due to the nature of the localised corrosion observed for uncoated Mg alloys (filiform-like) [2,8] taking place in the artificial coating defect/reservoir where the Mg alloy is uncoated.

Figure 4.1: Profiles of E_{corr} versus distance obtained for a PVB coated E717 Stratmann-type sample at various times after initiation of delamination using 1 M NaCl (aq). Time key: (i) 64 h, (ii) 72 h and 8 h intervals thereafter. The sample was maintained at room temperature and a constant RH. of 93% throughout.

In the previous chapter, it was shown (Figure 3.7) that the delamination rate remained unchanged, however at holding periods > ca. 50 h the delamination rate reduced substantially and this was presumed to be caused by the limited amount of electrolyte available in the scribed defect and consequent depletion of group I cations at protracted holding times. This decrease in the rate of delamination was not observed in the disbondment kinetics obtained using the Stratmann-type cell as it can be seen from Figure 4.2. The rate of cathodic failure increases linearly with time over the entire duration of the experiment (>100 h) with a relatively constant slope of approximately 0.1 mm h^{-1}. It, therefore, seems plausible to propose that the cathodic delamination rate will remain constant when a large excess of group I cations are available in the initiating electrolyte.
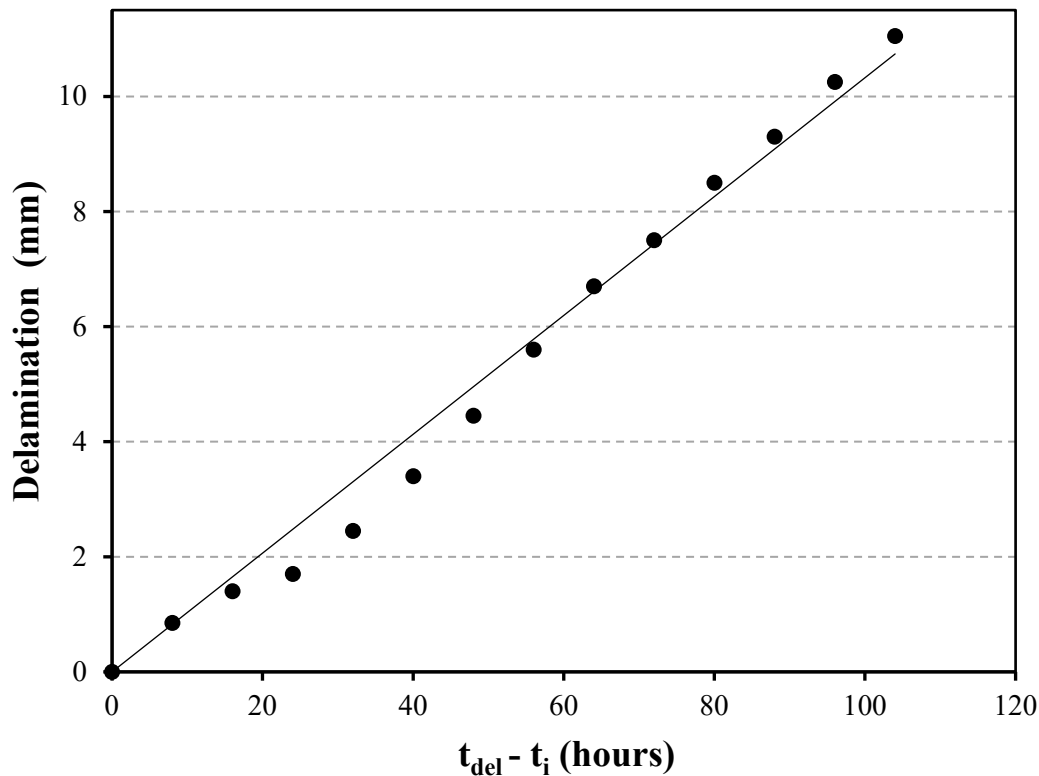
Figure 4.2: Plot of delamination distance versus (t_{del} - t_i) (SKP-derived) for a PVB coated E717 alloy specimens exposed to 93% RH and the electrolyte in contact with the artificial defect is 1 M NaCl (aq).

If the number of cations required to sustain the underfilm electrochemical cell drops below a certain threshold due to the migration of the finite available cations from the coating defect to the disbondment front, then it would be expected that the disbondment rate will decrease and eventually come to a halt. This is partially supported by the results obtained using ToF-SIMS (Figure 3.5) where it was shown that group I cations migrate from the artificial defect to the delaminated regions, continuously exhausting the available cations from the injected electrolyte. The linearity of the SKP-derived delamination distance with time throughout the experiment suggests that the rate-determining step in PVB coated Mg alloys is not the migration of cations from the external electrolyte to the disbondment front as postulated for other organic coated metals [1]. It has been shown in the literature that the delamination distance of an organic coated steel, determined using the SKP, increases linearly as a function of the square root of time in accordance

with Fick's law of diffusion, indicating that the cation migration along the coating/substrate interface is the rate determining step in the cathodic delamination process [1,9,10].

It has also been demonstrated in the past [1] that the type of group I cations present in the electrolyte can strongly influence the propagation of the delamination front in organic coated steel samples where a migration controlled disbondment mechanism is taking place. In more detail, the disbondment rate was proven to be higher with electrolytes containing Cs^+ compared to Li^+ and the disbondment rate increased in the order $Li^+ < Na^+ < K^+ < Cs^+$, which relates to the mobility ranking of these ions in an aqueous electrolyte [1]. This finding provided further evidence that the migration of cations to the delamination front is the rate limiting step in the disbondment rate of polymer coated steel.

In the previous chapter, time-lapse photographic sequences were used to analyse the kinetics of the halo area propagation and it was found that the rate did not depend on the type of group I cation present in the initiating electrolyte. Although this experimental method of determining delamination kinetics provided very useful insights about the delamination mechanism of coated Mg alloys, it does not provide any information with regards to the electrochemical phenomena taking place under the film when the artificial coating defect is in contact with a group I-containing electrolyte such as LiCl (aq). To investigate this in more detail, in-situ SKP was used to record the distribution of corrosion potentials under the film and the resulted E_{corr} versus distance profiles following initiation of delamination using 1 M LiCl (aq) are presented in Figure 4.3. As it can be observed, these E_{corr} profiles are similar to the profiles obtained when delamination was initiated using aqueous NaCl (Figure 4.1) with indistinguishable differences. As before, the regions closer to the defect are exhibiting more negative E_{corr} values of ca. -1.25 V vs. SHE while values of approximately -1.05 V vs. SHE are recorded for the adjacent uncorroded surface where the Li^+ have not yet migrated.
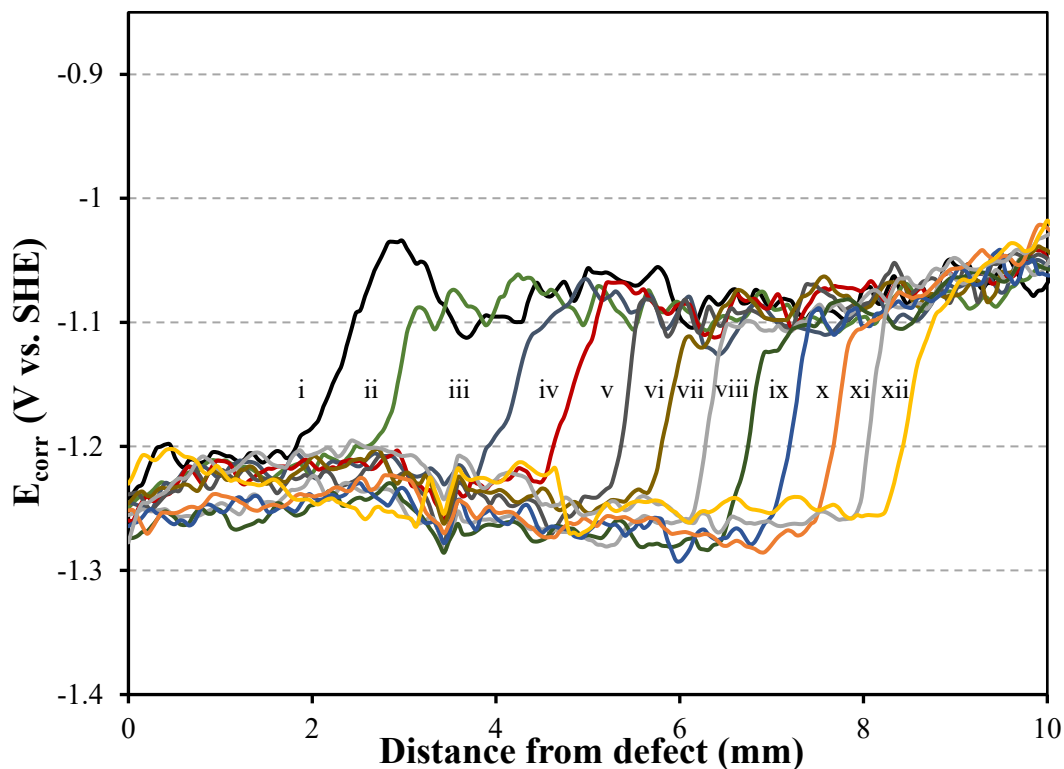
Figure 4.3: Profiles of E_{corr} versus distance obtained for a PVB coated E717 Stratmann-type sample at various times after initiation of delamination using 1 M LiCl (aq). Time key: (i) 55 h, (ii) 61 h and 6 h intervals thereafter. The sample was maintained at room temperature and a constant RH. of 93% throughout.

By additional analysis of these E_{corr} profiles, the delamination distance versus time is obtained and the results are shown in Figure 4.4. It can be observed that linear kinetics are retained for >100 h with a slope of approximately 0.093 mm h^{-1}, which demonstrates that the SKP-derived delamination kinetics observed in both cases (Na$^+$ and Li$^+$) are identical. As mentioned previously, the mobility of group I cations in aqueous solutions would be expected to strongly influence the delamination kinetics in a system where the migration of cations to the delamination front is the slowest step in the delamination process. The small Li$^+$ ion, which is the least mobile of all group I cations, due to its large and strongly bound hydration shell, would be expected to produce the slowest delamination kinetics, but as it can be seen from comparing the results in Figure 4.2 and 4.4, this is not the case. This provides further confirmation that the migration of cations to the disbondment front is not the rate limiting step in the coating disbondment of an organic coating from Mg alloys, confirming the mechanism presented in Figure 3.8.
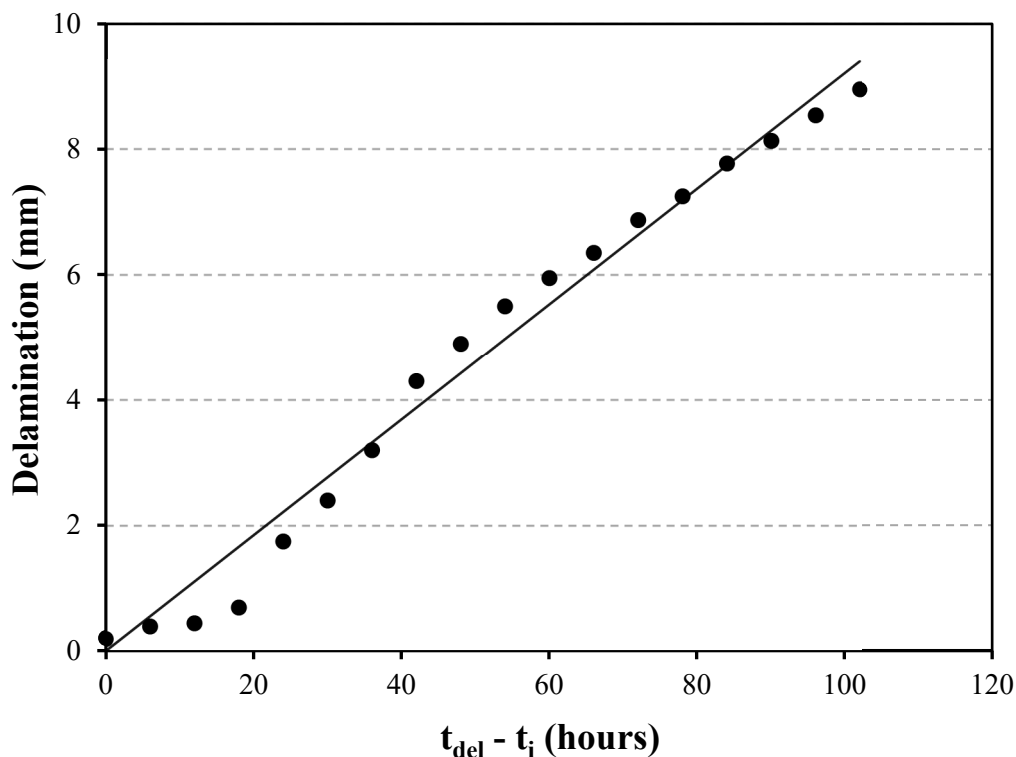
Figure 4.4: Plot of delamination distance versus (t_{del} - t_i) (SKP-derived) for a PVB coated E717 alloy specimens exposed to 93% RH and the electrolyte in contact with the artificial defect is 1 M LiCl (aq).

4.3.2 Delamination of Organic Coated E717 Mg Alloy in the Absence of Oxygen

The oxygen reduction reaction plays an important role in the cathodic disbondment of organic coatings from other metals (i.e. iron (Fe) and zinc (Zn)) [4,11]. However, in the previous chapter, it was shown that cathodic delamination can proceed in organic coated Mg alloys when the sample is held in a chamber with a humidified N_2 gas flow signifying that oxygen does not play a detrimental role in the loss of coating adhesion of coated Mg alloys. These observations were made by quantifying the delamination kinetics using time-lapse photographic sequences. This was proven to be challenging, due to the less defined visible halo front observed in the absence of oxygen. In the current chapter, the cathodic disbondment phenomenon under oxygen-free conditions is investigated using in-situ SKP to measure the corrosion potentials and consequently determine the delamination kinetics with higher confidence levels. A sample of E_{corr} distributions derived using the SKP under near oxygen-free conditions (ca. <1.4 % O_2) are presented in Figure 4.5 where the E_{corr} values are plotted versus distance from the coating defect.
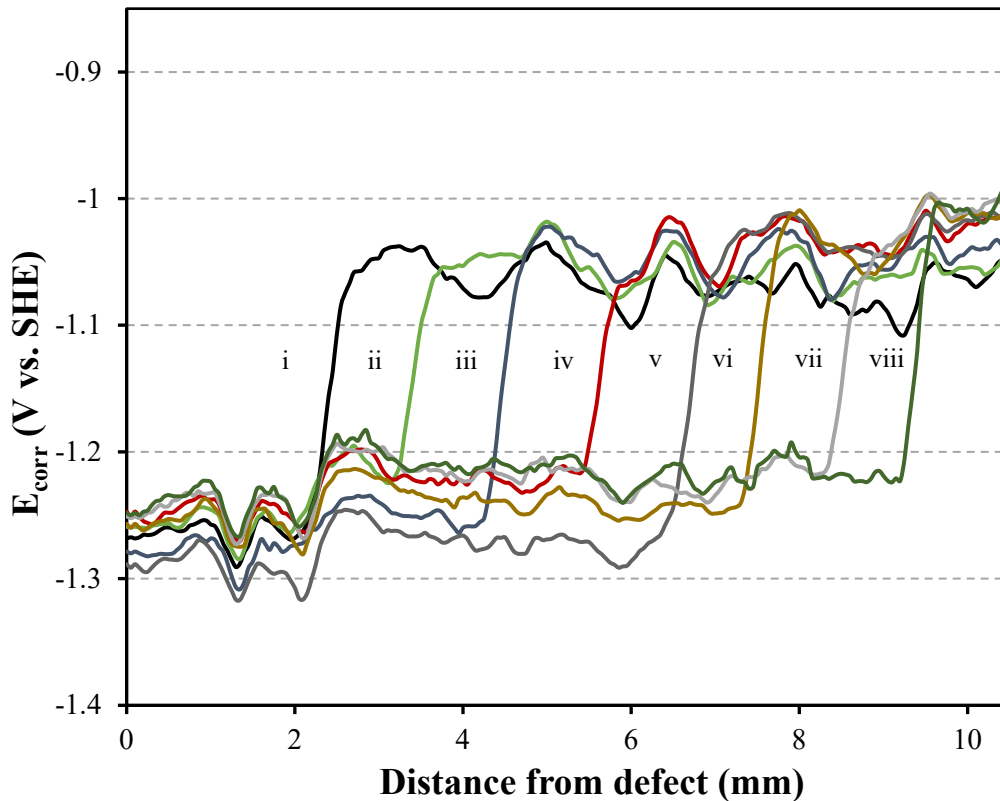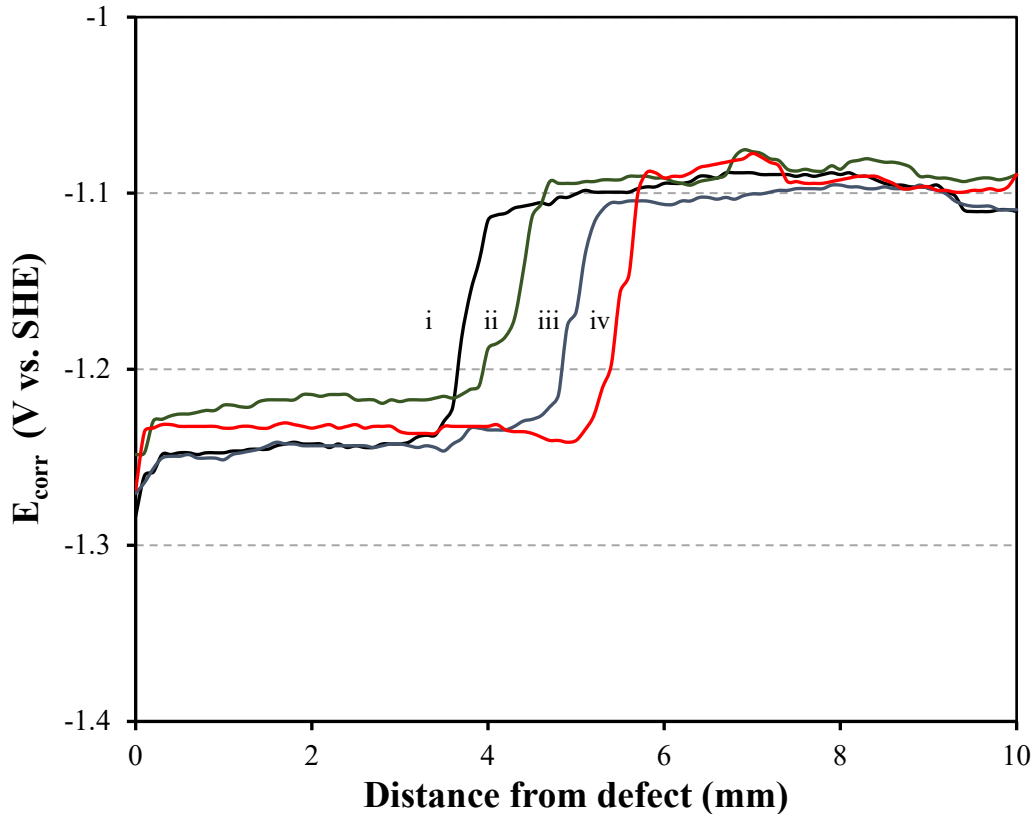
Figure 4.5: Profiles of E_{corr} versus distance obtained for a PVB coated E717 sample at various times after initiation of delamination using 1 M NaCl (aq). Time key: (i) 60 h, (ii) 70 h, (iii) 79 h and (iv) 89 h. The sample was held at room temperature and under near oxygen-free conditions (ca. <1.4 % O_2) and ca. 95% RH.

Seemingly, the E_{corr} profiles presented in Figure 4.5 indicate that the PVB coated Mg alloy undergoes delamination in the absence of oxygen where the region of a sharp shift in E_{corr} corresponds to the leading edge of the coating delamination. The E_{corr} versus distance profiles appear to be similar to the profiles obtained in air (see Figure 4.1 and Figure 4.3) albeit with less fluctuation in the values obtained in the delaminated and intact regions, which is attributed to the difference in the SKP instrumentation used for this particular experiment. The E_{corr} distributions measured adjacent to the artificial coating defect adopt more negative values (−1.25 V vs. SHE) compared to the values measured in the intact regions. These results appear to be consistent with the results obtained in humid air however the E_{intact} values are slightly more negative under these conditions of significantly reduced oxygen concentration. This in turn may signify that oxygen

plays a role in determining the E_{intact} values and that its reduction may contribute to the overall cathodic disbondment process. However, it is also possible that this occurred due to the fact that a different instrument was used for this experiment.

The SKP-derived delamination kinetics obtained for the PVB coated E717 under oxygen-free conditions (ca. <1.4 % O_2) are given in Figure 4.6. From this plot, it can be deducted that the delamination distance increases linearly with time throughout the experiment, with slopes of ca. 0.065 mm h^{-1}. After the delamination experiment in the absence of oxygen was completed, the PVB coating was carefully peeled off the surface and it was confirmed that the coating has lost its adhesion in the areas characterised by more negative E_{corr}. Repeat experiments to determine the reproducibility of the results obtained under reduced oxygen concentration with both Stratmann-type and scribed defect cells demonstrated similar kinetic behaviour, except in a few isolated cases where the delamination rate approached the rates obtained in air.

Overall, the rate of cathodic failure under oxygen-free conditions seemed to be slightly slower than the delamination rate measured for the samples held in humid air suggesting that oxygen might have a secondary effect on the overall disbonding mechanism. Recently, it was elegantly shown [12,13] that under atmospheric conditions, oxygen can potentially contribute to the cathodic process of Mg somewhat agreeing with the results shown herein. Nevertheless, the fact that de-adhesion took place in the absence of oxygen with not so dissimilar disbondment rates and E_{corr} values as in air denotes that oxygen is not essential for the cathodic delamination to take place on coated Mg alloys and that sufficient underfilm cathodic current is sustained by water reduction to drive the cathodic disbondment corrosion cell. As it has been earlier mentioned in this thesis, organic coating deadhesion from iron substrates has been attributed to the intermediate radicals that form during the oxygen reduction reaction [14,15]. However, due to the persistence of coating delamination from Mg surfaces under conditions of reduced oxygen concentration, this can be ruled out as a possible coating disbondment mechanism.
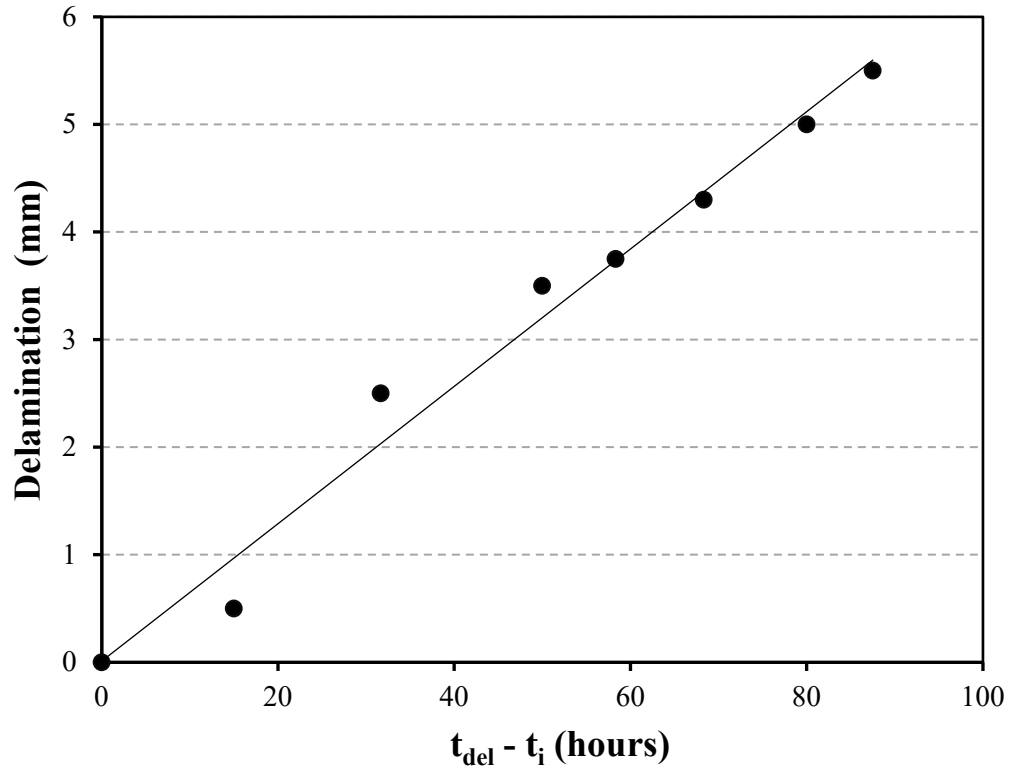
Figure 4.6: Plot of delamination distance versus (t_{del} - t_i) (SKP-derived) for a PVB coated E717 alloy specimens exposed to near-oxygen free conditions (ca. <1.4 % O_2), ca. 95% RH and the electrolyte in contact with the artificial defect is 1 M NaCl (aq).

Organic coating delamination from zinc surfaces (e.g. galvanised steel) is thought to arise because of the dissolution of the amphoteric zinc oxide surface layer caused by the presence of a high pH, which in turn causes the organic coating to be undermined [11]. As stated previously, the polymer/metal interface in a delamination cell is a zone of increased alkalinity. This high pH results from the OH⁻ ions produced by the cathodic reduction (Reaction (4.2)) and under these alkaline conditions the magnesium surface oxide is stable as it can be seen from the Pourbaix diagram presented in Figure 1.3, Section 1.3.2. Therefore, no significant metal dissolution will be expected in this zone of high alkalinity eliminating the metal dissolution as a potential cause for loss of coating adhesion in Mg alloys. Therefore, these observations tend to further support the claim made in the prior chapter that the loss of coating adhesion is presumably due to base catalysed polymer hydrolysis degradation and possible mechanical coating delamination due to the hydrogen gas produced by the underfilm cathodic hydrogen evolution.

4.3.3 Delamination of Organic Coated AZ-Series Mg Alloys

In the previous sections, it was shown that the PVB coated E717 Mg alloy undergoes delamination when underfilm corrosion is initiated with a group I-containing electrolyte. In the present section, PVB coated AZ31 and AZ91 were evaluated using SKP potentiometry. As their name suggests and as it was mentioned in Section 1.4.3, these Mg alloys contain Al and Zn as their main constituents producing a different microstructure compared to the E717 Mg alloy. In order to confirm if coating de-adhesion occurs on coated AZ31 and AZ91 Mg alloys, Stratmann-type cells were prepared for each alloy and the underfilm corrosion was initiated by adding 1 M of NaCl (aq) in the sample reservoir. The samples were then subsequently held in air at high relative humidity for >100 h. After the termination of this preliminary experiment, it was found that both samples had undergone de-adhesion with visual disbondment fronts "marking" the edge of the regions affected with loss of adhesion. This was confirmed by carefully peeling the PVB coating from the surface of both alloys and noticing that the regions where visible delamination has occurred, have suffered from loss of adhesion compared to the regions that remained unaffected by this visible front.

Additional experiments were conducted using in-situ SKP to verify these visual preliminary experiments, measure the distribution of the electrochemical potentials across the model polymer/substrate interface and subsequently determine the delamination kinetics. Initially, the in-situ SKP measurements on organic coated AZ31 and AZ91 alloys were conducted in a similar manner as with the coated E717 Mg alloy, by programming the SKP to scan a line normal and adjacent with the artificial coating defect. However, it was found that the SKP did not detect any significant potential changes in the visible delaminated regions as it can be seen from Figure 4.7 and hence the "traditional" trend, which is seen with the E_{corr} profiles for the E717 samples, was not observed in this case. Figure 4.7 shows a sample of the E_{corr} versus distance profiles obtained at various holding times for a PVB coated AZ31 with the dashed double arrow showing the estimated delaminated region at around 24 h after initiation of the delamination. Although Figure 4.7 is not as insightful as Figure 4.1 and Figure 4.3 in terms of precisely locating the disbondment front and consequently obtaining accurate kinetic data, it can somewhat provide a general estimation of the position of the disbondment front.

It may be seen that the regions closer to the artificial coating defect exhibit more stable E_{corr} values of ca. −1 V vs. SHE compared to the values measured in the more distant regions. The slightly more negative features (30 ± 10 mV) indicated by the black arrows seem to be the leading front of these stable E_{corr} values before they start fluctuating denoting the possible location of the disbondment front in each scan. One final note that can be made from Figure 4.7, is the two distinct peaks corresponding to significant more positive E_{corr} values. These peaks are located within the estimated intact areas during the 24 h and 48 h scan however they seem to adopt lower E_{corr} values after the estimated disbondment front has "covered" these spots in later scans.
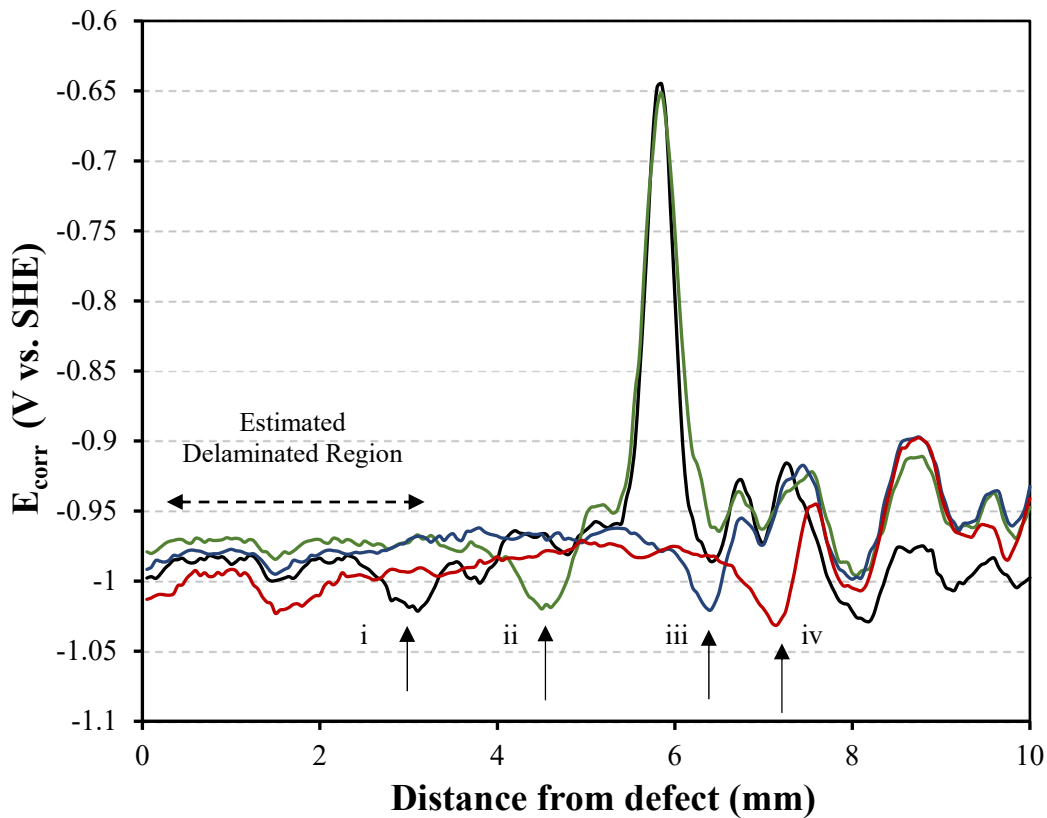
Figure 4.7: Profiles of E_{corr} versus distance (line scan) obtained for a PVB coated AZ31 sample at (i) 24 h, (ii) 48 h, (iii) 76 h and (iv) 96 h after initiation of delamination using 1 M NaCl (aq). The sample was maintained at room temperature and a constant RH. of 93% throughout.

This phenomenon occurred mostly on the PVB coated AZ31 alloy and although the AZ91 alloy showed analogous behaviour, the difference in the E_{corr} values between the delaminated and the E_{corr} in the intact regions was considerably greater than the AZ31 and more similar to the E717 alloy. In order to clarify the uncertainty with regards to the location of the disbondment front and the E_{corr} values over the surface of the PVB coated AZ series alloys, the SKP was programmed to scan a much greater area of 10 mm × 3 mm. This created a data map of 200 × 60 data points providing a clearer indication of the E_{corr} changes on the surface due to the increased lateral resolution in the y axis. The data presented in Figure 4.8 reveal a series of SKP-derived greyscale image maps at various holding times obtained by scanning an area of the PVB coated AZ31 surface to the left-hand side of the artificial coating defect as noted by the dashed rectangle in Figure 4.8e. The greyscale map in Figure 4.8a demonstrates the E_{corr} distributions obtained on the surface after the coating has started delaminating, with the white arrow indicating the disbondment front. Figure 4.8a–d show that the intact surface is characterised by E_{intact} values of ca. −1 V vs. SHE, however these values appear to be highly heterogeneous. Some regions (intense white spots) are characterised by E_{corr} values of ca. −0.7 V vs. SHE with some of them remaining constant throughout the entire experiment while in other intact regions more negative potentials of ca. −1.1 V are measured.

As mentioned in Chapter 1, the AZ31 Mg alloy is a single-phase alloy with Al–Mn secondary phase particles (few μm in size) dispersed in both the α-Mg matrix grains and at grain boundaries [16–18]. These Al–Mn particles have been identified as Al_8Mn_5 and numerous studies have shown that these particles are considerably more noble than the Mg-matrix and although they cover a relatively small area of the surface, they have high cathodic efficiency [16,17,19–22]. It is, therefore, logical to presume that the spots exhibiting considerably more positive potential than the rest of the surface (Figure 4.8a–d) consist of Al–Mn intermetallic particle clusters that are of sufficient size to be detected by the SKP. Figure 4.8d indicate that the markedly more positive E_{corr} spots, which can be spotted in earlier scans (Figure 4.8b and c), disappear when they are "consumed" by the delaminated regions and are not detected in later scans. Similar observations were also made from Figure 4.7, where the two more positive peaks in E_{corr} seem to adopt more negative values after the disbondment front has moved over these regions.

In the previous chapter, it was explained that the delaminated regions are zones with a rather increased alkalinity due to the hydroxide ions produced by the cathodic HER (Reaction (4.2)). Under these conditions, it may be possible that the Al–Mn clusters are activated due to the amphoteric nature of the aluminium oxide surface layer. Subsequently, these regions would be expected to adopt more negative E_{corr} values on the delaminated AZ31 surface as a consequence of a selective dissolution phenomenon occurring within regions of elevated pH [20]. In Figure 4.8a–d, it can be seen that the delamination front expands with time, progressively consuming the underfilm region and leaving stable, largely homogeneous E_{corr} values behind. Moreover, the leading edge of these stable E_{corr} values is characterised by slightly more negative values of ca. 30 mV, indicating the location of the delamination front. This can also be observed from the E_{corr} profiles obtained from the line scan in Figure 4.7.
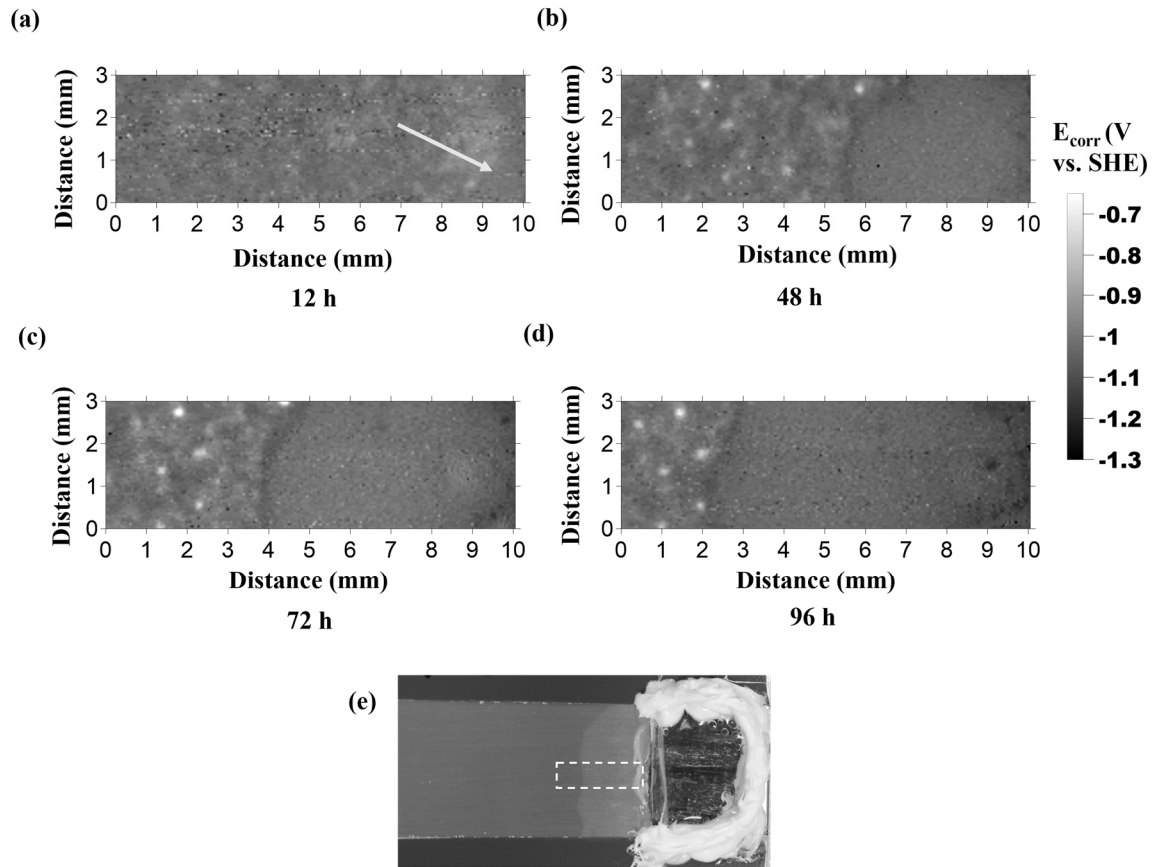
Figure 4.8: Greyscale maps showing E_{corr} distributions, measured by in-situ SKP, measured over a PVB coated AZ31 Mg alloy at various times after initiation of delamination using 1 M NaCl (aq). Time key: (a) 12 h, (b) 48 h, (c) 72 h, (d) 96 h while (e) shows a photographic image of a delaminated sample after exposure to 93% RH with the white dashed rectangle indicating the scanned region of the coated surface.

As it was seen from Figure 4.7 and Figure 4.8, the E_{corr} values obtained in the delaminated regions are similar to the measured E_{intact} values with the difference being that the delaminated regions seem to display more homogenous and stable E_{corr} values of -1 ± 0.05 V vs. SHE. It is not currently known why the delaminated regions of the PVB coated AZ31 alloy do not exhibit more negative E_{corr} values compared to the adjacent intact regions. After the experiment was terminated, the sample was removed from the SKP chamber and the PVB coating was carefully peeled off. It was observed that the coating has lost its adhesion in the regions characterised by the homogenous E_{corr} values. In addition, the regions characterised by marginally more negative E_{corr}, were determined as the location of the disbondment edge since there was a significant increase in adhesive strength, providing confirmatory evidence for the results obtained using the SKP. These observations have been confirmed by conducting repeat delamination experiments on PVB coated AZ31 alloys.

In this case, the delamination distance with time was quantified by following the edge of the delaminated regions in the greyscale E_{corr} distribution maps summarised in Figure 4.8, and the kinetics are presented in Figure 4.9. The delamination distance seems to increase relatively linear with time where the disbondment front travels a distance of ca. 8.5 mm in 100 h. Again, the linearity of the graph implies that the disbondment rate is not governed by the migration of the cations to the disbondment front on organic coated AZ31 alloys specimens, which is in agreement with the observations made for the E717 Mg alloy.
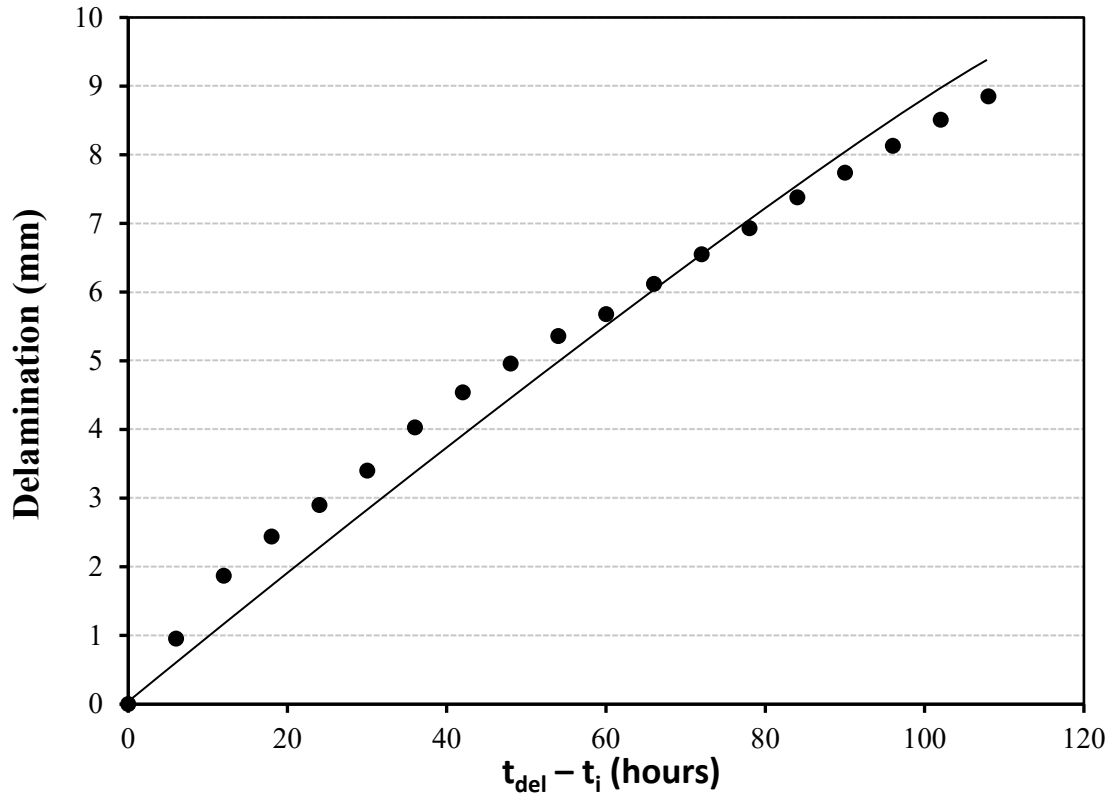
Figure 4.9: Plot of delamination distance versus (t_{del} - t_i) (SKP-derived) for a PVB coated AZ31 alloy specimen exposed to 93% RH and the electrolyte in contact with the artificial defect is 1 M NaCl (aq).

In a separate experiment, the SKP was used to map the free corrosion potentials on a PVB AZ91 surface. The SKP-derived greyscale maps presented in Figure 4.10 were obtained by scanning an area of 10 mm × 3 mm to the left-hand side of the artificial coating defect in a similar manner as with the AZ31. Figure 4.10a shows the E_{corr} distributions obtained on the surface of the coated AZ91 after delamination was initiated, with the black arrow indicating the disbondment front. The E_{intact} (Figure 4.10a–d) located to the far left of the maps vary in the range of −0.9 V to −1.05 V (vs. SHE) signifying the passive state of the sample surface. The region adjacent to the defect (right-hand side) is exhibiting more negative E_{corr} values averaging −1.15 V vs. SHE, denoting the regions where delamination is taking place. Although there is a variation in the E_{intact} values, the PVB coated AZ91 surface exhibits a rather homogeneous surface without signs of strong anodic or cathodic spots on the surface as it was detected with the AZ31. This is presumed to be due to the difference in microstructural distribution and local differences in the composition of the intermetallic phases observed for this alloy [17].
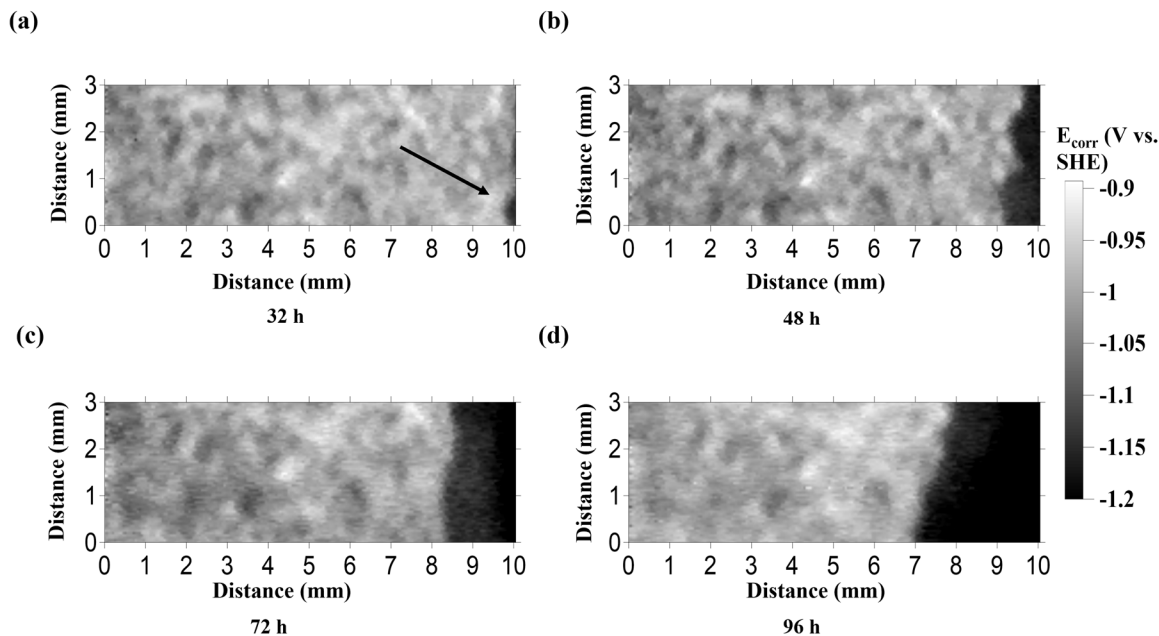
Figure 4.10: Greyscale maps showing E_{corr} distributions, measured by in-situ SKP, measured over a PVB coated AZ91 Mg alloy at various times after initiation of delamination using 1 M NaCl (aq). Time key: (a) 32 h, (b) 48 h, (c) 72 h and (d) 96 h. The sample was maintained at room temperature and a constant RH of 93% throughout.

By exploiting the difference in the E_{corr} values between the delaminated and intact regions, the exact location of the disbondment edge can be determined and therefore, the delamination kinetics. The plot of delamination distance with respect to time is given in Figure 4.11 and as it can be observed, the plot displays linear kinetics throughout the experiment (> 100 h) with a delamination rate of approximately 0.045 mm h^{-1}. This observation is consistent with the previously obtained delamination kinetics for other coated Mg alloys albeit with a slower rate. Nevertheless, the linearity of the plot again suggests that the rate determining step does not involve the transport of cations from the anode to the principal underfilm cathode.
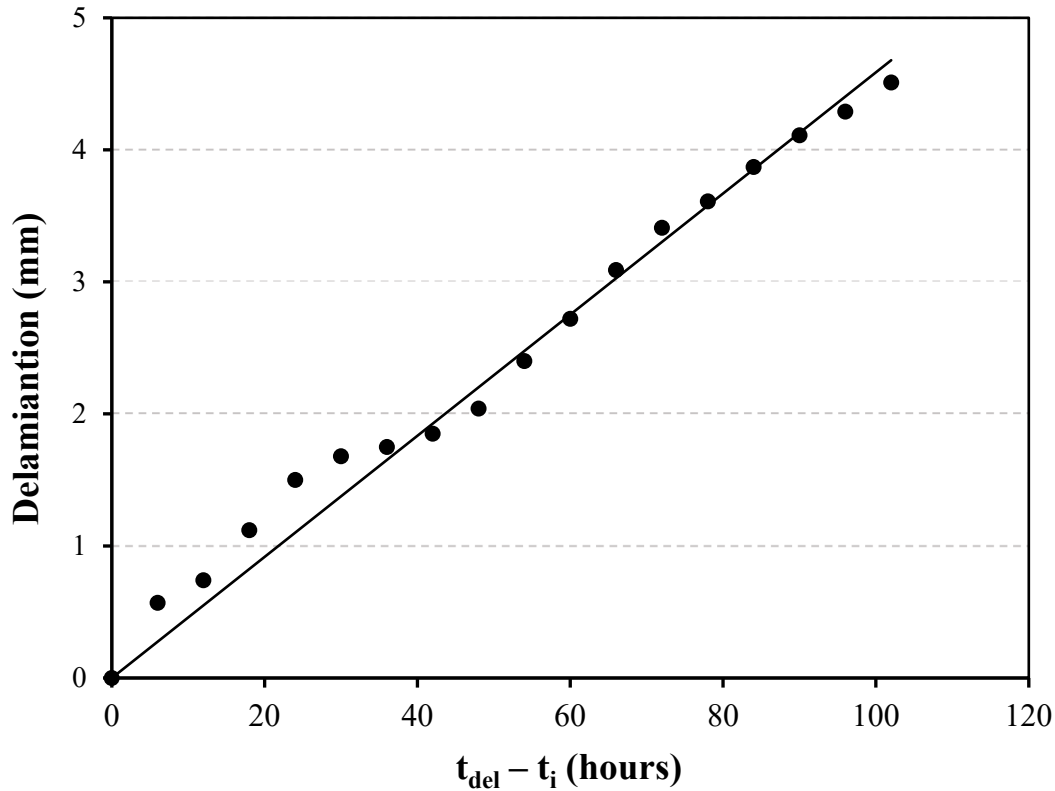
Figure 4.11: Plot of delamination distance versus (t_{del} - t_i) (SKP-derived) for a PVB coated AZ91 alloy specimen exposed to 93% RH and the electrolyte in contact with the artificial defect is 1 M NaCl (aq).

Overall, the PVB coating seemed to lose its adhesion from the E717 and AZ31 surfaces at a not so dissimilar rate, whereas the AZ91 proved to be the least susceptible alloy to coating delamination. This is presumed to be due to the high Al content of this alloy and the subsequent formation of $Mg_{17}Al_{12}$ β-phase [20] that could have potentially reduced the surface activity of the AZ91 and therefore the rate of disbondment. The measured E_{intact} and E_{corr} values for the PVB coated AZ-series alloys appear to be slightly more positive than the equivalent free corrosion potential values measured for the E717.

A plausible explanation for this small shift to more positive E_{corr} values for these Mg alloys is the presence of Al in their microstructure, which would tend to "ennoble" the potential to more positive values [20]. Moreover, Al-containing Mg alloys tend to grow an Al enriched oxide/hydroxide film [23–28] and it has been found that the oxide layer in some Al-containing

phases largely consists of Al_2O_3 [23]. The surface oxide of pure Al is a good electrical insulator meaning that it could act as a barrier to interfacial electron transfer (e.g. the reduction of oxygen at the Al/organic coating interface) [29,30]. Additionally, it has been shown that the surface activity and cathodic delamination rate can be reduced by ion implantation of Al into Fe [30,31] suggesting that Al could potentially be able to block the cathodic oxygen reduction [32]. However, in the case of Mg alloys, it would not be expected that the presence of Al could reduce the delamination rate by blocking the cathodic oxygen reduction on the surface since it was shown in the current chapter that cathodic delamination occurs in the absence of oxygen. It is possible however that the insulating Al-rich oxide regions on the surface of the AZ91 could disfavour the transfer of electrons needed for the water reduction to take place, disfavouring the formation of a continuous delamination front and therefore retarding the delamination rate. Another possible explanation for this phenomenon is that the delamination rate is lower due to the slower anodic dissolution at the defect site. The fact that the exposed Mg surface at the defect reservoir (anode) is corroding at a slower rate, as it would have been expected for the AZ91 alloy, would cause a lower supply of electrons to the cathode at the delamination front and thus retard the overall cathodic delamination rate.

Taken together, the findings from the previous and current chapter demonstrate that all the organic coated Mg alloys employed in this work undergo cathodic delamination. The Mg dissolution (anodic reaction) occurring in the exposed artificial defect (sample reservoir) is linked predominantly with the cathodic hydrogen evolution and some oxygen reduction taking place under the coating. The cathodic reaction leads to the formation of hydroxyl ions that would significantly increase the pH under the coating. The produced hydroxyl ions are counterbalanced by the current-carrying group I cations (e.g. Na^+), which migrate from the electrolyte to the disbondment front. This was confirmed in the previous chapter by using ToF-SIMS where a significant amount of group I cations were detected in the delaminated regions. The schematic diagram of the cathodic delamination mechanism presented in Figure 3.8 seems to have been further confirmed by the experiments conducted in this chapter. Except for the organic coated AZ31 where although the coating has lost its adhesion, no discernible drop in E_{corr} was observed in the delaminated regions. Thus, the idealised shape of the E_{corr} versus distance profile associated with Figure 3.8 will differ for this particular alloy. Conversely, the polymer coated AZ91 alloy

seems to be undergoing cathodic delamination in a similar manner as the E717 where the regions closer to the defect adopt low E_{corr} values (similar to that of a freely corroding Mg) while a region of sharp transition in E_{corr} is observed in the disbondment front where the coating disbondment is occurring. The E_{corr} values detected in the region linking the artificial coating defect/reservoir (anodic site) and the disbondment front (cathodic site) are stable in all cases denoting that the delamination distance does not have any effect on the magnitude of ionic current. #

4.4   Conclusion

Overall, in this chapter, it was demonstrated that the organic coating disbondment takes place on the surface of Mg alloys regardless of the initiating cation type (group I), absence or presence of oxygen or the type of Mg alloy being investigated. The disbondment phenomenon that takes place on PVB coated Mg alloys was studied using in-situ SKP and Stratmann-type cells. The Stratmann-type cell configuration was employed to allow for a more detailed kinetic investigation over longer holding periods under high relative humidity and significantly greater quantities of group I chloride electrolyte. It was found that the delamination distance increased linearly with holding time (>100 h) in all cases and this was explained in terms of the cation availability in the initiating electrolyte. It is therefore crucial to making sure that there is a satisfactory number of cations present in the initiating electrolyte when one is conducting delamination experiments for longer holding times.

The effect of group I chloride salts on the delamination rate of PVB coated E717 alloy was studied using in-situ SKP potentiometry. These experiments showed that the group I cation type present in the initiating electrolyte does not affect the rate of the delamination, contrary to what is expected with other organic coated metals. This provided additional evidence that the rate limiting step of this process is not the migration of cations to the front. Typically for cathodic disbondment on Fe or Zn, cation transport from the defect to the delamination front is postulated to be the rate-determining stage, giving rise to parabolic kinetics. Here the observed linear kinetics even at protracted times tend to suggest that the rate of the process is governed by the electron transfer at the underfilm cathode as it has been proposed by others in the past.

In-situ potentiometric measurements of the PVB coated Mg alloy surface in the absence of oxygen and high relative humidity demonstrated that delamination occurs in the absence of oxygen with

the E_{corr} values in the delaminated areas being similar to the E_{corr} values measured in humid air. The SKP-derived delamination rates appeared to be slightly slower under these conditions denoting that oxygen might be playing a partial role in the process, however, the occurrence of delamination in the absence of oxygen clearly indicates that the hydrogen evolution comprises the predominant cathodic reaction. This finding also suggests that coating/Mg bonds are not destroyed by the reactive intermediates formed during the cathodic oxygen reduction, ruling out this mechanism as a possible primary cause for the loss of organic coating adhesion in this system.

Further experiments using in-situ SKP potentiometry to study PVB coated AZ31 and AZ91 surfaces have revealed that these types of alloys undergo delamination when underfilm corrosion is initiated with an aqueous NaCl solution. The SKP-derived E_{corr} values measured within the delaminated areas of the AZ31 surface appeared to be similar to the average E_{intact} values, albeit with a considerably lower variation, thus exhibiting a slightly different delamination behaviour compared to the rest of the Mg alloys. The AZ91 alloy demonstrated similar behaviour to the E717 specimens, where the delaminated areas adopted more negative E_{corr} values compared to the E_{intact}.

Although the coating delamination rate from the surface of the AZ31 alloy was only slightly lower than the E717 alloy, the rates obtained for the AZ91 Mg alloy were notably lower. This is postulated to be caused by the increased Al content, a different microstructure and the subsequent lower supply of electrons at the principal underfilm cathode, which in turn controls the rate of delamination. Overall, the findings obtained from this series of experiments suggest that this organic coating disbondment phenomenon is universal for many technologically important Mg alloy surfaces.

4.5 References

[1]   A. Leng, H. Streckel, M. Stratmann, The delamination of polymeric coatings from steel. Part 2: First stage of delamination, effect of type and concentration of cations on delamination, chemical analysis of the interface, Corros. Sci. 41 (1998) 579–597.

[2]   G. Williams, R. Grace, Chloride-induced filiform corrosion of organic-coated magnesium, Electrochim. Acta. 56 (2011) 1894–1903.

[3]   M. Stratmann, A. Leng, W. Fürbeth, H. Streckel, H. Gehmecker, K.-H. Groβe-Brinkhaus, The Scanning Kelvin Probe; a new technique for the in situ analysis of the delamination of organic coatings, Prog. Org. Coatings. 27 (1996) 261–267.

[4]   A. Leng, H. Streckel, M. Stratmann, The delamination of polymeric coatings from steel. Part 1: Calibration of the Kelvin probe and basic delamination mechanism, Corros. Sci. 41 (1998) 547–578.

[5]   R.-G. Hu, S. Zhang, J.-F. Bu, C.-J. Lin, G.-L. Song, Progress in Organic Coatings: Recent progress in corrosion protection of magnesium alloys by organic coatings, Prog. Org. Coatings. 73 (2011) 129–141.

[6]   M. Esmaily, J.E. Svensson, S. Fajardo, N. Birbilis, G.S. Frankel, S. Virtanen, R. Arrabal, S. Thomas, L.G. Johansson, Fundamentals and advances in magnesium alloy corrosion, Prog. Mater. Sci. 89 (2017) 92–193.

[7]   G.S. Frankel, M. Stratmann, M. Rohwerder, A. Michalik, B. Maier, J. Dora, M. Wicinski, Potential control under thin aqueous layers using a Kelvin Probe, Corros. Sci. 49 (2007) 2021–2036.

[8]   P. Schmutz, V. Guillaumin, R.S. Lillard, J.A. Lillard, G.S. Frankel, Influence of dichromate ions on corrosion processes on pure magnesium, J. Electrochem. Soc. 150 (2003) B99.

[9]   H. Bi, J. Sykes, Cathodic disbonding of an unpigmented epoxy coating on mild steel under semi- and full-immersion conditions, Corros. Sci. 53 (2011) 3416–3425.

[10]   G. Williams, A. Gabriel, A. Cook, H.N. McMurray, Dopant effects in polyaniline inhibition

of corrosion-driven organic coating cathodic delamination on iron, J. Electrochem. Soc. 153 (2006) B425.

[11] W. Fürbeth, M. Stratmann, The delamination of polymeric coatings from electrogalvanised steel - a mechanistic approach. Part 1: delamination from a defect with intact zinc layer, Corros. Sci. 43 (2001) 207–227.

[12] M. Strebl, S. Virtanen, Real-time monitoring of atmospheric magnesium alloy corrosion, J. Electrochem. Soc. 166 (2018) C3001–C3009.

[13] M. Strebl, M. Bruns, S. Virtanen, Editors' Choice—Respirometric in situ methods for real-time monitoring of corrosion rates: Part I. Atmospheric corrosion, J. Electrochem. Soc. 167 (2020) 21510.

[14] M. Stratmann, R. Feser, A. Leng, Corrosion protection by organic films, Electrochim. Acta. 39 (1994) 1207–1214.

[15] M. Stratmann, H. Streckel, R. Feser, A new technique able to measure directly the delamination of organic polymer films, Corros. Sci. 32 (1991) 467–470.

[16] A. Pardo, M.C. Merino, A.E. Coy, F. Viejo, R. Arrabal, S. Feliú, Influence of microstructure and composition on the corrosion behaviour of Mg/Al alloys in chloride media, Electrochim. Acta. 53 (2008) 7890–7902.

[17] M.C. Merino, A. Pardo, R. Arrabal, S. Merino, P. Casajús, M. Mohedano, Influence of chloride ion concentration and temperature on the corrosion of Mg-Al alloys in salt fog, Corros. Sci. 52 (2010) 1696–1704.

[18] G. Williams, H.A.L. Dafydd, R. Grace, The localised corrosion of Mg alloy AZ31 in chloride containingelectrolyte studied by a Scanning Vibrating Electrode Technique technique, Electrochim. Acta. 109 (2013) 489–501.

[19] S. Pawar, X. Zhou, G. Thompson, G.M. Scamans, Z. Fan, The role of intermetallics on the corrosion initiation of twin roll cast AZ31 Mg alloy, J. Electrochem. Soc. 162 (2015) 442–448.

[20] M. Jönsson, D. Thierry, N. LeBozec, The influence of microstructure on the corrosion

behaviour of AZ91D studied by Scanning Kelvin Probe force microscopy and Scanning Kelvin Probe, Corros. Sci. 48 (2006) 1193–1208.

[21] G.-L. Song, Z. Xu, Effect of microstructure evolution on corrosion of different crystal surfaces of AZ31 Mg alloy in a chloride containing solution, Corros. Sci. 54 (2012) 97–105.

[22] F. Andreatta, I. Apachitei, A.A. Kodentsov, J. Dzwonczyk, J. Duszczyk, Volta potential of second phase particles in extruded AZ80 magnesium alloy, Electrochim. Acta. 51 (2006) 3551–3557.

[23] J.H. Nordlien, K. Nişancioglu, S. Ono, N. Masuko, Morphology and structure of oxide films formed on MgAl alloys by exposure to air and water, J. Electrochem. Soc. 143 (1996) 2564–2572.

[24] F. Hermann, F. Sommer, H. Jones, R.G.J. Edyvean, Corrosion inhibition in magnesium-aluminium-based alloys induced by rapid solidification processing, J. Mater. Sci. 24 (1989) 2369–2379.

[25] J.H. Nordlien, K. Nişancioglu, Morphology and structure of water-formed oxides on ternary MgAl alloys, J. Electrochem. Soc. 144 (1997) 461.

[26] S. Mathieu, C. Rapin, J. Steinmetz, P. Steinmetz, A corrosion study of the main constituent phases of AZ91 magnesium alloys, Corros. Sci. 45 (2003) 2741–2755.

[27] R.C. Phillips, J.R. Kish, Nature of surface film on matrix phase of Mg alloy AZ80 formed in water, Corrosion. 69 (2013) 813–820.

[28] S. Feliu, A. Pardo, M.C. Merino, A.E. Coy, F. Viejo, R. Arrabal, Correlation between the surface chemistry and the atmospheric corrosion of AZ31, AZ80 and AZ91D magnesium alloys, Appl. Surf. Sci. 255 (2009) 4102–4108.

[29] H.N. Mcmurray, G. Williams, Under Film/Coating Corrosion, Shreir's Corros. 2 (2010) 988–1004.

[30] H. Leidheiser, Cathodic delamination of polybutadiene from steel-A review, J. Adhes. Sci. Technol. 1 (1987) 79–98.

[31] R.D. Granata, M.A. De Crosta, J. Leidheiser, H, Corrosion and coating delamination properties of steel ion-implanted with aluminum and titanium, in: Proc. 9th Int. Congr. Met. Corros., Toronto, Canada; National Research Council of Canada, 1984: pp. 264–268.

[32] G.J. Reynolds, Z.S. Barrett, H.N. McMurray, G. Williams, An investigation of the influence of physical vapour deposited aluminium layers on the kinetics of organic coating disbondment on iron, Corros. Sci. 70 (2013) 82–92.

Chapter 5

The Kinetics and Mechanism of Filiform Corrosion affecting Organic Coated Magnesium Alloy Surfaces

The Kinetics and Mechanism of Filiform Corrosion Affecting Organic Coated Mg Alloy Surfaces

5.1 Introduction

It has been previously mentioned in this thesis that Mg and its alloys are candidates for various automotive and aerospace applications due to their good strength-to-weight ratio and high specific strength [1]. However, Mg and its alloys also require protection from environmental degradation since they are susceptible to corrosion due to their position in the electrochemical series. Relatively a few publications are devoted to investigations of organic coatings for corrosion protection for Mg and its alloys [2,3] and the lack of understanding of the prevailing mechanisms of organic coating failure on Mg and its alloys has hindered the adequate development of organic coating technologies that are tailored for Mg alloys.

In Chapter 3, it was shown that when organic coated Mg substrates are exposed to an atmosphere comprising a high relative humidity (RH) and aggressive inorganic salts, coating failure can proceed according to two principal mechanisms; cathodic delamination and/or filiform corrosion (FFC) [4–6]. Typically, corrosion-driven coating failure initiates at a penetrative coating defect such as cut-edges, scratches, and scribes where aggressive species, such as chloride ions can make contact to the bare metal and access the coating/substrate interface. Blistering is another phenomenon that can also occur especially at extremely high levels of relative humidity, normally through an intact organic coating [7–9]. In Chapter 3 and 4, it was demonstrated using model PVB coatings applied to automotive E717 Mg alloy surfaces under atmospheric corrosion conditions, the mechanism of coating failure originating from a penetrative coating defect was highly dependent upon the nature of the chloride salt employed to initiate corrosion. When underfilm corrosion was initiated using group I chloride salts, coating failure was characterised by the rapid development of a halo of disbonded coating surrounding the defect region, which expanded radially with time. Post corrosion surface analysis showed that the region affected by the halo was abundant in the initiating cation, but that chloride ions were not present and were conserved within the defect region. It was thus proposed that a cathodic disbondment mechanism was responsible for this phenomenon in which anodic Mg dissolution at the defect is coupled with underfilm

cathodic hydrogen evolution. However, in the absence of group I cations, which can sustain ionic current within a region of high alkalinity, no such disbondment halo was observed. Consequently, the use of HCl or $MgCl_2$ to initiate coating failure produced only anodic disbondment via filiform corrosion (FFC), characterised by the underfilm evolution of a network of dark tracks that lengthen with time.

FFC is well known to affect other organic coated metal surfaces, such as iron [10–13] and Al alloys [11,14–16], where the propagation of filaments is considered to proceed through a differential aeration cell located at the electrolyte-filled head at the filament leading edge. An oxygen concentration cell results from facile transport of O_2 through the corrosion product filled tail to the rear of the filament head [17], with a local anode at the leading-edge producing undermining of the organic coating.

However, it has been proposed in the case of PVB coated Mg, that where hydrogen evolution according to Reaction (5.1) is anticipated to be the dominant cathodic reaction, the mechanism of FFC propagation involves anodic Mg dissolution ((Reaction (5.2)) coupling with cathodic water reduction on a cathodically activated, corroded surface immediately behind the filament leading edge [6]. This differential electrocatalytic activation provides the driving force for filament advancement and explains in part why FFC rates of propagation remain unchanged in the absence of oxygen when PVB-coated Mg is maintained at a high relative humidity.

$$2H_2O + 2e^- \rightarrow H_2 + 2OH^- \tag{5.1}$$

$$Mg \rightarrow Mg^{2+} + 2e^- \tag{5.2}$$
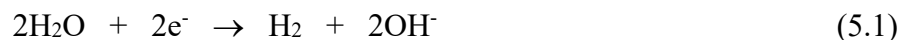
In the current chapter, the influence of factors such as chloride ion concentration and relative humidity on the kinetics of FFC propagation on model PVB-coated Mg alloy substrates, is systematically investigated using a combination of in-situ time-lapse photography and the SKP. Continuing from previous chapters, this investigation is concentrated on the technologically important, rare-earth containing E717 (Electron^{TM} 717) alloy, which is considered as a promising candidate for automotive applications [18,19]. It should also be noted that several recent publications [20–23] are devoted to furthering the understanding of the corrosion behaviour of this particular alloy. In addition, some key experiments are also repeated using other widely used AZ-series Mg alloys, such as the AZ31 and AZ91 to confirm FFC susceptibility under the same

conditions. The principal aims of this chapter are (i): to confirm whether observations regarding FFC initiation and propagation made in the past using pure Mg [6] also hold true for commercially available alloys, and (ii) to identity the principal factors that influence underfilm corrosion rates. FFC is inoculated by applying controlled quantities of aqueous HCl, $MgCl_2$ or $FeCl_2$ to scribed defects in PVB coated alloy specimens and quantification of FFC kinetics is achieved by time-dependent analysis of corrosion-affected areas via time-lapse photography. Post-corrosion surface analysis of FFC affected surfaces using SEM-EDX is used in combination with the results of in-situ SKP mapping of free corrosion potential distributions to elucidate the mechanism of FFC and explain observations on the influence of chloride ion concentration on propagation rates.

5.2 Experimental Details

5.2.1 Materials and Sample Preparation

Three different Mg alloys were used in this chapter, namely E717 (Electron[TM] 717), AZ31 and AZ91 and a detailed description of these Mg alloys is given in Section 2.1.1. Prior to the application of the organic coating, the samples were cut using electric discharge machining (EDM) into 50 x 50 mm specimens and prepared in a similar manner as the previous chapters and as described in Section 2.1.3. A PVB model coating was used in this study and was prepared in ethanol (15.5 % w/w). All other chemicals used for the experiments have analytical grade purity and were obtained from Sigma-Aldrich Ltd. In this chapter, all FFC experiments were conducted by utilizing the scribed-defect cell arrangement and the detailed description of this type of cell is given in Section 2.2.1.2.

5.2.2 Methods

In this chapter, the filiform corrosion was inoculated by applying controlled quantities of aqueous solutions of either $MgCl_2$, HCl and $FeCl_2$ to a 10 mm long penetrative coating defect scribed using a fresh scalpel blade perpendicular to the rolling direction of the Mg alloy. In all cases an electrolyte volume of 1 μL was used, injected into the coating defect using a microlitre syringe supplied by Hamilton Ltd. More information about this experimental method can be found in Section 2.8.

To understand the effect of the chloride ion concentration on the filiform of coated Mg alloys, four different concentrations of $MgCl_2$ were used: 5×10^{-3} M, 0.02 M, 0.1 M, and 0.5 M. A detailed description of this methodology is also provided in Section 2.8. Briefly, the different levels of relative humidity (RH) 31%, 52%, 76%, 93% and 99% were achieved by using reservoirs containing saturated aqueous solutions of the following: $CaCl_2 \cdot 2H_2O$, $Ca(NO_3)_2$, NaCl, $Na_2SO_4 \cdot 10H_2O$ and DI water at 20°C [24,25]. After injecting the respective electrolytes into the scribes, the coupons were held in bespoke environmental chambers comprising an optically flat window allowing the coated Mg alloy specimens to be photographed in-situ when maintained in air at a constant RH. The oxygen-free experiments were conducted by holding specimens in similar type of chamber that also comprised an inlet and outlet allowing humidified nitrogen to be introduced and the description of this methodology is given in Section 2.8.1. Close-up photographic images of the corroding surface were taken in-situ every 6 h over holding durations of up to 600 h using a Canon EOS 77D camera fitted with AF-microlens and macrotubes (see Section 2.3). The filiform corrosion affected areas were determined by taking measurements from the photographic images using ImageJ and Photoshop image analysis software.

In-situ mapping of free corrosion potential (E_{corr}) distributions associated with PVB-coated E717 specimens undergoing FFC was carried out using an SKP of in-house construction. Full details of the design and operation of the instrument, along with details of calibration procedure allowing Volta potential differences to be converted to measurements of E_{corr} are given in Section 2.2. The SKP reference probe consisted of a 125 μm diameter gold wire that was vibrated normal to the specimen surface at a vibration frequency of 280 Hz with a 30 μm peak-to-peak amplitude, while the probe-specimen distance was 100 μm. Following initiation of FFC as described above, PVB coated specimens were placed within the environmental chamber of the SKP apparatus and held at a RH of 93%, maintained using reservoirs of the appropriate saturated salt solution. Repetitive scans were carried out every 3 h on a 7 mm × 6 mm area positioned to one side of the scribed defect, using a data point density of 10 points/mm. After calibration the grids of spatially resolved E_{corr} values were visualised as greyscale image maps using the Surfer 10 mapping software. On completion of the experiment the PVB coating was carefully peeled away immediately and the FFC affected region was analysed for Cl^- deposits using a Hitachi TM3000 SEM with integrated Bruker Quantax 70 EDX Analyser.

5.3 Results and Discussion

5.3.1 Preliminary Studies of Filiform Corrosion

Generally, chloride-induced underfilm corrosion of organic coated Mg alloys is characterised by black thin propagating tracks, which tend to move in a random direction and away from their initiation point [4–6]. It was demonstrated in Chapter 3, that in the absence of group I cations, FFC commences shortly after inoculating underfilm corrosion by applying controlled quantities of either $MgCl_2$ or HCl to a penetrative coating defect on a PVB-coated E717 alloy. To investigate whether or not the initiating chloride salt has any effect on the propagation of the FFC on organic coated Mg alloys, a sample was prepared with three penetrative coating scribes into which 1 μL quantities of 0.5 M $FeCl_2$ (left scribe), 1 M HCl (middle scribe) and 0.5 M $MgCl_2$ (right scribe) were injected. The photographic images presented in Figure 5.1 show the appearance of the PVB coated E717 Mg alloy at different holding times when held in air at a constant relative humidity of 93% after filiform corrosion initiation. $FeCl_2$ was used to test out a hypothesis of whether enhanced electrocatalytic activity towards cathodic hydrogen evolution (Reaction (5.1)) at the scribe, caused by electrodeposition of metallic iron according to the following displacement reaction,

$$Mg\ (s)\ + Fe^{2+}\ (aq)\quad \rightarrow\quad Mg^{2+}\ (aq) +\ Fe\ (s) \tag{5.3}$$
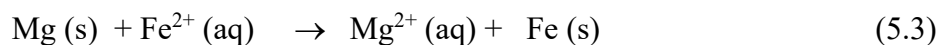
provides an additional driving force to increase filament propagation rates. It has been shown in the literature [26], that the corrosion rate of pure Mg immersed in $NaCl_{(aq)}$ can increase by up to a factor of 5 in the presence of dissolved Fe^{2+} (aq) at concentrations of up to 8×10^{-3} M. Upon injection of the different initiating electrolytes, a vigorous reaction involving a rapid darkening of the bare alloy, accompanied by generation of hydrogen bubbles, was observed in all penetrative defects. In the case of $FeCl_2$ (aq), a green colouration was also initially observed, which soon turned to brown colour, indicating that aerial oxidation of Fe^{2+}, followed by hydrolysis, occurs in competition to Reaction (5.3) [26].

Figure 5.1b shows that after 1 day exposure to high humidity, several filaments of up to 2 mm in length and varying width have initiated and propagated away from the defect regions in both left and right directions. However, at longer holding times (Figure 5.1c and d), neighbouring filaments

appear to coalesce, leaving a network of dark corroded surface surrounding the scribes, although individual filament extending up to 10 – 15 mm away from the scribes can also be identified.
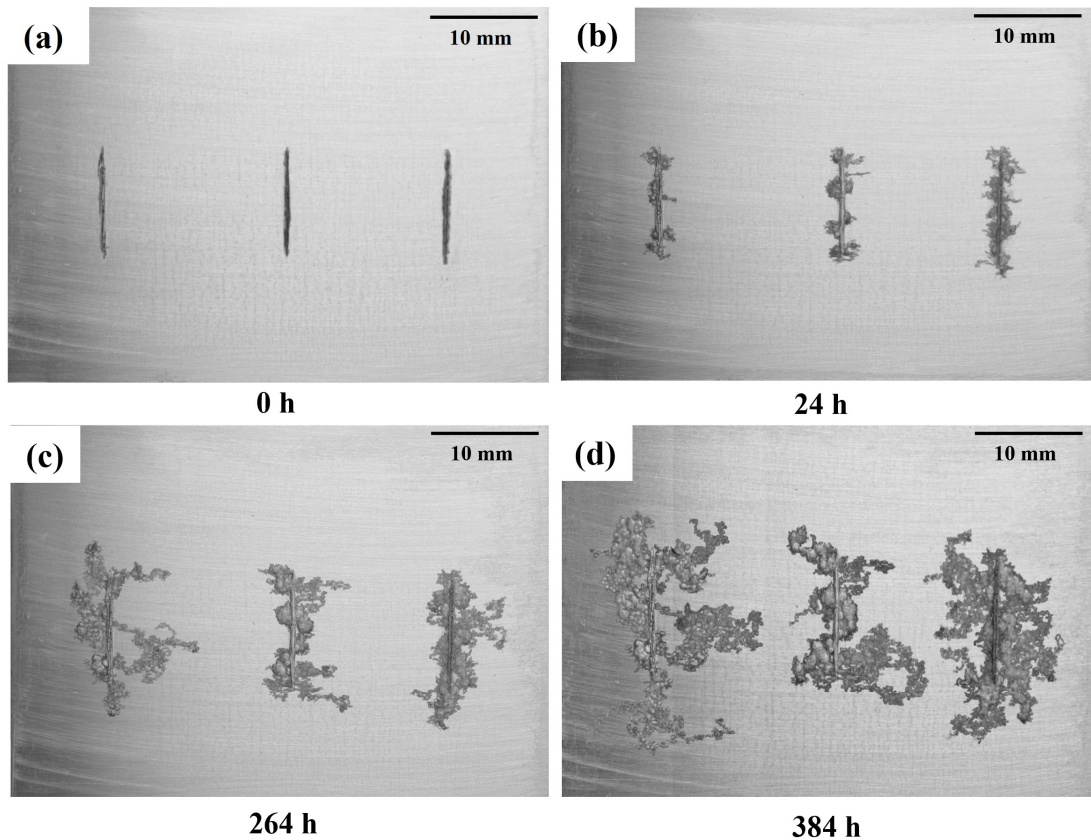
Figure 5.1: Photographic images showing the propagation of FFC on a PVB coated E717 alloy specimen held in air at 93% RH and 20°C following corrosion initiation using controlled quantities of $FeCl_2$ (left scribe), HCl (middle scribe) and $MgCl_2$ (right scribe). Time key: (a) 0 h, (b) 24 h, (c) 264 h and (d) 384 h.

At protracted holding times, the filaments appear to move in a "random walk" manner, where there is no apparent influence of the original rolling direction of the E717 sheet or direction of abrasive cleaning. In addition, from the similarity of the corrosion features observed in the vicinity of each scribed region, it is evident that the nature of the cation has little influence on the morphology or the extent of underfilm corrosion. The significant visual contrast between uncorroded areas and those affected by filiform-like corrosion was exploited by using image analysis of the time-lapse

sequence typified in Figure 5.1, as described in the experimental detail section, to generate time-dependent values of FFC area for each scribed region. Plots of filiform affected area versus holding time determined for each of the different initiating electrolytes are given in Figure 5.2. From the slopes of the plots determined over the first 200 h, FFC area propagation rates of 0.29, 0.27 and 0.2 mm^2 h^{-1} were established for MgCl$_2$, FeCl$_2$ and HCl initiating electrolytes respectively.
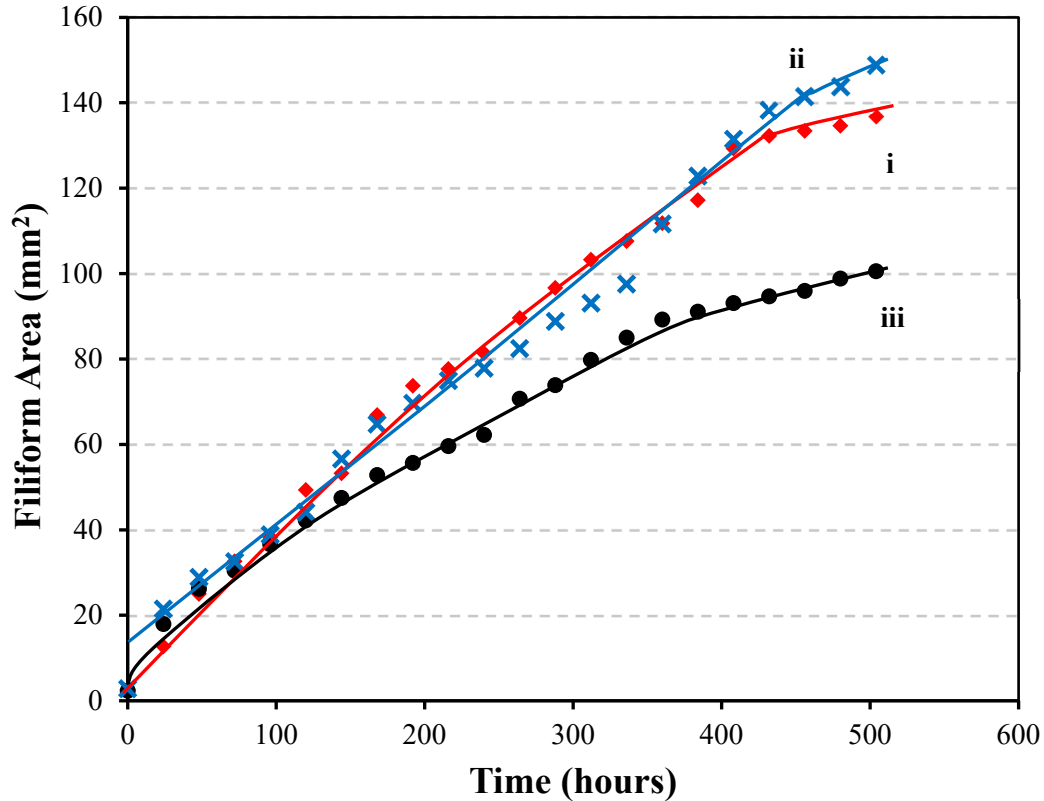
Figure 5.2: Plots of FFC area versus time measured for a PVB coated E717 alloy kept in a chamber at 93% RH and 20°C following initiation of underfilm corrosion using a 1 µL volume of (i) MgCl$_2$, (ii) FeCl$_2$ and (iii) HCl (aq) at a fixed chloride ion concentration of 1 M.

However, in each case, a noticeable deviation from linearity was observed at longer holding times, where area versus time relationships tend to lower gradients. Therefore, although FFC propagation kinetics are similar when divalent chloride salts are used to initiate underfilm corrosion, there is a discernible decrease in rate when HCl is employed. A repeat experiment using a lower chloride ion concentration of 0.2 M, produced the same trend in behaviour, albeit with markedly reduced

FFC area propagation rates. The consistently lower rate of underfilm corrosion propagation observed following initiation using HCl is unexpected, given the previously reported rapid development of HCl-induced FFC affecting PVB coated commercially pure Mg [6]. However, the researchers noted that the composition of the conserved underfilm electrolyte at the filament leading edges will comprise a concentrated aqueous solution of $MgCl_2$, and a certain induction period will be required in order to generate the requisite composition from HCl (aq) initiated corrosion [6]. If this process is relatively slow, then the known volatility of HCl may mean that less chloride is present than anticipated in order to sustain FFC propagation.

The similarity of the slopes for plots i and ii in Figure 5.2 implies that Fe electrodeposition in the defect region has little effect on subsequent FFC propagation, but implies that it may play a role in rapidly generating an appropriate underfilm electrolyte composition to allow FFC to develop in the same manner as when initiated using $MgCl_2$. Following this preliminary investigation of the influence of cation type on chloride-induced FFC, all other systematic studies presented in this chapter were conducted using $MgCl_2$ (aq) as the initiating electrolyte.

In order to determine the distribution of free corrosion potentials over a region of PVB coated E717 affected by actively propagating filaments, the SKP was employed. Following initiation of FFC by application of a 1 μL volume of 0.5 M of $MgCl_2$. (aq) to a scribed 10 mm long penetrative coating defect, the specimen was subsequently kept in a chamber with high relative humidity of 93% at 21 °C for 10 days to allow filament propagation to take place. Figure 5.3(a–e) shows a series of greyscale E_{corr} distribution maps obtained by scanning the surface at regular intervals over a 144-h period. In this particular experiment, an area of 7 mm × 6 mm adjacent to the scribed defect was repetitively scanned using the SKP. The scanned region is indicated by dashed lines in the photographic image given Figure 5.3f, which shows the appearance of the coated surface after the experiment was terminated. In Figure 5.3f three different filaments can be observed, with the main filament of interest denoted as I. This underfilm corrosion feature was the first one to propagate, followed by filaments II and III, which develop on the left side of the scan area and generally move towards the right.
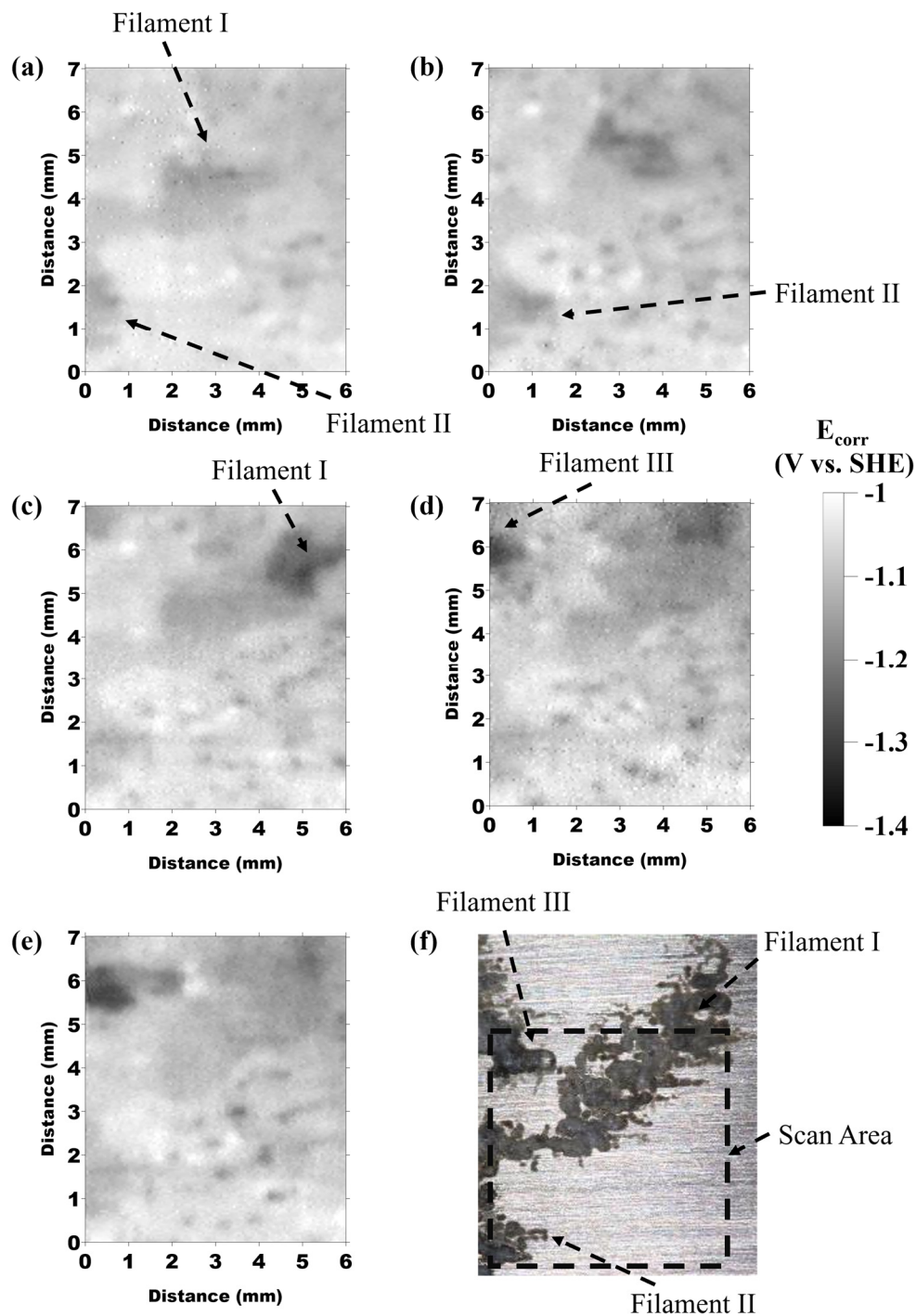
Figure 5.3: Greyscale maps showing SKP derived E$_{corr}$ distributions determined at 93% RH and 20°C for a PVB coated E717 specimen undergoing FFC. Time key: (a) 10 h, (b) 35 h, (c) 60 h, (d) 115 h, (e) 144 h holding times following initiation using a 1 µL quantity of 1 M MgCl$_2$ (aq), while (f) shows a photographic image scan area (indicated by the dashed line) at the end of the experiment.

The greyscale SKP-derived map (Figure 5.3a) indicates that the majority of intact (uncorroded) areas are exhibiting E_{corr} values (E_{intact}) of ca. −1.1 V vs. SHE, but some localised uncorroded regions exhibit potentials, which are ± 0.1 V of this mean value. This heterogeneity in E_{intact} values is explained on the basis of atmospheric corrosion occurring in high humidity at the coating/Mg interface producing heterogeneity in the surface (hydro)oxide layer, which develops with time. In Figure 5.3a–c, changes in E_{corr} distributions as Filament I moves in a diagonal manner, from the centre of the scan area to the top right corner can be observed. The leading edge of the filament appears to adopt more negative potentials than the remainder of the surface, with E_{corr} values ranging between ca. −1.25 and −1.35 V vs. SHE. However, as Filament I move from its original location in Figure 5.3a, E_{corr} values determined with the region left behind become more positive but remain ca. 100 mV more negative than the surrounding intact surface. Also visible in Figure 5.3a and b, is a second filament (denoted II), which initiates in the bottom left corner of the scanned area, elongates by ca. 1 mm and then becomes immobile (i.e. de-activates). Again, the leading edge is characterised by a more negative E_{corr} than the uncorroded surface, although the region becomes less distinct from the surrounding intact surface with time after the filament has ceased to propagate (Figure 5.3c–e).

In later scans, Filament III initiates in the top left corner and moves further inside the scan area, producing a region of more negative local E_{corr} values, which starts "trespassing" in the previously corroded tail region of Filament I. In Figure 5.3d and e it should be noted that the leading edge of Filament I has moved beyond the scan area, while its dark corroded tail, extending from the centre of the greyscale map to the top right corner remains slightly depassivated (by ca. 0.1 V) compared to the adjacent uncorroded surface.

After the conclusion of the experiment the sample was withdrawn from the SKP chamber, the PVB coating was carefully peeled away and regions affected by FFC were analysed using SEM-EDX to determine the location of chloride ions. Figure 5.4 shows false colour elemental maps superimposed over the secondary electron micrographs of a selection of filiform-like features, where red and green colours correspond with regions of high chloride ion and Mg abundance respectively. Figure 5.4a, along with a higher magnification image in Figure 5.4b, show an area of chloride ion activity near the front of a head region.
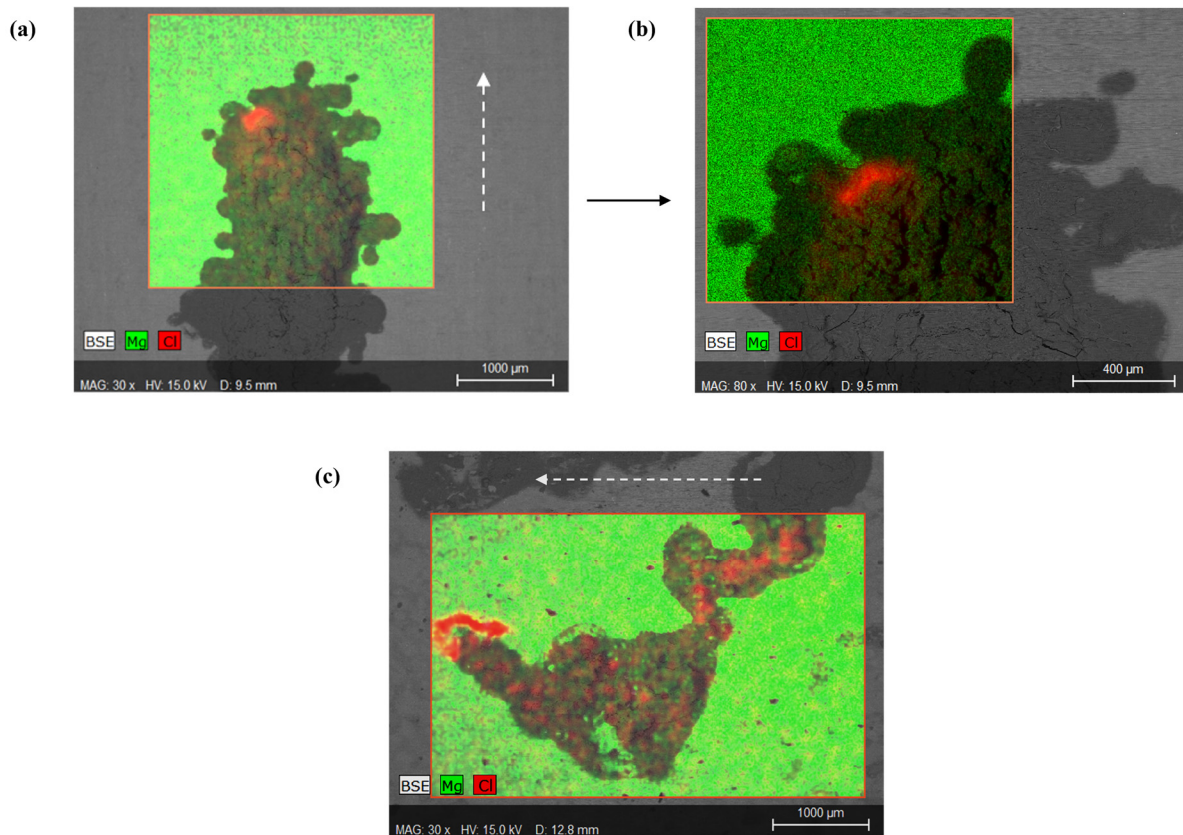
Figure 5.4: SEM-EDX images of FFC features on the surface of the E717 Mg alloy after the removal of the PVB coating following corrosion initiation with 1 μL quantity of 1 M $MgCl_2$ (aq). The white arrows indicate the direction of propagation of the filament. (a) shows a typical filament head, along with (b) magnified image of part of this feature, while (c) shows an entire filament consisting of both head and tail regions.

A similar high abundance of chloride at the leading edge of the filament was also found when a filament was analysed along its entire length as it can be seen from Figure 5.4c. These observations using coated E717 Mg alloy are in agreement with surface analysis findings on commercially pure Mg, where elemental maps obtained using secondary ion mass spectrometry (SIMS) showed chloride ion conservation within the head regions of filament propagating under a PVB coating [6]. However, careful examination of Figure 5.4c also shows evidence of chloride ion entrapment within some regions along the length of the filament tail suggesting that not all the chloride ions originally used to initiate FFC are conserved in the leading edges of the filament heads. This observation of Cl^- sequestration within the corrosion product in the tail regions seems consistent

with the observation made above that SKP-derived E_{corr} values measured within these regions remain ca. 0.1 V more negative than adjacent uncorroded areas. The distinction between potential values in the head, tail and intact regions of the FFC affected surface may perhaps be more clearly made in Figure 5.5, which shows a line profile of E_{corr} versus distance taken along the length of Filament I in Figure 5.3.
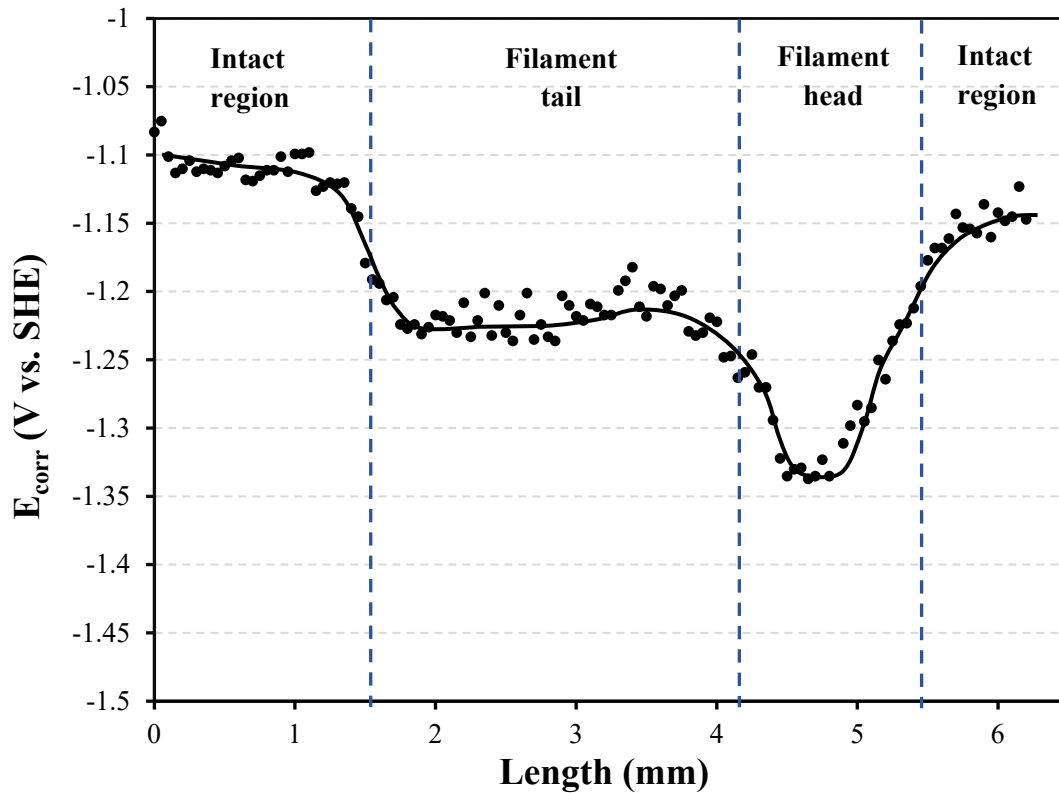
Figure 5.5: Plot of E_{corr} values versus distance measured for a propagating filament on a PVB coated E717 specimen exposed to 93% RH and 20°C.

In this particular profile, E_{intact} values of ca. –1.1 V vs. SHE are measured behind the tail region and ahead of the leading edge, while a minimum potential of ca. –1.35 V vs. SHE is observed within the head region. This is similar to typical values of ca. –1.4 V vs. SHE reported previously for FFC leading edges investigated on PVB coated pure Mg under similar conditions [6]. However, the persistence of a low potential of ca. –1.2 V vs. SHE within the tail region is not consistent with previous observation made for pure Mg, where potentials rise to values equal to E_{intact} as filaments move progressively further from their original location. It therefore seems

logical to assume that the significantly lower FFC propagation rate on E717, where the elongation of Filament I in Figure 5.3 proceeds at a rate of ca. 0.04 mm h^{-1} (compared with a rate of 0.1 mm h^{-1} reported for pure Mg), increases the possibility of progressive loss of chloride ions from the head electrolyte via entrapment in the corrosion product filled tail.

5.3.2   The Influence of the Chloride Ion Concentration

It has been shown in the literature [27–29] that the extent of localised corrosion observed on un-coated Mg alloy surfaces under full immersion can sometimes be dependent on the sodium chloride concentration of the bulk solution. This current chapter, tests whether or not a similar effect is operational in the development of underfilm filiform corrosion of PVB-coated E717 by varying the concentration of the injected electrolyte and holding the samples in air at a constant 93% relative humidity for 21 days. The effect of applying four different chloride ion concentrations of 1 μL MgCl$_2$ (5 × 10^{-3}, 0.02, 0.1 and 0.5 M) to a penetrative coating defect on the propagation of FFC was quantified by image analysis of time-lapse image sequences as discussed previously.

Figure 5.6 shows the visual appearance of 4 different samples that were scribed and injected with various concentrations of MgCl$_2$ and then exposed to 93% relative humidity for 21 days. It is evident that an increase in the concentration of the inoculating electrolyte produces a progressively greater corroded area surrounding the scribes after the same holding time. For specimens that have been inoculated with MgCl$_2$ (aq) concentrations of ≤ 0.02 M, several discrete filament-like features can be identified, while at higher concentrations the underfilm corrosion morphology suggests that many tracks have coalesced to produce a more uniform disbondment front.
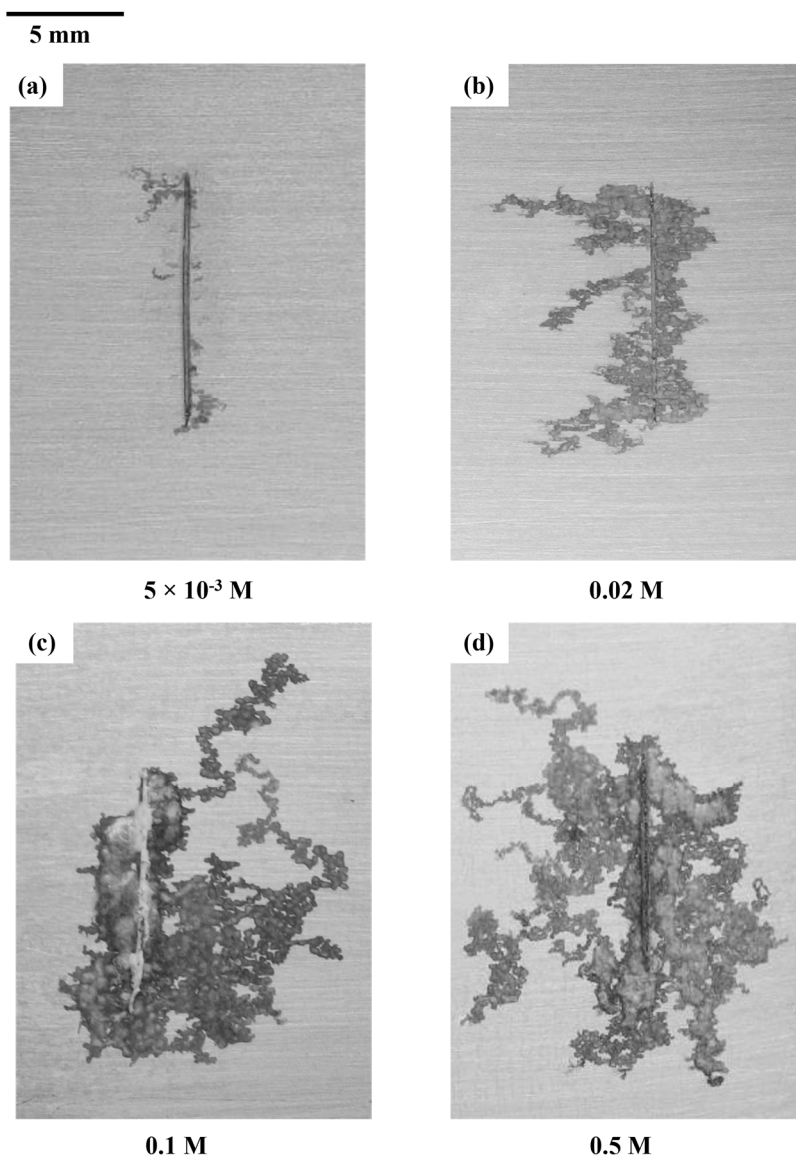
Figure 5.6: Photographic images of FFC affecting PVB coated E717 alloy after using $MgCl_2$ concentration of (a) 5×10^{-3}, (b) 0.02, (c) 0.1, (d) 0.5 M to initiate corrosion and exposing the samples to fixed 93% RH in air for 500 h at 20°C.

Quantification of the corroded area for the images obtained for each different specimen allowed the effect of chloride ion concentration on the kinetics of underfilm corrosion to be evaluated. Figure 5.7 shows plots of FFC area versus time for specimens held in air at 93% RH after initiation of corrosion using 1μL $MgCl_2$ (aq) injections in the concentration range 5×10^{-3} to 0.5 M.

The influence of increasing [MgCl₂] on the extent of the underfilm corroded area associated with each specimen is clearly observed, where final FFC affected areas of 10, 53, 100 and 140 mm² were measured for 5×10^{-3}, 0.02, 0.1 and 0.5 M inoculating concentration respectively after a 500 h holding period.
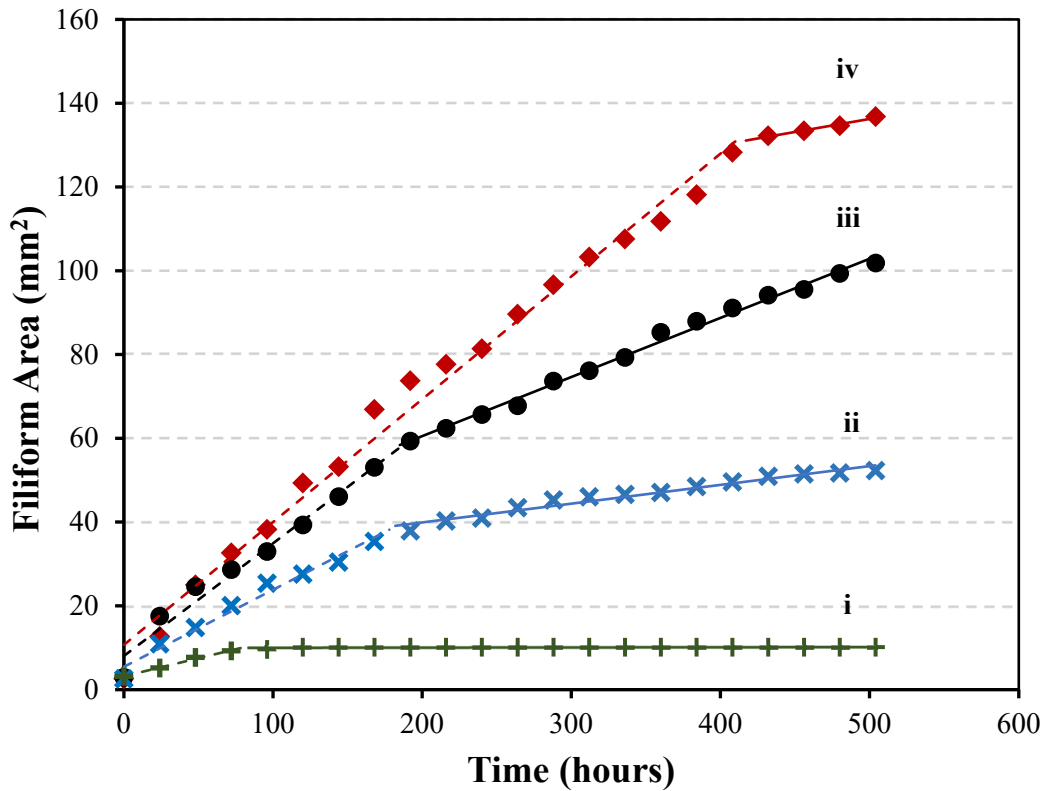
Figure 5.7: Plots of FFC area versus time for PVB coated E717 alloy following corrosion initiation using MgCl₂ concentrations of (i) 5×10^{-3}, (ii) 0.02, (iii) 0.1, (iv) 0.5 M and subsequent exposure of the coated samples to humid air (93% RH) at 20°C for 500 h.

It is also evident that the nature of the FFC area versus time plots is also highly dependent on the quantity of chloride ions used to initiate corrosion. Although an initial linear relationship is observed for each plot in Figure 5.7, a significant deviation from linearity is observed at protracted holding times. The time at which the divergence occurs appears to be lengthen with increasing quantity of initiating chloride ion, such that the slope of the area versus time plot tends to zero after 80 h for the lowest [Cl⁻] used. The point at which an inflection in the linear FFC area versus

time relationship is observed, it lengthens progressively with increasing [Cl⁻], such that a change in the gradient at the highest $MgCl_2$ (aq) initiating concentration occurs after ca. 400 h. This deviation from linear FFC area kinetics seems to contradict a published study on the FFC of PVB coated commercially pure Mg [6]. However, it should be taken into consideration that the aforementioned investigation [6] of pure Mg FFC kinetics was carried out over a significantly shorter timescale and that only a single, high chloride ion concentration was employed. Initial linear rates of FFC area propagation were also found to depend on the number of moles of chloride ions used to initiate underfilm corrosion. After converting $[MgCl_2]$ values to the μmol quantity of Cl⁻ ions applied to the defect (N_{Cl^-}), the initial rate of FFC area propagation (dA/dt) was shown to obey the following empirical relationship:

$$dA/dt = A + B \log_{10}(N_{Cl^-}) \tag{5.4}$$

with a slope (B) of 0.14 $mm^2\,h^{-1}$ per decade over a 2 order of magnitude range, and a value of A (equating to the FFC rate measured at 1 μmol applied Cl⁻ ions) of 0.36 $mm^2\,h^{-1}$. The logarithmic dependence of dA/dt with N_{Cl^-} differs considerably from predicted relationships derived elsewhere [16] using data derived from a systematic study of the influence of the quantity of hydrochloric acid used to initiate FFC on PVB coated AA2024-T3 alloy specimens. In this particular investigation, dA/dt was predicted to vary as a function $N_{Cl^-}^{-2/3}$ for a surface-controlled electrochemical process and $N_{Cl^-}^{-1/3}$ for a system under ohmic control for an equivalent number of individual filaments propagating from a penetrative coating defect to which a controlled quantity of HCl was applied. The lower sensitivity of dA/dt upon N_{Cl^-} observed for E717 Mg surfaces, implied by the logarithmic relationship, suggests that the assumption of complete Cl⁻ ion conservation within the filament head electrolyte made previously in deriving dA/dt vs. N_{Cl^-} relationships, do not hold true for this alloy.

Indeed, the evidence of significant Cl⁻ ion sequestration within the corrosion product filled tail regions given in Figure 5.4, suggests that a substantial fraction of the N_{Cl^-} used to initiate corrosion is removed progressively from the leading edges of the FFC tracks as they propagate, via entrapment within insoluble magnesium hydr(oxide) underfilm deposits or by reaction with the latter to form sparingly soluble magnesium hydroxychloride compounds [30].

The relative insensitivity of dA/dt on N_{Cl^-} observed here, compared to previous FFC kinetic investigations [16], suggests that the rate of Cl^- ion removal from the underfilm head electrolyte increases with N_{Cl^-}, giving rise to the empirically-derived logarithmic dependence given in Equation (5.4).

In addition, the deviation from linearity of the FFC area versus time plots shown in Figure 5.7 is again consistent with Cl^- ion depletion from the head electrolyte, which will eventually cause filament propagation to cease (at low N_{Cl^-}) or tend to a lower gradient (at higher N_{Cl^-}). The observation that the time at which the inflection in dA/dt gradients occurs increases with N_{Cl^-} also supports the theory that Cl^- ions become progressively lost from the head electrolyte of filament populations. At low N_{Cl^-}, corresponding with the most dilute initiating $[MgCl_2]$ of 5×10^{-3} M employed, plot i in Figure 5.7 may be understood in terms of the corroded area increasing linearly with time as several discrete filaments shown in Figure 5.6a (ca. 0.1 – 0.3 mm width) propagate away from the defect at a mean elongation rate (dL/dt) of 0.05 mm h^{-1} over a holding time of up to 100h. However, during this time, filaments become visibly narrower and as their widths decrease below 0.1 mm at t > 100 h, their forward motion ceases.

At the point where all filaments have stopped propagating, then dA/dt (Figure 5.7i) becomes zero. The same analysis of individual filaments propagating at a higher initiating $[MgCl_2]$ of 0.02 M exhibited similar mean velocity values of 0.06 ± 0.01 mm h^{-1}. In addition, filament widths were also seen to decrease by up to 50% over a holding period of 200 h, typically from initial values of ca. 0.5 mm, although for this higher initiating $[MgCl_2]$, the filaments analysed did not cease to propagate. It can therefore be concluded that varying N_{Cl^-} does not produce significant changes in individual filament velocity and that the increase in dA/dt observed with increasing N_{Cl^-} is principally due to a progressively higher number of individual filaments that coalesce to form larger unified underfilm corrosion features. The obvious decreases in dA/dt observed at protracted holding times in plots i – iv of Figure 5.7 are caused by a progressive removal of Cl^- from the electrolyte filled filament heads, which eventually cause de-activation of individual filaments (plot i) and/or decrease in the filament widths with time.

5.3.3 The Effect of Varying Relative Humidity and the Absence of Oxygen

Previous studies have shown that the availability and the activity of water at the coating/metal interface is an important controlling factor in the propagation rate of FFC on organic coated pure Mg samples [6]. In the present study, the influence of relative humidity (RH) on FFC corrosion of PVB coated E717 was investigated by varying the relative humidity in the holding environment using saturated salt solutions. The rate of filament propagation was studied using 5 different relative humidity levels of 31%, 53%, 76%, 93% and 99% at a constant temperature of 20°C. The inoculation of the FFC corrosion was achieved by applying 1 µl of 0.5 M $MgCl_2$ in a penetrative coating defect and the appearance of the samples after 21 days of exposure at varying humidity levels are presented in Figure 5.8. From Figure 5.8, it is evident that both the lowest and the highest levels of RH did not produce filiform corrosion. The lowest humidity of 31% produced no obvious underfilm corrosion as it can be observed from Figure 5.8a, whereas the highest level of humidity mostly resulted in blistering rather than features, which could be identified as FFC (Figure 5.8e). The samples exposed to the intermediate levels of relative humidity in the range 53% – 93% (Figure 5.8b–d) produced significant FFC in the immediate vicinity of the penetrative defect. The plots of FFC affected area as a function of holding time were determined by analysing the photographic time-lapse sequences as previously described and are given in Figure 5.9.
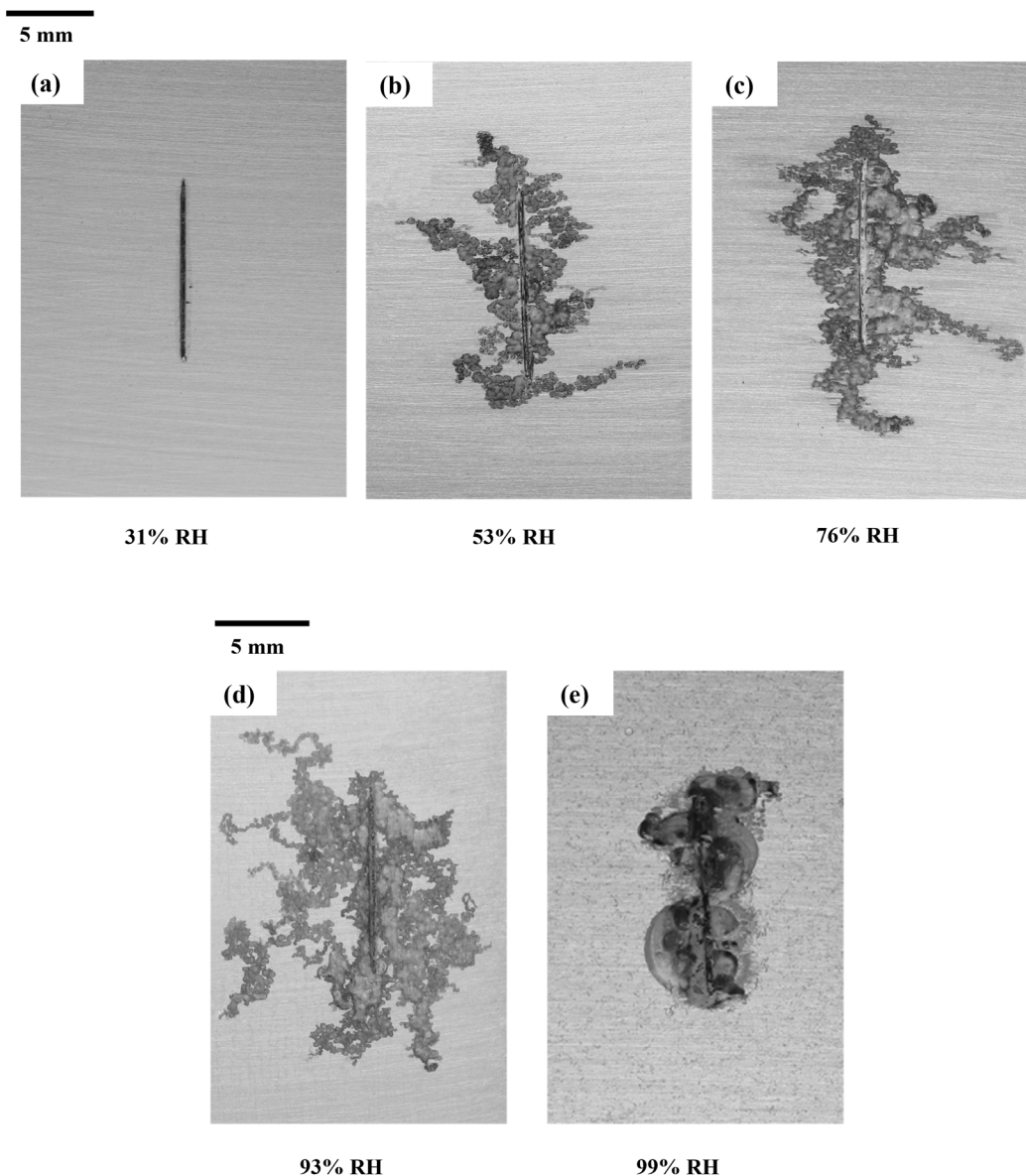
Figure 5.8: Photographic images of the appearance of FFC on PVB coated E717 alloy kept in air at 20°C and a constant RH of (a) 31%, (b) 53%, (c) 76%, (d) 93%, (e) 99% for 500 h following corrosion initiation using 1 μl of 0.5 M $MgCl_2$ (aq).

In literature, it has been suggested that the main constituent of the electrolyte conserved at the filament head in FFC of organic coated Mg is concentrated $MgCl_2$ (aq) electrolyte [6]. This was borne out of the fact that the reported deliquescence point of $MgCl_2$ is 33% RH [25] and that no Mg FFC was observed when PVB coated pure Mg samples were exposed to relative humidity

levels < 31%, [6]. Plot i in Figure 5.9 shows that PVB coated E717 behaves in the same manner, again providing supporting evidence that indeed $MgCl_2$ (aq) is the principal constituent of the electrolyte in FFC head regions.
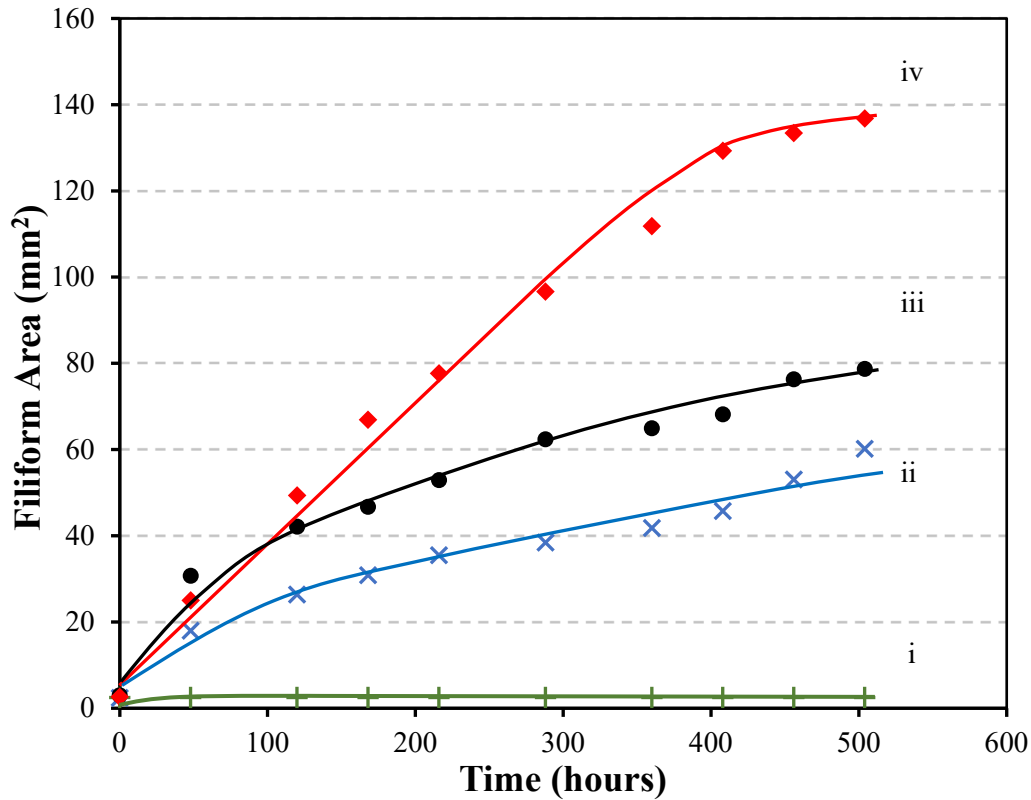
Figure 5.9: Plots of FFC area versus time determined for a PVB coated E717 alloy held in air at 20°C and a fixed RH of (i) 31%, (ii) 53%, (iii) 76%, (iv) 93% following corrosion initiation using 1 μl of 0.5 M $MgCl_2$ (aq).

As indicated by the SEM-EDX images in Figure 5.4, there is a significant abundance of chloride ions present in the head of the filaments where anodic Mg dissolution occurs as per Reaction (5.1). The production of Mg^{2+} (aq) from Reaction (5.1), along with the conservation of Cl^- supplied by the injected electrolyte, will combine to produce a concentrated aqueous $MgCl_2$ at the anodic leading edge. It would be expected that the highly deliquescent nature of $MgCl_2$ at RH >31% would cause water to be drawn to the head of the filament via osmosis [6]. However, as relative humidity is increased, it would be expected that the concentration of $MgCl_2$ electrolyte within the

filament head would become progressively dilute in order to maintain isopiestic equilibrium with the holding environment. At high RH (>99%), it appears that the head electrolyte composition is unable to support the propagation of filiform-like features and consequently underfilm corrosion takes the form of blistering (Figure 5.8e). This transition from FFC to blistering at high RH is consistent with behaviour observed previously on other organic coated metallic substrates to anodic disbondment phenomena [7–9,14]. In the range 31% < RH > 99%, the influence of varying RH is broadly similar to previously reported results obtained over a shorter exposure times for commercially pure Mg in the presence of model PVB coatings [6], where increasing filament propagation rates with RH was directly linked with the availability of water and its transport to the underfilm electrolyte.

In this chapter using E717 Mg substrates, a progressive rise in RH from 53% to 93%, (Figure 5.9, plots ii–iv) produced an increase in dA/dt from 0.094 to 0.29 $mm^2\,h^{-1}$, measured over the first 400 h of exposure. In terms of final corroded areas after the full 500 h holding time, RH values of 53, 76 and 93% produced FFC areas of 60, 80 and 140 mm^2 respectively surrounding each penetrative coating defect. An increase in the rate of FFC propagation with RH would be expected, given that the principal underfilm cathodic reaction is water reduction according to Reaction (5.1). However, for a fixed N_{Cl^-}, it would also be anticipated that a rise of humidity would also cause the concentration of underfilm $MgCl_2$ (aq) electrolyte within the FFC head regions to become progressively more dilute, in order to maintain isopiestic equilibrium with the holding environment. At first sight, the observation of increasing values of dA/dt with RH seems contradictory with the progressive dilution of [$MgCl_2$] at the filament leading edges. However, it should also be noted that for a constant N_{Cl^-}, there would also be a corresponding increase in underfilm electrolyte volume and hence the area of underlying substrate in contact with corrosive electrolyte. As such, providing that the head [$MgCl_2$] does not drop below a threshold level required for active propagation, the observation of increased dA/dt with RH can be understood in terms of a progressive increase in underfilm electrolyte area of contact with the E717 substrate.

As discussed previously in Section 5.3.2, the kinetics of FFC area propagation at 93% RH (Figure 5.9iv) shows a slight divergence from linearity at protracted holding times. This suggests that the higher rates of propagation may lead to a more rapid exhaustion of the available soluble chlorides from the underfilm electrolyte. This divergence from linearity is not observed for samples

subjected to lower levels of relative humidity (Figure 5.9ii and iii). The observation seems to be consistent with the notion of a more concentrated $MgCl_2$ (aq) underfilm electrolyte at lower RH, which in turn would take longer to become depleted of Cl^- ions to reach a threshold concentration at which filament propagation cannot be sustained. Although water reduction (Reaction (5.1)) is commonly regarded as the predominant cathode reaction on corroding Mg alloy surfaces, Chapter 4 and other recent investigations under both immersion and atmospheric corrosion conditions have demonstrated that oxygen reduction can provide a contribution to the overall cathodic process [31,32]. In order to ascertain the role of oxygen in the FFC of organic coated Mg alloys, a PVB coated E717 sample was placed in a chamber without oxygen (i.e., held in a humidified N_2 flow) and high relative humidity (93%) and underfilm corrosion was initiated as previously using 1 μL of 0.5 M $MgCl_2$ (aq). This experimental set-up is similar to the one used for the oxygen-free experiments in Chapter 3. The FFC kinetics obtained from this experiment are plotted in Figure 5.10 using a corroded area versus time axes and are compared with an experiment carried out in air using the same RH, temperature and initiating [$MgCl_2$]. The similarity of both plots indicates that the absence of O_2 has little effect on the FFC area propagation rate and in this respect is consistent with observations made previously for filament advance on commercially pure Mg [6].
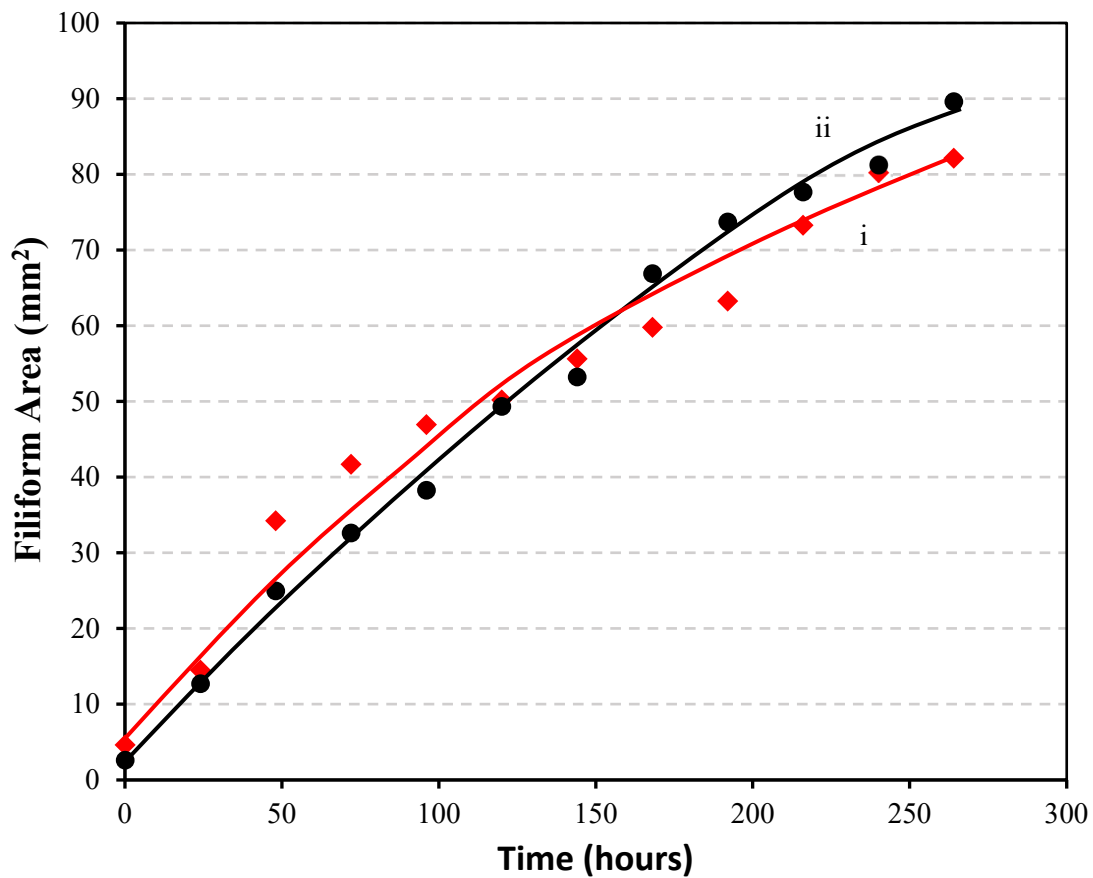
Figure 5.10: Plots of FFC area versus time for a PVB coated E717 alloy held at 20°C and 93% RH in (i) air and (ii) nitrogen following corrosion initiation using 1 μl of 0.5 M MgCl$_2$ (aq).

The insensitivity of filiform advance on E717 substrates to the presence of oxygen confirms the statement that differential aeration does not play a role in the underfilm FFC corrosion cell, as is the case for other metals such as Fe and Al [8,11,14]. It is therefore proposed the filament advance on E717 substrates is similar the one described in the literature for pure Mg [6] involving anodic undermining at the leading edge, driven by cathodic hydrogen evolution on an electro-catalytically enhanced corroded surface at the rear of the electrolyte filled head region.

5.3.4 FFC of Organic Coated AZ-Series Mg Alloys

To further understand the filiform corrosion phenomenon on organic coated Mg alloys, two more Mg alloys were employed in this chapter, namely the AZ31 and the AZ91 Mg alloy. The presence of Al makes these alloys microstructurally different to E717 due to the formation of Al-containing secondary phases and precipitates in the Mg matrix. The presence of principal secondary phases such as $Mg_{17}Al_{12}$ (β-phase) in AZ91 [33,34] and Al–Mn (Al_8Mn_5) intermetallic particles [35] in AZ31 play an important role in the corrosion behaviour of these alloys. In Chapter 4, it was found that the AZ91 Mg alloy is less susceptible to cathodic delamination compared to the other Mg alloys and this was presumed to be due the presence of high Al additions. However, there is debate in the literature on whether the corrosion resistance of Mg increases or decreases with higher Al content when un-coated samples are immersed in corrosive aqueous solutions. It has been suggested that the relative nobility of the $Mg_{17}Al_{12}$ phase formed in the microstructure of the AZ91 compared to the matrix can enhance the cathodic activity, hence reducing the corrosion resistance of the Mg alloy [36–39]. However, others researchers have stated that the high additions of Al can also improve the corrosion resistance of Mg in water by enriching the surface film with Al [40–43] and/or the β phase (if present) can act as an inert barrier [44,45].

Using the same methodology to initiate underfilm corrosion as with the PVB-coated E717, 1 µL of 0.5 M $MgCl_2$ (aq) was applied to the penetrative scribes and the visual evidence of the filiform corrosion produced on organic coated AZ31 and AZ91 after 15 days of exposure to 93% relative humidity and 20°C are presented in Figure 5.11. As in the case of E717, the use of both equivalent quantities of HCl (aq) or $FeCl_2$ (aq) to initiate FFC produced entirely similar results for both AZ alloy types as it can be seen from Figure 5.11. By analysing the photographic time-lapse sequences as previously described, the plots of FFC affected area as a function of holding time were determined for these two alloys and the results are provided in Figure 5.12 along with the area versus time plot for E717 under identical conditions for comparison purposes.
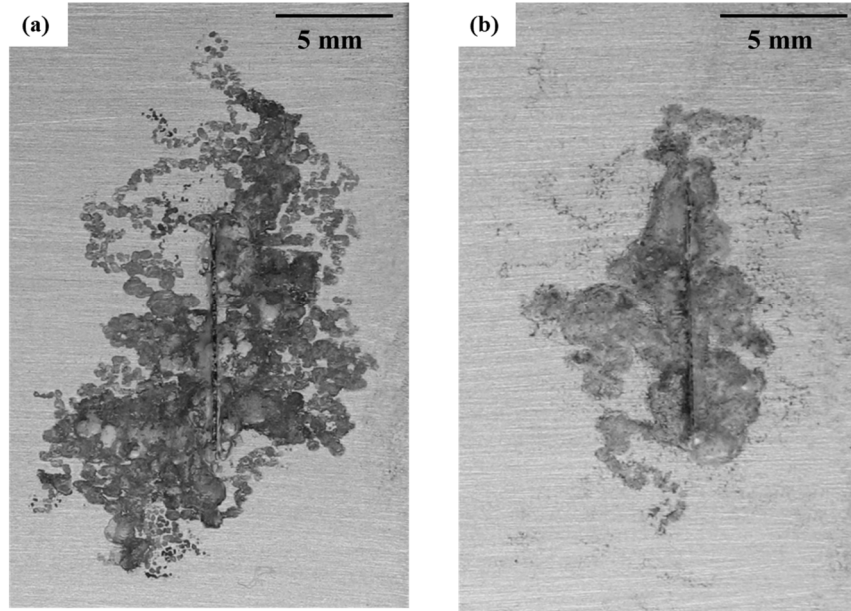
Figure 5.11: Photographic images of the appearance of FFC on PVB coated (a) AZ31 and (b) AZ91 samples, 360 h after initiation of corrosion using 1 µl of 0.5 M $MgCl_2$ and holding in air at 93% RH and 20°C.
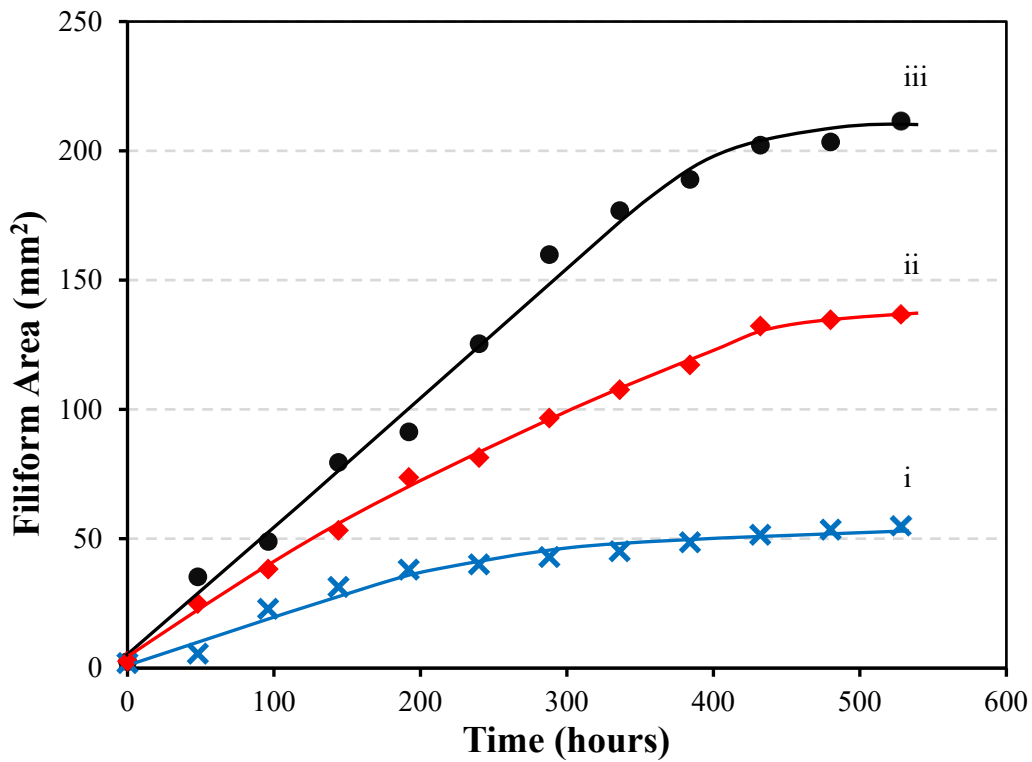
Figure 5.12: Plots of FFC area versus time for PVB coated (i) AZ91, (ii) E717 and (iii) AZ31 samples after initiation of underfilm corrosion using 1 µl of 0.5 M $MgCl_2$ and holding in air at 93% RH and 20°C.

The AZ31B appears to be the most susceptible to FFC, (dA/dt of 0.5 mm^2 h^{-1} over 400 h), compared to E717 where a dA/dt slope of 0.29 mm^2 h^{-1} was determined over the same holding time. The AZ91 surface was the most resistant to FFC advance, characterised by a dA/dt value of 0.13 mm^2 h^{-1} measured under identical conditions. This latter observation tends to support that the presence of a more corrosion resistant $Mg_{17}Al_{12}$ (β-phase) along the grain boundaries, can act as a barrier surrounding the α-matrix [33,45], impeding filament advancement when compared to alloys where this phase is absent. This is postulated to be due to the filament preferentially following the less corrosion resistant α grains and if the nobler β-phase is in its pathway, which is more corrosion resistant, [33,34,45] the filament is expected to require longer time to transverse this "barrier" or the filament will be completely blocked and then it will follow the path of least resistance.

Taking together all the findings discussed herein, a schematic diagram representing the mechanism of atmospheric FFC on organic coated Mg alloys is proposed in Figure 5.13. Also shown is the correlation of a typical SKP-derived E_{corr} versus distance profile with the principal features of the underfilm FFC anodic delamination cell. The mechanism is similar to the mechanism of atmospheric FFC on organic coated pure Mg [6], where anodic attack of the alloy surface at the filament leading edge produces a cathodically enhanced corroded surface, which becomes the principal cathode region during filament advance. Although chloride ions are conserved within the head electrolyte due to migration to the anodic leading edge in order to preserve electroneutrality, the findings of this investigation demonstrate that a significant fraction becomes progressively removed via entrapment in the corrosion product-filled filament tail. Consequently, once chloride ion concentration within the head electrolyte decreases below a threshold level capable of sustaining sufficient underfilm corrosion cell current to maintain filament advance, then the filament will de-activate.
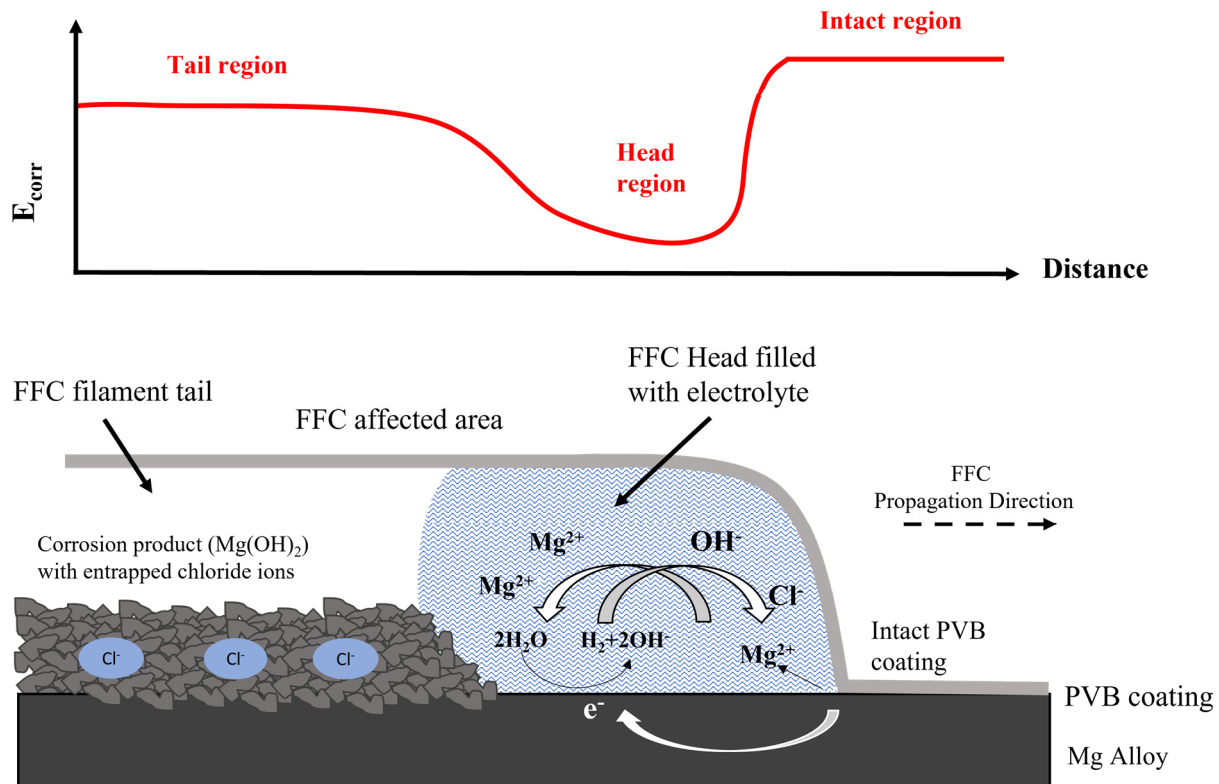
Figure 5.13: Schematic diagram of the proposed FFC corrosion mechanism occurring on organic coated Mg alloys with correlation to a typical SKP-derived E_{corr} versus distance profile.

5.4 Conclusions

In this chapter it was shown that all organic coated Mg alloys are susceptible to filiform corrosion (FFC) as exemplified by the behaviour of PVB coated E717 alloy where underfilm corrosion was initiated by applying different aqueous electrolytes including $MgCl_2$, HCl and $FeCl_2$ to a penetrative coating defect. Once FFC has become established, the FFC propagation rates do not seem to be significantly dependent on the initiating cation.

In order to map the free corrosion potentials (E_{corr}) associated with regions of PVB-coated E717 surfaces affected by FFC the SKP technique was utilised. It was shown that the leading edge of the filament tracks adopt local E_{corr} values of -1.3 ± 0.05 V vs. SHE, while typical values of ca. -1.1 V vs. SHE are obtained over the uncorroded surface. E_{corr} values measured over filament tail regions, left behind the advancing anodic leading edges, are typically 100 mV more negative than the surrounding intact surface.

By time-dependent analysis of corrosion-affected areas via time-lapse photography, the FFC kinetics were obtained and it was observed that the FFC propagation rate is dependent on the number of moles of Cl^- ions (N_{Cl^-}) used to initiate underfilm corrosion. The initial rate of growth of FFC affected areas (dA/dt) was shown to increase as a function of $log_{10}N_{Cl^-}$. At longer exposure times, dA/dt slopes decreased significantly and the time at which an inflection in the area versus time plot was observed, progressively lengthened with increasing N_{Cl^-} This behaviour is attributed to the depletion of the chloride ions from the filament head electrolyte by entrapment within corrosion product deposits in the tail regions left behind the advancing FFC leading edge. This was confirmed by using SEM-EDX, where chloride ion mapping showed high abundance at individual filament leading edges, but also within areas corresponding to the dark corrosion product filled tails.

Additional experiments to investigate the effect of relative humidity on the FFC of PVB coated Mg alloys were conducted in the range of 31 – 93% RH in air. From this series of experiments, it was found that by increasing the levels of relative humidity in air produced progressively greater rates of FFC propagation, with maximum dA/dt rates measured at 93%. Furthermore, no FFC propagation was observed for samples subjected to RH<31%, corresponding to the deliquescence point of $MgCl_2$, whereas exposure to 99% RH produced a blistering phenomenon. From the aforementioned results, it can be concluded that the water availability in the holding environment plays an important role in the FFC of coated Mg alloys. Additionally, experiments carried out both in the absence and presence of oxygen revealed that the rate of FFC propagation was insensitive to oxygen, since rates of FFC advance were found to be similar in both cases.

Finally, the FFC behaviour of other technologically important AZ31 and AZ91 series Mg alloys was investigated. Results showed that both PVB coated alloys produced FFC in a similar manner to E717, although propagation rates measured under identical conditions were greater for AZ31, while AZ91 showed the highest resistance to FFC advance.

5.5 References

[1] R.C. Zeng, J. Zhang, W.J. Huang, W. Dietzel, K.U. Kainer, C. Blawert, W. Ke, Review of studies on corrosion of magnesium alloys, Trans. Nonferrous Met. Soc. China (English Ed. 16 (2006).

[2] R.-G. Hu, S. Zhang, J.-F. Bu, C.-J. Lin, G.-L. Song, Progress in Organic Coatings: Recent progress in corrosion protection of magnesium alloys by organic coatings, Prog. Org. Coatings. 73 (2011) 129–141.

[3] S. Song, G.-L. Song, W. Shen, M. Liu, Corrosion and electrochemical evaluation of coated magnesium alloys, Corrosion. 68 (2012) 15005–15012.

[4] M. Van Loo, D.D. Laiderman, R.. Bruhn, Filiform Corrosion, Corrosion. 9 (1953) 277–283.

[5] G.M. HOCH, A review of filiform corrosion(Filiform corrosion of steel, magnesium and aluminum coated and uncoated surfaces in humid and corrosive atmospheres), in: Natl. Assoc. Corros. Eng. Int. Conf. Localized Corros. Williamsburg, Va, 1971: p. 1971.

[6] G. Williams, R. Grace, Chloride-induced filiform corrosion of organic-coated magnesium, Electrochim. Acta. 56 (2011) 1894–1903.

[7] W. Funke, Blistering of paint films and filiform corrosion, Prog. Org. Coatings. 9 (1981) 29–46.

[8] H.N. Mcmurray, G. Williams, Under Film/Coating Corrosion, Shreir's Corros. 2 (2010) 988–1004.

[9] B. Liu, Y. Wei, W. Chen, L. Hou, C. Guo, Blistering failure analysis of organic coatings on AZ91D Mg-alloy components, Eng. Fail. Anal. 42 (2014) 231–239.

[10] C.F. SHARMAN, Filiform nderfilm corrosion of lacquered steel surfaces, Nature. 153 (1944) 621.

[11] R.T. Ruggeri, T.R. Beck, An analysis of mass transfer in filiform corrosion, CORROSION. 39 (1983) 452–465.

[12] C. Hahin, Localised Corrosion, in: Met. Handb. Corros. Ed. SC Dexter, Am. Soc. Met. Met. Park. OH, 9th ed., 1987: pp. 104–122.

[13] G. Williams, H.N. McMurray, The mechanism of group (I) chloride initiated filiform corrosion on iron, Electrochem. Commun. 5 (2003) 871–877.

[14] A. Bautista, Filiform corrosion in polymer-coated metals, Prog. Org. Coatings. 28 (1996) 49–58.

[15] W. Schmidt, M. Stratmann, Scanning kelvinprobe investigations of filiform corrosion on aluminum alloy 2024-t3, Corros. Sci. 40 (1998) 1441–1443.

[16] G. Williams, H.N. McMurray, The kinetics of chloride-induced filiform corrosion on aluminum alloy AA2024-T3, J. Electrochem. Soc. 150 (2003) B380–B388.

[17] T.M. Watson, A.J. Coleman, G. Williams, H.N. McMurray, The effect of oxygen partial pressure on the filiform corrosion of organic coated iron, Corros. Sci. 89 (2014) 46–58.

[18] M.P. Brady, W.J. Joost, C.D. Warren, Insights from a recent meeting: current status and future directions in magnesium corrosion research, CORROSION. 73 (2017) 452–462.

[19] X.P. Niu, T. Skszek, M. Fabischek, A. Zak, Low temperature warm forming of magnesium ZEK 100 sheets for automotive applications, Mater. Sci. Forum. 783–786 (2014) 431–436.

[20] R.M. Asmussen, W.J. Binns, P. Jakupi, D. Shoesmith, The influence of microstructure on the corrosion of magnesium alloy ZEK100, Corrosion. 71 (2014) 242–254.

[21] M.P. Brady, G. Rother, L.M. Anovitz, K.C. Littrell, K.A. Unocic, H.H. Elsentriecy, G.-L. Song, J.K. Thomson, N.C. Gallego, B. Davis, Film breakdown and nano-porous $Mg(OH)_2$ formation from corrosion of magnesium alloys in salt solutions, J. Electrochem. Soc. 162 (2015) C140–C149.

[22] M.P. Brady, D.N. Leonard, H.M. Meyer, J.K. Thomson, K.A. Unocic, H.H. Elsentriecy, G.-L. Song, K. Kitchen, B. Davis, Advanced characterization study of commercial conversion and electrocoating structures on magnesium alloys AZ31B and ZE10A, Surf. Coatings Technol. 294 (2016) 164–176.

[23] B. Zaghloul, J.R. Kish, Corrosion inhibition of Mg alloy ZEK100 sheet metal by dissolved

lithium carbonate, J. Electrochem. Soc. 168 (2021) 81507.

[24]   L. Greenspan, Humidity fixed points of binary saturated aqueous solutions, J. Res. Natl. Bur. Stand. (1934). 81 (1977) 89–96.

[25]   R.. Weast, CRC Handbook of Chemistry and Physics, 69th ed., CRC Press, Boca Raton, FL, 1987.

[26]   E. Michailidou, H.N. McMurray, G. Williams, Quantifying the role of transition metal electrodeposition in the cathodic activation of corroding magnesium, J. Electrochem. Soc. 165 (2018) C195–C205.

[27]   M.-C. Zhao, M. Liu, G.-L. Song, A. Atrens, Influence of pH and chloride ion concentration on the corrosion of Mg alloy ZE41, Corros. Sci. 50 (2008) 3168–3178.

[28]   L. Wang, T. Shinohara, B.-P. Zhang, Influence of chloride, sulfate and bicarbonate anions on the corrosion behavior of AZ31 magnesium alloy, J. Alloys Compd. 496 (2010) 500–507.

[29]   G. Williams, H. Ap Llwyd Dafydd, R. Subramanian, H.N. McMurray, The influence of chloride ion concentration on passivity breakdown in magnesium, Corrosion. 73 (2017) 471–481.

[30]   C. Mažuranić, H. Bilinski, B. Matković, Reaction products in the system MgCl2-NaOH-H2O, J. Am. Ceram. Soc. 65 (1982) 523–526.

[31]   E.L. Silva, S. V Lamaka, D. Mei, M.L. Zheludkevich, The reduction of dissolved oxygen during magnesium corrosion, ChemistryOpen. 7 (2018) 664–668.

[32]   M. Strebl, S. Virtanen, Real-time monitoring of atmospheric magnesium alloy corrosion, J. Electrochem. Soc. 166 (2019) C3001–C3009.

[33]   O. Lunder, J.E. Lein, T.K. Aune, K. Nisancioglu, The role of Mg17Al12 phase in the corrosion of Mg alloy AZ91, CORROSION. 45 (1989) 741–748.

[34]   M. Jönsson, D. Thierry, N. LeBozec, The influence of microstructure on the corrosion behaviour of AZ91D studied by Scanning Kelvin Probe force microscopy and Scanning Kelvin Probe, Corros. Sci. 48 (2006) 1193–1208.

[35] G. Hamu, D. Eliezer, L. Wagner, The relation between severe plastic deformation microstructure and corrosion behavior of AZ31 magnesium alloy, J. Alloys Compd. 468 (2009) 222–229.

[36] G.-L. Song, Recent progress in corrosion and protection of magnesium alloys, Adv. Eng. Mater. 7 (2005) 563–586.

[37] G. Song, A. Atrens, X. Wu, B. Zhang, Corrosion behaviour of AZ21, AZ501 and AZ91 in sodium chloride, Corros. Sci. 40 (1998) 1769–1791.

[38] A. Samaniego, I. Llorente, S. Feliu, Combined effect of composition and surface condition on corrosion behaviour of magnesium alloys AZ31 and AZ61, Corros. Sci. 68 (2013) 66–71.

[39] I.B. Singh, M. Singh, S. Das, A comparative corrosion behavior of Mg, AZ31 and AZ91 alloys in 3.5% NaCl solution, J. Magnes. Alloy. 3 (2015) 142–148.

[40] J.H. Nordlien, K. Nişancioglu, S. Ono, N. Masuko, Morphology and structure of oxide films formed on MgAl alloys by exposure to air and water, J. Electrochem. Soc. 143 (1996) 2564–2572.

[41] J.H. Nordlien, K. Nişancioglu, Morphology and Structure of Water-Formed Oxides on Ternary MgAl Alloys, J. Electrochem. Soc. 144 (1997) 461.

[42] S. Mathieu, C. Rapin, J. Steinmetz, P. Steinmetz, A corrosion study of the main constituent phases of AZ91 magnesium alloys, Corros. Sci. 45 (2003) 2741–2755.

[43] M. Danaie, R.M. Asmussen, P. Jakupi, D.W. Shoesmith, G.A. Botton, The role of aluminum distribution on the local corrosion resistance of the microstructure in a sand-cast AM50 alloy, Corros. Sci. 77 (2013) 151–163.

[44] O. Lunder, J.E. Lein, T.K. Aune, K. Nisancioglu, The Role of Mg17Al12 Phase in the Corrosion of Mg Alloy AZ91, CORROSION. 45 (1989) 741–748.

[45] M.C. Zhao, P.J. Uggowitzer, M. Liu, P. Schmutz, G. Song, A. Atrens, Corrosion of AZ91 - Influence of the β-phase morphology, in: Mater. Sci. Forum, 2009.

Chapter 6

The Influence of Chloride Ion Concentration on the Localised Corrosion of E717 Mg Alloy

The Influence of Chloride Ion Concentration on the Localised Corrosion of E717 Mg Alloy

6.1 Introduction

In the previous chapters, organic coated E717 Mg alloys were investigated with the aim of elucidating the mechanisms of corrosion-driven coating failures. These chapters showcased that organic coated E717 Mg alloys are susceptible to coating delamination and filiform corrosion depending on the type of cation present in the initiating solution. The work presented in Chapter 5 demonstrated that the propagation rate of filiform corrosion under an organic coated E717 is dependent on the number of moles of Cl⁻ ions used to initiate underfilm corrosion. In this chapter, the principal aim is to determine how the chloride concentration influences the localised corrosion of uncoated E717 Mg alloys in bulk solutions by using a combination of conventional potentiostat-based studies along with in-situ Scanning Vibrating Electrode Technique (SVET) analysis of E717 in a range of chloride-containing electrolytes.

The E717 (Electron^{TM} 717) Mg alloys contain small quantities of the rare earth element Neodymium (Nd), along with Zirconium (Zr) and Zinc (Zn). Mg alloys containing Rare Earth (RE) elements have been the centre of interest lately due to the beneficial effect of the RE additions on both mechanical properties and corrosion resistance of Mg alloys. As it was mentioned in the Chapter 1, RE additions can improve the creep resistance [1,2] of Mg alloys and from a corrosion perspective they have the useful advantage of improving grain refinement [3–6], which in turn is proposed to reduce corrosion rate by limiting the size of noble β phase particles, such as Fe rich particles. Recent comparative studies of widely used AZ alloy types with prototype alloys of similar composition to E717 [7,8] have demonstrated improved corrosion resistance, which the authors attribute to a decreased cathode-to-anode area ratio within the microstructure of these alloys and a lower difference in the relative nobility between the principal second phases and the Mg matrix.

Recent investigations of E717 corrosion behaviour in more conventional, unbuffered sodium chloride aqueous test solutions demonstrated that the alloy is affected by filiform-like corrosion [9,10], which takes the form of discrete individual tracks at low Cl⁻ concentration, but covers

significantly larger areas of the exposed surface at higher concentration [9]. Scanning electron microscopy-based investigation of the microstructure identified several intermetallic phase type, including tertiary Mg–Zn–Nd (T-phase), Zn–Zr and Fe-containing Zr along with discrete Zr particles [9]. From experiments carried out in pure water, it was concluded that the Fe-containing Zr particles acted as local cathode sites during the corrosion of E717 alloy. Others have studied the influence of chloride ions concentration on the properties of the surface film formed on E717 under immersion conditions [11,12]. In comparison to a dense bilayered film, consisting of an inner MgO layer and an outer $Mg(OH)_2$ film formed in water, the presence of high Cl⁻ concentration produces a significantly thicker, nano porous outer layer [11]. Chloride ion penetration into the inner MgO-base layer was detected at high concentrations of $\geq 1\%$ w/v by using a combination of SEM and STEM, but not after immersion in more dilute concentration of 0.01% w/v [12], although the authors report a different growth mechanism within the dense MgO base layer.

From the current scientific literature dealing with the corrosion of E717, it is evident that relatively little electrochemical characterisation of its corrosion behaviour has been carried out to date. In this chapter the intention is twofold; firstly to determine the influence of chloride concentration on the breakdown of temporary passivity in E717 and secondly determine its effect on the kinetics of previously observed filiform-like corrosion [9] along with the magnitude of current density distributions associated with this phenomenon. Filiform-like corrosion is known to propagate on several technologically important Mg alloys, such as AZ31 [13–15], AZ61 [14] and AZ91 [13,16] alloy and is also observed for commercially pure Mg in certain inter-related chloride ion concentration and pH ranges [17–19].

SVET has been used in several previous studies to visualise the localised corrosion features connected with filiform-like corrosion initiation and propagation [15,18–22]. In most of these investigations, the leading edges of the filiform tracks are shown to be intense local anodes, while the remainder of the dark surface left behind is cathodically activated with respect to the intact surface. For commercial purity Mg, the cathodic activation of the previously corroded surface is thought to originate from accumulation of iron rich impurity phases caused by the dissolution of the Mg matrix [18,19,22]. There is also significant evidence that suggests a contribution due to re-plating of iron ions generated by self-corrosion of impurity particles that become electrically

detached from the matrix [22–24]. In the case of filiform-like corrosion affecting AZ31, an accumulation of noble Al–Mn–(Fe) has been suggested as the principal cause of enhanced cathodic activity [15]. By using a similar approach, the work described here seeks to confirm whether this type of localised corrosion mechanism occurs for freely corroding E717 alloy surfaces and how the [Cl⁻] influences the characteristics of any observed localised corrosion. The current study was conducted by using in-situ SVET coupled with time-lapse imaging (TLI), which enables simultaneous correlation of visual macroscopic corrosion features with corresponding current density distribution maps. This combination of methods has recently been employed in a recent investigation of localised corrosion behaviour of zinc alloy coated steel [25].

A final aim of this chapter is to determine the influence of chloride ion concentration on the initiation of localised corrosion of E717. Several previous studies have employed combinations of potentiodynamic polarisation, hydrogen evolution measurements and electrochemical impedance spectroscopy (EIS) to quantify the effect of changes in [Cl⁻] and pH on the corrosion behaviour of various Mg alloys [26–30]. Typically, these works indicate that increasing [Cl⁻] produces higher rates of corrosion, but do not address the relationship between corrosion initiation resulting from the breakdown of temporary passivity and the [Cl⁻] of the electrolyte. Recent published work, using a new method of establishing a breakdown potential (E_b) value for both pure Mg and AZ31 alloy by monitoring time-dependent free corrosion potential behaviour [31], demonstrated that E_b varied as a function of $\log_{10}[Cl^-]$. The findings obtained under freely corroding conditions were confirmed using conventional potentiodynamic experiments for the same specimens immersed at elevated pH, where well-developed passive regions were observed in the anodic branches of their polarisation curves. In the current chapter, the same combination of methodologies was used to investigate whether a similar relationship linking E_b to [Cl⁻] also exists for E717 immersed in different chloride-containing electrolytes.

————————————————

6.2   Experimental Details

6.2.1   Materials and Sample Preparation

In this chapter two Mg alloys were used, the E717(Electron^{TM} 717) and the AZ31. More information about these Mg alloys is given in Section 2.1.1. The samples were cut into 50 mm square coupons and prior to any experimentation they were prepared in the same way as it is described in Section 2.1.3.

The Scanning Vibrating Electrode Technique – Time-Lapse Imaging (SVET-TLI) experiments were performed as described in Section 2.4 where a detailed description of the SVET-TLI instrumentation, calibration and set-up methodology is given. In brief, the SVET measurements were conducted using a 125 μm diameter platinum microdisk electrode encased in a glass sheath, vibrating at a frequency of 140 Hz. The combination of SVET and TLI was achieved using a waterproof endoscope (Supereyes Y002), which was attached to the SVET probe vibrator assembly, as described elsewhere, enabling simultaneous capture of current density maps with corresponding photographic images. The SVET probe scanned areas of 36 mm^2 (5 data points per mm) at a probe-to-sample height of 100 μm and the SVET scans were performed immediately following immersion at intervals of 10 min for periods of up to 24 h, taking 144 scans in total and each SVET scan taking around 5 min to complete. The electrolytes used in these SVET-TLI experiments were 0.034 M, 0.17 M and 0.86 M aerated aqueous NaCl solutions.

The quantification of the area occupied by dark corrosion product was performed using Adobe Photoshop and ImageJ. After setting the measurement scale and calibrating each image, the black corroded areas were highlighted using the colour intensity function available in both software. The areas occupied by the dark corrosion product were then measured using the automatic measurement feature embedded into the software.

The open circuit potential (OCP) experiments were performed using a two-electrode setup and the potentiodynamic polarisation measurements were carried out using a three-electrode setup in conjunction with a Solartron 1280B Workstation. The setup consisted of a saturated calomel (SCE) reference electrode and a 1 cm^2 area platinum gauge as a counter electrode. These experiments were performed in a range of NaCl (aq) concentrations (10^{-2} M to 3.4 M) at near neutral and elevated pH. Any adjustment to pH of the solution was made by droplet additions of dilute

solutions of NaOH (aq) or HCl (aq). The detailed methodology followed for the OCP and potentiodynamic measurements is provided in Section 2.5 and 2.6, respectively.

The hydrogen gas evolution from freely corroding E717 and AZ31 Mg alloys in aerated aqueous NaCl solutions was collected volumetrically using 10 ± 0.02 cm^3-capacity conically ended burette and these experiments were carried out as detailed in Section 2.7. The electrolytes used in these series of experiments were aqueous NaCl solutions at a molar concentration range of 10^{-3} M to 0.86 M.

6.3   Results and Discussion

6.3.1   Characterisation of Localised Corrosion Propagation

A series of in-situ experiments employing combined SVET-TLI were conducted by immersing E717 specimens in naturally aerated NaCl (aq) containing solutions over a range of concentrations at pH 6.5 in order to characterise localised corrosion behaviour. When very dilute concentrations of $\leq 10^{-3}$ M were used, there was no evidence of passivity breakdown within 12 h of immersion and the exposed surface was shown to be largely inert with no clear evidence of discrete local anode and cathode regions. However, when the NaCl concentration was increased, breakdown of passivity leading to the propagation of a dark film, taking the form of filiform-like corrosion features were observed. A series of current density (j_z) distribution maps, along with associated photographic images correlating the visual corrosion features with the active local anode and cathode regions at various immersion times, is shown in Figure 6.1 for an E717 specimen immersed in 0.034 M NaCl (aq) at pH 6.5.
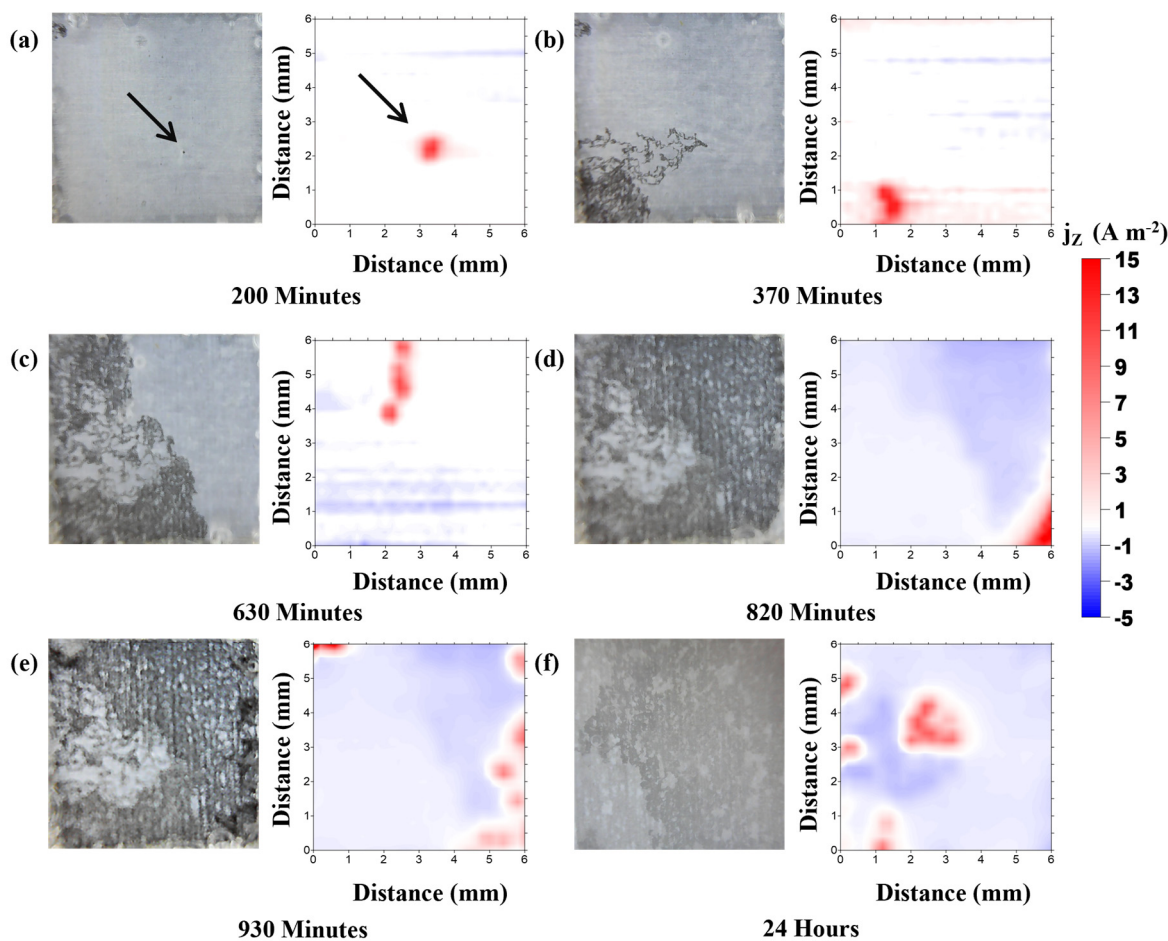
Figure 6.1: SVET-TLI-derived current density distribution maps with associated photographic images recorded for a corroding E717 Mg alloy surface obtained after (a) 200 min, (b) 370 min, (c) 630 min, (d) 820 min, (e) 930 min and (f) 24 h immersion in aerated 0.034 M NaCl (aq).

During the first stages of the immersion and before the surface breakdown, the surface is largely electrochemically inert with some evidence of broad, weakly anodic areas coupling with local cathodic regions ($-1.0 < j_z < 0$ A m^{-2}) in a similar manner to the early stages of the corrosion pure Mg [15,32]. At this point, it is believed that an imperfect Mg(OH)$_2$ film grows on the surface, caused when Mg^{2+} ions produced by the initial anodic dissolution combined with hydroxide anions generated by the corresponding hydrogen evolution cathodic reaction. At the time of the breakdown of the surface a black spot appears, which can be seen in Figure 6.1a (black arrow), that coincides with a region of intense net anodic activity (j_z ca. 5 A m^{-2}) observed on the corresponding current density map.

It should be borne in mind that the size of a corrosion feature revealed by the SVET does not necessarily reflect its physical size and this can be explained in terms of the limited lateral resolution of the technique. The signal peak width at half maximum (whm) is related to the probe height, which in this case was 100 μm. Isaacs [33] has shown that the SVET will record a whm of 1.533 h (where h=scan height or probe-to-sample distance) and since the h in this experiment is 100 μm and the diameter of the SVET micro-disk is 125 μm, the total whm will be approximately 250 μm. This limit in spatial resolution indicates that the SVET will not be able to resolve features separated by a distance < ca. 0.27 mm. So, the size of anode as revealed by SVET does not reflect the physical size of the anode due to the spatial resolution limitation of the SVET that makes it appear larger. Over the 2h period that follows this point of breakdown a network of black tracks appears to emanate from this point on the exposed E717 surface, where active anodes are located at the mobile leading edges of these tracks. After 250 minutes, individual local anodes coalesce into a 2 mm wide "front" moving along the surface consuming the previous intact surface, while measured j_z values have increased to values of ca. +15 A m^{-2}.

By comparing the SVET-derived color-scale j_z maps and the photographic images at the same immersion times, the anodes are seen to coincide with the front of the corrosion tracks where hydrogen bubble streams are seen to originate. It is also evident, especially in Figure 6.1d, where the localised corrosion feature traverses from top to bottom of the scan area, that the corroded area left behind the advancing anodic front is cathodically activated with respect to original intact surface, evidenced by j_z values of between −2 and −3 A m^{-2} measured on the right-hand side of the scan area. After the entire surface is covered with corrosion product (Figure 6.1e), the number of active anodes has markedly increased. However, it is also clear that the cathodic activation of the previously corroded areas is a temporary phenomenon and that the current density values associated with these regions decrease with time. For example, a comparison of Figure 6.1e and Figure 6.1f shows that typical current density values of −2 to −3 A m^{-2} have decreased to < 1 A m^{-2} during the intervening 8 h period between these 2 scans. It is proposed that the de-activation of local cathode sites occurs due to two possible effects. Firstly, Mg(OH)$_2$ deposition and the progressive thickening of a corrosion product film in these areas, due to the elevated local pH will produce a more effective barrier to interfacial electron transfer, which will slowly cause previously cathodically activated areas to become progressively more electrochemically inert.

Additionally, in order for local anodes to continue their propagation over the surface, there is a need for coupling with the cathodically activated corroded regions. This can only occur over finite distances primarily depending on the conductivity of the solution. So as local anodes move further away from their original locations, the cathodically activated corroded surface produced by prior anodic dissolution in these regions will necessarily de-activate because coupling with remote local anodes will become ohmically limited.

Figure 6.2 shows a selection of j_z distribution maps and corresponding visual images obtained for an E717 specimen freely corroding in a more concentrated 0.17 M NaCl (aq) solution. Although the localised corrosion features resemble those shown in Figure 6.1, there are some differences, especially in terms of the propagation of dark corrosion product. In this more concentrated electrolyte, there is less evidence of discrete filiform-like tracks and consequently the features comprise more uniform regions, which consume the intact surface more rapidly than previously observed in Figure 6.1. At this higher concentration, the entirety of the exposed surface became covered with a black film within 500 min of immersion, whereas previously this occurred within 900 min immersion period. It is also evident that the peak values of both anodic and cathodic values are significantly higher, with the more concentrated electrolyte, with typical values of $+ 70$ A m^{-2} and -5 A m^{-2} respectively.

The more rapid conversion of the intact surface appears related to the fact that individual propagating anodes rapidly combine to form a unified front, which propagates across the entirety of the width of the exposed surface (see Figure 6.2c and 2d). Again, there is clear evidence of cathodic activation of the previously anodically attacked surface left behind the advancing anodic front. However, it is also apparent that the most active local cathodes follow immediately behind the areas of anodic activity as shown in Figure 6.2c and 2d. As the anodic front moves further away from its original location, peak cathodic j_z values of up to -4 A m^{-2} measured in the region immediately to its left-hand size (indicated by the dashed circle), decrease to -1 A m^{-2} over an ensuing 40 min period. At longer immersion times, when the exposed surface is fully corroded and occupied by a black corrosion-induced film, several local anodic regions simultaneously travel backwards and forwards across the previously corroded surface, and leave a temporary cathodically activated zone, extending ca. 1 mm behind in their wake (see Figure 6.2f).
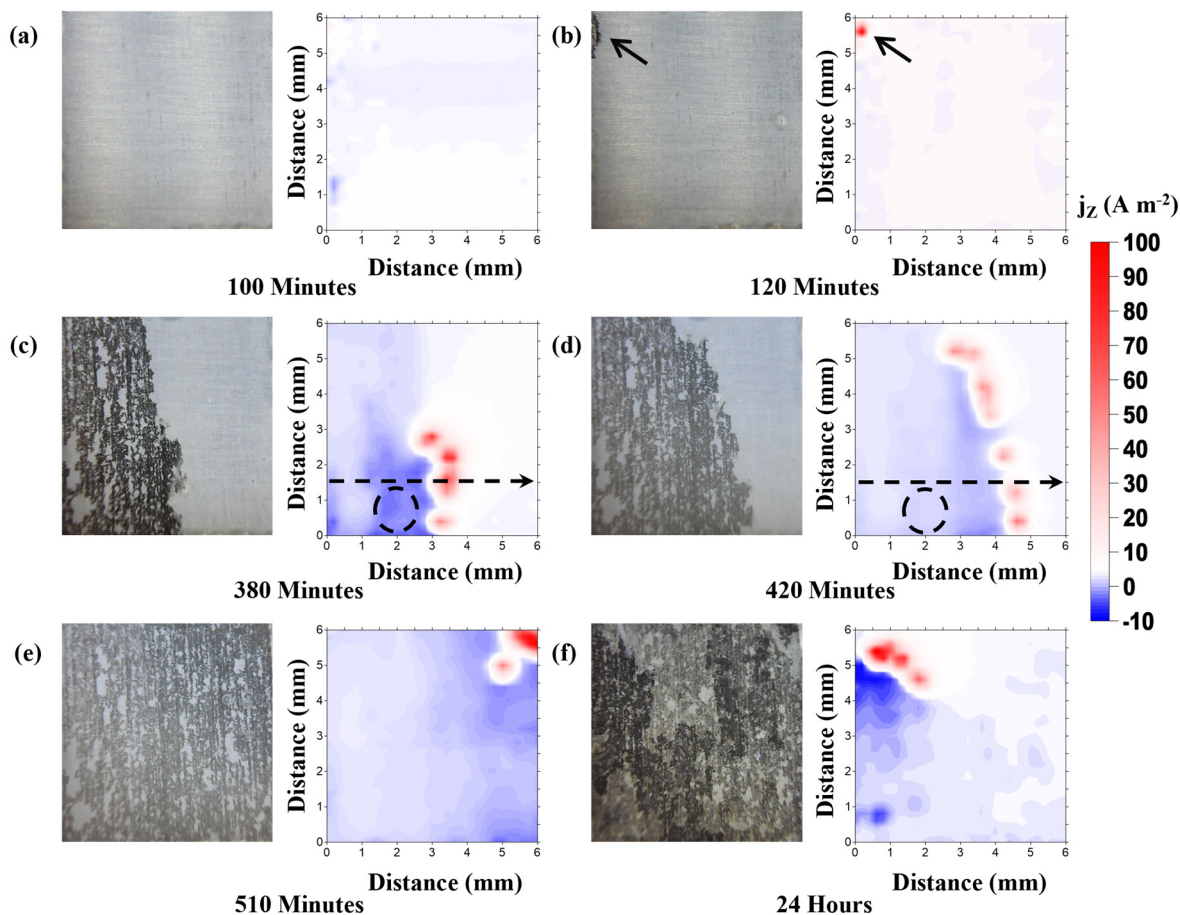
Figure 6.2: SVET-TLI-derived current density distribution maps with associated photographic images recorded for a corroding E717 Mg alloy surface obtained after : (a) 100 min, (b) 120 min, (c) 380 min, (d) 420 min, (e) 510 min and (f) 24 h immersion in aerated 0.17 M NaCl (aq).

The current density distributions associated with the propagating corrosion front observed in Figure 6.2c and 2d can perhaps be better understood in terms of the line profiles of j_z versus distance (Figure 6.3) extracted from regions of the SVET-derived j_z maps indicated by the dashed horizontal arrows. As the anodic front characterised by peak j_z values in the +25 to +35 A m^{-2} range in moves from left to right, a 2 mm local cathodic region behind develops to its left-hand side, where j_z values of between −2 and −3 A m^{-2} are measured. The intact surface to the right of the local anode region is shown to be electrochemically inactive ($j_z \leq \pm 0.1$ A m^{-2}).
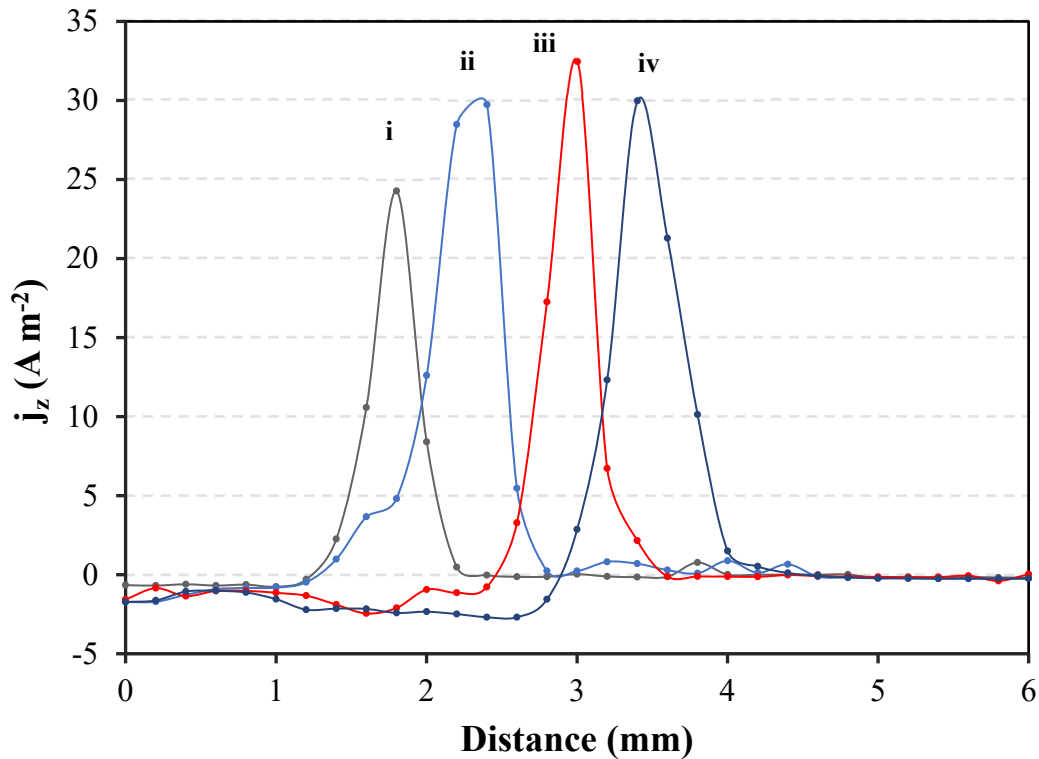
Figure 6.3: Local current density (j_z) versus distance profiles plotted for a propagating filiform-like corrosion feature observed for an E717 specimen immersed in 0.17 M NaCl (aq). Time key: plot (i) 340 min, with (ii) – (iv) obtained at 15 min intervals thereafter.

Figure 6.4 shows the current density maps with the corresponding images that were obtained by immersing the same alloy in a 0.86 M NaCl solution. In this much more concentrated electrolyte, breakdown occurs within 15 min of immersion (in this case in the top left corner of the exposed area) followed by propagation of filiform-like dark tracks into the centre of the scan area (See Figure 6.4a). Individual tracks rapidly coalesce to form an anodic front that rapidly sweeps across the intact surface until, after 5h, the entirety of the surface becomes covered with a dark corroded film. As observed in Figure 6.1 and Figure 6.2, the dark corroded surface affected by anodic dissolution becomes cathodically activated with respect to the intact surface. In this case typical cathodic current density values measured immediately behind the advancing anodic front (see Figure 6.4c) are generally higher (ca. –5 A m^{-2}) than those observed in less concentrated electrolyte. Significantly higher current density values (of up to +100 A m^{-2}) compared to those

measured at lower NaCl (aq) concentrations area also observed for the active anodes that subsequently traverse the fully corroded surface (Figure 6.4d, e and f). Their positions of these highly intense focal anodes can be correlated with regions, which evolve rising streams of fine H_2 bubbles, characterised by cloudy white features observed to the right-hand side of Figure 6.4f. Although it seems that new anodic sites are emerging from previously cathodic sites (Figure 6.1f, Figure 6.2f, Figure 6.4d), this is not the case since it is the same anode that initially appeared on the surface that later breaks apart to create an anodic front. The anodes that comprise the anodic front can change their formation giving the impression that new anodic sites have emerged on the surface.

Figure 6.4: SVET-TLI-derived current density distribution maps with associated photographic images recorded for a corroding E717 Mg alloy surface obt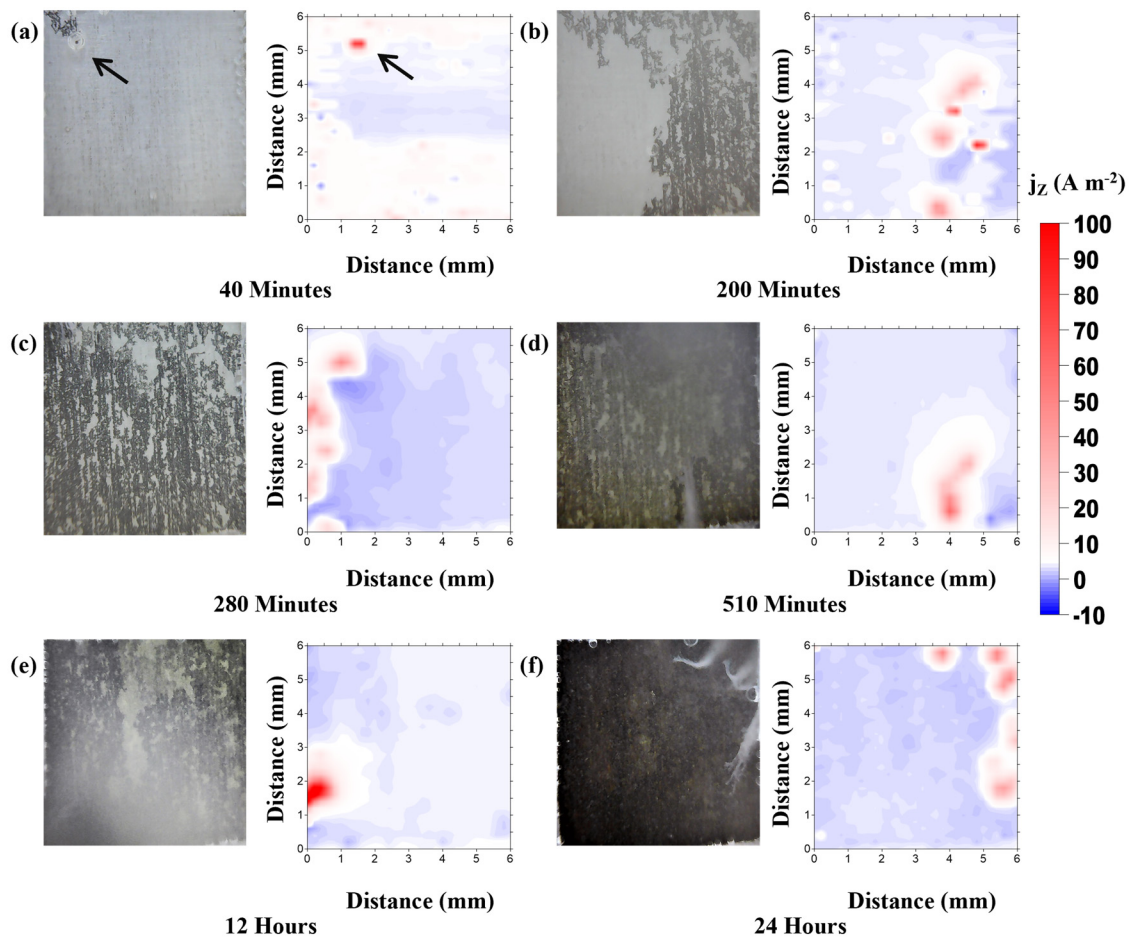ained after : (a) 40 min, (b) 200 min, (c) 280 min, (d) 510 min, (e) 12 h and (f) 24 h immersion in aerated 0.86 M NaCl (aq).

A comparison of the results presented in Figure 6.1, Figure 6.2 and Figure 6.4 shows that progressively increasing the sodium chloride concentration produces the following effects.

I.   More rapid propagation of localised corrosion as characterised by the development of a black film that consumes the intact surface and in time covers the whole exposed scanned area.

II.   A transition from discrete filiform-like dark tracks to larger corrosion features, resembling dendrites, that produce a unified corrosion front that traverses the exposed alloy surface.

III. A progressive increase in current density values associated with both local anodic regions along with cathodically activated areas corresponding to dark corroded areas produced by previous anodic dissolution.

The influence of [NaCl] on the propagation of localised corrosion can perhaps be better understood by quantifying the area occupied by dark corrosion product, carried out using image analysis of the time-lapse photographs, which is plotted as a function of immersion time in Figure 6.5. The results for each concentration show 2 discrete phases, which when correlated with each separate time-lapse sequence, shows an initial slower phase corresponding to the propagation of discrete filiform tracks, which subsequently transforms to a faster process, where a unified corrosion front moves across the E717 surface. The point of transition appears to correspond with the time at which discrete local anodes combine, which for a 0.86 M concentration occurs at an immersion period of 2h and progressively lengthens to 5h as [NaCl] is decreased to 0.034 M. For phase 1, the slopes of the area versus time plots decrease from 0.04 mm^2 min^{-1} to 0.025 mm^2 min^{-1} over the [NaCl] range studied here. The slopes of corroded area versus time plots in phase 2 are significantly higher, but show a more marked dependence on [NaCl] and are seen to progressively decrease from 0.17 to 0.11 and 0.06 mm^2 min^{-1} for concentrations of 0.86, 0.17 and 0.034 M respectively.

It therefore seems that an autocatalytic effect may be present under conditions where discrete filaments coalesce, causing the corrosion feature thus formed to propagate more rapidly. A similar observation has been made for the localised corrosion of an AZ31 welded specimen immersed in 5% w/v NaCl (aq) [21], where velocities of 0.05 mm min^{-1} measured for discrete filaments increased by 50% after these had coalesced into a large localised corrosion feature.
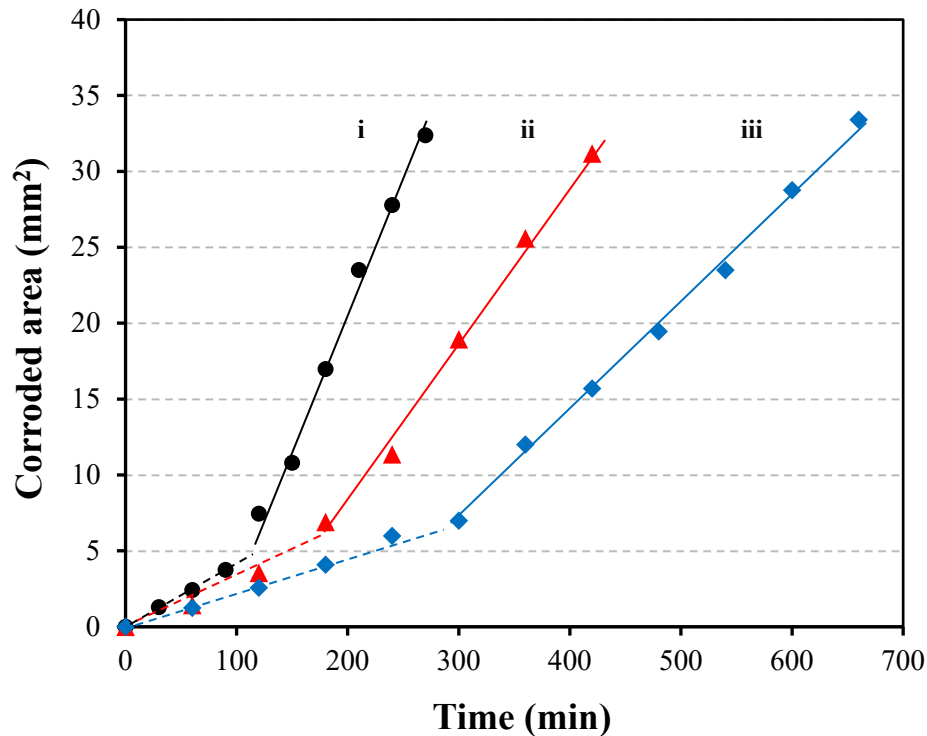
Figure 6.5: Plots of corroded area, estimated from visual image analysis, as a function of immersion time for freely corroding E717 samples held in (i) 0.86, (ii) 0.17 and (iii) 0.034 M aerated solutions of NaCl (aq) at pH 6.5.

Observations made regarding the role of [NaCl] in controlling morphologies of localised corrosion features affecting E717 are generally in line with previous investigations involving pure Mg [19] and AZ31 [15]. Disc-like propagation of the dark corrosion product film on pure Mg observed in highly concentrated electrolyte, which transforms to filiform-like in significantly more dilute NaCl (aq) solutions [19], was ascribed to a decrease in throwing power, where coupling of local anodes with cathodically activated corroded regions became limited to progressively smaller distances over the exposed surface. It is likely that the observations made here regarding the increased velocity of corrosion front propagation, coupled with progressively higher local anodic current densities measured in more concentrated electrolyte, can also be explained using the same argument regarding ohmically-controlled localised corrosion. However, it should also be noted that chloride ions are also known to increase the solubility of $Mg(OH)_2$ [31] and therefore at higher concentrations could disfavour corrosion product deposition on local cathodic sites.

Consequently, local cathode activity may become significantly prolonged at high chloride concentrations, in turn driving more anodic dissolution at the leading edges of the filiform like features. Another question to address is the origin of the cathodic activation of the corroded surface produced by previous anodic dissolution as clearly demonstrated in Figures 6.1-6.4. A previous SVET investigation of AZ31, which demonstrated the same behaviour in this alloy, albeit with significantly higher cathodic j_z values of up to -10 A m^{-2} proposed that the cathodic activation was caused by an accumulation of noble Al–Mn (Fe) particles remaining in electrical contact with the matrix within the regions affected by filiform-like attack [15]. Subsequent physical characterisation of cathodically activated regions of the corroded AZ31 surface confirmed the presence of such particles embedded in the filament region, but also revealed the formation of a Zn-enriched Mg solid at the metal/corrosion film interface [34]. It seems plausible therefore to postulate that the cathodic activation observed for corroding E717 is caused by enrichment of noble particles such as Fe-containing Zr, demonstrated by others [9] to be the most active sites for hydrogen evolution. Others however, have recently demonstrated enhanced rates of cathodic hydrogen evolution on hydroxide covered Mg, compared with a pristine Mg surface [35], and therefore the Mg(OH)$_2$ corrosion product formed on the filament tracks may also play a role in producing a cathodically activated region.

The data in Figure 6.1, Figure 6.2 and Figure 6.4 may be conveniently quantified and summarised by numerically integrating the time-dependent j_z distribution maps in a manner described previously [32]. Figure 6.6 shows the variation of area-normalised, total integrated anodic current (J_a) with respect to immersion time, determined at 3 different NaCl (aq) concentrations. The differences in the magnitude of the time-dependent J_a values in plots i – iii demonstrate the progressively higher localised corrosion rates measured with increasing electrolyte concentration. At a concentration of 0.86 M, fluctuating values of J_a observed during the initial filiform-like propagation phase eventually stabilise at a value of ca. 1.5 A m^{-2} after 8 h immersion, when the entire exposed area is covered by dark corrosion product. Plot ii obtained for a 0.17 M NaCl (aq) concentration shows that J_a values stabilise at a lower values of ca. 0.8 A m^{-2}, while the lowest concentration of 0.034 M, plot iii demonstrates that J_a becomes non-zero after an immersion time of 7h, after the breakdown of temporary passivity has occurred, thereafter progressively rising to a relatively constant value of 0.6 A m^{-2} following a further 10 h immersion period. By converting

each value of J_a to charge and summing these individual values over a 24h immersion period, a Mg mass loss estimate can be calculated for each NaCl (aq) concentration, using Faraday's law. Using this approach, values of mass loss through localised concentration of 14.0, 8.6 and 3.6 g m^{-2} day^{-1} for NaCl (aq) concentrations of 0.86, 0.17 and 0.034 M respectively can be determined.
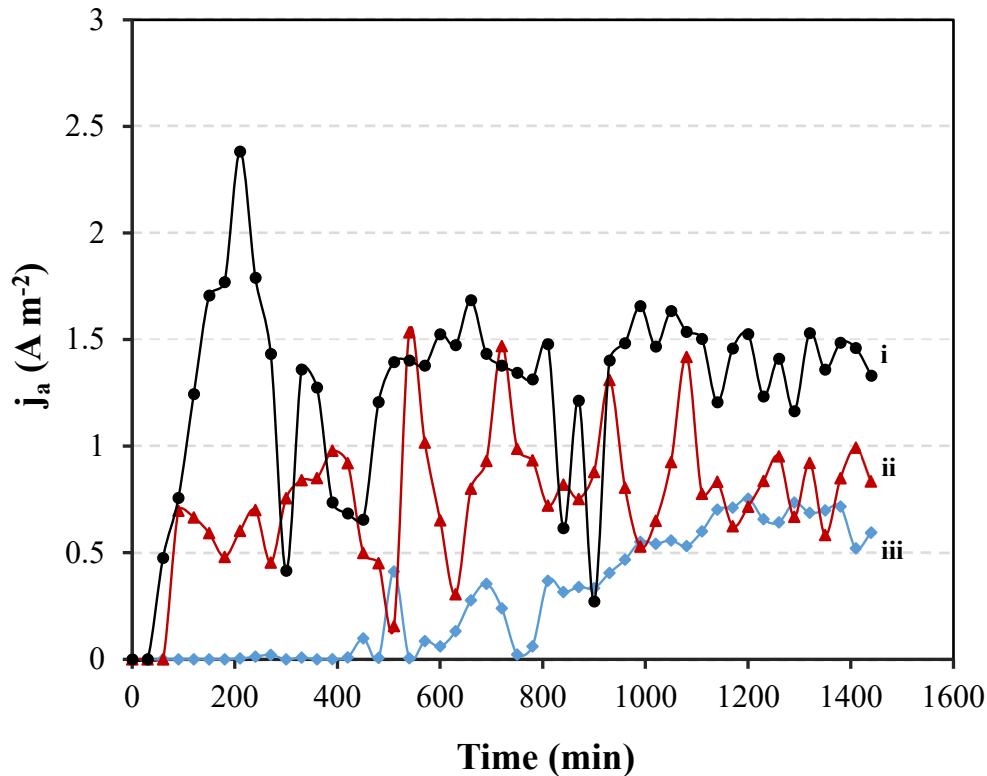
Figure 6.6: Area-averaged total anodic current density values calculated by numerical integration of SVET-derived current density distribution maps plotted as a function of time for E717 specimens immersed in aerated aqueous NaCl electrolyte at concentrations of (i) 0.86 M, (ii) 0.17 M and (iii) 0.034 M.

6.3.2   Characterisation of the Chloride Concentration Effects on Passivity Breakdown

From the immersion experiments carried out in Section 6.3.1, it is evident that chloride concentration plays an important role in the initiation of filiform-like corrosion. The time taken for breakdown to occur is seen to lengthen considerably with progressively more dilute concentrations, until a point is reached (at $\leq 10^{-3}$ M) where no filiform-like is observed over a 24h immersion period. Previously published work, using both pure Mg and AZ31, demonstrated that monitoring time-dependent free corrosion potentials following initial immersion could provide a

means of determining a breakdown potential (E_b) under circumstances where spontaneous breakdown is observed in the absence of external polarization [31]. The variation of free corrosion potential (E_{corr}) with time observed during the immersion of an E717 surface in 0.17 M NaCl (aq) at pH 6.5 is given in Figure 6.7a.
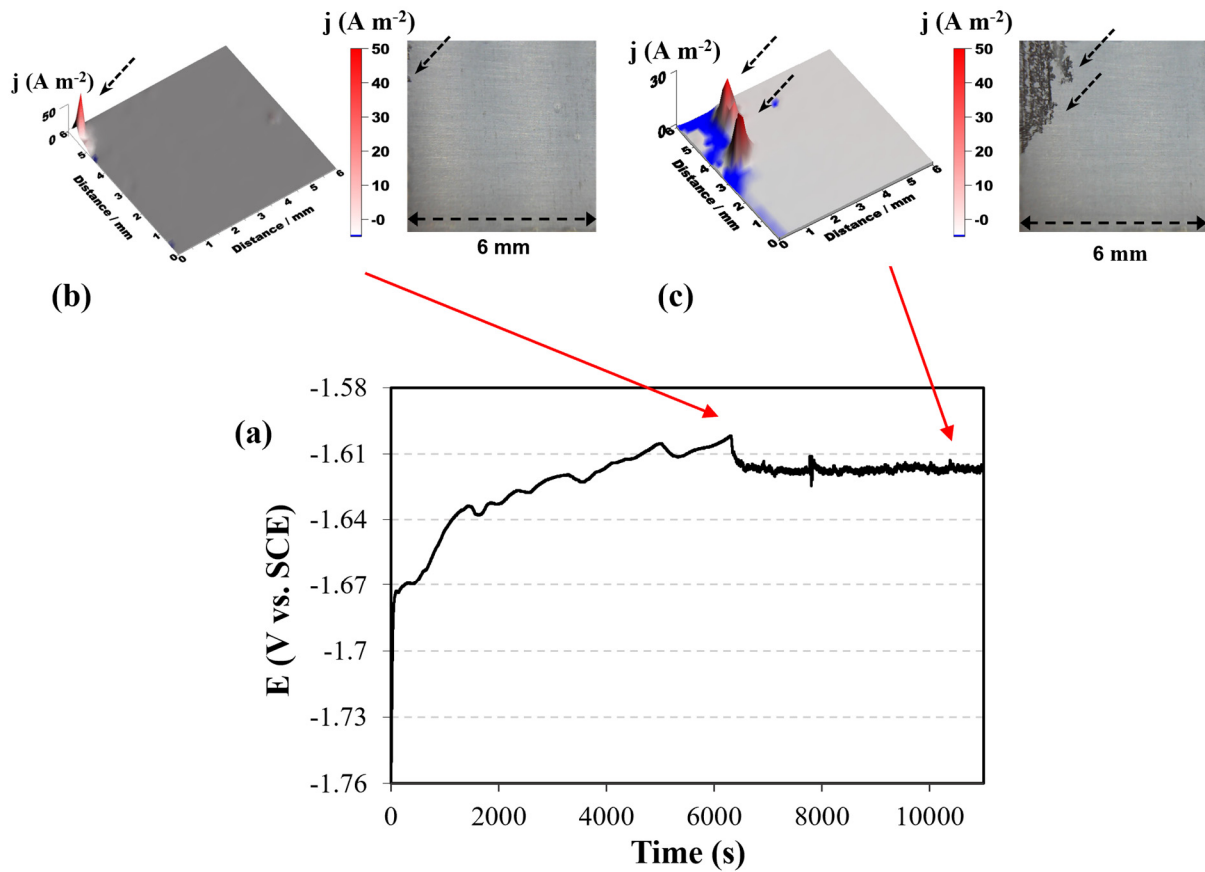
Figure 6.7: Time-dependent E_{corr} variation (a) observed for freely corroding E717 immersed in 0.17 M NaCl (aq) at pH 6.5, correlated with both photographic images and SVET-derived current density distribution maps of the corroding surface obtained at intervals of (b) 100 min and (c) 180 min following initial immersion.

In addition, SVET-derived current density distribution maps and associated close up visual images, given in Figure 6.7b and Figure 6.7c, allow features of the E_{corr} transient to be correlated with visualisations of localised corrosion behaviour. Immediately after immersion, but before any visible evidence of filiform-like initiation, E_{corr} rises with time over 100 min from an initial starting

potential of −1.7 V (vs. SCE). At a point where a localised corrosion feature is first observed, characterised by the appearance of a dark spot, which evolves a rising stream of fine H_2 bubbles, E_{corr} decreases sharply from a maximum of −1.6 V (vs. SCE) as shown by the arrow linking Figure 6.7b to the E_{corr} vs. time plot. From the associated SVET j_z distribution map, the location where breakdown occurs is revealed as an intense focal anode, and as such the sharp decrease in E_{corr} to more negative values can be explained in terms of mixed potential theory, where the corresponding cathodic current will rise in order to preserve electroneutrality.

The initial rise in E_{corr} has been explained previously in terms of a period of magnesium hydroxide $(Mg(OH)_2)$ film growth, producing temporary passivity and thus causing E_{corr} to become more positive [31]. The maximum point of the E_{corr} vs. time transient, prior to its sharp decrease by 20 mV is identified as a breakdown potential (E_b), which when reached, induces initiation of filiform-like as highly localised anodic attack occurs at a weak point in the imperfect $Mg(OH)_2$ surface film formed over the first 100 min of immersion. Figure 6.7c shows the appearance of the corroding E717 surface, along with its appropriate current density distribution observed 180 min following breakdown, where filiform like features, characterised by intense anodic leading edges and cathodically activated dark tracks has started to propagate over the upper top left quadrant of the exposed surface. During this stage, the E_{corr} vs. time plot shows significantly more superimposed noise (± 1 mV), presumably resulting from perturbations caused by hydrogen bubble formation and release from actively corroding, filiform-like affected regions.

Further experiments were subsequently carried out using a series of NaCl (aq) concentrations in the 0.034M to 3.4 M range to investigate the influence of [Cl⁻] on the apparent breakdown potential E_b, determined by monitoring changes in the E_{corr} versus time transient. Typical E_{corr} versus time curves obtained for E717 specimens at pH 6.5 for concentrations ranging over a 2 orders of magnitude range are given in Figure 6.8. At the highest NaCl (aq) concentrations of 3.4 and 2M, employed in this investigation (curves i and ii respectively), breakdown occurs within seconds and consequently E_b is determined by the initial value of E_{corr} at t = 0. When [Cl⁻] is progressively decreased at more dilute concentrations of ≤ 0.86 M, there is an increased delay time prior to breakdown, as evidenced by the arrows, that indicate filiform-like initiation on each of the E_{corr} transients in Figure 6.8, plots iii – vi. Immersion in a 0.86 M NaCl (aq) electrolyte leads to passivity breakdown within 15 min (curve iii) but takes up to 150 min in a 0.034 M concentration.
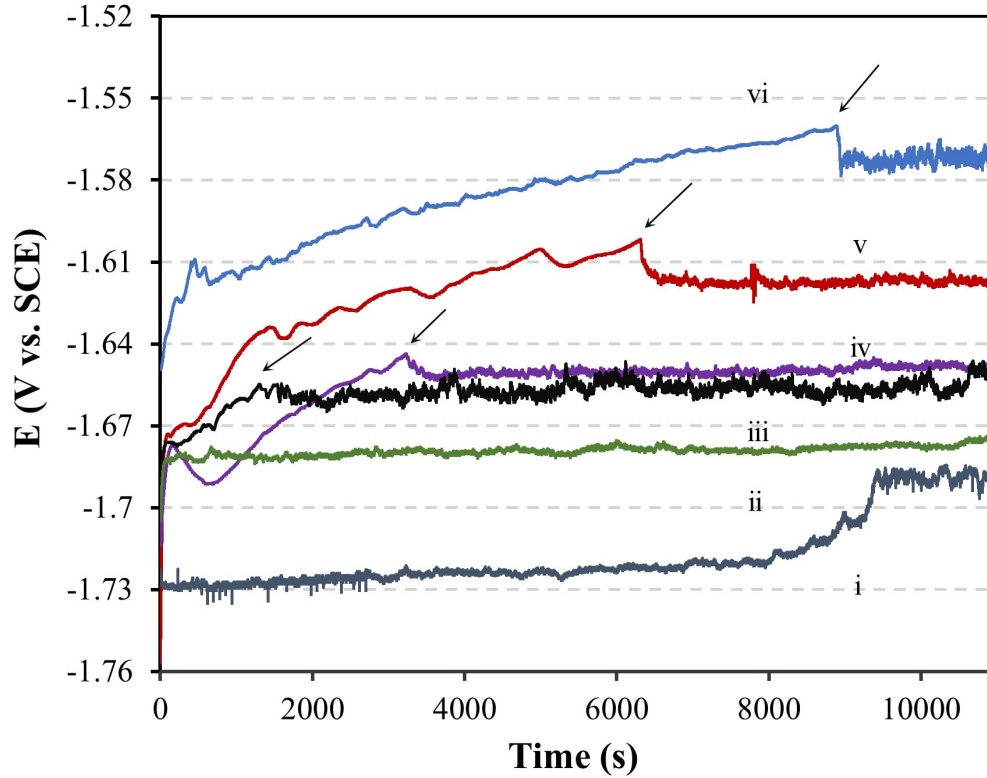
Figure 6.8: Plots of E_{corr} versus time obtained for E717 specimens immersed in pH 6.5, aerated NaCl (aq) electrolyte at concentrations of: (i) 3.4 M, (ii) 2 M, (iii) 0.86 M, (iv) 0.6 M, (v) 0.17 M and (vi) 0.034 M. The arrows indicate the point of passivity breakdown in each case.

Correspondingly, it is also evident from the same family of plots that the E_{corr} value marking the point of breakdown (E_b) is also shifted to progressively more positive values with decreasing [Cl$^-$], as previously observed for both pure Mg and AZ31 [31]. Values of E_b determined from the various E_{corr} vs. time curves given in Figure 6.8 were subsequently plotted as a function of chloride ion concentration and showed a clear dependence on [Cl$^-$] according to the Equation (6.1).

$$E_b = A + B \log_{10} [Cl^-] \tag{6.1}$$

The constant A equates to the value of E_b determined at a chloride ion concentration of 1 M, while B is a constant that depends on both the type of alloy and corrosive electrolyte. Under the conditions employed here, values of -1.66 V and -0.077 V/decade were obtained for A and B respectively for E717, which is in good agreement with values of -1.59 V and -0.072 mV/decade determined previously for AZ31 over a similar range of chloride concentration using the same

methodology [31] at neutral pH. This similarity with AZ31 implies that the value of B does not significantly depend on alloy composition, but rather on the nature of the protective magnesium(hydroxide) film formed in neutral aqueous solution.

Others have previously reported a dependence of the anodic branches of potentiodynamic polarisation data on sodium chloride concentration in the 0.016 – 1.6% w/v range for ZEK100 (generic E717 alloy type) substrates in neutral electrolyte [9]. Although the studies described here demonstrate that spontaneous breakdown in the absence of external polarisation is observed at the highest concentrations in this range, this previously published study ascribes inflections in the anodic current versus applied potential curves to a breakdown potential (E_b) and demonstrates that these values become more positive with decreasing chloride ion concentration.

A reworking of the data presented therein gave a linear plot of E_b versus $\log_{10}[Cl^-]$ with a slope of 0.072 V per decade, which is in good agreement with the value obtained in this present study, using time-dependent E_{corr} data to determine values of E_b. This potentiodynamic polarisation investigation of E717 chloride ion concentration dependence has been extended here to include conditions of elevated pH (in this case pH 11), where the Mg matrix would be expected to exhibit passivity [36]. In the range of concentrations used here (10^{-2} to 0.86 M), immersion of E717 specimens under freely corroding conditions at a pH of 11 produced no visual evidence of breakdown for periods of up to 6h. Typical polarization curves obtained over this [NaCl] range at pH 11 are shown in Figure 6.9a.
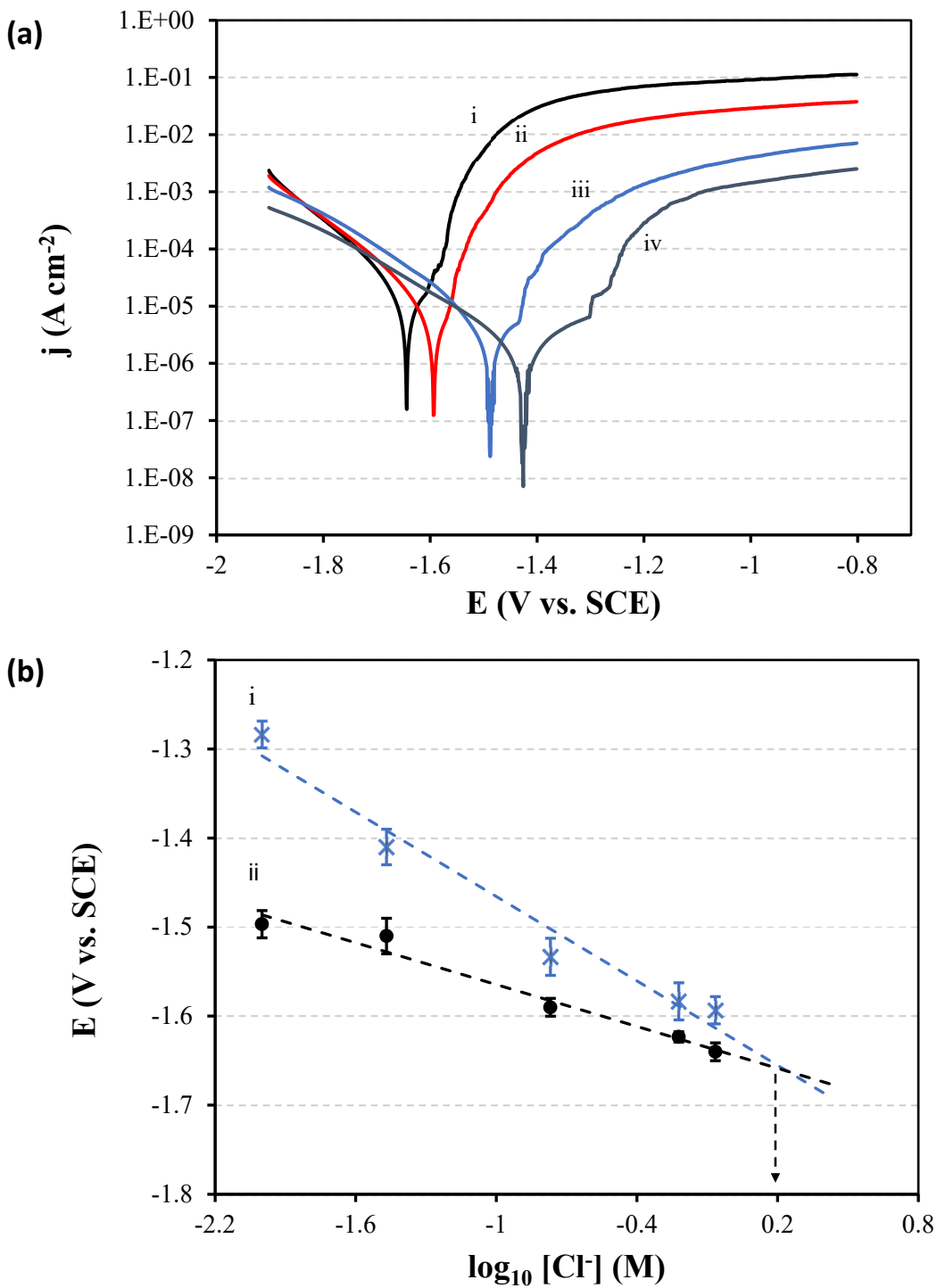
Figure 6.9: (a) Anodic-going potentiodynamic polarization curves obtained for E717 in NaCl (aq) solutions at concentrations of (i) 0.86 M, (ii) 0.17 M, (iii) 0.034 M and (iv) 10^{-2} M at pH 11 in aerated conditions at room temperature. A sweep rate of 1 mV/s was used in each case. (b) shows a summary plot of (i) breakdown potential (E_b) and (ii) free corrosion potential (E_{corr}) versus chloride ion concentration determined for E717 specimens in NaCl-containing electrolyte at pH 11.

Prior to the start of polarisation, each solution was purged with air for 15 min in order to minimise any potential interference from carbonate species formed as a result of dissolved carbon dioxide. At [NaCl] $\leq$ 0.034 M, clear inflections in the anodic branches of curves iii and iv are observed in Figure 6.9a, signifying passivity breakdown and consequently E_b can be conveniently identified as the point of a sharp increase in current density with applied potential. For concentrations $\geq$ 0.17 M, determination of E_b was less certain and consequently the potential at which current density exceeded a threshold of 1 mA cm^{-2} was assumed to constitute the breakdown potential. Figure 6.9b shows mean values of Eb determined in 3 repeat experiments (plot i), along with E_{corr} values measured over 10 min prior to the start of potentiodynamic polarisation (plot ii), plotted as a function of $\log_{10}$[Cl$^-$]. Under conditions of elevated pH used for these experiments, values of -1.63 V and -0.15 V/decade were obtained for A and B respectively.

E_{corr} is also shown to decrease with increasing [Cl$^-$], with a reduced gradient of -0.05 V/decade. At the point where plots i and ii intersect (i.e where $E_{corr} = E_b$, indicated by the downward arrow) spontaneous breakdown in the absence of external polarization would be anticipated, and under the conditions employed here, this is predicted to occur at a chloride ion concentration of 1.5 M. It should be noted that the value of B obtained from potentiodynamic measurements at elevated pH is significantly higher than when determined using E_{corr} vs. time data under neutral conditions. The underlying reasons are unclear, given the previous finding for pure Mg that similar values of -0.11 V/decade were established using both methods [31]. However, the pH dependence of B may be due to the presence of alloying additions such as Zn, which would not be predicted to maintain passivity in the same manner as Mg at elevated pH [36].

6.3.3   The Effect of Chloride Concentration on Hydrogen Evolution

Finally, a series of immersion experiments were conducted, using a range of NaCl (aq) concentrations in the $10^{-3} - 0.86$ M range at pH 6.5, to determine the influence of [Cl$^-$] on bulk corrosion rates, as measured using volumetric hydrogen gas capture. The principal aim was to correlate bulk corrosion rates with the trends observed using quantitative SVET data. Figure 6.10 shows data obtained for E717 specimens, converted to area-averaged moles of H2 evolved, plotted as a function of immersion time at various [NaCl]. Over the 10 h timescale of the experiments, the

hydrogen evolution rate is negligible at [NaCl] $\leq$ 0.034M (plots iv and v), reflecting the fact that although spontaneous breakdown can occur, a considerable delay is observed prior to visual evidence of filiform-like propagation. At [NaCl] $\geq$ 0.17 M (plots i – iii), there is a progressive increase in H_2 evolution rate with increasing concentration, while the linear relationship of moles H_2 with immersion time allows an area normalised cathodic current to be calculated at each different concentration. Values of 0.2, 0.35 and 0.55 A m^{-2} can be derived for E717 specimens immersed in 0.17, 0.6 and 0.86 M NaCl (aq) respectively. For the corresponding SVET data obtained at the highest of these concentrations (0.86 M), numerical integration of cathodic current density distributions (see maps shown in Figure 6.4) to produce an area averaged total cathodic current per scan, gave a constant value of 0.42 A m^{-2} over a 8h immersion period following an initial period of stabilisation. The underestimation of hydrogen evolution rate by numerical integration of SVET data has been demonstrated elsewhere [22], and is explained by the fact that the technique cannot detect local cathode sites that are co-located at, or immediately behind, the principal sites of anodic Mg dissolution.

Also included in Figure 6.10 for comparison is the area normalised hydrogen evolution rate for AZ31 obtained in 0.86 M NaCl (aq) electrolyte, showing a significantly higher slope than observed for E717 under the same conditions. A previous SVET-based investigation of this particular alloy reported significantly higher peak anodic and cathodic current density values determined at localised corrosion sites than measured here for E717 under the same conditions [15]. Consequently, the higher corrosion resistance of E717 in comparison to AZ31 under freely corroding conditions can, in part, be correlated to a significantly lower extent of cathodic activation produced by prior anodic dissolution.
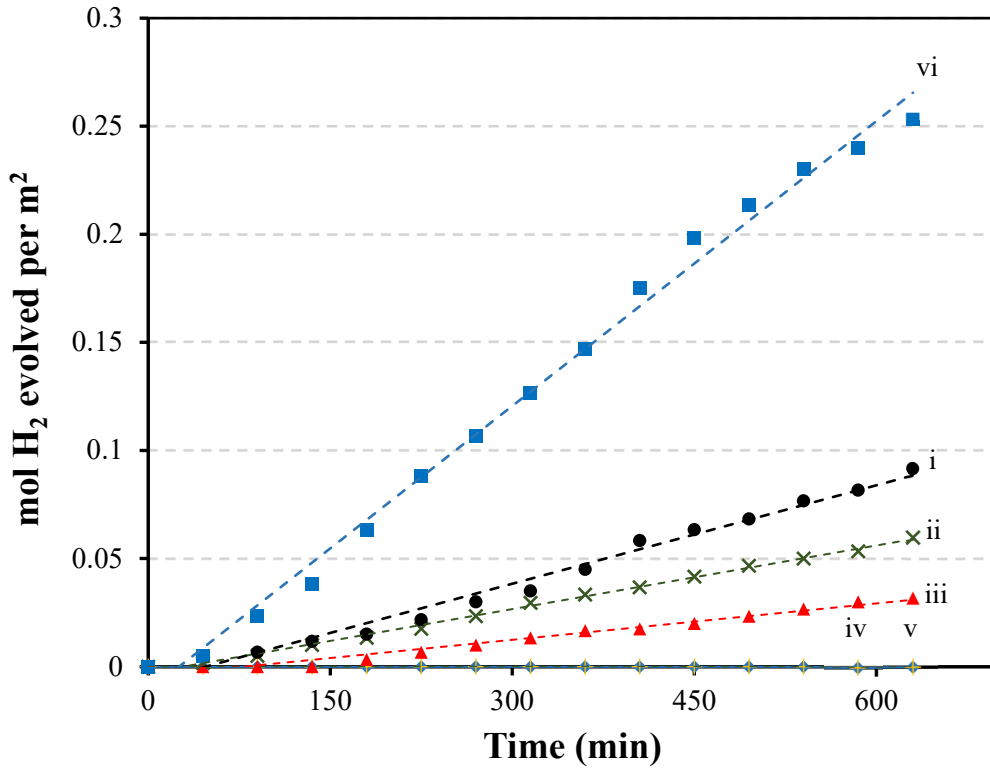
Figure 6.10: Plots of moles hydrogen gas per unit area evolved versus time for E717 immersed under freely corroding conditions in NaCl (aq) at pH 6.5: (i) 0.86 M, (ii) 0.6 M, (iii) 0.17 M , (iv) 0.034 M and (v) 10^{-3} M, while plot (vi) shows data obtained for AZ31 upon immersion in 0.86 M NaCl (aq).

6.4   Conclusion

In this chapter, the influence of the chloride ion concentration on the localised corrosion propagation of E717 Mg alloy was investigated using a SVET in conjunction with TLI. The alloy undergoes a filiform-like localised corrosion with the leading edge of the filaments being intense focal anodes that move over the surface leaving a cathodically activated dark surface behind.

A progressive increase in concentration leads to a more rapid propagation of filiform-like corrosion features as quantified by plots of corroded area versus immersion time. Two distinct phases in filiform-like propagation, comprising an initial slower development of discrete individual filaments, followed by a more rapid growth of uniform corrosion front. The time taken to transition from phase 1 to phase 2 progressively decreases with increasing electrolyte concentration. Typical peak current density associated with local anodes progressively increases with chloride ion

concentration, demonstrating the importance of galvanic coupling with cathodically activated regions over the entirety of the exposed Mg alloy surface.When the electrolyte concentration $\geq$ 0.034M the breakdown of the surface occurs spontaneously at neutral pH and in the absence of external polarisation. A breakdown potential (E_b) and can be identified by following time-dependent E_{corr} behaviour and is shown to vary as a function of $\log_{10}[Cl^-]$ with a slope of 0.077 V/decade, which is in good agreement with previous studies of other Mg alloys.

Finally, trends observed by numerically integrating SVET-derived current density distributions were confirmed by measuring volumetrically the hydrogen evolved from the alloy surface over a range of different electrolyte concentrations. Area averaged cathodic current densities estimated from bulk hydrogen evolution rates were shown to be 20% greater than those determined from SVET data. The difference was ascribed to cathodic hydrogen evolution at the principal sites of Mg dissolution, revealed as net local anodes, which remains undetected by SVET.

6.5 References

[1]   A.A. Luo, Recent magnesium alloy development for elevated temperature applications, Int. Mater. Rev. 49 (2004) 13–30.

[2]   B. Smola, I. Stulíková, J. Pelcová, B.L. Mordike, Significance of stable and metastable phases in high temperature creep resistant magnesium–rare earth base alloys, J. Alloys Compd. 378 (2004) 196–201.

[3]   Y. Fan, G. Wu, H. Gao, G. Li, C. Zhai, Influence of lanthanum on the microstructure, mechanical property and corrosion resistance of magnesium alloy, J. Mater. Sci. 41 (2006) 5409–5416.

[4]   Y.L. Song, Y.H. Liu, S.R. Yu, X.Y. Zhu, S.H. Wang, Effect of neodymium on microstructure and corrosion resistance of AZ91 magnesium alloy, J. Mater. Sci. 42 (2007) 4435–4440.

[5]   T.J. Luo, Y.S. Yang, Y.J. Li, X.G. Dong, Influence of rare earth Y on the corrosion behavior of as-cast AZ91 alloy, Electrochim. Acta. 54 (2009) 6433–6437.

[6]   W. Liu, F. Cao, L. Zhong, L. Zheng, B. Jia, Z. Zhang, J. Zhang, Influence of rare earth element Ce and La addition on corrosion behavior of AZ91 magnesium alloy, Mater. Corros. 60 (2009) 795–803.

[7]   J.W. Chang, X.W. Guo, P.H. Fu, L.M. Peng, W.J. Ding, Effect of heat treatment on corrosion and electrochemical behaviour of Mg-3Nd-0.2Zn-0.4Zr (wt.%) alloy, Electrochim. Acta. 52 (2007) 3160–3167.

[8]   J.W. Chang, L.M. Peng, X.W. Guo, A. Atrens, P.H. Fu, W.J. Ding, X.S. Wang, Comparison of the corrosion behaviour in 5% NaCl solution of Mg alloys NZ30K and AZ91D, J. Appl. Electrochem. 38 (2008) 207–214.

[9]   R.M. Asmussen, W.J. Binns, P. Jakupi, D. Shoesmith, The influence of microstructure on the corrosion of magnesium alloy ZEK100, Corrosion. 71 (2014) 242–254.

[10]   W. Jeffrey Binns, F. Zargarzadah, V. Dehnavi, J. Chen, J.J. Noël, D.W. Shoesmith, Physical

and electrochemical evidence for the role of a Mg hydride species in Mg alloy corrosion, CORROSION. 75 (2019) 58–68.

[11]   M.P. Brady, G. Rother, L.M. Anovitz, K.C. Littrell, K.A. Unocic, H.H. Elsentriecy, G.-L. Song, J.K. Thomson, N.C. Gallego, B. Davis, Film breakdown and nano-porous Mg(OH)$_2$ formation from corrosion of magnesium alloys in salt solutions, J. Electrochem. Soc. 162 (2015) C140–C149.

[12]   M.P. Brady, M. Fayek, D.N. Leonard, H.M. Meyer, J.K. Thomson, L.M. Anovitz, G. Rother, G.-L. Song, B. Davis, Tracer film growth study of the corrosion of magnesium alloys AZ31B and ZE10A in 0.01% NaCl solution, J. Electrochem. Soc. 164 (2017) C367–C375.

[13]   L. Wang, T. Shinohara, Z. B.-P. Zhang, Corrosion behavior of Mg, AZ31, and AZ91 alloys in dilute NaCl solutions, J. Solid State Electrochem. 14 (2010) 1897–1907.

[14]   A. Samaniego, I. Llorente, S. Feliu, Combined effect of composition and surface condition on corrosion behaviour of magnesium alloys AZ31 and AZ61, Corros. Sci. 68 (2013) 66–71.

[15]   G. Williams, H. ap Llwyd Dafydd, R. Grace, The localised corrosion of Mg alloy AZ31 in chloride containing electrolyte studied by a Scanning Vibrating Electrode Technique, Electrochim. Acta. 109 (2013) 489–501.

[16]   O. Lunder, J.E. Lein, S.M. Hesjevik, T.K. Aune, K. Nişancioğlu, Corrosion morphologies on magnesium alloy AZ91, Mater. Corros. 45 (1994) 331–340.

[17]   P. Schmutz, V. Guillaumin, R.S. Lillard, J.A. Lillard, G.S. Frankel, Influence of dichromate ions on corrosion processes on pure magnesium, J. Electrochem. Soc. 150 (2003) B99.

[18]   G. Williams, R. Grace, Chloride-induced filiform corrosion of organic-coated magnesium, Electrochim. Acta. 56 (2011) 1894–1903.

[19]   G. Williams, N. Birbilis, H.N. McMurray, Controlling factors in localised corrosion morphologies observed for magnesium immersed in chloride containing electrolyte, Faraday Discuss. 180 (2015) 313–330.

[20]   G. Williams, K. Gusieva, N. Birbilis, Localized corrosion of binary Mg-Nd alloys in chloride-containing electrolyte using a Scanning Vibrating Electrode Technique, Corrosion. 68 (2012) 489–498.

[21]   J.R. Kish, G. Williams, J.R. McDermid, J.M. Thuss, C.F. Glover, Effect of grain size on the corrosion resistance of friction stir welded Mg alloy AZ31B joints, J. Electrochem. Soc. 161 (2014) C405–C411.

[22]   E. Michailidou, H.N. McMurray, G. Williams, Quantifying the role of transition metal electrodeposition in the cathodic activation of corroding magnesium, J. Electrochem. Soc. 165 (2018) C195–C205.

[23]   S. V Lamaka, D. Höche, R.P. Petrauskas, C. Blawert, M.L. Zheludkevich, A new concept for corrosion inhibition of magnesium: Suppression of iron re-deposition, Electrochem. Commun. 62 (2016) 5–8.

[24]   D. Höche, C. Blawert, S. V Lamaka, N. Scharnagl, C. Mendis, M.L. Zheludkevich, The effect of iron re-deposition on the corrosion of impurity-containing magnesium, Phys. Chem. Chem. Phys. 18 (2016) 1279–1291.

[25]   R. Bolton, T. Dunlop, J. Sullivan, J. Searle, H. Heinrich, R. Westerwaal, C. Boelsma, G. Williams, Studying the influence of Mg content on the microstructure and associated localized corrosion behavior of Zn-Mg PVD coatings using SVET-TLI, J. Electrochem. Soc. 166 (2019) C3305–C3315.

[26]   G. Wu, Y. Fan, A. Atrens, C. Zhai, W. Ding, Electrochemical behavior of magnesium alloys AZ91D, AZCe2, and AZLa1 in chloride and sulfate solutions, J. Appl. Electrochem. 38 (2008) 251–257.

[27]   M. Zhao, M. Liu, G. Song, A. Atrens, Influence of pH and chloride ion concentration on the corrosion of Mg alloy ZE41, Corros. Sci. 50 (2008) 3168–3178.

[28]   F. El-Taib Heakal, A.M. Fekry, M.Z. Fatayerji, Influence of halides on the dissolution and passivation behavior of AZ91D magnesium alloy in aqueous solutions, Electrochim. Acta. 54 (2009) 1545–1557.

[29] L. Wang, T. Shinohara, B.-P. Zhang, Influence of chloride, sulfate and bicarbonate anions on the corrosion behavior of AZ31 magnesium alloy, J. Alloys Compd. 496 (2010) 500–507.

[30] F. El-Taib Heakal, A.M. Fekry, M. Abd El-Barr Jibril, Electrochemical behaviour of the Mg alloy AZ91D in borate solutions, Corros. Sci. 53 (2011) 1174–1185.

[31] G. Williams, H. Ap Llwyd Dafydd, R. Subramanian, H.N. McMurray, The influence of chloride ion concentration on passivity breakdown in magnesium, Corrosion. 73 (2017) 471–481.

[32] G. Williams, H. Neil McMurray, Localized corrosion of magnesium in chloride-containing electrolyte studied by a Scanning Vibrating Electrode Technique, J. Electrochem. Soc. 155 (2008) C340.

[33] H.S. Isaacs, The effect of height on the current distribution measured with a Vibrating Electrode Probe, J. Electrochem. Soc. 138 (1991) 722.

[34] Z.P. Cano, M. Danaie, J.R. Kish, J.R. McDermid, G.A. Botton, G. Williams, Physical characterization of cathodically-activated corrosion filaments on magnesium alloy AZ31B, CORROSION. 71 (2015) 146–159.

[35] S.H. Salleh, S. Thomas, J.A. Yuwono, K. Venkatesan, N. Birbilis, Enhanced hydrogen evolution on Mg(OH)2 covered Mg surfaces, Electrochim. Acta. 161 (2015) 144–152.

[36] M. Pourbaix, Atlas of electrochemical equilibria in aqueous solutions, Pergamon Press, Oxford, 1966.

Chapter 7

Conclusion and Further Work

Conclusions and Further Work

7.1   Conclusions

This thesis mostly focused on studying the corrosion-driven organic coating failures from Mg alloys, and more specifically the technologically important E717 Mg alloy, as well as two AZ-series alloys. From this investigation, two principal failure mechanisms were identified: cathodic delamination and filiform corrosion (FFC). These two mechanisms were extensively studied using the SKP and time-lapse photography that revealed important findings about the prevailing corrosion mechanisms of coated Mg alloys. The other focus of this thesis was to examine the localised corrosion behaviour of the E717 Mg alloy immersed in chloride-containing electrolyte using the SVET in conjunction with TLI.

Chapter 3: The failure mechanism of organic coatings from E717 Mg alloy surfaces was characterised by a combination of in-situ time-lapse photography and SKP analysis. Initiation of underfilm corrosion by application of HCl and $MgCl_2$ salts to a penetrative scribed coating defect produced filiform corrosion, while a halo detachment that expanded radially with time was formed when corrosion was inoculated with group I containing electrolyte. The latter phenomenon was then attributed to the ability of group I cations to sustain ionic current in high pH regions. In-situ SKP potentiometry analysis of the halo affected regions revealed that these areas are characterised by low corrosion potential values approaching those expected for actively corroding Mg, while the still intact regions adopted higher corrosion potentials. Time-lapse experiments conducted in the absence of oxygen indicated that this delamination phenomenon occurred both in the presence and absence of oxygen suggesting that the water reduction comprised the predominant underfilm cathodic reaction. Elemental analysis of the delaminated region using ToF-SIMS showed an abundance of group I cations, but no chloride similar to what is observed with cathodic delamination in other coated metals. All these observations led to the reporting of a cathodic delamination mechanism of organic coated Mg alloys where the Mg dissolution occurring at the coating defect is coupled with the underfilm cathodic hydrogen evolution and some oxygen reduction beneath the coating causing organic coating disbondment under conditions where cations can transport ionic current within a region of high alkalinity.

Chapter 4: A further study into the cathodic delamination on organic coated Mg alloys explored using in-situ SKP and Stratmann-type cells. This study is an extension of the coating delamination investigation presented in Chapter 3, where an effort was made to answer some questions that arose in the previous chapter. The SKP-derived delamination kinetics appeared to remain linear with time over protracted holding periods (>100 h) and under high RH while the group I cation type present in the initiating electrolyte did not affect the delamination rate contrary to what is normally observed for other metals coated with model organic coatings. These results provided confirmatory evidence to the preliminary findings from the previous chapter that the rate of the delamination process is not governed by the migration of cations to the front and further suggest that the rate limiting step is the electron transfer at the underfilm cathode. Further experiments conducted using the SKP and an organic coated E717 in the absence of oxygen revealed that the cathodic delamination proceeds in a similar manner as in air, albeit with slightly slower delamination rates signifying that although oxygen is not essential for coating delamination to take place, it is plausible for oxygen to play a minor role in the overall cathodic delamination process. These results suggest that the destruction of the polymer/Mg bonds was not caused by reactive intermediates produced during the cathodic oxygen reduction, ruling it out as a possible cause of the loss of coating adhesion. Additional SKP experiments on organic coated AZ31 and AZ91 Mg alloys showed that coating delamination also occurs in Al-Zn containing Mg alloys, with the AZ91 alloy exhibiting the highest resistance to coating disbondment. All findings presented in this chapter supported the cathodic delamination mechanism for organic coated Mg alloys suggested in the previous chapter.

Chapter 5: The anodic disbondment (filiform corrosion) of model organic coatings applied to E717, AZ31 and AZ91 Mg alloys was investigated using a combination of in-situ SKP potentiometry and time-lapse photography. Underfilm corrosion was initiated by injection of controlled quantities of $MgCl_2$, HCl and $FeCl_2$ into a penetrative coating defect for specimens held at constant relative humidity (RH) and room temperature. SKP potentiometry showed that the leading edge of the filament tracks exhibit more negative E_{corr} values compared to the intact uncorroded surface, while the filament tail regions adopted approximately 100 mV more negative E_{corr} values compared to the surrounding intact surface. FFC propagation rates, quantified by determining the underfilm corroded area with time using the time-lapse image sequences, seemed

to increase as a function of the logarithm of the chloride ion concentration. At protracted holding times, it was found that the FFC rate decreased and this was attributed to the progressive depletion of the chloride ions from the filament head in the tail regions as was confirmed by using SEM-EDX. Additional experiments to ascertain the influence of the relative humidity (RH) on the FFC showed that the propagation rate increases with increasing levels of RH, however a blistering phenomenon was observed with samples exposed to 99% RH, while exposure to RH<31% produced no FFC. From this series of experiments, it was found that the water availability in the holding environment plays an important role in the FFC of coated Mg alloys, whereas the absence of oxygen did not appear to have any significant effect. Finally, FFC experiments conducted on PVB coated AZ31 and AZ91 Mg alloys revealed that both alloys were susceptible to FFC with the later alloy showing the highest resistance to FFC. Overall, the mechanism of FFC propagation in these coated Mg alloys was consistent with chloride-induced anodic dissolution at the disbondment front coupling with reduction of water on a cathodically activated corroded surface immediately behind, similar to what is observed for pure Mg.

Chapter 6: The SVET in conjunction with TLI was used to investigate the influence of the chloride ion concentration on localised corrosion propagation of the E717 Mg alloy. It was found that this Mg alloy undergoes localised corrosion in a filiform-like manner where the leading edges of the filaments are the anodes that transverse the surface leaving a cathodically activated dark surface behind. The intensity of the local anodes seemed to be dependent on the chloride ion concentration of the solution where higher local anodic current densities are observed with increasing concentration along with progressively higher rates of volumetrically determined hydrogen evolution. The filiform-like propagation was characterised by two phases: an initial slower phase and a second faster phase where the filaments coalesce creating a unified localised corrosion front. From this series of experiments, it was also found that the filiform-like corrosion features propagated at a faster rate as the chloride ion concentration of the electrolyte was increased. The breakdown potential measured using time-dependent free corrosion potential transients and potentiodynamic polarisation at neutral and elevated pH, respectively, appeared to vary with the logarithm of chloride ion concentration and the time for localised corrosion initiation progressively increased with decreasing chloride concentration.

7.2 Future Work

This thesis was aimed to increase the understanding of the corrosion-driven coating failures of Mg alloys, as well as to study the corrosion behaviour of uncoated Mg alloys in aqueous media. In conclusion of this thesis, a list of possible suggestions for future work is provided below to further improve the understanding of the prevailing corrosion mechanisms of Mg alloys with the aim of facilitating their usage in the automotive industry.

With regards to the coating delamination phenomenon observed on Mg alloys, this thesis has already ruled out some modes of coating de-adhesion from Mg alloy surfaces and suggested a few possible modes using electrochemical methods, time-lapse photography and surface characterisation techniques. However, there is room for additional work to be performed to clarify the exact nature of the physical and/or chemical processes directly responsible for the loss of organic adhesion from the Mg alloy surface. It is recommended that future work should be conducted using other surface analysis techniques (e.g. X-ray photoelectron spectroscopy (XPS)) to provide further information about the interfacial bonding mechanisms and the interface chemistry between the organic coating and the Mg surface before and after coating delamination.

It has been noted in Chapter 4, that the SKP-derived corrosion potential profiles of the delaminated areas on the coated AZ31 did not follow the trend observed with other Mg alloys and this was postulated to be due to the different microstructure of this particular alloy. It is therefore suggested that further experiments can be carried out using XPS to investigate the nature of the surface areas affected by delamination (before/after) in order to confirm this assertion.

Overall, the AZ91 Mg alloy appeared to have the highest resistance to organic coating delamination and filiform corrosion; the good corrosion performance of this alloy was attributed primarily to its high Al content and unique microstructure. A detailed study on the microstructure of this alloy and its subsequent film formation could potentially provide useful insights on how to increase the resistance of other alloys to corrosion-driven coating failures.

In Chapter 6, the hydrogen gas evolution from corroding Mg alloy surfaces was collected volumetrically by using a conically ended burette placed on top of the sample with the aim of determining the influence of [Cl$^-$] on bulk corrosion rates. Although this method can give a good assessment of the hydrogen evolution rates and has been widely used in the literature, a gravimetric

method based on the buoyant force exerted by hydrogen gas could potentially provide a higher level of accuracy as well as better collection efficiency than the conventional volumetric method.

Finally, although this thesis was not focused on inhibiting the aforementioned corrosion-driven coating failures on Mg alloys, future research can take into consideration the findings presented herein and identify potential inhibition strategies to improve the corrosion performance of these systems. These strategies could potentially include in-coating dispersed inhibitor systems (e.g. smart release inhibitor pigments-ion exchange) and/or Mg alloy pre-treatments/conversion coatings (e.g. silane or titanium/zirconium).